

THÈSE

En vue de l'obtention du

DOCTORAT DE L'UNIVERSITÉ DE TOULOUSE

Délivré par :

Institut National Polytechnique de Toulouse (Toulouse INP)

Discipline ou spécialité :

Energétique et Transferts

Présentée et soutenue par :

M. QUENTIN DOUASBIN

le vendredi 30 mars 2018

Titre :

Acoustic waves in combustion devices: interactions with flames and boundary conditions

---

Ecole doctorale :

Mécanique, Energétique, Génie civil, Procédés (MEGeP)

Unité de recherche :

Institut de Mécanique des Fluides de Toulouse (I.M.F.T.)

Directeur(s) de Thèse :

M. THIERRY POINSOT

M. LAURENT SELLE

Rapporteurs :

M. PASCAL BRUEL, UNIVERSITE DE PAU ET DES PAYS DE L ADOUR

M. WOLFGANG POLIFKE, TECHNISCHE UNIVERSITAT MUNICH

Membre(s) du jury :

M. FRANCK NICOUD, UNIVERSITE DE MONTPELLIER, Président

M. LAURENT SELLE, CNRS TOULOUSE, Membre

M. SÉBASTIEN DUCRUIX, CENTRALESUPELEC GIF SUR YVETTE, Membre

M. THIERRY POINSOT, CNRS TOULOUSE, Membre

Remerciements

Je remercie mes directeurs de thèses, Dr. Thierry Poinsot et Dr. Laurent Selle, pour m'avoir accueilli dans leur équipe de recherche, pour leurs précieux conseils et pour l'ambiance de travail, à la fois pleine d'énergie et détendue, qu'ils arrivent à créer et entretenir.

Je tiens à remercier tout particulièrement Prof. Carlo Scalo pour m'avoir reçu à Purdue University et de m'avoir tout de suite intégré dans son groupe de recherche comme un de ses étudiants.

Evidemment, ces trois années passées à l'IMFT n'auraient pas été les mêmes sans nos discussions enflammées chaque midi. Je remercie tous les titulaires, post-docs, thésards, stagiaires et l'ensemble du personnel administratif pour avoir rendu ces années passées ensemble si agréables.

Merci à tous mes amis de Damville, de Rouen, de Paris, de Cranfield, de Toulouse, de Purdue, ...bref, merci à vous tous. Ces trois années passées à Toulouse m'ont permis de rencontrer beaucoup de personnes fantastiques et je tiens à les remercier tout particulièrement.

Je souhaite remercier ma famille pour avoir toujours cru en moi et pour m'avoir montré comment affronter toutes les épreuves avec le sourire.

Last but not least, Morgane, je tiens à te remercier du fond du cœur pour ton soutien inépuisable et pour toute la joie que tu m'apportes chaque jour.

Merci.

Abstract

Combustion devices are prone to combustion instabilities. Classically, they arise from a constructive coupling between the unsteady heat release rate of the flame and the resonant acoustic modes of the entire system. The occurrence of such instabilities can pose a threat to both performance and integrity of combustion systems. Although these phenomena have been known for more than a century, avoiding their appearance in industrial engines is still challenging.

The objective of this thesis is threefold: (1) study the dynamics of the resonant acoustic modes, (2) investigate the flame response of a liquid rocket engine under unstable conditions using Large Eddy Simulation (LES) and (3) derive, use and study Time Domain Impedance Boundary Conditions (TDIBCs), *i.e.* boundary conditions modeling complex acoustic impedances.

First, a new method for the study of the dynamics of the entire acoustic field from a few pressure probes is derived and used to analyze the acoustic field of a 42-flame liquid rocket engine exhibiting transverse combustion instabilities. The results show that it can track the evolution of each of the unstable acoustic modes in time and reconstruct the entire acoustic pressure and velocity fields with good precision.

Second, a study of the individual flame response to transverse acoustic modes of a 42-injector H_2/O_2 liquid rocket engine is performed from time-resolved 3D LES results. For both considered modes, the results show that the flame response is maximum at the pressure antinodes in the chamber. A flame response mechanism is proposed in which the bulk pressure variation at the injector outlet generates unsteady shear through the variation of the hydrogen velocity, ultimately resulting in heat release rate fluctuations.

Finally, a TDIBC method is presented and a novel formulation based on the reflection coefficient is proposed. A modeling strategy allowing to impose a time-delay to the acoustic waves reflection is derived and applied in time domain simulations in order to account for truncated portions of the physical domain. The results show that the time-delay is accurately reproduced in both 1D and 2D reactive DNS and the boundary condition is applied to combustion instability prediction with an excellent agreement. The proposed formalism is compared to another TDIBC method based on state-space modeling and the formal equivalence between the two approaches is demonstrated.

Résumé

Les systèmes de combustion sont sujets aux instabilités de combustion (IC). Elles résultent d'un couplage constructif entre le taux de dégagement de chaleur instationnaire et des modes acoustiques du système. Les IC peuvent mettre en danger la performance et l'intégrité des systèmes de combustion. Même si ces phénomènes sont connus depuis plus d'un siècle, éviter qu'elles aient lieux dans les chambres de combustions industrielles reste difficile.

Les objectifs de cette thèse sont les suivants : (1) étudier la dynamique des modes acoustiques, (2) analyser la réponse de flamme d'un moteur de fusée à propergol liquide H_2/O_2 (appelé "BKD"), sujet aux IC, à l'aide de la Simulation aux Grandes Echelles (SGE) et (3) dériver, utiliser et étudier des conditions limites permettant d'imposer des impédances acoustiques complexes en SGE.

Tout d'abord une nouvelle méthode, visant à étudier la dynamique des modes acoustiques à partir d'un faible nombre de capteurs de pression, est proposée. Elle est utilisée afin d'analyser le champ acoustique dans le BKD. Les résultats montrent que la méthode permet de suivre l'évolution temporelle des modes instables et qu'il est possible de reconstruire le champ acoustique entier avec une bonne précision.

Ensuite, une étude de la réponse de flamme aux oscillations acoustiques transverses est réalisée pour chacune de 42 flammes du BKD en analysant une base de données provenant de la SGE 3D résolue en temps. Pour les modes considérés, la réponse de flamme est maximale lorsque celles-ci font face aux ventres de pression dans la chambre de combustion. Un mécanisme de réponse de flamme est proposé dans lequel les variations de pression à la sortie des injecteurs génèrent une fluctuation du cisaillement de la couche de mélange par des fluctuations de vitesse dans l'injecteur d'hydrogène. A leur tour, celles-ci provoquent des fluctuations de taux de dégagement de chaleur des flammes.

Enfin, une méthode appelée "TDIBC", permettant d'imposer des impédances acoustiques complexes aux conditions limites, est présentée et une nouvelle formulation basée sur le coefficient de réflexion est proposée. Une stratégie de modélisation permettant d'imposer un retard temporel à la réflexion d'ondes acoustiques est dérivée et appliquée dans des simulations temporelles, afin de modéliser la propagation d'ondes dans un tronçon tronqué du domaine physique. Les résultats montrent que le retard temporel est reproduit avec précision dans des Simulations Numériques Directes 1D et 2D réactives. La condition limite est appliquée à la prédiction d'IC en utilisant des domaines tronqués et l'accord avec la simulation non-tronquée est excellent. Dans un dernier temps, le formalisme mathématique proposé est comparé à une méthode similaire utilisant un modèle de représentation d'état et l'équivalence formelle entre les deux approches est démontrée.

Contents

Page

1 Introduction **1**
- 1.1 Background . . . 1
- 1.2 Prediction of combustion instabilities . . . 3
  - 1.2.1 The brute force approach . . . 4
  - 1.2.2 Joint use of an acoustic solver and a flame-response model . . . 5
  - 1.2.3 Low Order Models . . . 6
- 1.3 Objective & Outline of the work . . . 7

2 Governing equations & numerical tools for thermoacoustics **11**
- 2.1 Governing equations . . . 11
  - 2.1.1 Navier-Stokes equations for reactive flows . . . 11
  - 2.1.2 Equation of state for a multi-species gas . . . 12
  - 2.1.3 Acoustic equations . . . 13
- 2.2 Numerical tools . . . 18
  - 2.2.1 AVBP . . . 18
  - 2.2.2 AVSP . . . 19

I Transverse combustion instabilities in a liquid rocket engine **21**

3 Modal Analysis & Reconstruction of 3D acoustic fields **25**
- 3.1 Introduction . . . 25
- 3.2 Method . . . 27
  - 3.2.1 Modal decomposition . . . 27
  - 3.2.2 Acoustic field reconstruction . . . 32
- 3.3 Validation . . . 35
  - 3.3.1 Test case presentation . . . 35
  - 3.3.2 Helmholtz simulation . . . 36
  - 3.3.3 Temporal simulation . . . 37
  - 3.3.4 Instantaneous Modal Decomposition . . . 38
  - 3.3.5 Acoustic pressure reconstruction . . . 42
  - 3.3.6 Acoustic velocity reconstruction . . . 46

3.4 Conclusion . . . 48

4 Acoustic field in the BKD: analysis & reconstruction 49
4.1 Introduction . . . 49
4.1.1 Experimental setup . . . 49
4.1.2 Real gas effects . . . 51
4.1.3 Transverse combustion instabilities in the BKD . . . 54
4.1.4 Helmholtz simulation of the BKD . . . 55
4.2 IMD of LES signals . . . 59
4.2.1 Acoustic triggering & initial solutions . . . 59
4.2.2 Instantaneous Modal Decomposition of LES pressure signals . . . 61
4.2.3 Results . . . 63
4.3 IMD of experimental signals . . . 76
4.4 Conclusion . . . 79

5 Flame response to transverse acoustic modes in LRE 81
5.1 Introduction . . . 82
5.2 LES dataset . . . 83
5.3 Description of the limit cycle . . . 84
5.4 Maps of flame response . . . 86
5.5 Individual injector dynamics . . . 88
5.6 Conclusions . . . 91

II Acoustic boundary conditions for time domain simulations 93

6 Time domain impedance boundary condition 97
6.1 Introduction . . . 98
6.2 Method . . . 101
6.2.1 Time domain imposition of complex wall softness coefficient . . . 101
6.2.2 Time domain imposition of complex reflection coefficient . . . 103
6.2.3 Block diagram representation of multi-pole TDIBC . . . 103
6.3 Validation of reflection-coefficient-based TDIBC . . . 104
6.3.1 Validation of TDIBC based on reflection coefficient: single-pole . . . 106
6.3.2 Validation of TDIBC based on reflection coefficient: multi-pole . . . 109
6.4 Conclusion . . . 113

7 Delayed-time domain impedance boundary condition 115
7.1 Time-delayed reflection coefficient . . . 115
7.2 Methodology . . . 116
7.2.1 Pole Base Function properties . . . 118
7.2.2 Iterative multi-pole modeling technique . . . 120
7.3 Validation for one-dimensional waves . . . 122

7.3.1 Test case presentation . . . 122
7.3.2 Delayed reflection coefficient modeling . . . 122
7.3.3 One-dimensional wave propagation . . . 123
7.4 Validation for a combustion chamber . . . 129
7.4.1 Experimental setup . . . 129
7.4.2 Numerical setup . . . 130
7.4.3 D-TDIBC: reflection coefficient model . . . 131
7.4.4 Results and discussion . . . 131
7.5 Conclusion . . . 134

8 TDIBC: the state-space approach **135**
8.1 Introduction to the state-space representation . . . 135
8.1.1 The state equation . . . 136
8.1.2 The output equation . . . 138
8.1.3 Block diagram of a state-space . . . 139
8.2 CBSBC: the state-space model approach for TDIBC . . . 140
8.2.1 Characteristic Based State-space Boundary Condition: transfer function modeling . . . 141
8.3 Link between state-space and pole & residue method . . . 143
8.3.1 Single pole base function as a controllable form state space . . . 143
8.3.2 Multiple Pole Base Functions as a controllable form state space . . . 144
8.3.3 Numerical simulations: CBSBC & pole & residue . . . 149
8.4 Discussion . . . 151
8.4.1 Limitations . . . 151
8.4.2 Perspectives . . . 152
8.5 Conclusion . . . 154

Conclusion and perspectives **157**

A D-TDIBC Model: 1D wave propagation problem **161**

B D-TDIBC Model: 2D reactive DNS of the INTRIG Burner **163**

C Laplace transform **165**

D Single BKD flame simulation **167**

Bibliography **170**

List of Figures

1.1 Damaged (left) and undamaged (right) burner assembly. Reproduced from [16, 17]. 2

2.1 One-dimensional wave propagation. 15
2.2 Pressure of transverse acoustic modes in a cylindrical cavity. 17

3.1 Real part, imaginary part and modulus of an analytic pressure signal $p^{\mathrm{A}}(t)$. . 28
3.2 Illustrations of the determination of the complex coefficients a_1, a_2 (and a_3) by projection (Eq. 3.11) for a time $T = t_j$ considering two (a) and (three) modes. 31
3.3 Simplified LRE configuration setup. 35
3.4 Modulus and argument of the pressure eigenmodes $1T$ and $1T'$. 37
3.5 Pressure modulus over the x axis for injectors facing a pressure anti-node. . . 38
3.6 (a) Pressure probes located on the "Ring C" at $x = 5.5$ mm, (b) pressure traces of the simplified LRE configuration. 39
3.7 IMD complex amplitudes a_{1T} and $a_{1T'}$ obtained by projection. 41
3.8 Acoustic pressure signals from temporal simulation ("AVBP") and signals reconstructed ("IMD Rec.") at Ring C (data used for IMD). 42
3.9 Acoustic pressure signals from temporal simulation ("AVBP") and signals reconstructed ("IMD Rec.") at Ring C (data not used for IMD). 43
3.10 Drawing of the chamber and injector probes' location. 43
3.11 Acoustic pressure signals from temporal simulation ("AVBP") and signals reconstructed ("IMD Rec.") in the chamber. 44
3.12 Acoustic pressure signals from temporal simulation ("AVBP") and signals reconstructed ("IMD Rec.") in an injector A. 44
3.13 Acoustic pressure signals from temporal simulation ("AVBP") and signals reconstructed ("IMD Rec.") in an injector N. 45
3.14 Acoustic velocity signals from temporal simulation ("AVBP") and signals reconstructed ("IMD Rec.") in the chamber. 46
3.15 Acoustic velocity signals from temporal simulation ("AVBP") and signals reconstructed ("IMD Rec.") in a injector N. 46
3.16 Acoustic velocity signals from temporal simulation ("AVBP") and signals reconstructed ("IMD Rec.") in an injector A. 47

4.1 Drawing of the BKD setup: (a) Detailed view of the HF measurement ring and (b) split view of the BKD. 50
4.2 LN_2/GHe coaxial jet. Reproduced from Mayer and Smith [141] 51
4.3 Phase diagram for a single species. The pressure P and the temperature T of the triple and the critical points are indicated by the subscripts $_T$ and $_C$. . . . 53
4.4 Power Spectral Density of p' for (a) LP1 and (b) LP4. 54
4.5 Real part of pressure eigenmodes $1T$, $1T'$ and $1R$. 58
4.6 Pressure perturbation shape $p'_{1\mathrm{T}}$ superimposed to the thermoacoustically stable unsteady pressure field. (Reproduced from [121]) 60
4.7 Nodal line orientation of initial solution of the 4 LESs used in the study. . . . 61
4.8 Pressure traces LP4 LES90. 62
4.9 Temporal evolution of the modulus of the complex amplitudes corresponding to the modes $1T$, $1T'$ and $1R$ for $\theta = 0°$, $\theta = 45°$, $\theta = 90°$ and $\theta = 135°$. . . . 64
4.10 Maximum of acoustic pressure in time for the four cases. 65
4.11 Power Spectral Density (PSD) of the complex amplitudes for the four cases. . 66
4.12 Angle θ of the nodal line of the first tangential mode in time using the complex amplitudes a_{1T} and $a_{1T'}$. 68
4.13 Probability Density Functions (PDFs) of the angle θ on 10° intervals for the four cases. 69
4.14 Acoustic pressure from LES ("AVBP") and signals reconstructed ("IMD Rec.") at Ring C (data used for IMD). 70
4.15 Acoustic pressure from LES ("AVBP") and signals reconstructed ("IMD Rec.") at Ring C (data not used for IMD). 71
4.16 Acoustic pressure from LES ("AVBP") and signals reconstructed ("IMD Rec.") in the chamber. 71
4.17 Drawing of the injector probes' location. 72
4.18 Acoustic pressure from LES ("AVBP") and signals reconstructed ("IMD Rec.") in an injector A. 72
4.19 Acoustic pressure from LES ("AVBP") and signals reconstructed ("IMD Rec.") in an injector N. 72
4.20 Acoustic velocity v' from LES ("AVBP") and signals reconstructed ("IMD Rec.") at Ring C (data used for IMD). 73
4.21 Acoustic velocity v' from LES ("AVBP") and signals reconstructed ("IMD Rec.") at Ring C (data not used for IMD). 73
4.22 Acoustic velocity v' from LES ("AVBP") and signals reconstructed ("IMD Rec.") in the chamber. 74
4.23 Acoustic velocity u' from LES ("AVBP") and signals reconstructed ("IMD Rec.") in an injector A. 74
4.24 Acoustic velocity v' from LES ("AVBP") and signals reconstructed ("IMD Rec.") in an injector N. 75
4.25 Modulus of complex amplitudes in time for (a) LP1 and (b) LP4. 76
4.26 Power Spectral Density for the complex amplitudes a_i for (a) LP1 and (b) LP4. 77

4.27 Histograms of the percentage of the presence of the angle θ on 10° intervals for the operating points (a) LP1 and (b) LP4. 78

5.1 Overview of the computational domain for the BKD (top). Transverse (bottom left) and longitudinal (bottom right) cuts of instantaneous temperature field. . 84
5.2 Power spectral density of pressure fluctuations at the chamber wall 5.5 mm downstream the injection plate. 85
5.3 Spatial structure of the pressure fluctuations for the two dominant frequencies of Fig. 5.2 from the 3D-FT of 200 instantaneous LES fields. 85
5.4 Maps of unsteady heat release rate integrated around each flame. 86
5.5 Maps of individual flames Rayleigh index for both 1T and 1R modes, normalized by the total Rayleigh index of the chamber. 87
5.6 Comparison of heat release rate fluctuations for a: A-flame (thin gray line) and N-flame (bold black line). 88
5.7 Schematic of the coaxial injector and reference surfaces for the extraction of velocities and pressure fluctuations used to evaluate the flame responses. . . . 89
5.8 Velocity fluctuation at the location of the recess: $u'_{\mathrm{H_2}}$ (thin gray line) and $u'_{\mathrm{O_2}}$ (bold black line). 89
5.9 Fluctuations over two periods of the 1T mode ($T = 1/f_1$) for an A-flame: p' (solid line), $u'_{\mathrm{H_2}}$ (dashed line) and q' (dotted line). Reference surfaces are indicated in Fig.5.7 90

6.1 Orientation of ingoing and outgoing acoustic waves A_n^{in} and A_n^{out} on an Impedance Boundary Condition defined from the outward pointing normal $\vec{n}$. 99
6.2 Block diagram of a multi-pole TDIBC under Fung and Ju's formalism. 104
6.3 Initial solution for the outgoing wave $A_n^{\mathrm{out}}(x, t = 0)$ for $A = 1$, $\alpha = 0.8$ and $k = 7$ in Eq. 6.17. 105
6.4 Modulus of the Fourier transform of the initial temporal Gaussian wave $\mathcal{F}(A_n^{\mathrm{out}}(x = x_{\mathrm{BC}}, t))$. 106
6.5 Modulus (a) and phase (b) of the reflection coefficient modeled by the boundary condition for p_1 and μ_1 in Eq. 6.21. 108
6.6 Validation of TDIBC based on the reflection coefficient for a single pair of conjugate pole p_1 and residue μ_1 ($n_0 = 1$ in Eq. 6.14). The ingoing wave imposed by TDIBC corresponds to model reflection coefficient R_{BC} (*cf.* Fig. 6.5) as it is exactly equal to the analytical solution. The analytical solution is computed by resolving the integral in Eq. 6.20. 108
6.7 Modulus (a) and phase (b) of each sub-system $R_{\mathrm{k}}(\omega)$ in Table 6.1. 110
6.8 Modulus (a) and phase (b) of the reflection coefficient $R_{\mathrm{BC}}(\omega)$ modeled by the boundary condition the three poles & residues presented in Table 6.1. 110
6.9 Output signal (I_k) from each sub-system R_k giving the global response, the ingoing wave A_n^{in}, of the multi-pole TDIBC (black dashed line). 111
6.10 Ingoing wave prescribed by TDIBC compared to the analytical solution. . . . 112

7.1 Typical case where the computational domain can be cut at $x = x_1$. The propagation of acoustic waves in the truncated portion (between x_1 and x_2) is accounted for by the reflection coefficient R_τ (Eq. 7.1). 116
7.2 Acoustic variables for two theoretical limit cases: (a) the flanged open end, and (b) the closed end (hard wall) cases. Both configurations are fully reflective and have a purely real reflection coefficient R at all frequencies in $x = x_2$. The truncation of the grey areas can be modeled by the imposition of a time-delay τ. The delayed reflection coefficient R_τ, expressed in $x = x_1$, is complex. At the bottom of the figure both real (solid lines) and imaginary parts (dashed lines) of R_τ and R are shown on the left and right-hand sides, respectively. . . 117
7.3 Real part of a typical PBF R_k (Eq. 7.3). Three properties are visualized: $\omega_{0,k}$, $h_{0,k}$ and $\Delta\omega_\epsilon$. At the resonant angular frequency $\omega_{0,k}$, the real part of R_k is maximum. The peak heigh $h_{0,k}$ is the value of $R_k(\omega)$ at $\omega = \omega_{0,k}$. For a given percentage ϵ ($\epsilon \in [0,\ 1]$), the half-width $\Delta\omega_\epsilon$ is defined on the right-hand side. ω_- and ω_+ are the solutions of the equation $\Re(R_k) = \epsilon$ and are used to define the width. 118
7.4 (a) Influence of the c_k parameters for $f_{0,k} = \frac{1}{2\pi}\omega_{0,k} = 100$ Hz and $h_{0,k} = 1$. (b) Real part of a purely delayed reflection coefficient R_τ for a time-delay τ. The real part is a periodic function (cosine) of period $T = \frac{2\pi}{\tau}$. 120
7.5 (a) Initial solution and visualization of the computational (Ω_c) and modeled (Ω_m) domains. (b) Theoretical (gray solid line) and filtered (black solid line) delayed reflection coefficients. The filter shape (Eq. 7.12) is shown (black dashed line). 124
7.6 Reflection coefficient $R_{\mathrm{BC}}(\omega)$ modeled by the Iterative Multi-Pole Modeling Technique algorithm (Algorithm 1 in Sec. 7.2.2) a several iterations. An accurate model is obtained for $n_0 = 20$, where n_0 is the number of PBF R_k as in Eq. 7.2. 125
7.7 Propagation and reflection of a Gaussian pressure wave in the domain $\Omega_c + \Omega_m$ by simulating only Ω_c. The acoustic properties of Ω_m are imposed using D-TDIBC. 126
7.8 (a) Acoustic velocity (dashed line) and pressure (solid line with circles) at the boundary condition. (b) Temporal response of 20 PBF (dashed and dotted lines) and of the ingoing wave imposed by the D-TDIBC (black solid line) . . 128
7.9 Sketch of a transverse cut of the INTRIG Burner (top). The computational domain of the FULL configuration goes from the glass balls array ($x = -0.367$ m) to the exhaust ($x = 0.35$ m) while it is cut (at $x = x_{\mathrm{BC}} = 0.1$ m) in the TRUNCATED configuration. A zoom (bottom) of the flame region of the initial solution used in DNS is shown. The light grey and dark grey regions represent the zero and high CO_2 mass fraction levels. The streamlines are plotted in white. 129
7.10 Schematic of the computational domains and BC used for the two simulations: FULL and TRUNCATED cases. 130

7.11 Model of the delayed reflection coefficient $R_{\mathrm{BC}}(\omega)$ with $n_0 = 18$ (*cf.* Eq. 6.14) for a time-delay of $\tau = 0.30$ ms in the laminar combustor of Fig. 7.9. 131
7.12 (a) spectra obtained for the FULL and the TRUNCATED simulations. D-TDIBC allows an accurate prediction of the thermoacoustic stability observed in the FULL configuration. The spectra are based on a probe located at $x = -8.5$ mm. The shapes of the first (b), second (c) and third (d) modes are shown. The markers correspond to the probes in the simulation (lines are added for the sake of clarity). 132

8.1 Linear time-invariant system with n state variables, r inputs and m outputs. . 136
8.2 Block diagram of a linear time-invariant system modeled using a state-space representation. 139
8.3 Comparison of the ingoing wave corresponding to the analytical solution, the state-space model built from the multi-pole TDIBC model and the multi-pole TDIBC model. 150
8.4 Comparison the ingoing wave for the analytical solution, the CBSBC-TF model built from the multi-pole model and the multi-pole model. 151
8.5 Block diagram of a example of Time Domain Impedance Boundary Conditions used in cascade. 153

D.1 Longitudinal cuts through the mesh for the LES of the single injector. 168
D.2 Instantaneous temperature iso-surface colored by axial velocity, without acoustic forcing. 168
D.3 LES of the single injector: longitudinal cut of temperature and iso-surface of density ($\rho = 500$ kg.m^{-3}) colored by axial velocity. 169

List of Tables

3.1 Geometric properties of the Simplified LRE configuration. 35
3.2 Mean flow conditions for the Simplified LRE case. 36

4.1 Injection conditions in the BKD experiment for the two load points considered. "ROF" denotes the Oxidizer/Fuel mass ratio. and the "i" subscript refers to the values at the injection stage. 51
4.2 Critical conditions for H_2 and O_2. 53

6.1 Parameters of the poles & residues used for the validation of the multi-pole TDIBC. 109

7.1 Parameters used in the two simulations. 130

A.1 poles & residues used in the one-dimensional pure delayed Gaussian wave propagation problem. 161

B.1 poles & residues used in the two-dimensional reactive DNS of the INTRIG Burner. 163

Chapter 1

Introduction

1.1 Background

The development of clean, efficient and sustainable energy systems has become a central challenge in our society. Today, combustion still provides 80 to 90% of the world's energy needs [1, 2]. Most scenarios forecast that combustion will stay predominant in our energy usage [3]. Although combustion has been studied for decades, it is still an active field of research motivated by the reduction of pollutant emission.

The problem stems from the fact that combustion releases pollutants into the atmosphere. The research effort to reduce pollutant emission concentrates particularly on: (1) carbon dioxide (CO_2) and (2) nitric oxide (NO) and nitrogen dioxide (NO_2) often referred to as "NO_x". CO_2 is the largest single source of greenhouse gas emissions from human activities. Apart from being greenhouse effect gases, NO_x are also considered as air pollutants as they may cause or worsen respiratory diseases.

On one hand, the mass of CO_2 emitted is given by the mass of hydrocarbon fuel burnt in the combustion chamber. The only lever to diminish the CO_2 emissions is to increase combustion systems' efficiency. In practice, in most combustion systems, nearly all the fuel is burnt and the optimization of such devices focuses on the efficiency of energy conversion (*e.g.* in the form of mechanical or electrical energy).

On the other hand, NO_x are highly dependent of the combustion conditions. For instance, for premixed combustion, NO_x production can be minimized by lowering the flame temperature as much as possible [4]. Other air pollutants, *e.g.* carbon monoxide (CO), follow opposite trends so that low flame temperature yields high emission levels.

In order to cope with pollutant emission limits imposed by the legislation, the industry needs to develop combustion devices that can perform in a narrow operating range in the lean combustion regime [5]: all reactants are mixed before combustion and the gas composition is such that the oxidizer is in excess, *i.e.* the gaseous mixture fuel-oxidizer ratio is below stoichiometry

One of the benefits of lean combustion is that the flame temperature reached is lower than

the adiabatic flame temperature, hence reducing the NO_x production. One of the drawbacks of this combustion regime is that the systems become prone to combustion instabilities (CIs) [6].

Like combustion noise, they arise from perturbations of the heat release rate [7–10] which in turn cause flow perturbations and sound wave emissions [11].

When the heat release rate perturbations are caused by turbulence, they are mostly incoherent and they radiate low-frequency broadband sound waves [12]. If there is no coherent feedback from the combustion chamber then the sound emitted is referred to as "combustion noise" [13].

However, in some cases the feedback from the combustion chamber becomes coherent and the heat release rate perturbations become tuned at resonant acoustic eigenfrequencies of the entire combustion system [14, 15]. Such a feedback loop may result in self-sustained oscillations due to the constructive coupling between the unsteady heat release rate and acoustic perturbations. These phenomena are called CIs, or thermoacoustic instabilities. Figure 1.1 shows a burner assembly before and after the failure of the engine due to the occurrence of CIs.



Figure 1.1: Damaged (left) and undamaged (right) burner assembly. Reproduced from [16, 17].

For high-performance engines such as liquid rocket engines (LRE), the energy density is very high. For instance, the F-1 engine developed for the Apollo mission has a power density of 22 $\mathrm{GW\,m^{-3}}$ [18]. This is to be compared with typical solid rocket engines and fighter aircraft's afterburner which have a power density of about 1 $\mathrm{GW\,m^{-3}}$ and 0.3–0.4 $\mathrm{GW\,m^{-3}}$, respectively [18]. With such power densities, high performance systems are extremely prone to combustion instabilities as only a minute fraction of the energy released by combustion (as low as 10^{-4}) is sufficient to cause pressure oscillations resulting in structural vibration and thrust fluctuations large enough to endanger the integrity of the system [19].

A famous example of this phenomenon is the aforementioned F-1 engine development where CIs were encountered and billions of dollars were spent to find a solution to mitigate them [20, 21]. To reach performance and stability requisites, 108 different injector designs and 1332 full-scale hot-fire tests were necessary [20, 22].

To reduce pollutant emissions and to develop more efficient high-performance engines it is, hence, essential to: (1) be able to predict the appearance of CIs in real combustion devices and (2) to eliminate such instabilities when they emerge.

1.2 Prediction of combustion instabilities

CIs in real engines are still challenging to master as they generally occur in the last stages of development and are difficult to predict [21]. CI prediction requires, on one hand, an accurate prediction of reacting flows so that it relies heavily on fluid mechanics, thermodynamics, kinetics and transport and, on the other hand, the use of many fields of physics such as, for instance, acoustics, control theory, heat transfers and hydrodynamic stability.

It is also a multiscale problem as the typical flame thickness is of the order of 100 µm [9] and the acoustic wavelengths to capture are typically of the order of a few meters [21]. Similarly, the typical sound speed in burnt gases is at least 600 $\mathrm{m\,s^{-1}}$ and the laminar flame speed is below 1 $\mathrm{m\,s^{-1}}$ [9, 10]. The acoustic power generated by the flame is key information to predict CIs but it is challenging to precisely compute it as the power released by combustion is generally 10^8 times higher [8, 23].

In this context, it is a tedious task to predict the acoustic wave/heat release rate coupling that is essential to predict CIs.

When CIs occur, the acoustic energy in the combustion system increases so that it is at the basis of CI prediction. The acoustic energy balance[1] in a system is given by [24, 25]:

$$\frac{\partial E_a}{\partial t} + \nabla \cdot F = S - D \tag{1.1}$$

where E_a is the acoustic energy, F represents the net flux of acoustic energy $p'u'$ at the boundaries with the acoustic pressure p' and the acoustic velocity u', S is the acoustic energy source/sink term also known as the "Rayleigh" term. It corresponds to the rate of heat addition/extraction to/from the acoustic energy and D is the acoustic energy dissipation. The values in Eq. 1.1 are integrated over the volume of the combustion device V and time-averaged over at least one oscillation period T.

The Rayleigh term S is:

[1] This formulation is simplified as many assumption are used. Here, the volume forces, the heat sources, the change of entropy and the viscous terms are neglected. Additionally, this expression stands in the linear acoustics framework, *i.e.* in the small fluctuations hypothesis. Although the relevance of this acoustic energy balance equation on the field of combustion instabilities is questionable, it provides some insights on basic phenomenon occurring in thermoacoustically unstable devices.

$$S = \frac{1}{T}\int_V \int_T \frac{\gamma - 1}{\gamma p_0} p'(t) q'(t) dv dt \tag{1.2}$$

where γ is the specific heat ratio, p_0 is the mean pressure and q' is the unsteady heat release rate. The Rayleigh criterion states that it is necessary that $S > 0$ for thermoacoustic instabilities to occur [26, 27]. Under such conditions, a constructive coupling between the heat release rate and acoustic waves results in an increase of acoustic energy in the system.

For purely harmonic pressure and heat release rate fluctuations the sign of S is due to the phase shift θ_{pq} between p' and q':

- if $0 < \theta_{pq} < \pi/2$ the Rayleigh term S is positive so that S is an acoustic energy *source* term. In this case the heat injected by the flame into the flow will amplify the acoustic oscillations.

- if $\pi/2 < \theta_{pq} < \pi$ the Rayleigh term S is negative and S becomes an acoustic energy *sink* term. The heat release rate fluctuations will damp the acoustic fluctuations.

An analogy can be made with an oscillating pendulum. When one applies a periodic forcing on the pendulum, the timing (*i.e.* the phasing between the oscillations and the forcing) determines whether the amplitude of the pendulum's oscillations increase or decrease: applying a force in the direction of the pendulum's motion will increase the oscillations' amplitude while applying a force in the opposite direction of the pendulum's motion will decrease the oscillations' amplitude. Here, the gas expansion due to the perturbation of heat release rate – the forcing – performs net work on the acoustic pressure waves – the pendulum –.

The Rayleigh criterion is a necessary but insufficient condition for CIs to occur. The acoustic energy E_a in the domain (*cf.* Eq. 1.1) increases if $S > \nabla \cdot F + D$, that is if the source term is high enough to overcome both acoustic fluxes at the boundaries and the acoustic dissipation [9, 28]. It follows that CI predictions in a system can be made only if one accurately measures or models the flame/acoustic coupled contribution S, the dissipation D and the fluxes at the boundaries F.

Three computational approaches can be used to predict CIs in real engines: (1) the brute force approach, (2) the joint use of an acoustic solver with a flame-response model and (3) low (or reduced) order models.

1.2.1 The brute force approach

In most combustion devices, the flow is turbulent in order to increase the heat release levels so that turbulence modeling is essential.

The Direct Numerical Simulation (DNS) approach consists in solving the Navier-Stokes equations on a mesh with a cell size smaller than the smallest length scale present in the flow. For turbulent flows, the length scale is the smallest turbulent vortex.

DNS is known to provide detailed information on turbulent flows and turbulent flame fronts [29–35]. Unfortunately, Kolmogorov theory states that, for a uniform mesh, the minimum number of mesh points necessary to solve for the smallest turbulent length scale – called the Kolmogorov length scale – is $Re_t^{9/4}$ where Re_t is the turbulent Reynolds number [36–38]. From this relation, it becomes obvious that such an approach is limited to low Reynolds numbers and, hence, cannot be used in high-performance engines such as rocket propulsion stages or aeroengines.

A common approach to study turbulent flows is to utilize Reynolds Averaged Navier-Stokes (RANS). This approach focuses on mean flow field prediction and does not produce high fidelity prediction of the turbulent flow. Given the high level of accuracy needed to predict CIs, this approach yields only limited results [9].

An interesting compromise can be found in the Large-Eddy Simulation (LES) approach which main idea lies in solving the large turbulent scales – containing most of the turbulent kinetic energy – and to use a turbulent model to account for the small scales. As LES aims to discriminate between large and small eddies, it is naturally based on a spatial filtering procedure. While this approach is more expensive than RANS, its added value is recognized in the CI community as it has been used numerous times to predict the thermoacoustic stability of real combustion devices [39–46].

However, the computational cost associated with LES is such that generally only a few milliseconds of physical time can be computed. The use of such computations has not become a routine yet as the determination of stability maps is out of reach. In this context, more affordable approaches are necessary.

1.2.2 Joint use of an acoustic solver and a flame-response model

A cost-effective approach to predict CIs is the joint use of an acoustic solver and a flame-response model [47].

The acoustic solver can be either a Helmholtz solver or a Linearized Euler Equations solver[2] (LEE) [49, 50]. The Helmholtz equation will be presented in Chapter 2. Solving for the acoustic eigenmodes and eigenfrequencies requires a sound speed field. If the LEE is used, a mean sound speed field is required.

The flame-response model is necessary to model the flame/acoustic coupling without solving the reacting flow field. The first flame-response model, called the $n - \tau$ model, was proposed by Crocco [51, 52]. The central idea is to relate p' and q' by a gain n and a time-delay τ. The concept was later extended by the Flame Transfer Function FTF formalism to

[2]The low Mach number assumption allows the use of a cost-effective Helmholtz solver. However, Nicoud and Wieczorek [48] have shown that in some cases the mean flow effects may contribute to the disturbance energy equation in the same proportions than the Rayleigh term (*i.e.* the flame reponse term)

account for a broadband description of the flame response [53, 54] further extended to consider nonlinear effects by the Flame Describing Function (FDF) framework [55].

Although some attempt has been made on premixed laminar flames, flame-response models for real engines (*e.g.* for swirled or shear coaxial turbulent flames) are virtually impossible to derive from theoretical considerations. In practice, FTF or FDF have to be measured in an experiment or computed using the brute force approach.

If the flame-response is properly modeled, the linear stability of the eigenmodes can be assessed, hence, allowing to identify the appearance of CIs. This approach has been successfully used by several authors [47, 56–63].

1.2.3 Low Order Models

The use of Low Order Models (LOM) – also known as Reduced Order Models (ROM) – is another approach for thermoacoustic stability prediction of a combustion chambers. Its low CPU cost makes it useful as a design tool so that such computations have become a routine in the industry.

LOM in CI studies are based on the joint use of an acoustic network and a flame-response model. The latter has already been discussed above. Acoustic networks are based on the representation of the system as acoustic elements where only one-dimensional acoustic wave propagates.

The use and the derivation of such models are beyond the scope of this manuscript and the interested reader is referred to the work of several authors that have used this approach successfully to predict CIs [64–79], or at least characterized the thermoacoustic properties of a combustion device [80–82].

1.3 Objective & Outline of the work

In the CI community, the research effort is directed toward a single goal: be able to predict the occurrence of CI in *any* system in order to design both cleaner and more efficient combustion devices.

The purpose of the present work, although more modest, falls within the scope of this objective.

First of all, the methods and concepts used in this manuscript are built upon the general equations used in thermoacoustic, which will be presented in Chapter 2. At the exception of a few canonical cases, these equations cannot be solved analytically so that, most of the time, numerical methods must be used to approximate their solutions. The numerical framework will be briefly discussed.

As discussed above, the acoustic energy balance equation (*cf.* Eq. 1.1) is at the foundation of CI predictions and it is therefore essential to accurately account for each of its terms. All the chapters in Part I and Part II are related to either the study or the evaluation of these terms.

Part I: Transverse combustion instabilities in a liquid rocket engine

In Part I a liquid rocket engine (LRE) operated at DLR Lampoldshausen (Germany) is studied: the BKD configuration. It is a reduced-scale LRE fed by 42 shear coaxial injectors with cryogenic H_2/O_2 as fuel and oxidizer. This configuration exhibits transverse CIs, *i.e.* the unsteady heat release rate couples with transverse resonant acoustic modes of the combustion chamber.

First, a novel methodology, called *Instantaneous Modal Decomposition* (IMD), enabling to study and reconstruct the three-dimensional acoustic field from pressure measurements is presented and validated on a simplified LRE configuration in Chapter 3.

In Chapter 4, the BKD configuration is presented in details and the IMD method is then applied to pressure measurements from both the numerical simulation (LES) and the experimental rig.

As IMD allows the reconstruction of the entire acoustic field (pressure and velocity) at all instants it allows to track the evolution of the acoustic energy (E_a in Eq. 1.1).

The BKD exhibits high-frequency CIs: the heat release rate fluctuations are coupled with transverse resonant acoustic modes in the combustion chamber. Consequently, each of the 42 flames in the BKD experiences transverse and/or axial fluctuations of acoustic pressure and/or acoustic velocity. In such conditions, it is unclear which variables drive the flame-response. Chapter 5 focuses on the study of the flame-response (the Rayleigh term, S in Eq. 1.1) of each of the 42 flames from a LES database. The unsteady heat release rate and the flame-response of each of the 42 flames are studied for the two dominant transverse modes. The flames

responsible for most of the heat addition to the acoustic energy are further investigated and the question of which variables are the most relevant for a flame-response model is addressed.

Part II: Acoustic boundary conditions for time domain simulations

The acoustic fluxes, F in Eq. 1.1 are driven by the boundary conditions. It is vital to accurately evaluate this flux if one is to predict CIs because the growth rate is a balance between S and F (and other losses).

Acoustic boundaries can be described using many quantities (*e.g.* the impedance, the admittance, the reflection coefficient, the wall softness, *etc.*) but all of them prescribe the expression between the acoustic velocity u' and the acoustic pressure p' at the boundary. This relation characterizes the reflection of an acoustic wave at the boundary as follows:

1. They specify the ratio of the acoustic wave's amplitudes before and after reflection. This condition imposes the acoustic energy fluxes (F in Eq. 1.1) at the boundaries.

2. They prescribe the phase difference between the acoustic wave before and after reflection. As discussed above, the necessary condition for thermoacoustic instabilities to occur is given by the Rayleigh criterion (*cf.* Eq. 1.2) which states that the physical mechanism leading to an acoustic energy increase yields in the phase difference between the acoustic fluctuations and the heat release rate perturbations.

From these two statements, it becomes clear that the boundaries' acoustic properties need to be accurately considered by the thermoacoustic studies in order to predict both the acoustic fluxes and the Rayleigh source term in Eq. 1.1.

The imposition of acoustic properties at boundary conditions in DNS/LES studies is the topic of Part II. As the acoustic properties are defined in the spectral domain, methods called *Time Domain Impedance Boundary Condition* (TDIBC) are needed to efficiently compute the time domain unsteady values imposed by the boundary conditions.

Chapter 6 presents the Pole & Residue TDIBC formulation of Fung and Ju [83–86] and the proposed extension using the reflection coefficient as a modeling quantity [87–89]. The new formulation is validated in simple test cases.

Although all TDIBC methods should, in principle, be able to impose any reflection coefficient, in practice one case remains difficult: the imposition of a reflection coefficient corresponding to a pure time-delay. Such a boundary condition allows to account for reflection of acoustic waves after a time-delay τ and is useful to truncate computational domains.

This problem is tackled in Chapter 7. The proposed reflection-coefficient-based TDIBC is used along with a specifically derived algorithm to accurately model any reflection coefficients allowing the imposition of pure time-delays in DNS/LES.

The method is validated on a one-dimensional test case before being used on a thermoacoustically unstable CH_4/Air combustion chamber: the INTRIG Burner (IMFT, France).

Finally, the reflection-coefficient-based Pole & Residue method is compared to another TDIBC method based on state-space models: the Characteristic Based State-space Boundary Condition (CBSBC) method developed at TUM (Munich, Germany) by Kaess *et al.* [90] and Jaensch *et al.* [91]. The formal equivalence between a reflection-coefficient-based Pole & Residue model and a CSCBC model is demonstrated.

Chapter 2

Governing equations & numerical tools for thermoacoustics

The study of CIs relies on the reacting compressible Navier-Stokes equations. They are sufficient to accurately study the phenomena present when thermoacoustic instabilities occur but, most of the time, their solution can only be numerically approximated at a great computational cost. In practice, simplified formulations can be derived and used.

The objective of this chapter is to briefly recall the multi-species equations for thermoacoustics that will be used and solved for in this manuscript: the Navier-Stokes equations and the acoustic equations.

2.1 Governing equations

2.1.1 Navier-Stokes equations for reactive flows

Quantities such as mass, momentum and total energy are conserved in the absence of external forcing. The Navier-Stokes equations for compressible reactive flows are expressed here in the conservative form.

Conservation of mass and species

Using the Einstein summation rule [92] (when the index i or j is repeated at least twice the terms must be summed n times in a n-dimensional problem), the mass conservation equation is:

$$\frac{\partial \rho}{\partial t} + \frac{\partial u_i}{\partial x_i} = 0 \tag{2.1}$$

From the mass conservation equation, it is clear that any local density change is thus due to a mass flux.

A reactive gas is a mixture of multiple species that must be handled individually. For a chemical reaction evolving N_{sp} species, the mass fraction of a species k ($k \in [1, N_{\text{sp}}]$) is denoted Y_k. The mass conservation equation for the species k is:

$$\frac{\partial \rho Y_k}{\partial t} + \frac{\partial \rho u_i Y_k}{\partial x_i} = \underbrace{-\frac{\partial \rho V_{k,i} Y_k}{\partial x_i}}_{\text{Diffusive fluxes}} + \underbrace{\dot{\omega}_k}_{\text{consumption/production}} \tag{2.2}$$

The first and second right-hand side terms correspond to the diffusive fluxes of species of species k and to the consumption (or production) of species k, respectively. The diffusive fluxes are controlled by the diffusion velocity $V_{k,i}$ (ith component of diffusion velocity of the species V_k). Depending on the sign of $\dot{\omega}_k$, the mass fraction of species k can increase or decrease.

Conservation of momentum

The reactive momentum equation is [93]:

$$\frac{\partial \rho u_i}{\partial t} + \frac{\partial \rho u_i u_j}{\partial x_j} = -\frac{\partial p}{\partial x_i} + \frac{\partial \tau_{ij}}{\partial x_i} + \rho \sum_{k=1}^{N_{\text{sp}}} Y_k f_{k,j} \tag{2.3}$$

In Eq. 2.3, the change in momentum ρu_i is linked to volume forces: the pressure gradient, the viscous stress tensor τ_{ij} and volume forces $f_{k,j}$ acting on species k in direction j. Although Eq. 2.3 is identical to its non-reactive formulation, the momentum is strongly influenced by combustion. Indeed, flow properties, such as density and viscosity, are different in the fresh and burnt gases [93, 94].

Conservation of energy

Many formulations of the energy conservation can be written [9]. Choosing the total energy e_t as the conserved quantity, the energy balance equation is:

$$\frac{\partial \rho e_t}{\partial t} + \frac{\partial \rho u_i e_t}{\partial x_i} = -\frac{\partial q_i}{\partial x_i} + \frac{\partial \sigma_{ij} u_i}{\partial x_j} + \dot{\mathcal{Q}} + \rho \sum_{k=1}^{N_{\text{sp}}} Y_k f_{k,i} (u_i + V_{k,i}) \tag{2.4}$$

where q_i is the enthalpy flux [9], $\sigma_{ij} = \tau_{ij} - p\delta_{ij}$, $\dot{\mathcal{Q}}$ is the total energy volume source term and $f_{k,i}$ are the volume forces acting on species k in the direction i.

2.1.2 Equation of state for a multi-species gas

For a mixture of N_{sp} perfect gases the density and pressure of the multi-species gas are:

$$\rho = \sum_{k=1}^{N_{\text{sp}}} \rho_k \quad \text{with} \quad \rho_k = \rho Y_k \tag{2.5}$$

and

$$p = \sum_{k=1}^{N_{\text{sp}}} p_k \quad \text{with} \quad p_k = \rho_k \frac{R}{W_k} T \tag{2.6}$$

where ρ_k and p_k are the partial density and partial pressure of the species k, respectively, T is the temperature, $R = 8.314\ \text{J}\,\text{mol}^{-1}\,\text{K}^{-1}$ is the perfect gas constant and W_k is the atomic weight of species k.

The state equation for the perfect gas is:

$$p = \rho r T \quad \text{with} \quad r = \frac{R}{W} = R \sum_{k=1}^{N_{\text{sp}}} \frac{Y_k}{W_k} \tag{2.7}$$

2.1.3 Acoustic equations

Many thermoacoustic studies can be made without solving the reactive Navier-Stokes equations [9]. After recalling the reactive wave equation, linearized formulations are presented. They can be recast in the spectral domain as Helmholtz equations.

Both reactive and non-reactive linearized wave equations are used in Chapters 3 and 4 to study acoustic modes dynamics and in Chapters 6, 7 and 8 to derive and study time domain impedance boundary conditions.

General acoustic equation for reactive flows

For reactive gaseous flows, the derivation of a wave equation is difficult. Contrary to non-reactive flows where the waves are generally considered isentropic, entropy variations must be considered here.

Assuming that no volume force nor heat source play a role in the considered reactive flow, the Navier-Stokes equations presented in Sec. 2.1.1 can be used to derive a reactive wave equation [9]:

$$\begin{aligned} \nabla \cdot \left(\frac{c_0^2}{\gamma} \nabla \ln(p) \right) - \frac{D}{Dt} \left(\frac{1}{\gamma} \frac{D}{Dt} \ln(p) \right) = \\ \nabla \cdot \left(\frac{\nabla \cdot \tau}{\rho} \right) - \frac{D}{Dt} \left[\frac{D}{Dt} \Big(\ln(r) \Big) \right] - \frac{\partial u_i}{\partial u_j} \frac{\partial u_i}{\partial x_j} \\ - \frac{D}{Dt} \left[q - \sum_{k=1}^{N_{\text{sp}}} h_{sk} \dot{\omega}_k + \frac{\partial}{\partial x_i} \left(\lambda \frac{\partial T}{\partial x_i} \right) - \frac{\partial}{\partial x_i} \left(\sum_{k=1}^{N_{\text{sp}}} C_{p,k} Y_k V_{k,i} \right) + \tau_{ij} \frac{\partial u_i}{\partial x_j} \right] \end{aligned} \tag{2.8}$$

where $\nabla \cdot f = \text{div}(f)$ and $\nabla f = \text{grad}(f)$ are the divergence and gradient operator, respectively. c_0 refers to the local sound speed, h_{sk} is the sensible energy, q is the heat release rate and $\dot{\omega}_k$ is the reaction rate per mass unit of the kth species.

Linearized wave equation for reacting flows

Although generic, Eq. 2.8 is rarely used because of its complexity. In many studies, most of the sink and sources terms in Eq. 2.8 can be neglected and a simplified reactive wave equation can be used.

The assumptions generally used when studying combustion devices are:

- **Low mach**
  For a mean flow u_0, if $u_0 << c_0$ then the Mach number $\mathcal{M}$ is close to zero: $\mathcal{M} \simeq 0$ This assumption is fulfilled in many combustion devices.
- **Same molecular weight**
  We assume that the molecular weight is the same for all the species.
- **Constant heat capacities**
  The heat capacities C_p and C_v are assumed to be constant. As a consequence, the ratio of specific heat capacities γ is also constant.
- **Low diffusion**
  All the diffusive terms (viscous terms included) in Eq. 2.8 are neglected. In his work, Kotake [95] has shown by an order of magnitude study that the diffusive terms are negligible in comparison to the heat release rate term.

Using these assumptions, Eq.2.8 can be recast as:

$$\nabla \cdot \left(c_0^2 \nabla \ln(p) \right) - \frac{\partial^2}{\partial t^2} \ln(p) = -\frac{\partial}{\partial t} \left(\frac{q}{\rho C_v T} \right) \tag{2.9}$$

In order to linearize Eq. 2.9, one must decompose a quantity into a sum of mean value and perturbations. The quantities of interest here are p, ρ, q and $\boldsymbol{u}$, leading to:

$$p = p_0 + p' \tag{2.10}$$
$$\rho = \rho_0 + \rho' \tag{2.11}$$
$$q = q_0 + q' \tag{2.12}$$
$$\boldsymbol{u} = \underbrace{\boldsymbol{u_0}}_{\simeq 0} + \boldsymbol{u'} = \boldsymbol{u'} \tag{2.13}$$

where the mean value of the velocity vector $\boldsymbol{u_0}$ is set to zero due to the low Mach assumption. Substituting Eqs. 2.10 to 2.13 into Eq. 2.9 and neglecting high order terms yields [9]:

$$\nabla \cdot \left(c_0^2 \nabla p' \right) - \frac{\partial^2}{\partial t^2} p' = (1 - \gamma) \frac{\partial q'}{\partial t} \tag{2.14}$$

The right-hand side term in Eq. 2.14 is the production of acoustic pressure due to the unsteady heat release of the flame. This term of major importance when studying thermoacoustic instabilities.

Linearized wave equation for non-reacting flows

For non-reacting flows, the right-hand side of Eq. 2.14 is null which leads to the linearized wave equation for non-reacting flows:

$$\nabla \cdot \left(c_0^2 \nabla p' \right) - \frac{\partial^2 p'}{\partial t^2} = 0 \tag{2.15}$$

1D plane waves Considering one-dimensional waves, Eq. 2.15 can be written:

$$\frac{\partial^2 p'}{\partial x^2} - \frac{1}{c_0^2} \frac{\partial^2 p'}{\partial t^2} = 0 \tag{2.16}$$

The solution of Eq. 2.16 consists in the superposition of two characteristic traveling waves [9, 96]. Figure 2.1 illustrates these two characteristic waves in a duct. The traveling wave A^+ propagates in the increasing x direction and the traveling wave A^- propagates in the decreasing x direction.

The acoustic pressure and velocity can be expressed from the characteristic waves:

$$p' = A^+ \left(t - \frac{x}{c_0} \right) + A^+ \left(t + \frac{x}{c_0} \right) \tag{2.17}$$

$$u' = \frac{1}{\rho c_0} \left[A^+ \left(t - \frac{x}{c_0} \right) - A^+ \left(t + \frac{x}{c_0} \right) \right] \tag{2.18}$$

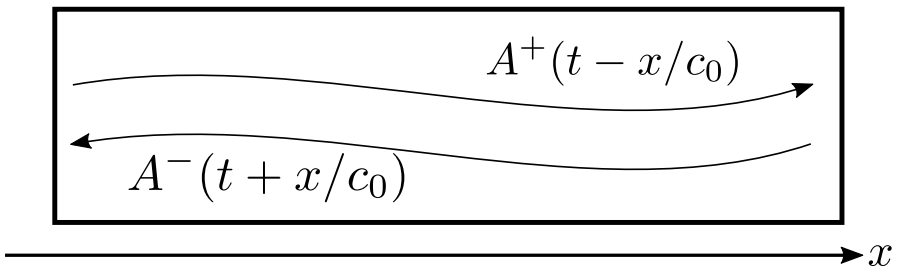


Figure 2.1: One-dimensional wave propagation.

Resonant acoustic modes in cylindrical cavities Many combustion chambers of LRE are cylindrical. When CIs occur in such devices, the unsteady heat release rate couples with at least of its resonant acoustic modes. In practice, low-frequency CIs (*i.e.* coupling to longitudinal modes) can be mitigated but high-frequency CIs (*i.e.* due to transverse modes) are much more complex to deal with [97].

Solutions of the wave equation applied to a cylindrical cavity with homogeneous sound speed are presented here. Using the cylindrical coordinate system (r, θ, z), the resonant acoustic pressure modes of a cylindrical cavity of radius a and length L are [9**?**]:

$$p(r, \theta, z) = J_n \left(\frac{\pi \beta_{mn} r}{a} \right) \cos \left(\frac{q \pi z}{L} \right) \left(A_+ e^{in\theta} + A_- e^{-in\theta} \right) \tag{2.19}$$

where:

- (m, n, q) correspond to the radial, tangential and longitudinal mode number, respectively.
- J_n is the Bessel function of order n.
- β_{mn} is the root of $J'_n(\pi\beta_{mn}) = 0$.
- A_+ and A_- are the amplitudes of the tangential (*i.e.* azimuthal) waves rotating in the directions $+\theta$ and $-\theta$, respectively. If either amplitude is zero, the tangential mode is a "rotating mode". If both amplitudes are equal the resulting mode is referred to as "standing mode". Finally, mixed modes appear if $A_- \neq 0$, $A_+ \neq 0$ and $A_+ \neq A_-$.

The firsts transverse modes of a cylindrical cavity are illustrated on Fig. 2.2. The longitudinal contribution is set to zero ($q = 0$ in Eq. 2.19). The dark blue and dark red colors correspond to the minimum and maximum levels of p', respectively, and white color corresponds to $p' = 0$ (*i.e.* the pressure nodes). The modes are labeled such that, for instance, "Mode 1R2T" refers to a mode made of the superposition of the first radial mode ($m = 1$ in Eq. 2.19) and the second tangential mode ($n = 2$ in Eq. 2.19).

Helmholtz equation Determining the solutions of Eq. 2.15 can be eased by assuming harmonic waves. By doing so, temporal and spatial information can be separated:

$$p' = \Re\left(\widehat{p}e^{-i\omega t}\right) \tag{2.20}$$

$$\rho' = \Re\left(\widehat{\rho}e^{-i\omega t}\right) \tag{2.21}$$

$$\boldsymbol{u}' = \Re\left(\widehat{\boldsymbol{u}}e^{-i\omega t}\right) \tag{2.22}$$

where i is the imaginary unit ($i^2 = -1$). $\widehat{p}$, $\widehat{\rho}$ and $\widehat{\boldsymbol{u}}$ are complex functions of space and angular frequency ω. Using the harmonic waves defined in Eqs. 2.20, 2.21 and 2.22 the linearized mass conservation equation and the momentum conservation equations can be recast as:

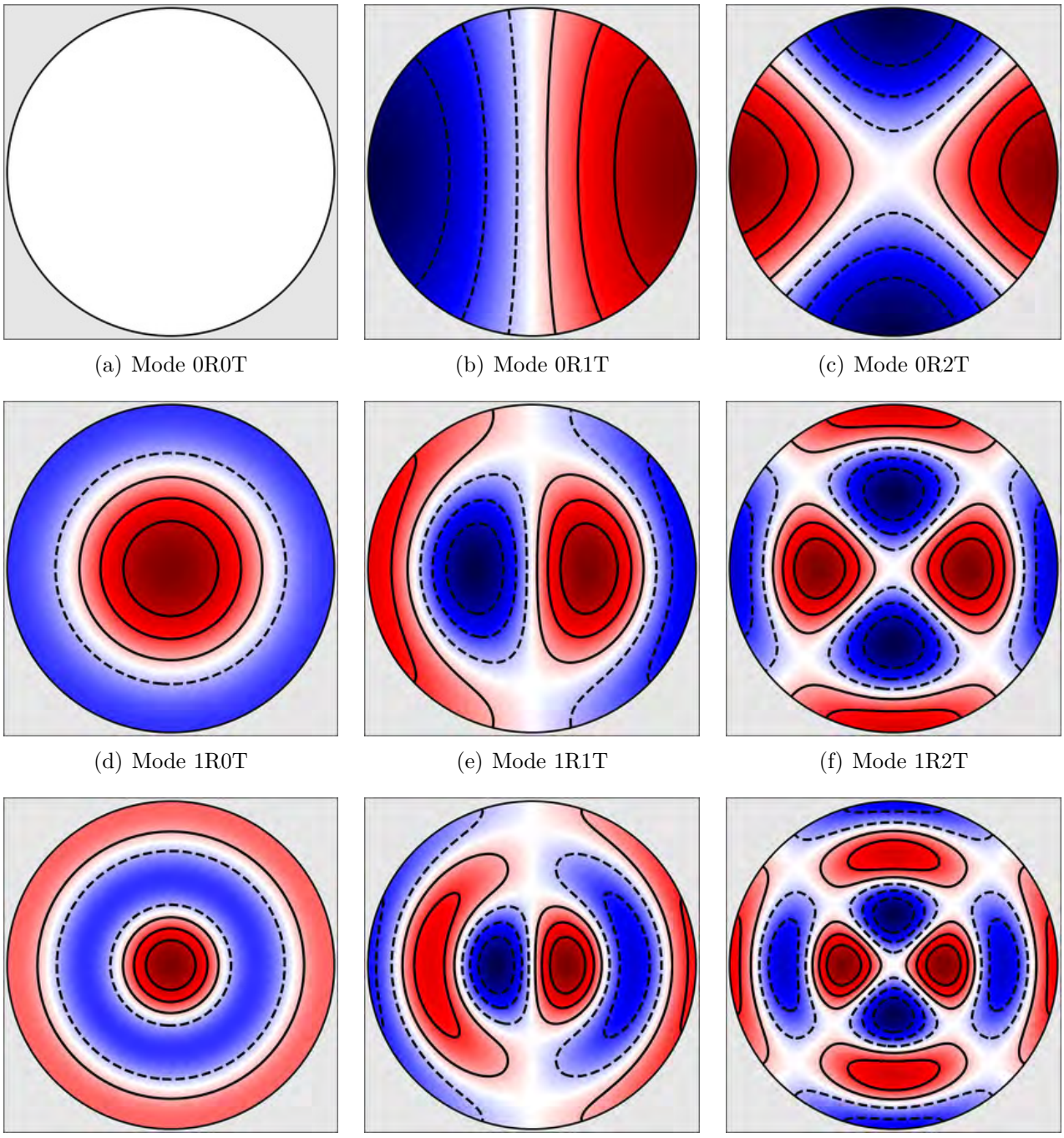
$$-i\omega\widehat{p} + \rho_0 c_0^2 \nabla \cdot \boldsymbol{u} = 0 \tag{2.23}$$

$$-\rho_0 i\omega\widehat{\boldsymbol{u}} + \nabla\widehat{p} = 0 \tag{2.24}$$

As for the wave equation, Eqs. 2.23 and 2.24 can be combined, yielding the homogeneous Helmholtz equation:

$$\nabla \cdot \left(c_0^2 \nabla\widehat{p}\right) + \omega^2\widehat{p} = 0 \tag{2.25}$$

The same derivation can be done from the reactive conservation equations yielding the inhomogeneous Helmholtz equation with a single right-hand side source term: the chemical heat release term.



(a) Mode 0R0T (b) Mode 0R1T (c) Mode 0R2T

(d) Mode 1R0T (e) Mode 1R1T (f) Mode 1R2T

(g) Mode 2R0T (h) Mode 2R1T (i) Mode 2R2T

Figure 2.2: Pressure of transverse acoustic modes in a cylindrical cavity.

$$\nabla \cdot \left(c_0^2 \nabla \widehat{p} \right) + \omega^2 \widehat{p} = \frac{\gamma - 1}{\gamma p_0} \, \widehat{\Omega}_T \tag{2.26}$$

2.2 Numerical tools

Throughout this manuscript, numerical solvers are used. In this section, a brief description of these tools is given. The flow solver used in AVBP and the acoustic solver is AVSP.

2.2.1 AVBP

The AVBP solver is jointly developed by CERFACS (Toulouse, FRANCE) and IFPEN (Rueil-Malmaison, FRANCE). It is a parallel solver for the laminar and turbulent compressible reactive 3D Navier-Stokes equations on unstructured and hybrid grids. Using such meshes allows the quick generation of meshes for complex geometries and makes AVBP a Computational Fluid Dynamics (CFD) code suited for research of industrial interest. AVBP uses the perfect gas assumption and a real-gas version called AVBP-RG exists [98–100]. The latter accounts for multicomponent real-gas thermodynamics and transport [101, 102].

Explicit numerical schemes are used in AVBP and the solver relies on cell-vertex and finite-volume methods [103–105]. The numerical convection schemes in AVBP are (1) the well-known Lax-Wendroff scheme [106] and (2) Finite-Element type low-dissipation Taylor-Galerkin schemes. While the Lax-Wendroff scheme is second order accurate in both space and time, the Taylor-Galerkin schemes implemented in AVBP have higher orders [107–110].

The Taylor-Galerkin schemes used in this manuscript are:

1. **TTG4A**
   TTG4A is a two-step Taylor-Galerkin which is third-order in space and fourth-order in time. It has excellent dispersion properties and low dissipation for large wave numbers [111].

2. **TTGC**
   TTGC is a two-step Taylor-Galerkin similar to TTG4A which has been developed to lower the levels of numerical dissipation in order to accurately predict the turbulent kinetic energy transfers in LES [111].

For laminar and moderate Reynolds number flows AVBP can fully solve the Navier-Stokes equations, *i.e.* using the DNS approach. For higher Reynolds number, the LES approach requires the use of subgrid-scale (SGS) models to close the subgrid stress tensor [38]. The SGS model used in this manuscript is the Wall Adapting Linear Eddy (WALE) model [112] and an eddy-diffusivity approach is adopted for thermal and species subgrid contributions (constant turbulent Prandtl and Schmidt number: $\mathrm{Pr}_t = 0.6$, $\mathrm{Sc}_t = 0.6$).

Combustion usually involves a large number of species and chemical reactions. Transporting all of the species and solving for all the chemical reactions is too cumbersome for computationally intensive approaches such as DNS/LES. In practice, only a few species are transported. Moreover, the turbulent flames thickness is typically smaller than the mesh resolution used in LES so that flame models are requires.

In this manuscript, two reactive simulations are carried out.

1. A LES of a H_2/O_2 liquid rocket engine is performed and four species are transported (H_2, O_2, OH and H_2O) and source terms are computed following the method described in [100]. An infinitely-fast chemistry model [100], relying on the assumption of local chemical equilibrium and a β-pdf description of the filtered mixture fraction $\widetilde{Z}$, is adopted.

2. A DNS of a CH_4/Air premixed laminar flame is realized. The flame thickness is fully resolved and 19 species are transported [113] for the modeling of chemical kinetics.

Finally, AVBP uses characteristic boundary conditions under the Navier-Stokes Characteristic Boundary Condition (NSCBC) framework [114]. Characteristic boundary conditions allow the separation of acoustic, convective and entropic information at the boundaries. Using such methods, low levels of acoustic reflection can be achieved [114–116].

2.2.2 AVSP

AVSP is developed at CERFACS (Toulouse, FRANCE). It is a parallel solver for the low-mach Helmholtz equation recast as an eigenvalue problem. If the inhomogeneous Helmholtz equation is solved for then a flame response model is needed.

The solutions consist of a set of eigenvalues and eigenmodes. The eigenvalues, *i.e.* the eigenfrequencies, are complex: their real and imaginary parts correspond to the frequencies of the resonant acoustic modes and to their linear growth rates, respectively. Hence, the linear thermoacoustic stability of a system can be inferred using this tool. The eigenmodes correspond to the spatial structure of each of the modes. The AVSP simulations performed in this manuscript use the Arnoldi solver [117–120].

AVSP simulations have a reasonable cost compared to AVBP simulations. Indeed, in combustion devices the focus is mainly on low-frequency modes that have length scales significantly larger than the length scales usually present in the flow. As a consequence, AVSP computations permit coarser meshes than AVBP computations.

The numerical schemes used in AVSP are cell-vertex volume methods inherited from AVBP. High-order schemes are not needed so that the Taylor-Galerkin scheme used is second order accurate. The interested reader is referred to Nicoud *et al.* [47] where a more detailed description is made.

Part I

Transverse combustion instabilities in a liquid rocket engine

Context & Outline

When occurring in high-performance devices such as gas turbines, aero-engines or rocket propulsion stages, combustion dynamics can have serious consequences on the system's performance. In many cases, the phenomena responsible for such combustion dynamics are *combustion instabilities* (CIs). They result from a constructive coupling between the unsteady heat release rate (due to the unsteadiness of the flame in combustion systems) and the resonant acoustic modes of the combustion device.

In Liquid Rocket Engines (LREs), the occurrence of combustion instabilities has prevented the developement of more efficient high-performance propulsion systems. Both reduced and full-scale hot-fire liquid rocket engines tests have revealed that these propulsion systems, when unstable, exhibit high-frequency oscillations which are hard to mitigate. These peculiar oscillations are due to transverse CIs: the unsteady heat release rate is coupled with transverse (*i.e.* orthogonal to the mean flow direction) resonant acoustic modes of the chamber. These phenomena can jeopardize the integrity of the combustion device by (1) enhancing the heat fluxes (leading to the melting of chamber walls), (2) cause large structural vibrations and (3) thrust fluctuations [19].

Although experimental studies in the field of LRE are essential to gain understanding of mechanisms leading to transverse CIs, the diagnostics available are limited by the extreme conditions of the flow field. Pressure measurements are the easiest experimental diagnostics to implement in such conditions. On the contrary, velocity measurements in the chamber or in the fuel/oxidizer injectors cannot be achieved.

In this part of the manuscript, a 42-injector reduced-scale LRE is studied: the BKD setup operated at DLR Lampoldshausen (Germany). The objective of this work is twofold:

1. **Chapters 3 and 4: Study of acoustic modes dynamics in a LRE**
   A method, called Instantaneous Modal Decomposition (IMD), is proposed to study the acoustic mode dynamics from pressure measurements. The goal is to gain understanding in the evolution of transverse modes in the BKD and to reconstruct the three-dimensional pressure and velocity acoustic fields. Both experimental and numerical (LES) results are studied.

2. **Chapter 5: Study of the Rayleigh source term in the BKD**
   The numerical investigation of the BKD by Urbano *et al.* [121] allows the study of the flame response. Two unstable transverse modes are observed in the LES and the contribution of each mode to the unsteady heat release rate and to the Rayleigh index is investigated. The goals are: (1) to identify which flames are feeding most of the energy to the acoustic field and (2) to develop a deeper knowledge of the mechanisms leading to such transverse CIs.

Chapter 3

Modal Analysis & Reconstruction of 3D acoustic fields

Pressure measurements are the most common experimental diagnostics in the liquid rocket engines (LREs). They are useful to develop a deeper knowledge of the transverse thermoacoustic instabilities taking place in such devices.

In this chapter, a method specifically developed to analyze pressure signals, called *Instantaneous Modal Decomposition* (IMD), is presented. It has the double objective of analyzing the contribution of each acoustic mode to the acoustic field in time and to reconstruct the entire acoustic field (pressure and velocity) from a few local pressure measurements.

The IMD method is based on the decomposition of pressure signals as a superposition of individual contributions of eigenmodes. The temporal evolution of an eigenmodes' contribution is obtained by projecting the pressure signals onto the eigenmodes shape.

The general principle is presented in Sec. 3.1 and the details of the method are presented in Sec. 3.2. In Section 3.3, the method is applied to pressure signals of a Navier-Stokes simulation of a simplified LRE configuration. The setup comprises injectors mounted on a cylindrical cavity such as typical LRE combustors. The temporal evolution of an injector-chamber coupled acoustic mode is studied and the acoustic pressure and velocity fields are reconstructed in the areas of interest.

3.1 Introduction

In many thermoacoustically unstable devices the acoustic velocity fluctuations have been found to drive the flame dynamics [6, 9, 10, 18, 53, 54, 122, 123]. Consequently, it has been used by many authors [47, 56–63, 72] as the input variable for a flame-response model. The joint use of acoustic solvers and flame-response models – FTF or FDF (*cf.* page 6)– is a computationally efficient procedure to predict the thermoacoustic stability of real engines that can be applied in the industry [57, 121]. Hence, the acoustic velocity field is key information to study and predict combustion instabilities.

When investigating high performance propulsion systems such as aero-engines or rocket engines, the extreme conditions at which such a device is operating make the acoustic velocity field challenging to measure. However, pressure measurements techniques have become a routine even in high-pressure liquid rocket engines [124–127].

In this context, there is a need for advanced pressure signal post-processing techniques allowing to have a better insight into the entire acoustic field. In this work we present a method, called Instantaneous Modal Decomposition (IMD), that is developed in order to provide a diagnostic on the dynamics of the acoustic modes of the system and a procedure to reconstruct the acoustic field.

The method relies on pressure measurements at several spatial locations. These measurements provide both *spatial* and *temporal* information. The IMD method identify the contribution of a set of acoustic modes to the pressure measurements. The benefits of the method are multiple:

1. **Dominant mode identification**
   IMD gives access to the amplitude of each mode and, thus, provides a methodology to identify which acoustic modes are dominant and how they evolve in time.

2. **Acoustic pressure field reconstruction**
   Using the amplitudes determined by the IMD methodology from *local* measurements, the acoustic pressure field can be reconstructed *everywhere* in the domain.

3. **Acoustic velocity field reconstruction**
   The acoustic pressure and acoustic velocity fields are linked by the momentum equation. Using this equation and the amplitudes determined by IMD, the acoustic velocity field can be reconstructed *everywhere* in the domain. This is especially useful in thermoacoustic as the acoustic velocity have been found to be driving the flame response in many unstable configurations [6, 9, 10].

4. **Tangential mode orientation identification**
   Due to the high-power density in LRE, the flames' heat release rate perturbations couples with many acoustic modes. Such CIs are discriminated by their frequency contents:

   (a) Low-frequency acoustic modes. Their shapes are mainly longitudinal (*i.e.* pressure and velocity fluctuations are parallel to the mean flow). The CIs due to these modes can be dealt with using passive control such as baffles or resonators [20, 128, 129].

   (b) High-frequency acoustic modes. These modes often have a transverse shape in the combustion chamber (*i.e.* pressure and velocity fluctuations are orthogonal to the mean flow) [18, 20, 130]. In practice, transverse CIs are hard to mitigate so that it is essential to gain understanding on the mechanisms leading to such phenomenon.

   In a cylindrical geometry, the orientation of tangential modes is an important parameter that can be determined using IMD results. This is discussed in details in Chapter 4.

3.2 Method

The general principles of the IMD method and the expected results were presented in the previous section. In this section, the method is presented in details.

3.2.1 Modal decomposition

In the linear acoustic framework, it is a common practice to decompose the acoustic field as temporal and spatial fluctuation assuming harmonic waves [9**?**]. In this context, the acoustic pressure field can be written as [18]:

$$p'(\boldsymbol{x},t) = \Re\left[\sum_{k=1}^{\infty} \underbrace{A_k(t)e^{-i\omega_k t}}_{\text{Temporal}} \underbrace{p_k^{\mathrm{H}}(\boldsymbol{x})}_{\text{Spatial}}\right] \tag{3.1}$$

where $p'(\boldsymbol{x},t)$ is the acoustic pressure field, $\Re[\cdot]$ denotes the real part, the subscript k refers to the kth mode, A_k is the envelope (*i.e.* zero-to-peak) amplitude of a mode oscillating at an angular frequency ω_k and $p_k^{\mathrm{H}}(\boldsymbol{x})$ is the Helmholtz pressure mode (*i.e.* the pressure associated to the solution of the Helmholtz equation at the angular frequency ω_k). The temporal contribution of the kth mode can be reduced to a single complex amplitude $a_k(t)$:

$$a_k = A_k(t)e^{-i\omega_k t} \tag{3.2}$$

Using the definition of a_k, Eq. 3.1 can then be expressed as follows:

$$\boxed{p'(\boldsymbol{x},t) = \Re\left[\sum_{k=1}^{\infty} a_k(t)\ p_k^{\mathrm{H}}(\boldsymbol{x})\right]} \tag{3.3}$$

The goal of IMD is to identify the a_k from a known set of p_k^{H} and known pressure measurements $p'(t)$. To do so, it is proposed to extend the pressure measurements to the complex space so that the real part operator in Eq. 3.1 is not dealt with while seeking for a_k.

A convenient method to obtain these complex-valued pressure signals is to build *analytic signals*. In signal processing theory, an analytic signal is a complex-valued function, obtained from a real-valued function, which facilitates many mathematical operations, especially the determination of the envelope and the instantaneous phase of the signal. Obtaining an analytic signal from a real-valued signal is done by the use of the Hilbert transform $\mathcal{H}[\cdot]$. Here, the complex-valued pressure measurements are, hence, called the *analytic pressure signals* and denoted p^{A}.

They are defined as:

$$p^{\mathrm{A}}(\boldsymbol{x},t) = p'(\boldsymbol{x},t) + i\mathcal{H}\Big[p'(\boldsymbol{x},t)\Big] \tag{3.4}$$

An example of analytic pressure signal $p^{\mathrm{A}}(t)$ built from an acoustic pressure measurement

$p'(t)$ is illustrated in Fig. 3.1. Here, $p'(t) = \cos(2\pi f_0 * t + \phi)$ where $f_0 = 10$ Hz and $\phi = 0.79$ rad. As the pressure signal $p'(t)$ is monochromatic, the imaginary part signal is phase-shifted by $\pi/2$ when taking the Hilbert transform. A consequence of this property is that the modulus of p^{A} is the envelope of the signal. Figure 3.1 was obtained by numerical approximation using the scipy.signal.hilbert function of the scientific library SciPy of the Python programming language [131]. The numerical algorithm of the scipy.signal.hilbert function gives a very good overall estimate of the Hilbert transform with the exception of the beginning and the end of the signal where spurious oscillations are present. The experimental or numerical pressure signals are usually quite long compared to the time scale of the change of amplitude of an acoustic mode. Hence, this end-effect is not a strong limitation when tracking the envelope amplitude of a mode.

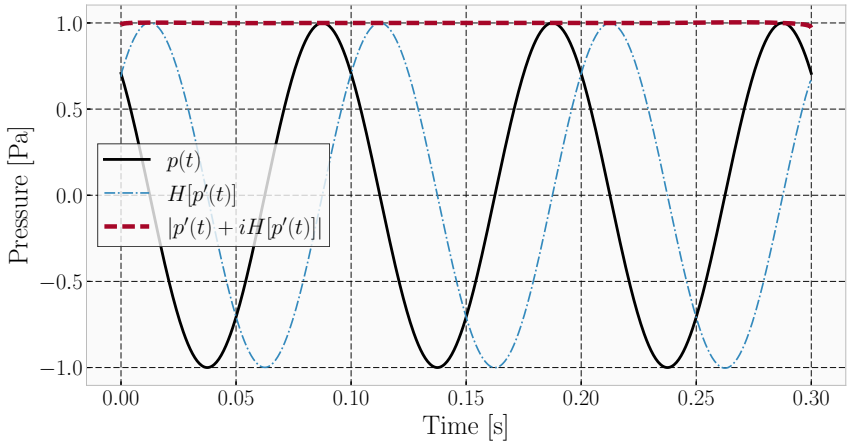


Figure 3.1: Real part, imaginary part and modulus of an analytic pressure signal $p^{\mathrm{A}}(t)$.

It should be noted that taking the real part of the analytic signal yields the original signal. From this observation, Eq. 3.3 can obtained by taking the real part of the following modal decomposition:

$$p^{\mathrm{A}}(\boldsymbol{x}, t) = \sum_{k=1}^{\infty} a_k(t) p_k^{\mathrm{H}}(\boldsymbol{x}) \tag{3.5}$$

Equation 3.5 will be used to determine the a_k. By building a vector space where the Helmholtz eigenmodes are orthogonal, there is a unique solution for the set of $(a_1(t), a_2(t), \dots)$. The study of the acoustic modes in IMD is therefore an optimization problem. Vector spaces are convenient mathematical tools that allow to solve such problems. As all functions are complex valued in Eq. 3.5, the formalism of IMD will therefore be expressed in a complex vector space: the Hilbert space.

IMD vector space: the Hilbert space

A vector space is a collection of unit vectors, that can be used to construct any vector as a linear combination. As seen in Eq. 3.5, the vector $\boldsymbol{p}^{\mathrm{A}}(\boldsymbol{x}, t)$ can be constructed as a linear

combination of $\boldsymbol{p}_k^{\mathrm{H}}(\boldsymbol{x})$. The Helmholtz eigenmodes will therefore be chosen to be the unit vectors.

Hilbert space are commonly used for the study of vibrations, making it a very popular choice in fields such as quantum mechanics. The Hilbert space is a normed vector space: the vector space comes with a metric allowing to measure the length and angles of the vectors: the *inner product*. The inner product used here is the Hermitian inner product, defined as:

$$\langle f, g\rangle = \int f(\boldsymbol{x}) \cdot g^*(\boldsymbol{x}) d\boldsymbol{x} \tag{3.6}$$

where g^* denotes the conjugate of g. The inner product defined in Eq. 3.6 allows to define the L^2-norm:

$$L^2(f) = ||f||_2 = \sqrt{\langle f,\ f\rangle} \tag{3.7}$$

The unit vectors $p_i^{\mathrm{H}}(\boldsymbol{x})$ are normed, that is:

$$||p_i^{\mathrm{H}}(\boldsymbol{x})||_2 = \sqrt{\langle p_i^{\mathrm{H}}(\boldsymbol{x}),\ p_i^{\mathrm{H}}(\boldsymbol{x})\rangle} = 1 \tag{3.8}$$

As $p_i^{\mathrm{H}}(\boldsymbol{x})$ are solutions of the homogeneous Helmholtz equation, they are orthogonal:

$$\langle p_i^H,\ p_j^H\rangle = \begin{cases} 0, & \text{for } i \neq j \\ 1, & \text{for } i = j \end{cases} \tag{3.9}$$

Under these conditions, the collection of vectors $p_i^{\mathrm{H}}(\boldsymbol{x})$ form an orthonormal basis $\mathcal{B}$. In an orthonormal basis, the unit vectors are: (1) **Orthogonal** (the inner product of a vector by another is zero – checked in Eq. 3.9 –) and (2) **Normed** (the norm of each vector is one – checked in Eq. 3.8 –).

$$\mathcal{B} = (p_1^{\mathrm{H}}(\boldsymbol{x}),\ p_2^{\mathrm{H}}(\boldsymbol{x}), \dots) \tag{3.10}$$

The properties of the orthonormal basis $\mathcal{B}$ allow directly the determination of the $a_k(t)$ by projecting the analytic acoustic pressure signal $p^{\mathrm{A}}(\boldsymbol{x}, t)$ on the unit vector $p_k^{\mathrm{H}}(\boldsymbol{x})$:

$$\boxed{a_k(t) = \langle p^{\mathrm{A}}(\boldsymbol{x}, t),\ p_k^{\mathrm{H}}(\boldsymbol{x})\rangle} \tag{3.11}$$

Practical considerations for real case applications

Although mathematically exact, the formulation of IMD such as presented in Sec. 3.2.1 cannot be used in many real case applications. Several strong assumptions were made and some of them may not be fulfilled in complex setups such as in propulsion systems. Yet, if special care is taken, some of these assumptions can be weakened and IMD can still yield accurate results. In this section, we discuss the weakened assumptions often made for real case applications.

1. **Reduced set of points $\boldsymbol{\chi}$**
   In real case applications, the modal decomposition is made of a finite set of point $\boldsymbol{\chi} = (\chi_1, \chi_2, \ldots, \chi_k)$. These $\boldsymbol{\chi_k}$ corresponds to the location of the pressure measurements. For instance, in Cartesian coordinates:

$$p^{\mathrm{A}}(\boldsymbol{\chi_k}, t) = p^{\mathrm{A}}(x_k, y_k, z_k, t) \tag{3.12}$$

$$\boldsymbol{p}^{\mathrm{A}}(\boldsymbol{\chi}, t) = \begin{bmatrix} p^{\mathrm{A}}(\boldsymbol{\chi_1}, t) \\ p^{\mathrm{A}}(\boldsymbol{\chi_2}, t) \\ \vdots \\ p^{\mathrm{A}}(\boldsymbol{\chi_k}, t) \end{bmatrix} \tag{3.13}$$

   The analysis is thus *local* as it is performed on a reduced set of location $\boldsymbol{\chi}$ where $\boldsymbol{\chi} \in \boldsymbol{x}$. The same set of points is used for the Helmholtz eigenmodes $\boldsymbol{p}_k^{\mathrm{H}}(\boldsymbol{\chi})$ where $\boldsymbol{p}_k^{\mathrm{H}}(\boldsymbol{\chi}) \in \boldsymbol{p}_k^{\mathrm{H}}(\boldsymbol{x})$.

2. **Truncation of the series**
   Although the Helmholtz equation has an infinite number of solutions, in many real case applications the acoustic field is dominated by a few modes only. Taking this into consideration, the modal decomposition in Eq. 3.5 can be truncated to a number of modes m considered[1]:

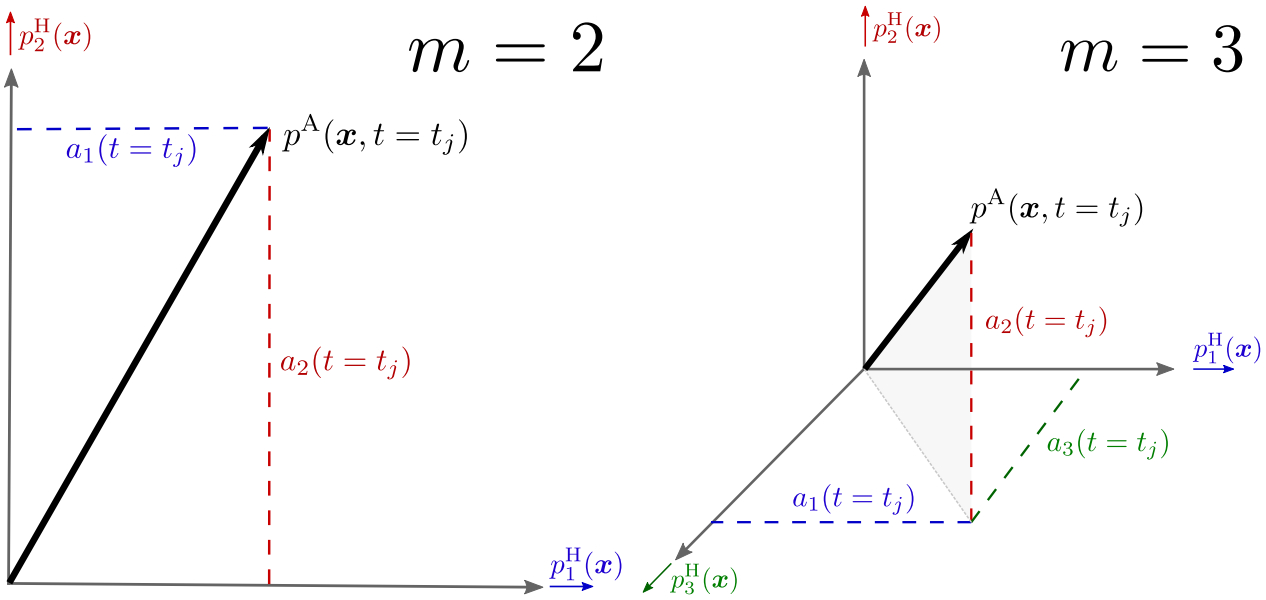
$$\boldsymbol{p}^{\mathrm{A}}(\boldsymbol{\chi}, t) = \sum_{k=1}^{m} a_k(t)\ \boldsymbol{p}_k^{\mathrm{H}}(\boldsymbol{\chi}) \tag{3.14}$$

   Figure 3.2 illustrates the modal decomposition of an analytic pressure vector $\boldsymbol{p}^{\mathrm{A}}$ using two (*cf.* Fig. 3.2(a)) and three (*cf.* Fig. 3.2(b)) modes in Eq. 3.14 at time t_j. The determination of the a_k coefficients by a projection onto the unit vectors $\boldsymbol{p}_i^{\mathrm{H}}$ is illustrated. As in an Euclidian space, the values of a_k are the component of the vector $\boldsymbol{p}^{\mathrm{A}}$. For a number of modes considered higher than three, no direct visualization of the projection can be made but the principle remains.

   At each instant t of the pressure signal, a projection of the analytic pressure onto each mode is performed and the a_k coefficients are determined.

3. **Helmholtz eigenmodes**
   For simple geometries (*e.g.* rectangular and cylindrical cavities) and homogeneous sound speed fields, the Helmholtz modes are known [9**?**]. For more complex cases,

[1] The number of modes m considered in the modal decomposition imposes a criterion on the minimum number of points l necessary in the set $\boldsymbol{\chi}$: $l \geq m$. However, the number l often needs to be strictly greater than m if mixed modes are considered (*e.g.* acoustic eigenmodes with both longitudinal and transverse contributions)



(a) 2D projection (b) 3D projection

Figure 3.2: Illustrations of the determination of the complex coefficients a_1, a_2 (and a_3) by projection (Eq. 3.11) for a time $T = t_j$ considering two (a) and (three) modes.

the Helmholtz eigenmodes are determined using a Helmholtz solver. It is a numerical tool that approximates the solution of the Helmholtz equation (Eq. 2.26), yielding the Helmholtz eigenmode. In this manuscript, the Helmholtz solver used is called AVSP [47, 132] and is developed by CERFACS (Toulouse, France) as discussed in Sec. 2.2.2 (*cf* page 19).

4. **Quasi-orthogonality condition**
   As discussed above, the IMD method is based on the decomposition on a vector $\boldsymbol{p}^{\mathrm{A}}$ as a linear combination of unit vectors of an orthonormal basis. Therefore, to be exact, IMD should be limited to purely orthogonal Helmholtz eigenmodes. This is the case if no complex acoustic impedance is considered at the boundaries and if no flame contribution is considered. Altough IMD is not exact in the more complex aforementioned cases, the error caused by these effects is marginal and the decomposition yields relevant results if the vectors of the basis $\mathcal{B}$ in Eq. 3.10 fulfill the quasi-orthogonality condition, that is:

$$\frac{\langle \boldsymbol{p}_i^{\mathrm{H}}(\boldsymbol{\chi}), \boldsymbol{p}_j^{\mathrm{H}}(\boldsymbol{\chi}) \rangle}{||\boldsymbol{p}_i^{\mathrm{H}}(\boldsymbol{\chi})||_2 \cdot ||\boldsymbol{p}_j^{\mathrm{H}}(\boldsymbol{\chi})||_2} \ll 1 \quad , \quad \text{for } i \neq j \tag{3.15}$$

5. **Degenerate modes**
   Some acoustic modes are referred to as “degenerate modes”. These modes have different mode shapes but oscillate at the same frequency. For IMD to be able to reproduce the acoustic oscillations at a frequency of degenerate modes it needs to take into account all them.

3.2.2 Acoustic field reconstruction

The modal decomposition presented in Sec. 3.2.1 allows the determination of the complex pressure amplitudes a_k at each instant t of pressure measurements. In this section, we present how the acoustic field can be reconstructed from the amplitudes a_k.

First, the methodology to reconstruct the 3D acoustic pressure field is presented. Then, this acoustic reconstruction is extended to the acoustic velocity field. Finally, an analysis can be made to track the envelope amplitude corresponding to a single mode and to investigate its evolution in time.

Acoustic pressure reconstruction

Once the $a_k(t)$ have been determined using the analytic pressure measurements the acoustic pressure field can be reconstructed. Although the a_k were determined at the pressure measurements locations only[2], they are valid for the entire acoustic field.

$$p^{\mathrm{A}}(\boldsymbol{x},t) = \sum_{i=1}^{m} a_k(t)\ p_k^{\mathrm{H}}(\boldsymbol{x}) \tag{3.16}$$

As defined in Eq. 3.4, the acoustic pressure field can be reconstructed by taking the real part of the analytic signal:

$$\boxed{p'(\boldsymbol{x},t) = \Re\left[\sum_{i=1}^{m} a_k(t)\ p_k^{\mathrm{H}}(\boldsymbol{x})\right]} \tag{3.17}$$

The contribution of a single mode $p_k^{\mathrm{H}}(\boldsymbol{x})$ to the analytic pressure field is:

$$p_k^{\mathrm{A}}(\boldsymbol{x},t) = a_k(t)\ p_k^{\mathrm{H}}(\boldsymbol{x}) \tag{3.18}$$

Consequently, the contribution of a single mode $p_k^{\mathrm{H}}(\boldsymbol{x})$ to the acoustic pressure field $p'_k(\boldsymbol{x},t)$ is:

$$p'_k(\boldsymbol{x},t) = \Re\left[a_k(t)\ p_k^{\mathrm{H}}(\boldsymbol{x})\right] \tag{3.19}$$

Acoustic velocity reconstruction

Similarly to the modal decomposition of the pressure field using the Helmholtz pressure modes, the acoustic velocity field can be decomposed as:

$$\boxed{u^{\mathrm{A}}(\boldsymbol{x},t) = \sum_{i=1}^{m} b_k(t)\ u_k^{\mathrm{H}}(\boldsymbol{x})} \tag{3.20}$$

Considering a single mode k, Eq. 3.20 becomes:

[2]The a_k have been determined using a reduced set of point rather than the entire field.

$$u_k^{\mathrm{A}}(\boldsymbol{x},t) = b_k(t)\ u_k^{\mathrm{H}}(\boldsymbol{x}) \tag{3.21}$$

The coefficient $b_k(t)$ is the *complex velocity amplitude* and is unknown. As presented in Sec. 2.1.3 the linearized inviscid momentum equation (Eq. 2.24 on page 16) gives a direct link between the acoustic pressure and the acoustic velocity. Considering a single Helmholtz eigenmode k, the linearized inviscid momentum equation reads:

$$\rho_0 \frac{\partial u_k^{\mathrm{A}}(\boldsymbol{x},t)}{\partial t} = -\nabla p_k^{\mathrm{A}}(\boldsymbol{x}) \tag{3.22}$$

Using the modal decomposition of both pressure and velocity yields:

$$\rho_0 u_k^{\mathrm{H}}(\boldsymbol{x}) \frac{\partial b_k(t)}{\partial t} = -a_k(t) \nabla p_k^{\mathrm{H}}(\boldsymbol{x}) \tag{3.23}$$

The linearized inviscid momentum equation for a Helmholtz eigenmode k is (Eq. 2.24):

$$i\omega\rho_0 u_k^{\mathrm{H}}(\boldsymbol{x}) = -\nabla p_k^{\mathrm{H}}(\boldsymbol{x}) \tag{3.24}$$

Introducing Eq. 3.24 in Eq. 3.23 leads to:

$$\frac{\partial b_k(t)}{\partial t} = i\omega a_k(t) \tag{3.25}$$

In order to determine the complex velocity amplitude $b_k(t)$, let's assume that it is the composition of two functions: an envelope function $E(t)$ and a pure complex harmonic signal[3]:

$$b_k(t) = E(t) \times e^{-i\omega t} \tag{3.26}$$

This assumption is reasonable as the eigenmodes are known to oscillate at a given eigenfrequency ω. The time derivative of $b_k(t)$ is:

$$\frac{\partial b_k(t)}{\partial t} = (\epsilon - i\omega) b_k(t) \tag{3.27}$$

where ϵ is the rate of change of the envelope function (in s^{-1}):

$$\epsilon = \frac{1}{E(t)} \frac{\partial E(t)}{\partial t} \tag{3.28}$$

Equations 3.25 and 3.27 give the exact value of the complex velocity amplitude $b_k(t)$:

$$b_k(t) = \frac{-1}{1 + i\frac{\epsilon}{\omega}} a_k(t) \tag{3.29}$$

Although mathematically correct[4], Eq. 3.29 is not practical as one needs to know the envelope function $E(t)$ to compute the coefficient $b_k(t)$ from $a_k(t)$. Luckily, in many real case applica-

[3] In this manuscript the $-i\omega t$ convention is used.

[4] For the $+i\omega t$ convention $b_k(t) = \frac{+1}{1+i\frac{\epsilon}{\omega}} a_k(t)$

tions the rate of change of the modes envelope is small compared to the angular frequency ω. In such cases the complex velocity amplitude $b_k(t)$ reduces to[5]:

$$\boxed{b_k(t) = -a_k(t)} \tag{3.30}$$

Using Eqs. 3.20 and 3.30, both analytic and real acoustic velocity fields can be reconstructed.

Acoustic mode envelope amplitude

The temporal amplitude for a mode k is defined in Eq. 3.2 from the envelope amplitude k, *i.e.* zero-to-peak amplitude. Taking the norm (*cf.* Eq. 3.8) of the complex amplitude $a_k(t)$ yields the envelope amplitude A_k(t):

$$\begin{aligned}
||a_k(t)||_2 &= ||A_k(t)e^{i\omega_k t}||_2 && (3.31)\\
&= \left(A_k(t)e^{i\omega_k t}\overline{A_k(t)e^{i\omega_k t}}\right)^{\frac{1}{2}} && (3.32)\\
&= \left(A_k^2(t)\underbrace{e^{i\omega_k t}\overline{e^{i\omega_k t}}}_{=1}\right)^{\frac{1}{2}} && (3.33)\\
&= A_k(t) && (3.34)
\end{aligned}$$

The same derivation can be done on the acoustic velocity but the acoustic velocity vectors are not normed. In Cartesian coordinates, it leads to:

$$\begin{aligned}
A_k^u(t) &= ||b_k(t)||_2 \; ||u_k^{\mathrm{H}}(\boldsymbol{x})||_2 && (3.35)\\
A_k^v(t) &= ||b_k(t)||_2 \; ||v_k^{\mathrm{H}}(\boldsymbol{x})||_2 && (3.36)\\
A_k^w(t) &= ||b_k(t)||_2 \; ||w_k^{\mathrm{H}}(\boldsymbol{x})||_2 && (3.37)
\end{aligned}$$

[5]For the $+i\omega t$ convention $b_k(t) = a_k(t)$

3.3 Validation

This section presents the validation of the IMD methodology on a simple configuration.

3.3.1 Test case presentation

The geometry and mesh used in the study are presented in Fig. 3.3. It is a simplified Liquid Rocket Engine (LRE). The main part of the Simplified LRE configuration is made of a cylindrical cavity mimicking the combustion chamber such as the one used in the BKD (*cf.* Chapter 4). In LRE configurations, a strong coupling between the transverse modes in the chamber and the longitudinal modes in the injectors have been observed [18, 20, 121, 127, 130]. Five small cylinders are mounted on a cylindrical cavity: they represent the acoustic impact of coaxial injectors such as in the BKD.



Figure 3.3: Simplified LRE configuration setup.

Table 3.1 summaizes the dimensions of the setup. The diameter of the chamber is the same as the one of the BKD. Its length corresponds to the one used in the Helmholtz simulation of the BKD in Urbano *et al.* [121] and Douasbin *et al.* [133]. The injection faceplate (surface where the injectors and the main cylinder meet) is located at $x = 0$ m. The inner injector is located on the center of the chamber. The center of the other four outer injectors are located at 3 cm at the inner injector's center. These injectors are located at an equiangular spacing of 90°.

Part	Length [m]	Diameter [m]	Aspect Ratio [-]
chamber	2.16×10^{-1}	8×10^{-2}	2.7
injectors	3.28×10^{-2}	5×10^{-3}	6.556

Table 3.1: Geometric properties of the Simplified LRE configuration.

The mean flow conditions are summarized in Table 3.2. The setup is a cavity, so that every boundary condition is set as a slip wall. The working fluid is air and is considered as a perfect gas.

Name	Variable	Value	Unit
Specific Heat ratio	γ	1.4	-
Mean Density	ρ_0	1.172	$\mathrm{kg\,m^{-3}}$
Mean sound speed	c_0	347	$\mathrm{m\,s^{-1}}$
Mean Temperature	T_0	300	K
Mean Pressure	P_0	1.01325×10^5	Pa
Mean speed (x axis)	u_0	0	$\mathrm{m\,s^{-1}}$
Mean speed (y axis)	v_0	0	$\mathrm{m\,s^{-1}}$
Mean speed (z axis)	w_0	0	$\mathrm{m\,s^{-1}}$

Table 3.2: Mean flow conditions for the Simplified LRE case.

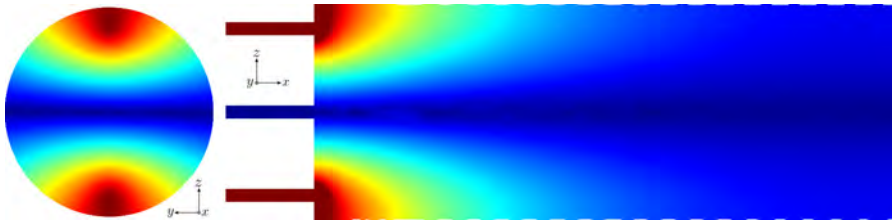
3.3.2 Helmholtz simulation

A Helmholtz simulation of the setup is conducted with the AVSP solver [47, 132] for the flow parameters presented in Table 3.2. Transverse modes in LRE are very difficult to mitigate so that they are the focus of the present study. Two degenerte 1T (*i.e.* first tangential) eigenmodes are found by the Helmholtz solver at a eigenfrequency of $f_{1\mathrm{T}} = 2428$ Hz: they will be referred to as $1T$ and $1T'$. These solutions are presented in Fig. 3.4.

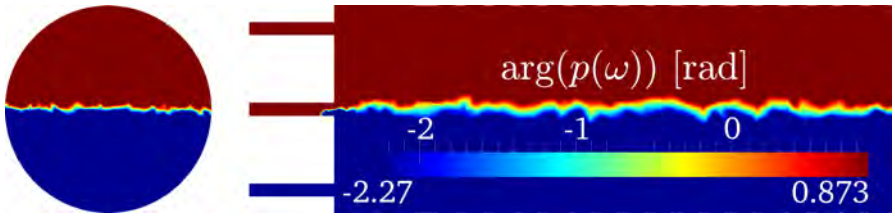
On Fig. 3.4(a) and 3.4(c) the modulus of the pressure modes is shown in a transverse cut (left) and in longitudinal cut (right) in the chamber. The dark blue represents the minimum amplitude of the pressure fluctuation, *i.e.* the pressure node ($p_{1\mathrm{T}}||(\omega)|| = 0.$), and the dark red represents the maximum of the modulus. The $1T$ and $1T'$ modes have a nodal line oriented along the y and z axis, respectively: they are shifted by a 90° angle.

On Fig. 3.4(b) and 3.4(d) the argument (or phase) of the pressure modes is shown in a transverse cut (left) and in longitudinal cut (right) in the chamber. The dark blue represents the minimum phase of $\arg(p(\omega))$ and the dark red represents the maximum phase $\arg(p(\omega))$. The phasing is different on both sides of the nodal line for both $1T$ and $1T'$ modes. The values indicated in the colormaps can be misleading: the values of the maximum and minimum are in the interval $[-\pi, \pi]$ and the phase difference between the two sides of the nodal line is of $\pm\pi$ so that the pressure oscillations are in phase opposition.

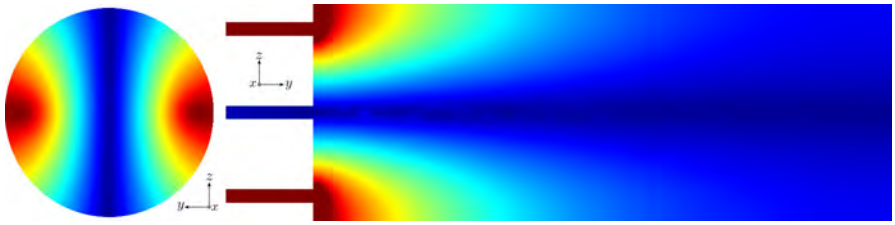
Both modes have a similar transverse structure to the one presented in Fig. 2.2(b): the first order tangential mode of a cylindrical cavity. Because of the asymmetry in the x direction, the modes also have a longitudinal structure. The longitudinal structure exists both in the chamber and in the injectors. The longitudinal mode structure in the chamber can be seen in Fig. 3.4(a) and 3.4(c) as the modulus is high in the faceplate region and low about $x \simeq 2.16 \times 10^{-1}$ m: it corresponds to a quarter-wave mode. The longitudinal modal structure in the injectors cannot be visualized on these figures due to the saturation of the color map. One-dimensional plots of the pressure modulus along the longitudinal coordinate x are presented in Fig. 3.5 for injectors facing a pressure anti-node for modes $1T$ and $1T'$, respectively. The



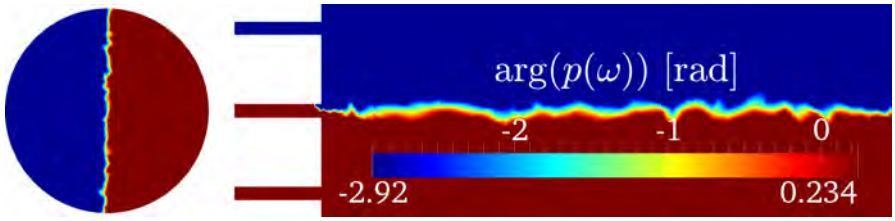
(a) $||p_{1\mathrm{T}}(\omega)||$



(b) $\arg(p_{1\mathrm{T}}(\omega))$



(c) $||p_{1\mathrm{T}'}(\omega)||$



(d) $\arg(p_{1\mathrm{T}'}(\omega))$

Figure 3.4: Modulus and argument of the pressure eigenmodes $1T$ and $1T'$.

pressure modulus profile illustrates that the pressure mode has a longitudinal structure in the injectors (negative x). The maximum pressure modulus in the chamber is about an order of magnitude lower that the one in the injectors: a pressure oscillation of 1 Pa in the chamber will trigger a pressure oscillation of about 10 Pa in the injector facing the pressure antinode.

3.3.3 Temporal simulation

In order to validate the IMD method Navier-Stokes simulation is conducted to study the evolution of the acoustic modes in the domain.

The initial solution consists in superimposing the $1T$ standing mode found using the Helmholtz solver (*cf.* Fig. 3.4) to the mean flow conditions presented in Table 3.2. The pressure field is initialized as:

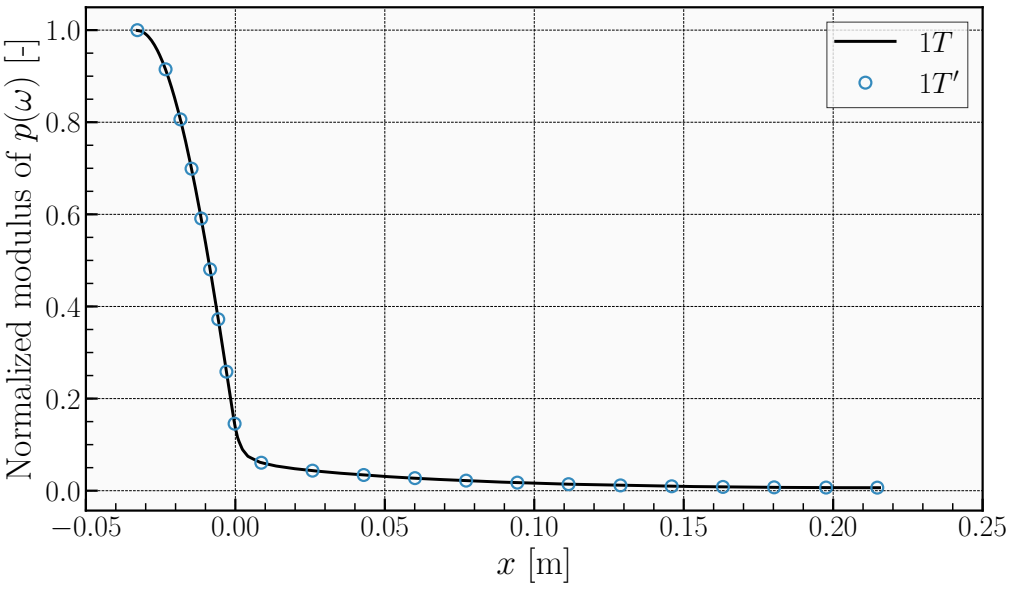


Figure 3.5: Pressure modulus over the x axis for injectors facing a pressure anti-node.

$$p(x,y,z) = p_0 + A \times \underbrace{|p_{1T}(x,y,z,\omega)| \cos\left[\arg\left(p_{1T}(x,y,z,\omega)\right)\right]}_{p'_{1T}} \tag{3.38}$$

where A is the maximum pressure amplitude of the mode (in Pa) at time $t = 0$ s. The amplitude A chosen for the validation test case is $A = 10$ Pa.

The temporal simulation has been carried out with the perfect-gas version of the AVBP code, jointly developed by CERFACS (Toulouse, FRANCE) and IFPEN (Rueil-Malmaison, FRANCE). The temporal integration is performed with a two-step Taylor-Galerkin scheme called TTG4A, which is third order accurate in space and fourth order accurate in time [134, 135]. The walls are assumed to be adiabatic and are treated as slip boundaries everywhere (in the injectors, in the injection faceplate and in the chamber). The computational domain is discretized with a 1.5 M element mesh.

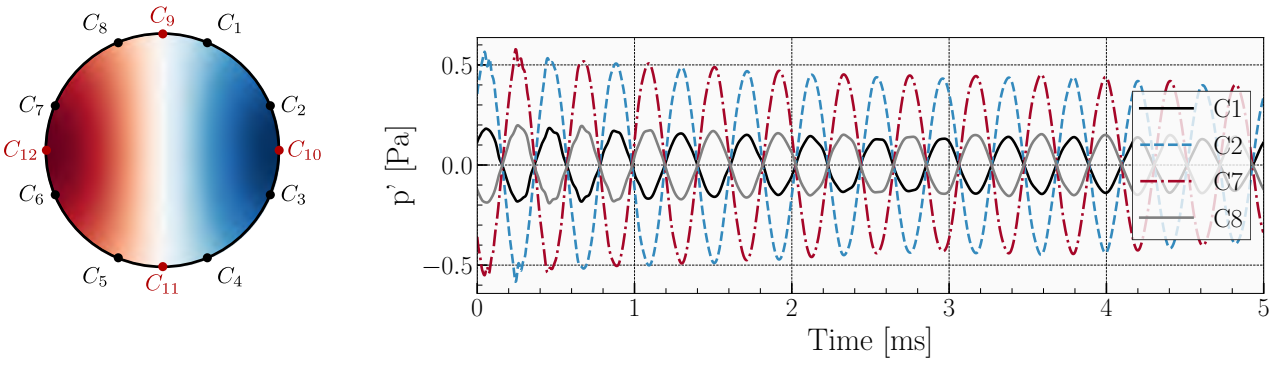
3.3.4 Instantaneous Modal Decomposition

An IMD is performed using the results from the temporal simulation. In order to do so:

- The pressure traces of the probes of the "Ring C" (C1-C8) (*cf.* Fig. 3.6(b)) are used to build the analytic pressure signals as defined in Sec. 3.2.1,
- The values of the Helmholtz pressure modes $1T$ and $1T'$ at the aforementioned probes (C1-C8) (*cf.* Fig. 3.4) are used to build the vectors of the basis.

Figure 3.6(a) shows the location where the pressure measurements are performed. In the numerical simulation, four probes are added to the Ring C: the probes C9, C10, C11 and C12.

They are at a 90° angle with each other's and are located at the minima and maxima of the considered transverse modes (*cf.* Fig 3.6(a)).



(a) (b)

Figure 3.6: (a) Pressure probes located on the "Ring C" at $x = 5.5$ mm, (b) pressure traces of the simplified LRE configuration.

Pressure signals used for the modal decomposition

The pressure traces at the probe locations are extracted from the temporal simulation and presented in Fig. 3.6(b). Only four probes are presented here.

Construction of the basis for IMD

As explained in Sec. 3.2.1, the instantaneous modal decomposition consists in a projection of pressure measurements onto acoustic modes at the same locations and at each time step of the signal. Here, we use the pressure signals at the probe C1 to C8 for the IMD (*cf.* Fig. 3.6), hence, the reduced set of point $\boldsymbol{\chi}$ (*cf.* Eq. 3.12) used here is:

$$\boldsymbol{\chi} = (C_1, C_2, C_3, C_4, C_5, C_5, C_7, C_8) \tag{3.39}$$

The basis will be made of only two Helmholtz pressure eigenmodes from the numerical simulation (AVSP): $1T$ and $1T'$ (*cf.* Fig. 3.4). For instance, the vector corresponding to the 1T will be constructed as follows:

- An *unormed* vector $\boldsymbol{\varphi}_{1T}$ is created for the set of points $\boldsymbol{\chi}$. This vector contains the complex values of the Helmholtz pressure eigenmodes at the 8 considered probe locations.

$$\boldsymbol{\varphi}_{1T} = \begin{bmatrix} p_{1T}(C_1) \\ p_{1T}(C_2) \\ \vdots \\ p_{1T}(C_8) \end{bmatrix} \tag{3.40}$$

- The normed vector $\boldsymbol{p}_{1T}^{\mathrm{H}}$ (used for the projection) is created from $\boldsymbol{\varphi}_{1T}$.

$$\boldsymbol{p}_{1T}^{\mathrm{H}} = \frac{\boldsymbol{\varphi}_{1T}}{||\boldsymbol{\varphi}_{1T}||_2} = \frac{1}{\sqrt{\langle \boldsymbol{\varphi}_{1T},\ \boldsymbol{\varphi}_{1T} \rangle}} \times \begin{bmatrix} p_{1T}(C_1) \\ p_{1T}(C_2) \\ \vdots \\ p_{1T}(C_8) \end{bmatrix} \tag{3.41}$$

The same procedure is used to build the second vector of the basis $\boldsymbol{p}_{1T'}^{\mathrm{H}}$.

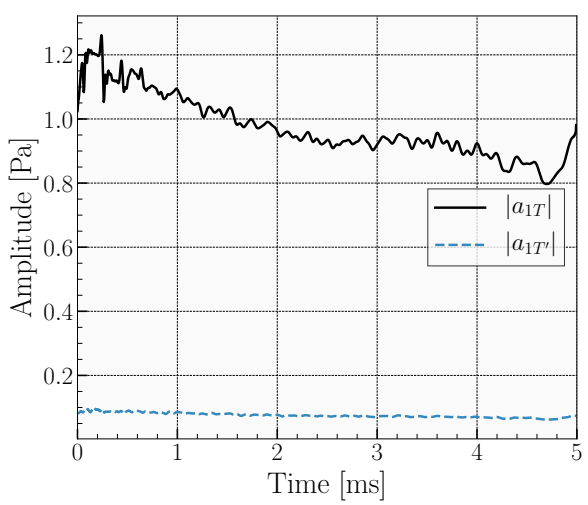
Construction of the analytic pressure signals vector

Using Eq. 3.4 yields the analytic signals vector:

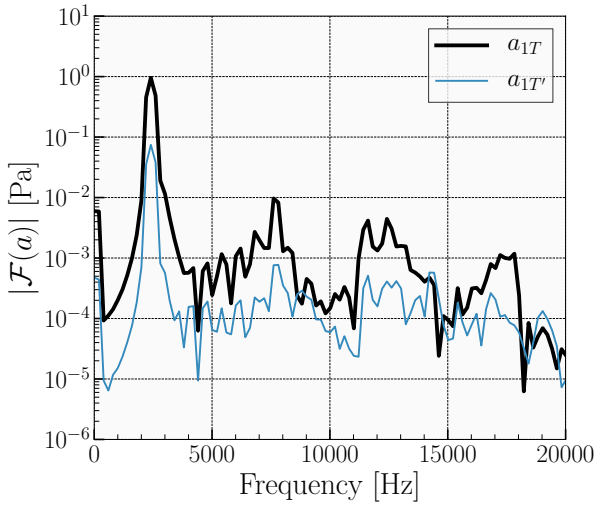
$$\boldsymbol{p}^{\mathrm{A}}(t) = \begin{bmatrix} p'(C_1,t) + i\mathcal{H}\left(p'(C_1,t)\right) \\ p'(C_2,t) + i\mathcal{H}\left(p'(C_2,t)\right) \\ \vdots \\ p'(C_8,t) + i\mathcal{H}\left(p'(C_8,t)\right) \end{bmatrix} \tag{3.42}$$

Results

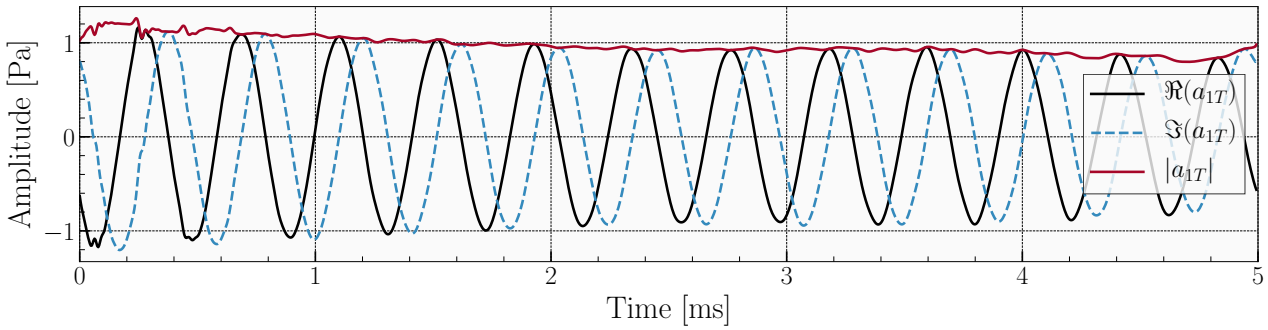
Figure 3.7(a) shows the modulus of the complex amplitudes a_{1T} and $a_{1T'}$. As shown in Fig. 3.1, the modulus of a complex amplitude yields the envelope of the signals. The modulus is representative of the acoustic energy of an acoustic mode [9]. As expected, the energy contained by the $1T$ mode is dominant: the envelope of the signal is an order of magnitude higher than the one of the $1T'$ mode.



(a) Modulus of the complex amplitudes



(b) Spectrum of the real part of the amplitudes



(c) Real part, imaginary part and modulus of the complex amplitude a_{1T} of the dominant $1T$ mode

Figure 3.7: IMD complex amplitudes a_{1T} and $a_{1T'}$ obtained by projection.

The signal of the modulus of a_{1T} in time is noisy. This may be due to the fact that a_{1T} is not purely monochromatic and to the saturation effect observed on the pressure signals (*cf.* Fig. 3.6(b)) Additionally, the Hilbert transform has an impact on the IMD results: at the beginning ($t < 0.5$ ms) and at the end of the signal ($t > 4.5$ ms) the modulus of the complex amplitude a_{1T} has spurious oscillations. This "end-effect" was discussed in Sec. 3.2.1 and is due to the numerical approximation of the Hilbert transform.

Performing the Fourier transform $\mathcal{F}(\cdot)$ of the amplitudes' real part and taking their modulus gives the spectra shown in Figure 3.7(b). The Fourier transform of the imaginary part (not

shown here) yields the same spectra[6]. Both amplitudes have a strong frequency content at 2400 Hz. This is in agreement with the eigenfrequency found by the Helmholtz solver which is of 2428 Hz. Interestingly, only spatial information was taken from the Helmholtz eigenmodes to perform IMD: the frequencies of the pressure oscillations are given by the flow conditions. Here, the fact that IMD yields the correct frequencies should be considered as a sanity check.

Figure 3.7(c) shows the real part, imaginary part and modulus of the amplitude a_{1T}. The modulus (red solid line) is the same that on Fig. 3.7(a) and it is confirmed that it is a good approximation of the envelope of the real and imaginary parts of a_i signals.

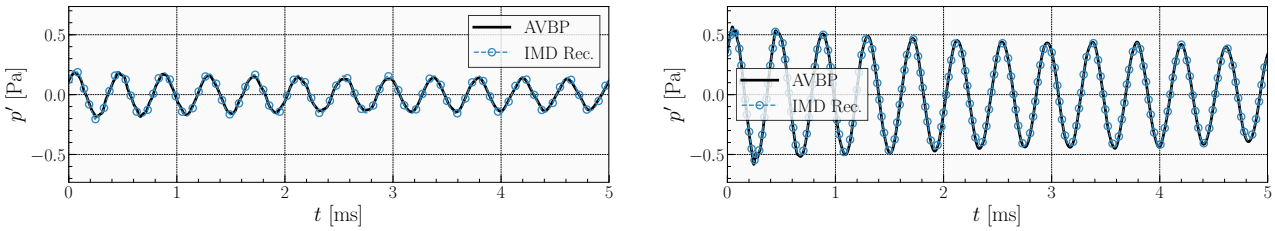
Acoustic energy seems to dissipate fast as the envelope at $t = 4.5$ ms is about 0.3 Pa lower, that is 25% less, than its initial value in 11 periods. The mechanisms involved in the acoustic energy dissipation are beyond the scope of this study and will not be discussed here.

The amplitudes obtained here are useful to analyze which modes are dominant, *i.e.* which modes drive the acoustic field. They can also be used to determine the gain or loss of acoustic energy of a given acoustic mode. In the next sections, the amplitudes will be used to reconstruct the acoustic pressure and acoustic velocity fields in the entire domain from the amplitudes obtained locally using only 8 probes.

3.3.5 Acoustic pressure reconstruction

The methodology presented in Sec. 3.2.2 in order to reconstruct the acoustic pressure field is used here. Applying Eq. 3.17, the acoustic pressure field reconstructed everywhere in the domain. It combines the amplitudes determined by IMD and the Helmholtz pressure modes.

The signals reconstructed using IMD are shown in Figs. 3.8 to 3.13. The acoustic pressure signals from the temporal simulation are shown in black solid line (labeled "AVBP") and the reconstruction signals are shown in dashed blue lines and circle markers (labeled "IMD Rec.").



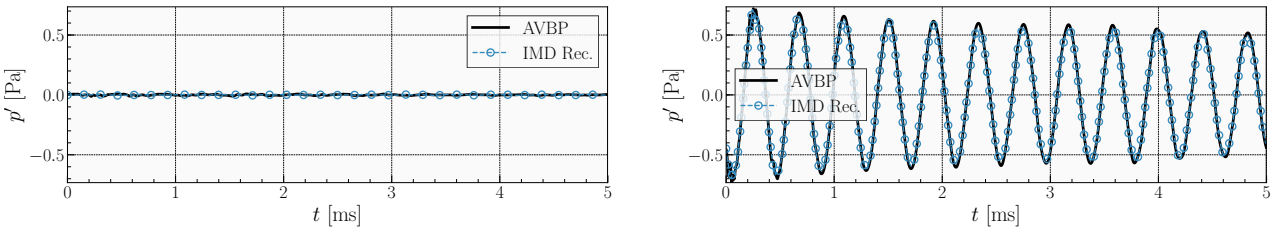
(a) Probe C1 (Ring C)

(b) Probe C2 (Ring C)

Figure 3.8: Acoustic pressure signals from temporal simulation ("AVBP") and signals reconstructed ("IMD Rec.") at Ring C (data used for IMD).

[6] A property of analytic signals is that both their real and imaginary parts have the same frequency content. The a_k are inheriting this property.

First, the pressure signals are reconstructed at the locations where acoustic pressure signals and Helmholtz pressure modes were used for the determination of the amplitudes: the 8 pressure probes from C1 to C8 at Ring C. Two probes are shown here: the probe C1 in Fig. 3.8(a) and the probe C2 in Fig. 3.8(b). The acoustic pressure signals reconstructed from the IMD amplitudes are in excellent agreement with the simulation.



(a) Probe C11 (Ring C)

(b) Probe C12 (Ring C)

Figure 3.9: Acoustic pressure signals from temporal simulation ("AVBP") and signals reconstructed ("IMD Rec.") at Ring C (data not used for IMD).

Figures 3.9(a) and 3.9(b) show the pressure signals obtained at the same axial location (Ring C). Contrary to the probes C1 and C2, the probes C11 and C12 were not used for the determination of the amplitudes a_{1T} and $a_{1T'}$. Once again, the pressure signals reconstructed from the IMD are in excellent agreement with the signals from the simulation.

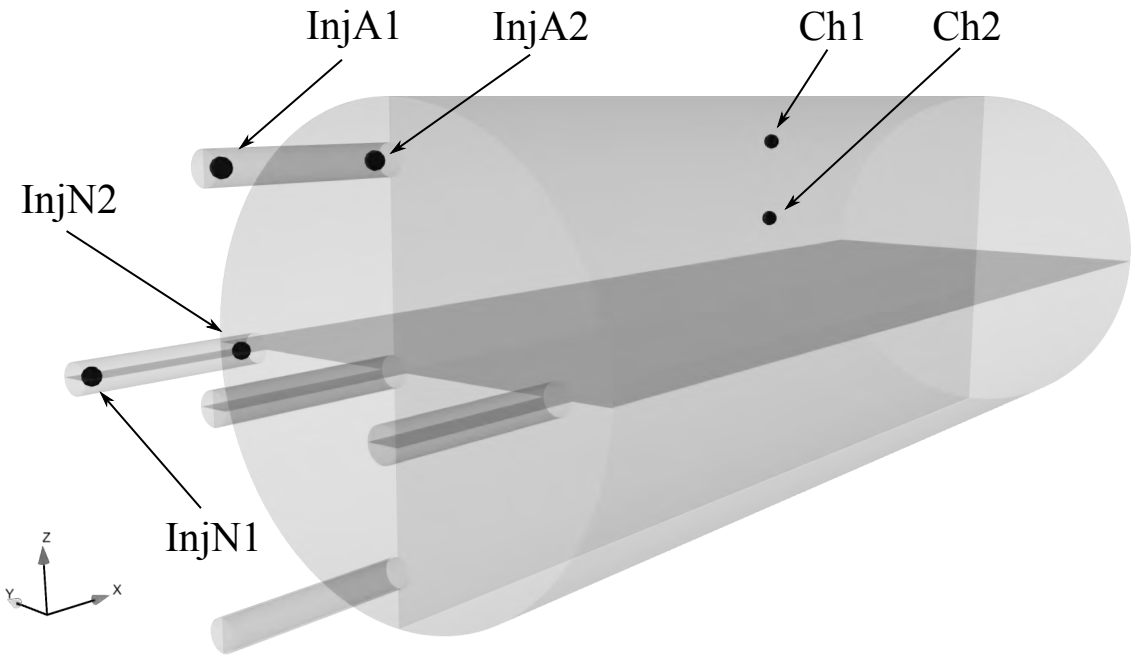
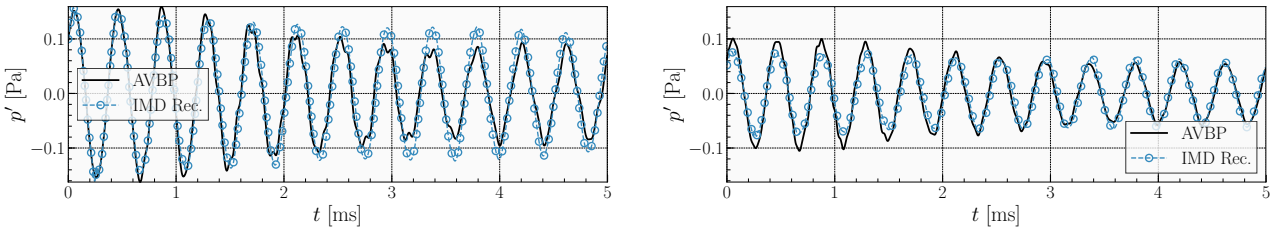


Figure 3.10: Drawing of the chamber and injector probes' location.

Figure. 3.10 is an illustration of other probes location studied here. The probes Ch1 and Ch2 shown in Figs. 3.11(a) and 3.11(b) are located in the chamber, far from the Ring C.



(a) Probe Ch1 (chamber)

(b) Probe Ch2 (chamber)

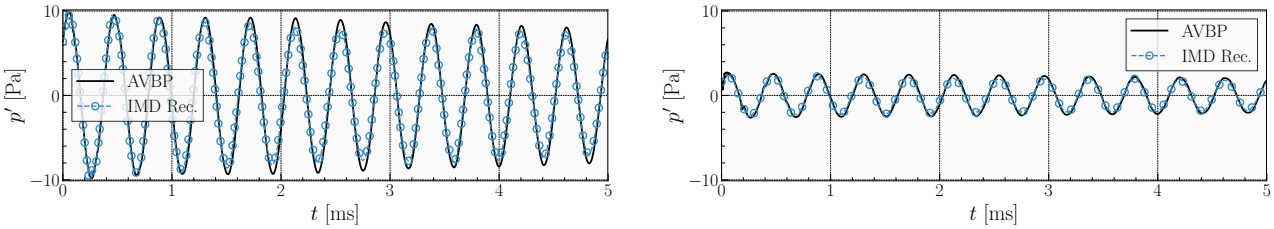
Figure 3.11: Acoustic pressure signals from temporal simulation ("AVBP") and signals reconstructed ("IMD Rec.") in the chamber.

Both probes are located at $x = 10.75$ cm, $y = 0$ m and $z_{Ch1} = 3.1$ cm and $z_{Ch2} = 1.55$ cm, respectively. The probe Ch2 is closer to the nodal line of the $1T$ modes than probe Ch1 and thus has lower amplitude fluctuations. As they stand on the same side of the nodal line, they oscillate in phase. The IMD reconstruction is in good overall agreement with the simulation signals.

For LRE configurations, the coupling between the chamber transverse modes and the longitudinal modes in the injector is of interest as several studies have highlighted the fact that the flame response in LREs could be driven by the acoustic fluctuations in and/or near the injectors [18, 20, 121, 126, 127, 130, 136]. On the 5 injectors present in this setup, we distinguish them by creating two categories: injectors A and injectors N.

On one hand, injectors A are the injectors facing the pressure antinode of the transverse $1T$ mode in the chamber. In an injector A, the pressure fluctuations are strongly coupled to the transverse pressure fluctuations in the chamber. Injectors A see the maximum pressure fluctuation as described by Fig. 3.5 and maximum axial velocity u fluctuations. Finally, they see small transverse velocity fluctuations.

On the other hand, injectors N are facing the pressure node of the transverse $1T$ mode in the chamber. These injectors see near-zero pressure and axial velocity fluctuations but the maximum transverse velocity fluctuations.

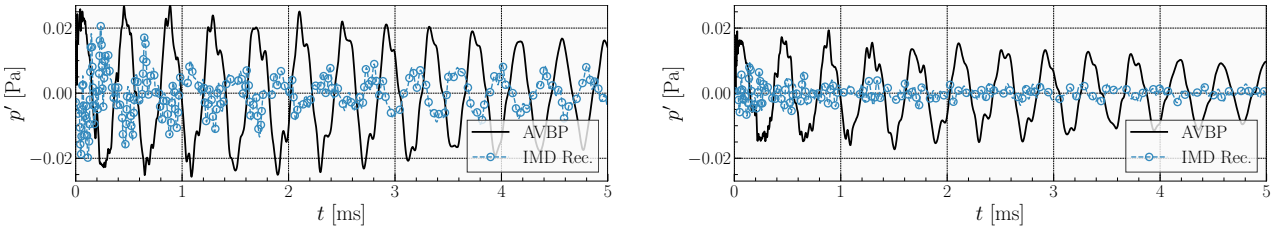


(a) Probe InjA1 (injector A)

(b) Probe InjA2 (injector A)

Figure 3.12: Acoustic pressure signals from temporal simulation ("AVBP") and signals reconstructed ("IMD Rec.") in an injector A.

Figures 3.12(a) and 3.12(b) show pressure fluctuations in an injector A for distinct axial locations ($x_{InjA1} = -3$ cm and $x_{InjA2} = -3$ mm). For both axial locations, the pressure signal obtained by IMD reconstruction is in good agreement with the signals extracted from the temporal simulation.



(a) Probe InjN1 (injector N)

(b) Probe InjN2 (injector N)

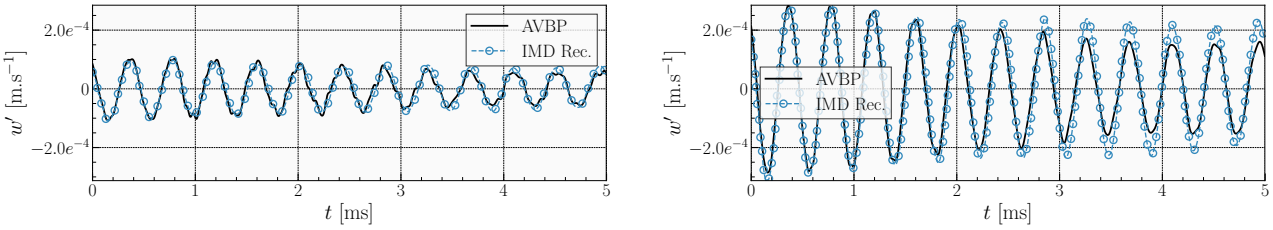
Figure 3.13: Acoustic pressure signals from temporal simulation ("AVBP") and signals reconstructed ("IMD Rec.") in an injector N.

Finally, pressure signals in an injector N are plotted in Figs. 3.13(a) and 3.13(b) for two axial locations ($x_{InjN1} = -3$ cm and $x_{InjN2} = -3$ mm). In this region, the pressure levels are 500 times lower that in an injector A. This low-pressure levels is retrieved by IMD reconstruction.

3.3.6 Acoustic velocity reconstruction

The acoustic field reconstructed by IMD is compared with the one extracted from temporal simulation.

First, the pressure oscillations in the chamber trigger transverse acoustic fluctuations. As the contribution of the $1T'$ mode is small compared to the one of the $1T$ mode, the velocity fluctuations in the chamber can be simply explained from the shape of the eigenmode $1T$. As the nodal line of the $1T$ mode is along the y axis, there is a strong pressure gradient along the z axis inducing w velocity fluctuations.

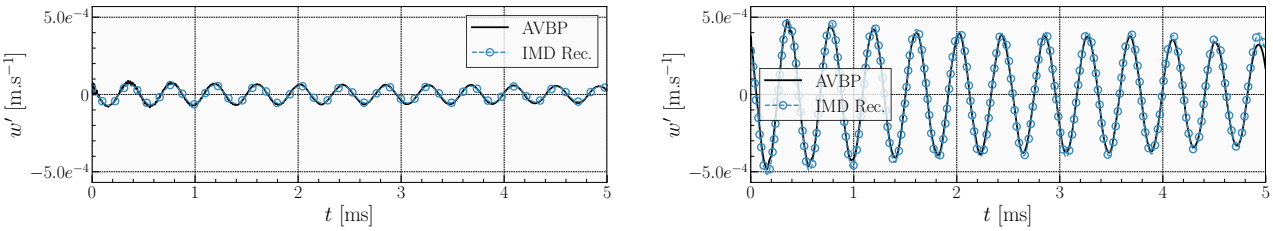


(a) Probe Ch1 (chamber)

(b) Probe Ch2 (chamber)

Figure 3.14: Acoustic velocity signals from temporal simulation ("AVBP") and signals reconstructed ("IMD Rec.") in the chamber.

Figures 3.14(a) and 3.14(b) show the w velocity component in the chamber for the probes Ch1 and Ch2. The probe Ch2 is closer to the nodal line than the probe Ch1, and is thus exhibiting higher amplitude w velocity fluctuations. Some discrepancies are observed even though there is a good overall agreement. As for its pressure signal, the velocity signal of probe Ch1 is not fully monochromatic and, hence, cannot be perfectly reconstructed with the IMD basis used here as only two modes with the same eigenfrequency are considered. The amplitude tends to be overpredicted for probe Ch2. Nevertheless, the acoustic velocities are fairly well reconstructed.



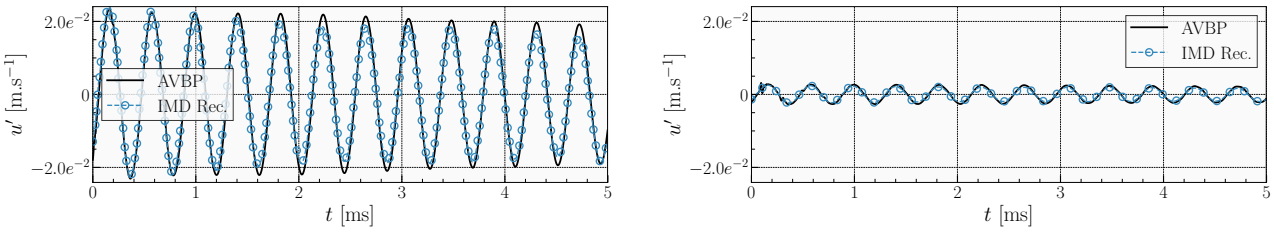
(a) Probe InjN1 (injector N)

(b) Probe InjN2 (injector N)

Figure 3.15: Acoustic velocity signals from temporal simulation ("AVBP") and signals reconstructed ("IMD Rec.") in a injector N.

Figures 3.15(a) and 3.15(b) show the w velocity fluctuations in probes InjN1 and InjN2 ($x_{InjN1} = -3$ cm and $x_{InjN2} = -3$ mm). As the injector N is facing the pressure node of the chamber, it exhibits high w velocity fluctuations (twice as high as for probes Ch1 and Ch2).

The acoustic velocity reconstructed are in excellent agreement with the temporal simulation.



(a) Probe InjA2 (injector A)

(b) Probe InjA1 (injector A)

Figure 3.16: Acoustic velocity signals from temporal simulation ("AVBP") and signals reconstructed ("IMD Rec.") in an injector A.

Finally, the u velocity signals obtained in an injector A are plotted in Figs. 3.16(a) and 3.16(b). The axial velocity fluctuations are extremely high compared to the one in the chamber. The reconstructed axial velocity signals are in good agreement with the temporal simulation signals.

3.4 Conclusion

A novel method called Instantaneous Modal Decomposition (IMD) is presented and validated. It is based on the decomposition of pressure measurement signals onto contributions of Helmholtz eigenmodes for every signal's sample. The analysis takes place in a complex Hilbert vector space where successive projections of the pressure signals onto the Helmholtz eigenmodes yield the temporal evolution of each modes, which is harvested as complex signals called "the complex amplitudes".

The IMD methodology allows to identify the dominant modes in numerical and experimental setups and to study the temporal evolution of the contribution of the modes to the acoustic field. Although IMD uses local pressure signals to analyze the acoustic field, it provides results which can, in turn, be used to reconstruct the entire acoustic field. This can be useful in the combustion instability community as the acoustic velocity fluctuations are known to be a driving mechanism of flame/acoustic coupling.

The method was validated on a temporal simulation of a simplified LRE configuration where IMD was found to give accurate prediction of the mode dynamics and to produce a satisfactory approximation of the 3D acoustic field.

In the next chapter, a more ambitious use of IMD is made: experimental and LES pressure signals are analyzed using IMD.

Chapter 4

Acoustic field in the BKD: analysis & reconstruction

In the previous chapter, the IMD methodology was presented and validated. It allows to study the evolution of the acoustic modes from pressure measurements in a reduced set of locations and to reconstruct both acoustic pressure and acoustic velocity fields.

Some assumptions used to derive IMD cannot be satisfied in real thermoacoustically unstable engine. In such systems, as discussed in Chapter 3, IMD can still yield insights on the acoustic field if particular care is taken.

In this chapter, IMD is applied to an actual configuration: a 42-flame liquid rocket engine operated at DLR Lampoldshausen (Germany) called BKD.

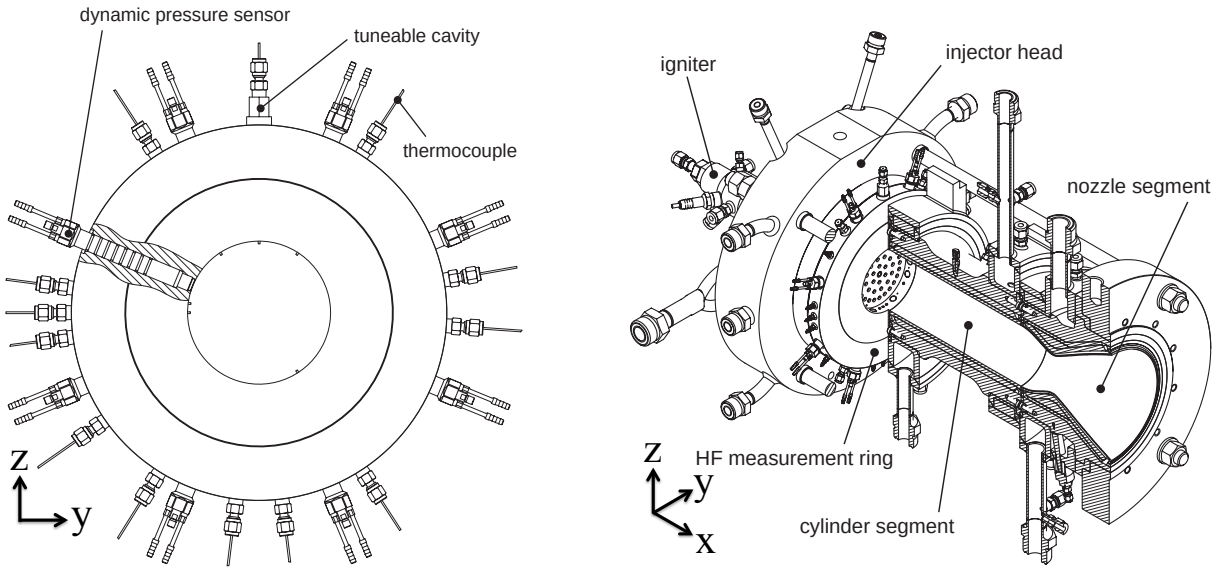
After introducing the experimental setup in Sec. 4.1.1, some experimental and numerical results will be presented in Sec. 4.1.3. Section 4.1.4 will discuss the set of Helmholtz eigenmodes dominant in an unstable operating point before using them as an IMD basis to study both LES and experimental results in Sec. 4.2 and Sec.4.3, respectively.

4.1 Introduction

4.1.1 Experimental setup

The BKD is a LRE at DLR Lampoldshausen (Germany), which operates under conditions representative of a liquid propellant rocket engine. The cylindrical thrust chamber is fed by 42 shear coaxial injectors and has a diameter of 8 cm and a length of slightly more than 20 cm. It is closed by a choked nozzle. The injection plate pattern comprises three concentric rings of respectively 6, 12 and 24 injectors. The propellants, liquid oxygen (LOx) and gaseous hydrogen (H_2) are introduced in the domes through 2 and 6 manifolds, respectively. Geometrical details are given in Fig. 4.1, which also shows the location of the pressure transducers (HF measurement sensors). A more complete description of the experimental setup can be found in Gröning *et al.* [124–126].

The BKD is operating under extreme conditions (high pressure and temperature levels



(a) HF measurement ring

(b) Isometric split view of the experimental setup

Figure 4.1: Drawing of the BKD setup: (a) Detailed view of the HF measurement ring and (b) split view of the BKD.

in addition to very large fluctuations) which makes it a challenging setup for experimental diagnostics. The experimental diagnostics used by DLR are :

1. 8 HF water cooled dynamic pressure sensors located on one ring, *i.e.* at a single axial location

2. 2 static pressure sensors.

3. 3 or 10 fiber-optical probes – depending on the version of the setup [137] – which outputs can be transferred to a photomultiplier (PM) which recognize the OH^* radiations [138].

These diagnostics are located near the faceplate region where moderate temperature conditions (in comparison to further downstream) are present.

In this manuscript, two operating points labeled LP1 and LP4 are considered. They correspond to thermoacoustically stable and unstable operating points, respectively. The injection rates, temperature and pressure of the propellants are summarized in Table 4.1.

Assuming that chemical equilibrium is reached in the chamber and that the nozzle throat is choked, Urbano *et al.* [121] have estimated the chamber pressure p_c using the Chemical Equilibrium and Applications (CEA) software developed by the National Aeronautics and Space Administration (NASA) [139]. The resulting theoretical equilibrium conditions are a chamber pressure of $p_\mathrm{c} = 70$ bar and $p_\mathrm{c} = 80$ bar and a temperature of $T_\mathrm{c} = 3066$ K and $T_\mathrm{c} = 3627$ K for LP1 and LP4, respectively [121]. Finally, the theoretical thermal power produced is approximately 66 MW for LP1 and 86.2 MW for LP4. The thrust of the BKD has been approximated to be about 25 kN [137].

	LP1	LP4	Unit
ROF	4	6	-
$\dot{m}_{H_2}$	1.11	0.96	$kg\,s^{-1}$
$\dot{m}_{O_2}$	4.44	5.75	$kg\,s^{-1}$
T_{i,H_2}	94	96	K
$T_{i,0_2}$	112	111	K
p_{i,H_2}	100	103	bar
$p_{i,0_2}$	78	94	bar

Table 4.1: Injection conditions in the BKD experiment for the two load points considered. "ROF" denotes the Oxidizer/Fuel mass ratio. and the "i" subscript refers to the values at the injection stage.

4.1.2 Real gas effects

High pressure jets studies have been driven by the need of performance gains in the field of cryotechnical liquid rocket engines. In such conditions, both thermodynamic and transport properties are modified with respect to perfect gases.

Typical non-reacting jets of liquid nitrogen (LN_2) in gaseous Helium (GHe) have been studied experimentally by Mayer *et al.* [140, 141] and shadowgraphs of the experiment are shown in Fig. 4.2. In Fig. 4.2a The nitrogen is injected at 10 bar (*cf.* Fig. 4.2a) and 60 bar (*cf.* Fig. 4.2b). The jets observed in the two cases are very distinct.

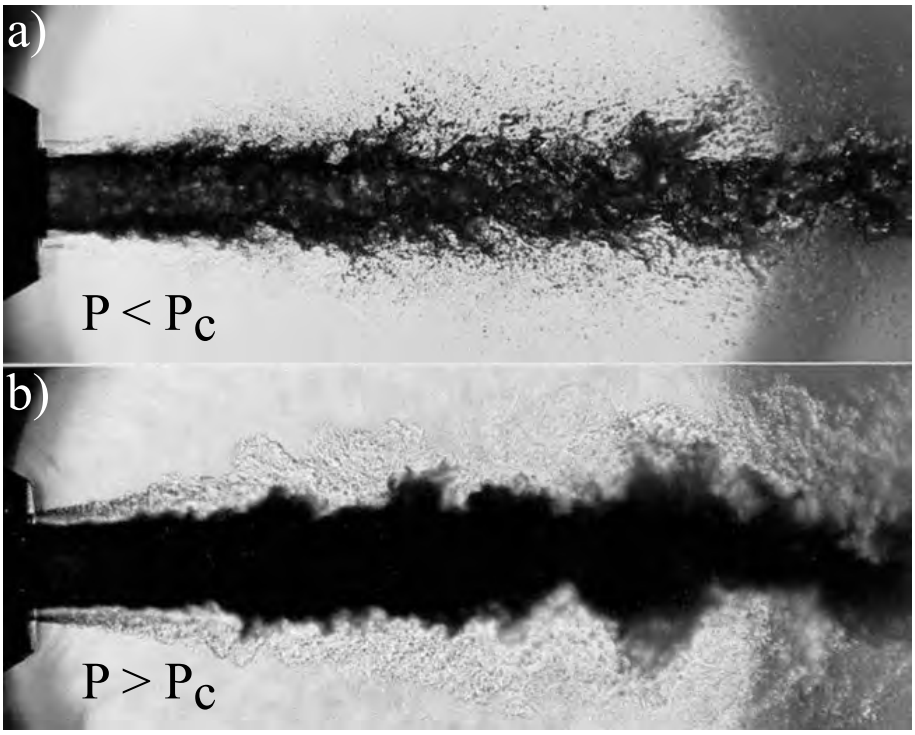


Figure 4.2: LN_2/GHe coaxial jet. Reproduced from Mayer and Smith [141]

In the case of the low-pressure LN_2 jet, the typical behavior of a spray is observed. The jet destabilizes and finger-like structures are present. These structures further destabilize to form droplets as typically noticed in coaxial jet atomization. Here, both liquid and gaseous phases can be seen and the interface between the two phases is clear.

For the high-pressure case (60 bar), no droplets are present and the interface between the two phases becomes blurry. Here, only a dense phase and a light phase can be identified and the thermodynamic properties between the two phase evolve smoothly rather than abruptly as seen in Fig. 4.2a. The topology of the jet becomes similar to a gaseous jet with density variations.

These two kinds of jet topologies can be explained by the pressure levels used in both cases with respect to the *critical pressure* of nitrogen P_C.

The phase diagram of a single species is shown in Fig. 4.3 and the critical point is illustrated. For subcritical values of pressure P and temperature T (i.e. for $P < P_C$ and $T < T_C$), the phase diagram indicates the phase of the species at the thermodynamic equilibrium (solid, liquid or gas).

The interface between two phases (red lines in Fig. 4.3) is clear and at these values of T and P two phases may coexist. These lines are often referred to as the coexistence lines [142, 143]. Between two phases, the properties of the fluid, such as its density, evolve discontinuously. The intersections of the three lines is the triple point, *i.e.* the only temperature and pressure conditions at which the three phases can be present.

Finally, for high pressure and high temperature conditions, the supercritical regime is indicated. Such a regime is achieved when both pressure and temperature exceed the critical pressure (P_C) and critical temperature (T_C). For supercritical fluids, the interface between the liquid and gaseous phases becomes unclear and the properties are varying continuously. It is well established that under such conditions a fluid will not experience surface tension nor enthalpy of vaporization.

The jet in Fig. 4.2a is at subcritical condition while the one in Fig. 4.2b is at supercritical pressure.

The transcritical regime, typical of liquid rocket engines, is reached when the fluid is, at first, at a pressure above the critical pressure, but at a temperature below the critical value and when the temperature rises in the system to reach supercitical conditions.

Accounting for the properties of transcritical and supercritical fluids in LES is vital in order to accurately reproduce the physics. It can be achieved by the use of a “real-gas” (by opposition to perfect gas) equation of state. More details on cubic equation of states can be found in [101, 144–148].

The critical properties of oxygen and hydrogen are recalled in Table 4.2.

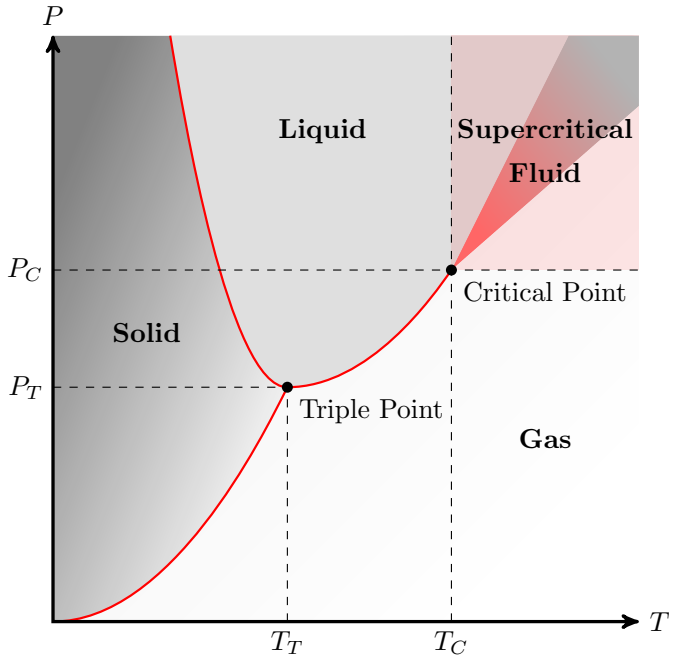


Figure 4.3: Phase diagram for a single species. The pressure P and the temperature T of the triple and the critical points are indicated by the subscripts $_T$ and $_C$.

In the BKD, the fuel (gaseous H_2) is injected at supercritical conditions. Even though the BKD operates at nominal pressure above oxygen's critical point, the oxidizer is not at supercritical condition in the injection stage: the oxidizer's injection temperature is below $T_{\mathrm{cr,O2}}$. Hence, the transcritical regime is reached in the BKD.

As a comparison, in the Vulcain and Vinci engines – the liquid propellant engines of ArianeGroup, the main contractor of the Ariane Rocket propulsion system – the ratio of the pressure chamber (p_c) to critical pressure of the O_2 ($p_{\mathrm{cr,O2}}$) are of 2.18 and 1.19, respectively [6]. Here, this ratio is of 1.39 and 1.59 for LP1 and LP4, respectively.

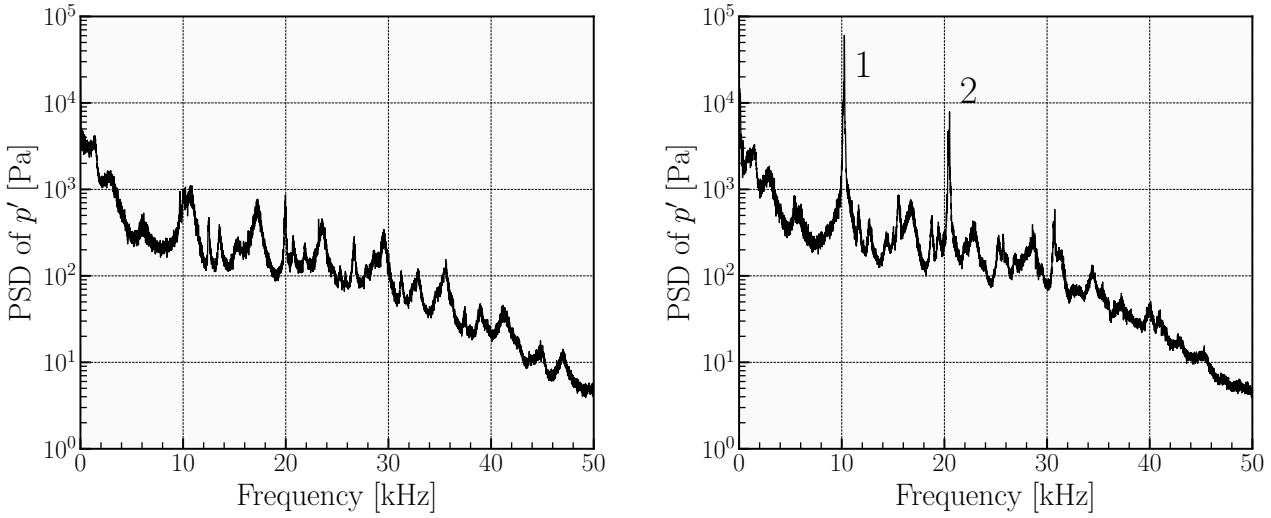
Propellant	Quantity	Notation	Value	Unit
H_2	Critical pressure	$p_{\mathrm{cr,H2}}$	13	bar
	Critical temperature	$T_{\mathrm{cr,H2}}$	33	K
O_2	Critical pressure	$p_{\mathrm{cr,O2}}$	50.4	bar
	Critical temperature	$T_{\mathrm{cr,O2}}$	155	K

Table 4.2: Critical conditions for H_2 and O_2.

4.1.3 Transverse combustion instabilities in the BKD

The BKD configuration exhibits self-sustained transverse combustion instabilities such as typically observed in such systems. It was used in the HF-7 test case for the French-German cooperation on rocket engine stability (REST) where the goal was to compare several state-of-the-art approaches to study high-frequency pressure oscillations [137]. In particular, the mean flow field, the acoustic field and flame excitation mechanisms were being investigated. Airbus DS, EM2C, IMFT, and TUM have participated to the workshop and the results from IMFT and TUM can be found in [97, 121, 133, 136, 149] and [49, 50], respectively. A complete comparison between all approaches can be found in Hardi *et al.* [137]. In this workshop four load points were considered, comprising LP1 and LP4 presented in Sec. 4.1.1.

The Power Spectral Density (PSD) of the experimental pressure measurements provided by DLR Lampoldshausen (Germany) are shown in Fig. 4.4. The PSD is calculated on each of the 8 HF pressure sensors of the ring C (*cf.* Fig. 4.1(a)) using the Welch method [150] and, consistently to the procedure used by DLR in the REST workshop, the modulus of the 8 PSDs are averaged [137]. Figure 4.4 shows two spectra corresponding to LP1 and LP4, respectively.



(a) LP1 (b) LP4

Figure 4.4: Power Spectral Density of p' for (a) LP1 and (b) LP4.

First, LP1 exhibits low levels of acoustic fluctuations. The pressure fluctuations at frequencies above 2 kHz are of 1 kPa at the maximum, that is, only 1.5% of the pressure chamber. The low-frequency content exhibits high fluctuation levels but are not the object of the HF-7 test case, which focuses on high-frequency oscillations.

On the contrary, high levels of pressure oscillations are observed for the operating point LP4. Two high-frequency peaks are clearly identified (labeled "1" and "2" in Fig. 4.4(b)).

The first peak, at $f = 10,260$ Hz, has been identified by DLR to be the resonant acoustic mode with a first order tangential structure (*cf.* Fig. 2.2(b)). The placement of the dynamic

pressure transducers in the experiment is optimized to provide accurate measurement of the amplitude of this mode [137]. Sliphorst *et al.* [151] have developed a method based on a least-square fit of the pressure signals in order to yield accurate evaluations of both the first tangential amplitude and its nodal line orientation. First the pressure signals are oversampled and filtered using a bandpass filter centered at the frequency of the first tangential (peak 1). Since a pure tangential mode has a sine structure in the azimuthal direction, the least-square fit is performed so that the pressure signals are decomposed as follows:

$$p'(\theta, t) = A(t) \sin\left(\theta + \varphi(t)\right) \tag{4.1}$$

where $A(t)$ is the zero-to-peak amplitude, θ is the azimuth in the cylindrical coordinates system (r, θ, z) and φ is the angle corresponding to the orientation of the nodal line.

IMD is capable of performing a similar analysis and it was, in fact, the starting point for the development of this approach. The results obtained by IMD are compared to the ones obtained by Sliphorst's method [151] in Sec. 4.2 and Sec. 4.3 for LES and experimental results, respectively.

The second peak, at $f = 20,500$ Hz, cannot, in principle, be identified in the experiment as all of the pressure probes are located at the same radial and axial location. At this frequency, neither a first order tangential structure nor a second order tangential structure was found. At 20.5 kHz, it is observed that all pressure signals are in phase, which makes it impossible to discriminate between a radial or a longitudinal mode.

Large-Eddy Simulations of the complete setup, from the injection domes to the choked nozzle, have been performed by Urbano *et al.* [121, 136] (*cf.* Chapter 5) and Douasbin *et al.* [133].

The details of the LESs are given in Chapter 5. Nonetheless, it is interesting to note that LES allows the determination of both peaks in Fig. 4.4(b): the first peak is identified to be a mode with a first order tangential structure and the second peak to a mode with a first order radial structure [121] (*cf.* Figs. 2.2(b) and 2.2(d), page 17). These modes are not purely tangential or radial but coupled with longitudinal structures in the chamber and, as typically observed in liquid rocket engines, coupled with longitudinal structures in the injector posts. The frequencies of the transverse combustion instabilities predicted by the LES are in excellent agreement with the experimental measurements with a relative error lower than 5%.

As discussed in Chapter 3, the IMD methodology requires a basis of eigenmodes for the projection. We now discuss the use of a Helmholtz solver to obtain this basis.

4.1.4 Helmholtz simulation of the BKD

The acoustic modes shapes are evaluated by solving the homogeneous Helmholtz equation (Eq. 2.25). This approach was used by Urbano *et al.* [121] to identify the modes shapes of the unstable modes in the BKD under the LP4 operation point.

As discussed in Chapter 2, several assumptions are necessary to derive the homogeneous Helmholtz equation. Some of these assumptions are questionable and are discussed here.

First, the determination of acoustic modes requires a baseline flow. As the homogeneous Helmholtz equation is used here, only the sound speed field $c_0(\boldsymbol{x})$ is needed. If the linearized Euler equations were used, a mean velocity field would also have been needed, that is: $u_0(\boldsymbol{x}), v_0(\boldsymbol{x}), w_0(\boldsymbol{x})$.

The sound speed field used by the Helmholtz solver is the time-averaged sound speed field predicted by the LES in the limit cycle [121].

This sound speed field is believed to be (1) accurately predicted as the LES results are in excellent agreement with the experimental data and (2) of high impact on the triggering mechanisms of the thermoacoustic instabilities as discussed in [97, 136].

The derivation of the homogeneous Helmholtz equation requires the use of the wave equation. When deriving the homogeneous Helmholtz equation (Eq. 2.25), the mean flow effects are neglected.

In the BKD, the mean Mach number in the chamber is about $\mathcal{M} \simeq 0.25$, before being accelerated by the choked nozzle. Obviously, the low-Mach assumption does not stand near (or inside) the nozzle. Moreover, the longitudinal structure of the chamber eigenmodes is expected to be impacted by the Mach number. However, in this study we focus on the structure and eigenfrequencies of the transverse modes in the combustion chamber and their coupling with the injectors.

In the chamber, no mean flow is present in the transverse direction so that the transverse structure of the eigenmodes is expected to be well predicted by the Helmholtz solver. In the O_2 injectors, the Mach number is $\mathcal{M} \simeq 0.04$ so that, in these regions, the low-Mach assumption should be considered fulfilled.

As demonstrated by several authors [57, 61, 62, 130], solving the inhomogeneous Helmholtz equation with the acoustic source term being modeled by a flame-response model – a Flame Transfer Function[1] (FTF) – allows the determination of the mode shapes and their associated growth rate. This approach is computationally efficient and is very useful to study the thermoacoustic linear stability of industrial burners.

The goal of the current study is much more modest as we only seek for the mode shapes in order to define a IMD basis. In this context, the use of the homogeneous Helmholtz equation is sufficient. In addition, the question of which flow variable is relevant to model the flame-response of a transcritical H_2/O_2 coaxial flame is yet to be addressed so that no trustworthy flame-response model can be used. Here, the influence of the heat release rate fluctuation q' on the eigenfrequency and the spatial structure of the eigenmodes is neglected[2] [121].

[1] A Flame Describing Function (FDF) can also be used [55]. It is the nonlinear representation a FTF [6]. The basic idea is to define a FTFs taking into consideration the input level of the velocity fluctuations upstream of the flame. It allows to predict limit cycles, mode switching and nonlinear triggering [152–154].

[2] It should be noted that the sound speed field – and consequently the eigenfrequencies and the spatial structures of the eigenmodes – is strongly impacted by the transverse combustion instabilities: the flame are

When deriving the inhomogeneous Helmholtz equation (*cf.* Eq. 2.25, page 16), no equation of state is needed. Here, real gas thermodynamics is accounted for indirectly by the mean sound speed field solved by LES (AVBP-RG, real gas version of AVBP). If the Rayleigh source term is considered, real gas thermodynamics is required in the Helmholtz solver.

The details and the results of the Helmholtz simulation carried out to determine the BKD eigenmodes are now discussed. Two simplifications of the geometry are done for the acoustic simulation:

- **Impedance of the nozzle:**
  The low-Mach assumption used to derive the Helmholtz equation makes it impossible to compute the entire domain. The Mach number reaches high values at the end of the cylinder segment (*cf.* Fig. 4.1(b)), that is when the convergent of the choked nozzle accelerates the fluid. To avoid this issue, only the cylinder segment is kept and the nozzle is replaced by its equivalent impedance boundary condition [155, 156].

- **Hydrogen post:**
  In the LES, small acoustic fluctuation levels are observed in the hydrogen dome. This portion of the setup is also modeled by an impedance boundary condition. The actual impedance of the injector posts is computed from the LES in [121] for the two unstable frequencies of the LP4 operating point. The resulting impedances are[3]: $Z(f_1) = -1.160 - i0.255$ and $Z(f_2) = -1.454 - i0.261$. In preliminary simulations, Urbano *et al.* [121] have found that the hydrogen post impedance only has a marginal impact on the predicted eigenfrequencies and mode shapes.

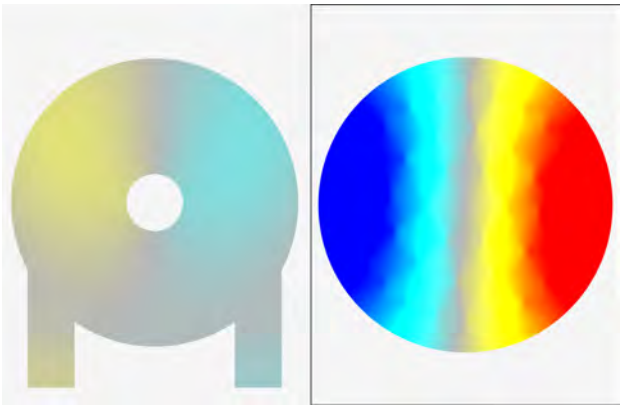
It should be pointed out that the Helmholtz eigenmodes obtained by the AVSP solver are not independent from the LES results as the sound speed field used for the baseline flow is the time-averaged field predicted by the LES.

The simulation is conducted with a 4.3 million cells mesh. The boundary conditions are set to hard walls ($u' = 0$) with the exception of the H_2 injectors and the nozzle that have been replaced with their equivalent impedance as discussed above.

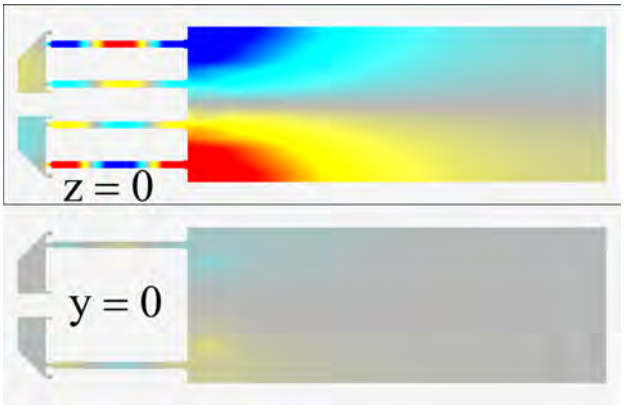
Two modes are identified for the peak 1 and a single mode is identified for the peak 2 in Fig. 4.4(b). The two first modes have the same eigenfrequency $f_1 = 10900$ Hz and they are denoted $1T$ and $1T'$. The real pressure field corresponding to the modes $1T$ and $1T'$ are shown in Figs. 4.5(a), 4.5(b) and 4.5(c), 4.5(d).

shortened. This is especially true for the inner flames at the maximum transverse velocity fluctuation location of the $1T$ mode. This effect is accounted for indirectly by the sound speed field used in the acoustic solver.

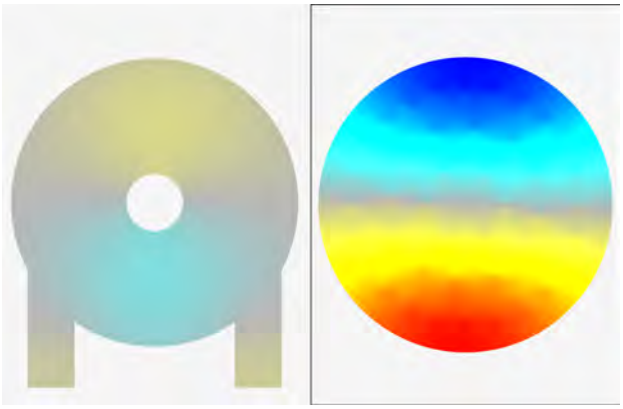
[3] In this manuscript the $-i\omega t$ convention is used.



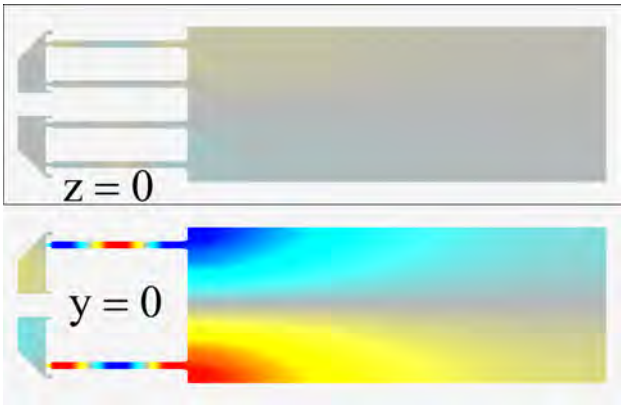
(a) x planes for mode $1T$



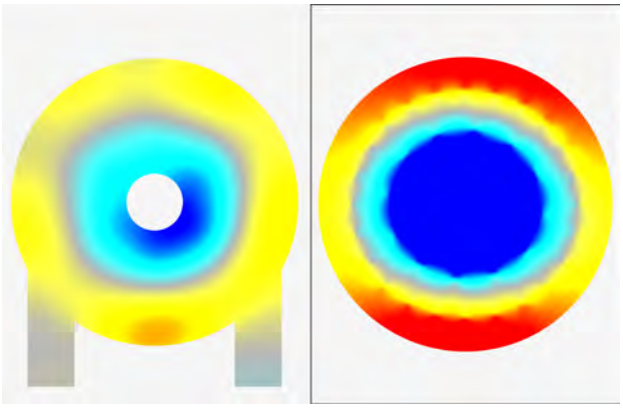
(b) y and z planes for mode $1T$



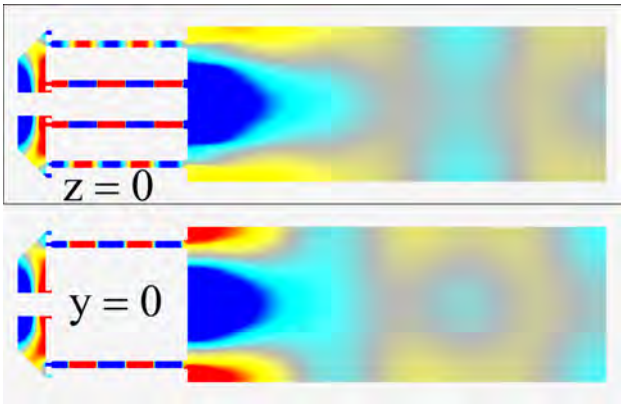
(c) x planes for mode $1T'$



(d) y and z planes for mode $1T'$



(e) x planes for mode $1R$



(f) y and z planes for mode $1R$

Figure 4.5: Real part of pressure eigenmodes $1T$, $1T'$ and $1R$.

Both modes share similar modal structures:

1. A strong first order tangential structure in the chamber such as shown in Fig. 2.2(b) for a cylindrical cavity,
2. The oxygen dome also has a first order tangential modal structure but it is phase shifted by π in comparison with the chamber's structure,
3. A quarter-wave like longitudinal structure can be seen in the chamber,
4. A three-quarter-wave like longitudinal structure in the oxygen posts.

These two modes are tangential standing modes. The nodal lines of the modes $1T$ and $1T'$ are almost perfectly oriented along the $y = 0$ and $z = 0$ planes, respectively. Any other orientation of the nodal line can be obtained as a superimposition of these two modes.

The mode corresponding to the eigenfrequency $f_2 = 21800$ Hz is denoted $1R$ and is shown on Figs. 4.5(e) and 4.5(d). In the chamber, near the injection faceplate, the modal structure is a first order radial mode (*cf.* Fig. 2.2(d), page 17) and the same structure is present in the O_2 injection dome. The pressure oscillations in the dome are in phase with the ones of the chamber. Similarly to the $1T$ and $1T'$ modes, the radial pressure fluctuations in the chamber are coupled with longitudinal pressure modes of the oxidizer posts.

For the three modes presented in Fig. 4.5, a strong acoustic activity is observed in the near-injector region of the chamber.

4.2 IMD of LES signals

In this section, IMD is applied to 4 LESs of the BKD in order to gain understanding on the complex dynamics of the 2 resonant acoustic modes playing a role in the combustion instabilities: the $1T$ and $1R$ modes. Each of the LESs corresponds to the LP4 operating point, which is thermoacoustically unstable. The orientation of the nodal lines is different in each of the 4 LESs and the resulting combustion instabilities exhibit various non-linear limit cycles.

4.2.1 Acoustic triggering & initial solutions

The experimental and numerical setups have been presented in Sec. 4.1.1. In addition to the database generated by Urbano *et al.* [121], three LESs were conducted. The objective of this section is to use IMD to study the mode dynamics in 4 LESs of the BKD setup.

In experiments, self-excited combustion instabilities may occur after a few seconds or even minutes. For example, the walls of an experiment can take a few minutes to heat up to the equilibrium temperature and it is known that the wall heat fluxes have a large impact on thermoacoustic stability [157–159].

The computational burden of high-fidelity simulations, such as LES, is such that only a few milliseconds of physical time can be simulated. In this context, Urbano *et al.* [121] have used a "bomb-test-like" triggering technique in order to excite the acoustic energy.

The "bomb-test" is an experimental technique where actual explosive charges are used to produce an acoustic perturbation in the combustion chambers. When designing a LRE, one has to ensure that no combustion instability can arise as it could lead to a lack of performance, failure or explosion of the system [18, 19]. The explosive charge would excite all the resonant acoustic modes of the chamber which would trigger potential combustion instabilities (if the system is prone to such phenomenon). In the space propulsion industry, this test is a common practice as it is part of the guidelines for design and flight certification of rocket engines [160].

The triggering approach of Urbano *et al.* [121] consists in superimposing an acoustic perturbation to the pressure field as shown in Fig. 4.6. This perturbation is the transverse contribution of first tangential resonant mode – *i.e.* neither radial nor longitudinal contribution is used – similarly to the cross-section view in Fig. 2.2(b). This choice is justified by the fact that authors [18, 20, 130] have shown that the dominant resonant mode in LRE when subject to combustion instabilities is, most of the time, the first tangential mode. This statement is also valid for the BKD setup, as discussed by [121, 127].

The resulting solution is used as an initial solution for the next LES. The pressure field is, hence, initialized as:

$$p_{\text{init}}(x, y, z, t) = p(x, y, z, t) + A \times p'_{1\text{T}}(x, y, z) \tag{4.2}$$

where A is the maximum pressure amplitude of the mode (in Pa) at time $t = 0$ s.

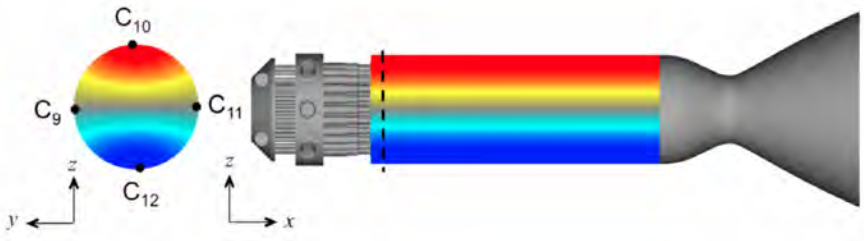


Figure 4.6: Pressure perturbation shape $p'_{1\text{T}}$ superimposed to the thermoacoustically stable unsteady pressure field. (Reproduced from [121])

The BKD configuration operating at the load point LP4 was found to be linearly stable at relatively low amplitudes A (2.5 and 5 bar, *i.e.* 3 % and 7 % of the mean pressure in the chamber p_c, respectively). However, for an amplitude of $A = 10$ bar (13 % of p_c), the triggering resulted in a self-sustain limit cycle [121]. This phenomenon is called *nonlinear triggering* and it has been observed in experimental setups [161] and discussed by several authors [162, 163].

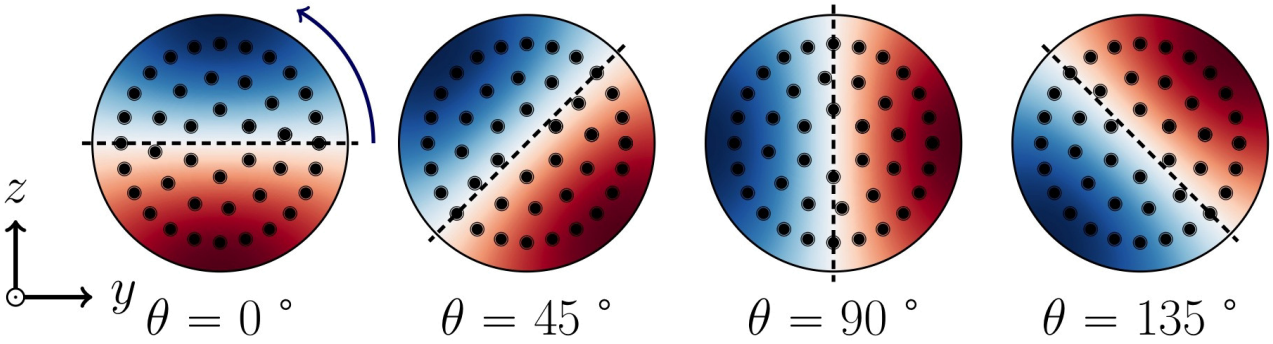


Figure 4.7: Nodal line orientation of initial solution of the 4 LESs used in the study.

Each of the LESs considered in this study are conducted with this initialization strategy. Every bomb-test solution uses the same initial field but the superimposed perturbation is different:

1. **Same amplitude:** the mean-to-peak amplitude is $A = 10$ bar for all the perturbations,
2. **Same mode shape:** the mode shape is the same as the one shown in Fig. 4.6,
3. **Different orientation:** the nodal line orientation of the first tangential mode changes for each solution.

The angle of the orientation, denoted θ, and the four resulting initial solutions are shown in Fig. 4.7. The angle θ is defined such that:

- $\theta = 0°$ when the nodal line is aligned with the y axis,
- $\theta > 0°$ when the nodal line moves toward the z axis counter clockwise (*cf.* Fig. 4.7),
- $\theta = 90°$ when the nodal line is aligned with the z axis,
- $\theta \in [0°, 180°]$.

In the following, the four LESs triggered by the perturbations presented in Fig. 4.7 will be referred to as: “LES0”, “LES45”, “LES90” and “LES135”.

4.2.2 Instantaneous Modal Decomposition of LES pressure signals

The 4 LES are conducted with AVBP-RG with the same numerical setup as presented in Sec. 4.2.1. In this section, the data used to perform the IMD analysis is presented.

Pressure signals used for IMD

The pressure signals used in the current IMD analysis are the 8 probes of the “ring C” such as defined in Figs. 3.6(a). These pressure probes correspond to the HF transducers present in the experimental setup (*cf.* Fig. 4.1(a)).

Figure 4.8 shows the acoustic pressure signals obtained in the LES90 (the LES for the initial perturbation with the nodal line oriented as $\theta = 90°$) for the probes C1, C2, C3 and C4 between 1 ms and 2 ms. These pressure signals are much more complex than the ones studied in Sec. 3.3 (*cf.* Fig. 3.6(b)) to validate the IMD methodology.

A few observations can be made on the presented signals:

1. The maximum mean-to-peak amplitude goes as high as 30 bar *i.e.* about 40% of the mean pressure in the chamber. Such a high value indicates that the linear acoustic theory might not be sufficient to accurately describe the acoustic phenomena in the BKD.

2. The signals are non-monochromatic which indicates the presence of several acoustic modes.

3. The peak values observed in the signals are changing quickly. Under such conditions, the "slow varying envelope" assumption used to reconstruct the acoustic velocity field might not be fulfilled (*cf.* Eqs. 3.29 and 3.30, Sec. 3.2.2, page 33), hence, introducing an error in the acoustic velocity field reconstructed.

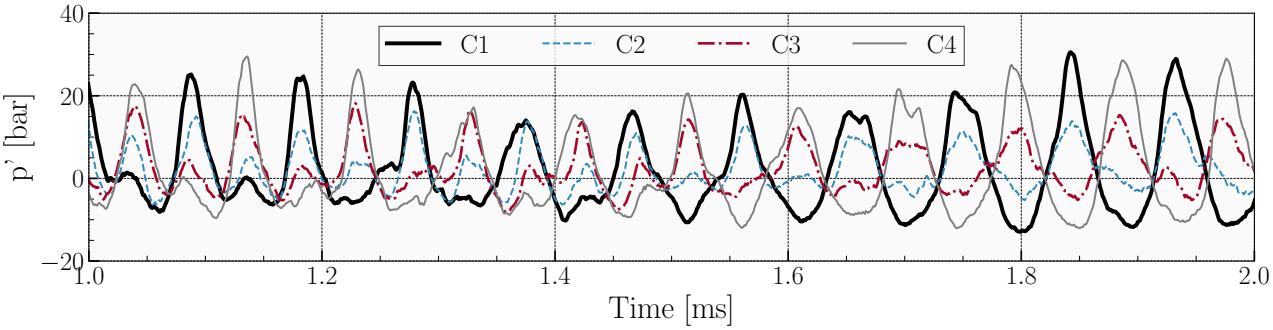


Figure 4.8: Pressure traces LP4 LES90.

Construction of the basis for IMD

Similarly to the construction of the IMD basis for the Simplified LRE configuration (*cf.* Sec. 3.3.4), the basis used for the IMD analysis is constructed using the values of the complex pressure eigenmodes found by the Helmholtz solver AVSP. Since the investigation of Urbano *et al.* [121] has found that the high-frequency CIs present in the BKD are due to two transverse modes ($1T$ and $1R$, *cf.* Fig. 4.5), the IMD basis chosen here comprises the eigenmodes needed to capture the dynamics of these two transverse modes. Three eigenmodes are considered: the $1T$, $1T'$ – two eigenmodes are needed to study the first tangential mode (*cf.* Chapter 3) – and the $1R$ – a single eigenmode is needed to study the first radial mode –. These eigenmodes are shown in Fig. 4.5.

4.2.3 Results

The modal decomposition is used to analyze the four LESs: "LES0", "LES45", "LES90" and "LES135"(*cf.* Fig. 4.7). In this section, a spectral analysis will be conducted on complex amplitude signals and the nodal line orientation will be recovered from the complex amplitudes a_{1T} and $a_{1T'}$. At last, the acoustic field will be reconstructed and compared to the LES signals.

Mode dynamics

As three modes are considered in the IMD analysis ($1T$, $1T'$ and $1R$), three complex amplitudes signals are obtained: $a_{1T}(t)$, $a_{1T'}(t)$ and $a_{1R}(t)$. Figure 4.9 shows the modulus of the complex amplitudes signals for the four cases.

For instance, in Fig. 4.9(a) the modulus of the amplitudes is shown for LES0. At $t = 0$ ms, the first tangential mode is triggered. As explained above, $\theta = 0°$ corresponds to the case where the nodal line is on the y. Consequently, the acoustic field is dominated by the $1T$ contribution as the contribution of $|a_{1T}|$ is roughly one order of magnitude higher that $|a_{1T'}|$.

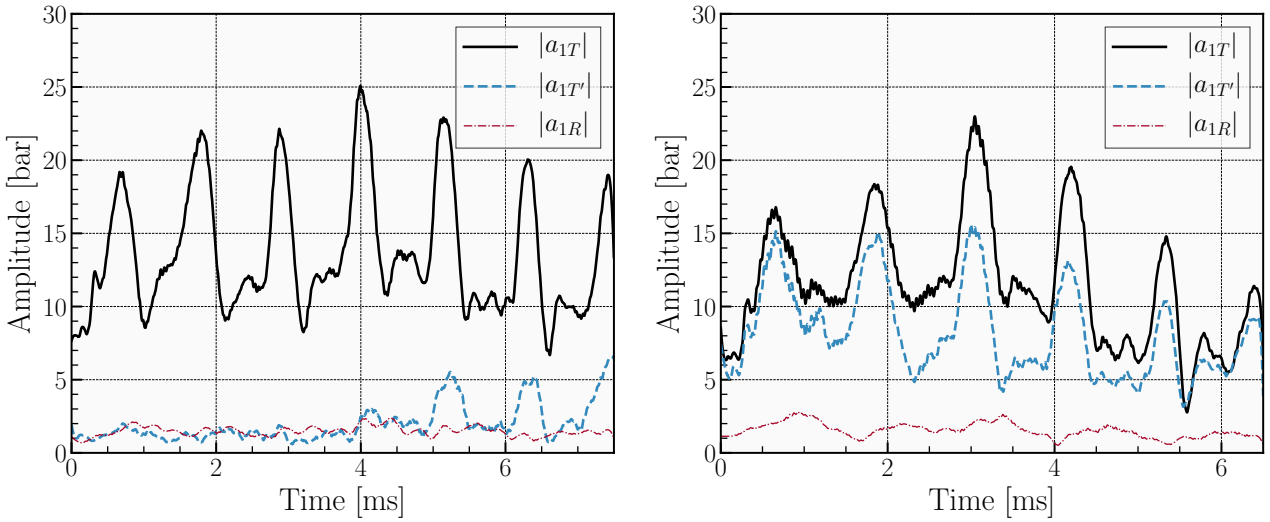
Similarly, the case LES90 corresponds to an initial solution very close to the eigenmode $1T'$ so that the acoustic field is dominated by the $1T'$ contribution.

On the contrary, for LES45 and LES135 (*cf.* Figs. 4.9(b) and 4.9(d)) the amplitudes of $|a_{1T}|$ and $|a_{1T'}|$ are the same at $t = 0$ ms.

Unlike in the simplified LRE configuration (*cf* Chapter 3) where the envelope amplitude was decreasing monotonously, here the envelope has a cyclic regime as observed by Urbano *et al.* [121]: a rough peak-to-peak analysis indicates that this cyclic regime has a frequency of about 1 kHz. This cyclic regime is triggered in the four LESs. However, the exact period of these fluctuations varies for each of the four cases considered.

In the case LES0, $|a_{1T'}|$ increases while $|a_{1T}|$ decreases. This corresponds to a rotation of the nodal line. For LES90, $|a_{1T'}|$ decreases while $|a_{1T}|$ maintains a constant level. This indicates both a nodal line rotation and a dampening of the CIs.

IMD predicts that the first radial mode appears naturally in each of the four cases although, contrary to the first tangential mode, no radial contribution was added to the initial solution. However, the first radial mode does not play a major role here as its amplitude does not get higher than 3 bar.



(a) Modulus of amplitudes for case $\theta = 0°$

(b) Modulus of amplitudes for case $\theta = 45°$

(c) Modulus of amplitudes for case $\theta = 90°$

(d) Modulus of amplitudes for case $\theta = 135°$

Figure 4.9: Temporal evolution of the modulus of the complex amplitudes corresponding to the modes $1T$, $1T'$ and $1R$ for $\theta = 0°$, $\theta = 45°$, $\theta = 90°$ and $\theta = 135°$.

Maximum amplitudes of acoustic pressure fluctuations

Knowing the complex amplitudes, one can retrieve the maximum amplitudes yielded by the fluctuation of a single mode, *e.g.* $1R$, or a combination of two modes, *e.g.* $1T$ and $1T'$.

The temporal evolution of the maximum combined amplitude of the two transverse modes is plotted in Fig. 4.10. As seen in Fig. 4.9, the case LES90 shows a decrease in overall fluctuation level while the others are quite steady.

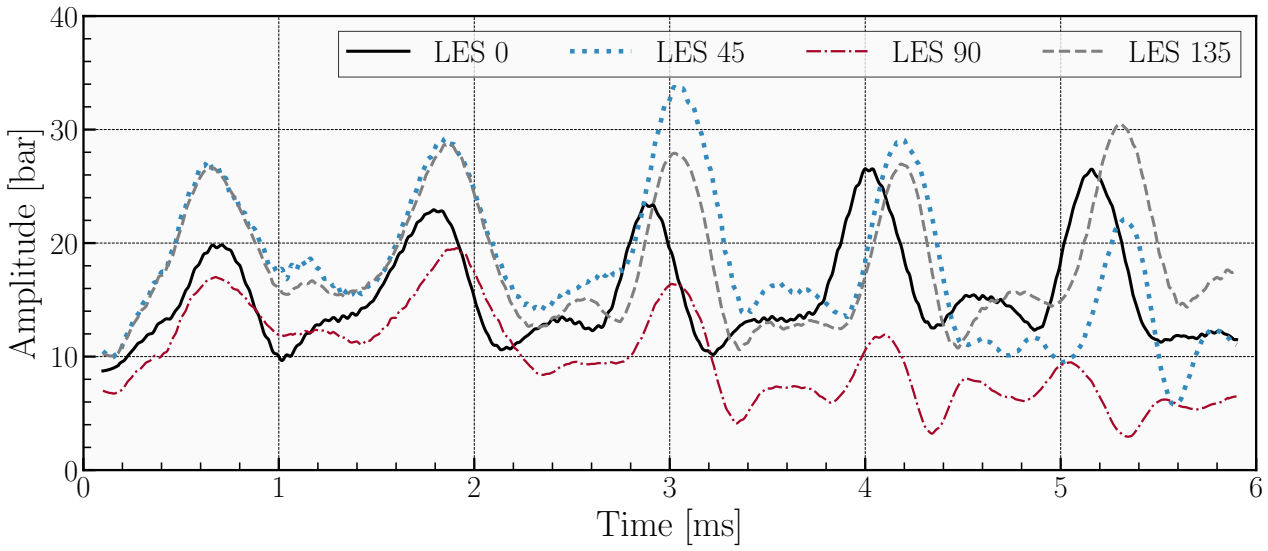


Figure 4.10: Maximum of acoustic pressure in time for the four cases.

Spectral analysis of the complex amplitudes

A spectral analysis of IMD's complex amplitudes is conducted using the Welch method [150]. The Power Spectral Densities (PSDs) of the 4 cases are shown in Fig. 4.11.

For each case, the PSDs corresponding to the $1T$, $1T'$ and $1R$ modes are shown. The spectra of the four cases are similar. The dominant modes identified in Fig. 4.10 are recovered in the PSD spectra:

- the mode $1T$ is dominant for LES0,
- the mode $1T'$ is dominant for LES90,
- the modes $1T'$ and $1T'$ have the same contribution for LES45 and LES135.

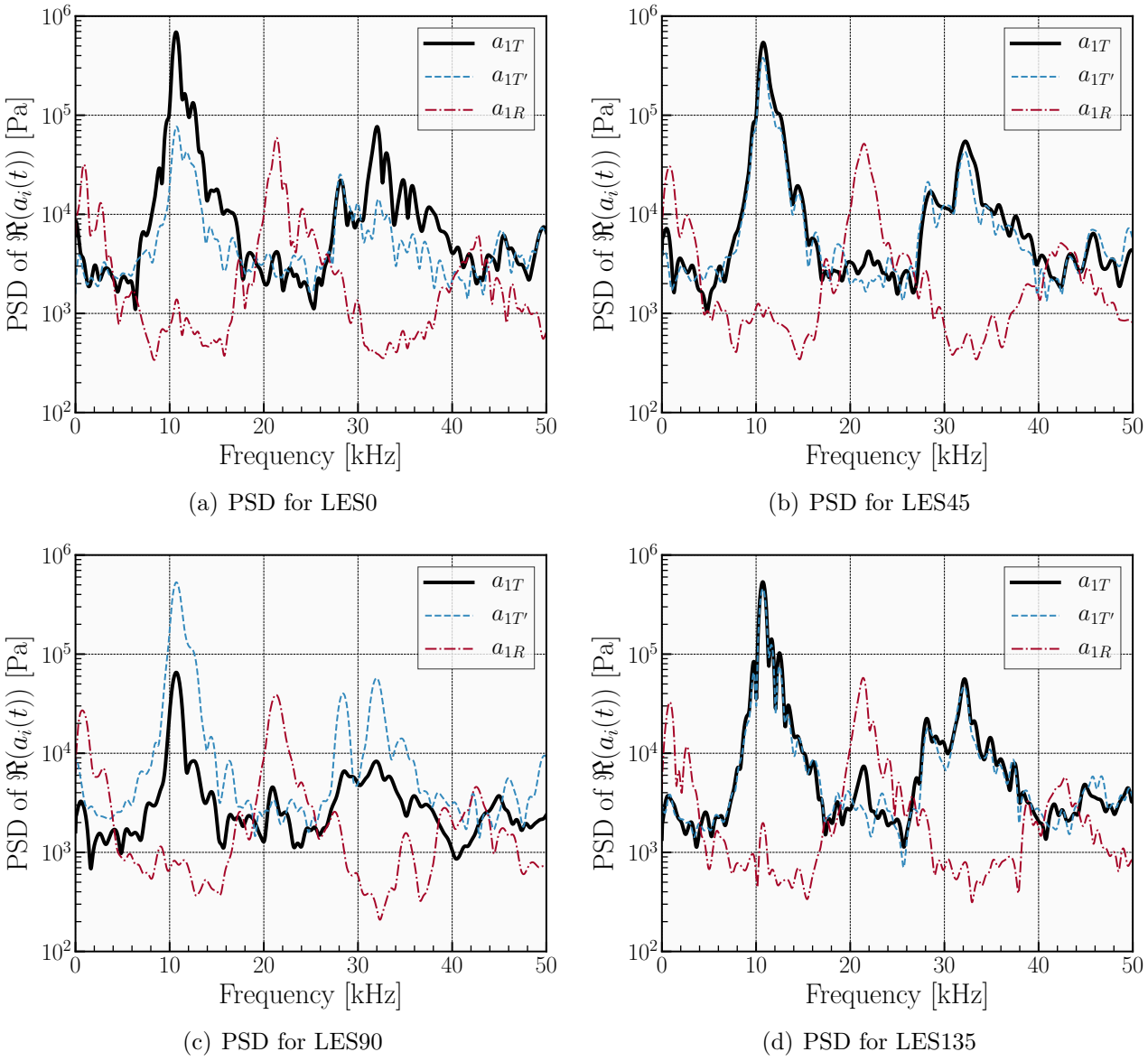
Despite the fact that the IMD analysis does not constrain the frequency of a given mode, the spectra of the $1T$ and $1T'$ are found to peak at 11 kHz, which is the expected values from the experiment, the LES and the Helmholtz simulations. The $1R$ also peaks at the correct frequency (21 kHz) but, it also has a lot of low-frequency content.

This effect is caused by the fact that IMD is a *spatial* method: only the mode's shape is constrained so that the locations of the pressure measurements are essential for the determination of the modes' contribution to the pressure field.

For instance, here all the probes are located at an identical axial and radial position so that pressure oscillations having a "bulk" contribution to the pressure measurements[4] can be either attributed to a longitudinal or radial mode.

Hence, it can be speculated that the low-frequency content of the $1R$ mode is caused by longitudinal modes. Similarly, the peak observed at 32 kHz for $1T$ and $1T'$ can be due to a higher order tangential/longitudinal coupled modes.

[4]That is, pressure oscillations that are of the same amplitude and phase at for all probes



(a) PSD for LES0

(b) PSD for LES45

(c) PSD for LES90

(d) PSD for LES135

Figure 4.11: Power Spectral Density (PSD) of the complex amplitudes for the four cases.

Nodal line orientation

Experimental studies have highlighted the fact that, in the BKD, the first tangential mode is dominant [121, 127, 136, 149] and that, for the operating point LP4, the nodal line has a preferred orientation [137, 151, 164]. The goal of this section is to recover the evolution of the nodal line orientation of the first tangential mode from the complex amplitude a_i provided by the IMD.

At this point it is useful to recall that any first tangential mode, *i.e.* for any orientation and amplitude, can be expressed as a superposition of two degenerate first tangential modes. These modes – often called "basis" – can be standing or rotating [9**?**]. Here, the IMD was performed using a standing basis as the Helmholtz solver (AVSP) determines the standing modes. The two standing modes of a first tangential mode are similar but their nodal lines

are perpendicular. The nodal line orientation of the tangential mode resulting from the superposition of these complementary modes can be simply expressed as:

$$A_{1T} + A_{1T'} e^{i\left(\delta + \frac{\pi}{2}\right)} = A_0 e^{i\theta} \tag{4.3}$$

The maximum amplitude A_0 in the ring C can be found at the angle $\theta \pm \pi/2$ and is calculated as:

$$A_0 = \sqrt{A_{1T}^2 + A_{1T'}^2 + 2A_{1T}^2 A_{1T'}^2 \cos(\delta)} \tag{4.4}$$

The phasing difference δ is given by:

$$\delta(t) = \angle\Re(a_{1\mathrm{T}'}(t)) - \angle\Re(a_{1\mathrm{T}}(t)) \tag{4.5}$$

It can be determined on the interval $[0, \pi]$ using the arctan function[5]

$$\theta = \angle \arctan\left(\frac{A_{1T'} \sin\delta}{A_{1T} + A_{1T'} \cos\delta}\right) \tag{4.6}$$

Equation 4.6 is used here to track the evolution of θ in the 4 LESs considered here (*cf.* Fig. 4.7). The evolution of $\theta(t)$ obtained by this method are shown in Fig. 4.12 for the 4 LESs. In order to provide meaningful information, two additional treatments were used:

1. A Savitzky-Golay filter was applied to the raw signal $\theta(t)$ obtained when using Eq. 4.6. The Savitzky-Golay filter used is a digital filter designed for smoothing the data to increase the signal-to-noise ratio [165, 166]. They perform much better than standard averaging FIR filters (in particular unweighted moving average filters), which tend to filter out a significant portion of the signal's high frequency content along with the noise [167]. Here, the temporal window used by the Savitzky-Golay filter is the period of the 1T mode: $T_{\mathrm{SG}} = 1/11600 \simeq 90$ µs. Such a window is a reasonable assumption as long as the time scale of the nodal line orientation change is long when compared to the period of the 1T fluctuations, which is thought to be the case here.

2. the signal obtained for the initial orientation $\theta_0 = 0°$ is oscillating around 0°. As θ is defined within the interval $\theta \in [0, \pi]$, the values of the angle "jumps" from 0° to 180°. In order to visualize the evolution of the angle in this case, the angle was expressed on the interval $[-\pi/2, \pi/2]$.

Figure 4.12 shows the evolution of the angle θ, *i.e.* the nodal line orientation, in time for the 4 LESs. At first, the angle θ is close to the initial value (*cf.* Fig. 4.7). The case LES90 have variations from -10° to +25° and there seems to be a slow increase of θ but a longer simulation would be required to confirm this trend.

The other three cases stay fairly constant even if a few abrupt changes in θ are present due to sudden changes in the ratio $||a_{1T}||_2/||a_{1T'}||_2$ (*cf.* Fig. 4.9).

[5]Mathematically speaking, the angle θ can be determined for $\theta \in [0, 2\pi]$ using the values of $A_{1T}(t)$, $A_{1T'}$ and δ. Here, as we consider the first tangential mode, the angle θ is within the interval $\theta \in [0, \pi]$.

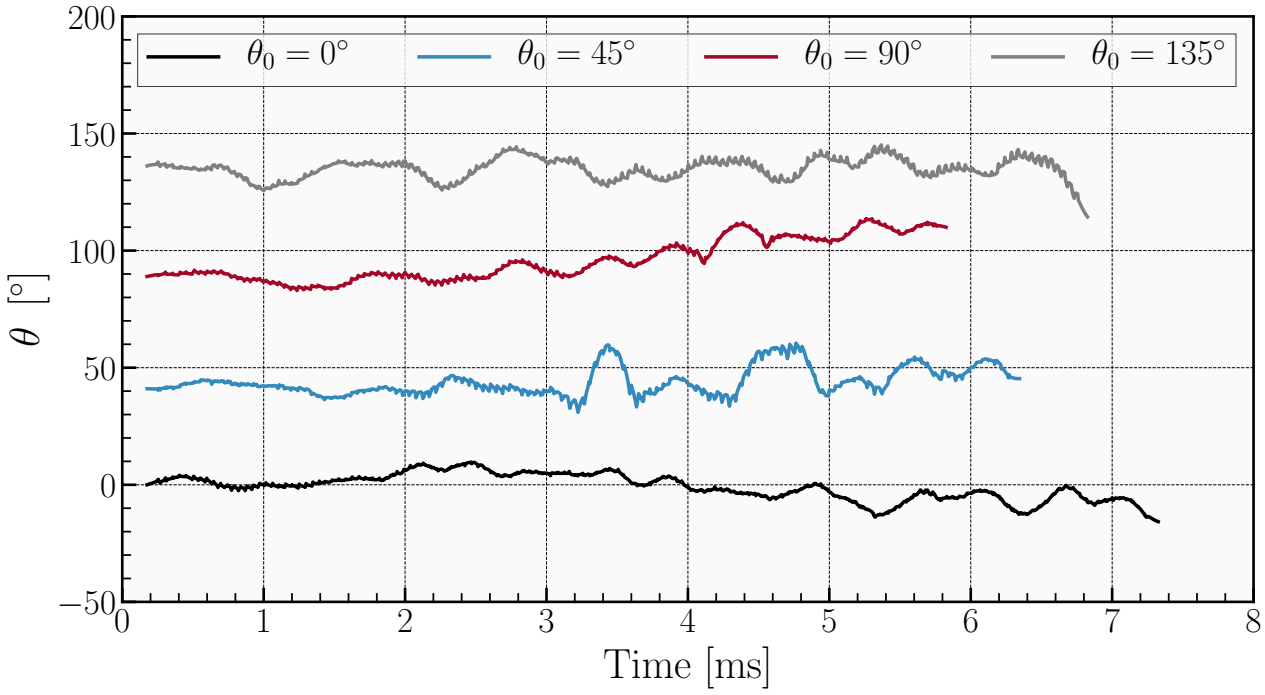


Figure 4.12: Angle θ of the nodal line of the first tangential mode in time using the complex amplitudes a_{1T} and $a_{1T'}$.

The DLR team in Lampoldshausen have also developed a method to track the nodal line orientation [127, 151, 164]. This method is based on a least-square fit of the pressure signals onto a cosine function. The amplitude and offset of the fitted cosine allows to determine the angle of the nodal line. Before the least-square fit, the signals are oversampled (interpolation on smaller time steps) and filtered around the 1T frequency. This filtering procedure is a major difference with the method used here and this signal pre-processing step should be borne in mind when comparing the results of the two methods.

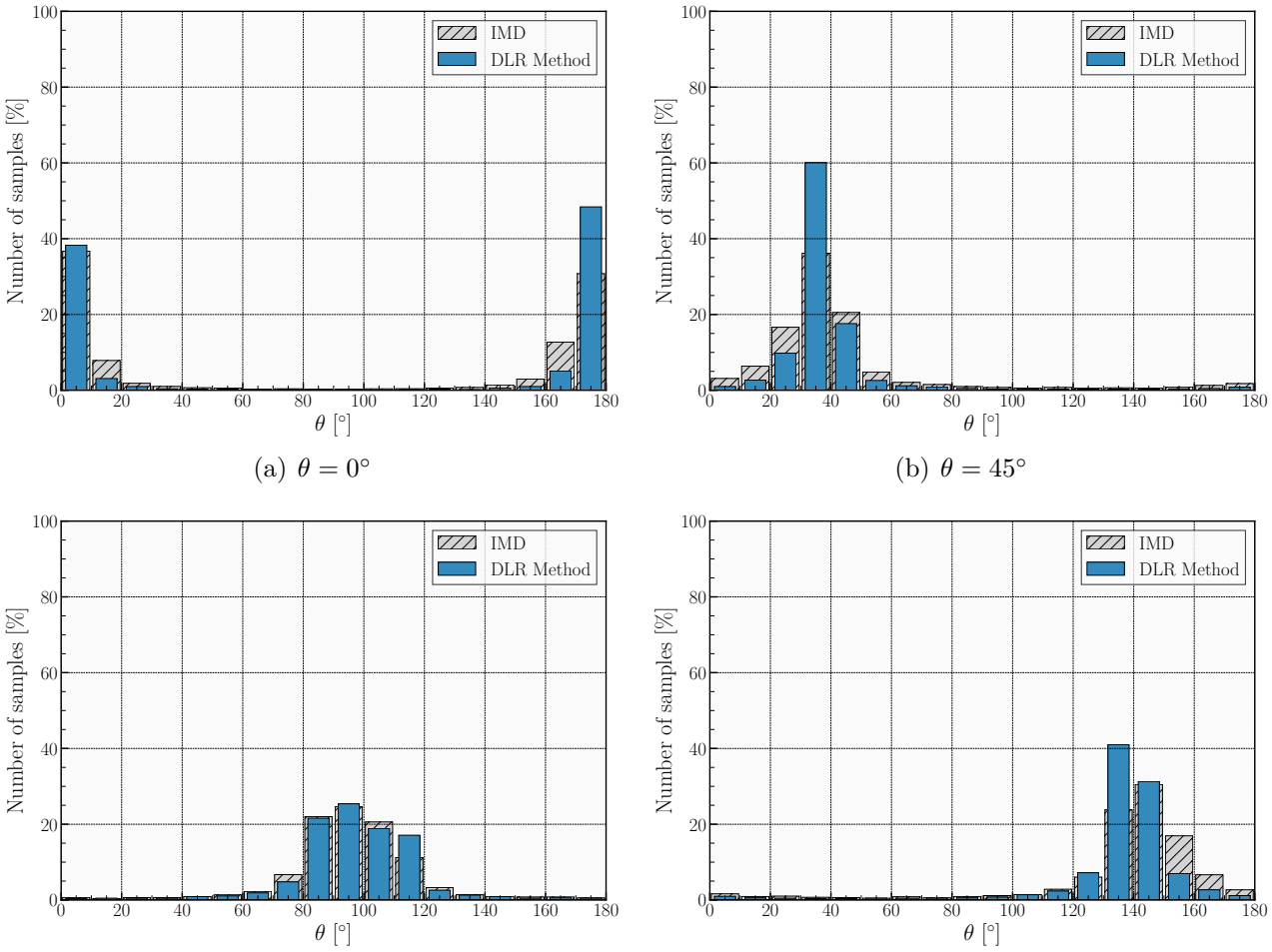
The LES pressure signals were analyzed by DLR Lampoldshausen using their method [127, 151, 164].

A comparison between DLR method and IMD method is drawn in Fig. 4.13. For each case, the results are presented as histogram charts. The abscissa corresponds to the angle θ sliced into 18 intervals of 10° each. The height of the bars refers to the percentage of samples were the angle θ was found to be in a given interval: it is a Probability Density Function (PDF).

For instance, in the LES0 case IMD and DLR method found that 37% and 38% of the samples are corresponding to $\theta \in [0°, 10°]$, respectively.

The overall agreement between IMD and DLR methods is good but some differences can be observed.

The general trend is that the DLR method tends to provide a narrower range of angle θ than IMD. This is thought to be due to the filtering procedure in the preprocessing stage.



(a) $\theta = 0°$

(b) $\theta = 45°$

(c) $\theta = 90°$

(d) $\theta = 135°$

Figure 4.13: Probability Density Functions (PDFs) of the angle θ on 10° intervals for the four cases.

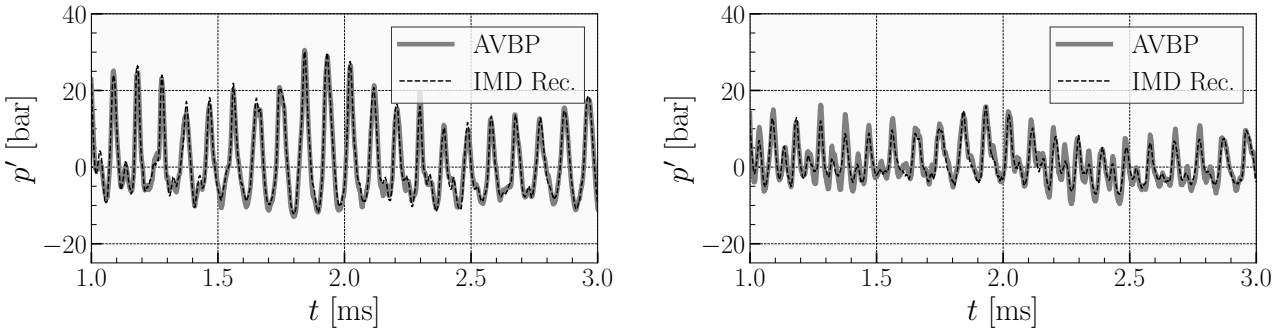
The Savitzky-Golay filter utilized to provide the angle θ from IMD's complex amplitude is less selective but works without knowing *a priori* the frequency of the dominant tangential mode. Furthermore, a similar filtering can be used for IMD instead of using a Savitzky-Golay filter. This is done to analyze the experimental pressure measurements of the BKD in Sec. 4.3.

Finally, the broad range of θ in the case LES90 (*cf.* Fig. 4.12) is retrieved by both methods. In fact, for this particular case, the agreement is excellent.

Acoustic pressure reconstruction

As shown in Sec.3.3.5, the acoustic pressure field can be reconstructed everywhere in the domain using the complex amplitudes determined by IMD and the 3D Helmholtz eigenmodes determined by AVSP.

The results of the acoustic pressure reconstruction are shown in Figs. 4.14 to 4.19. For clarity's sake, only the case LES90 is shown here and only 2 ms are plotted.



(a) Probe C1 (RingC) (b) Probe C2 (RingC)

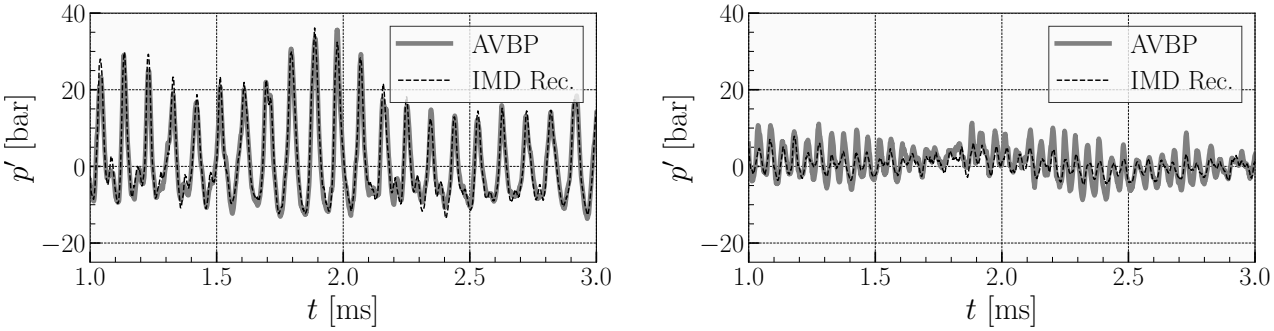
Figure 4.14: Acoustic pressure from LES ("AVBP") and signals reconstructed ("IMD Rec.") at Ring C (data used for IMD).

First, the pressure signals used for IMD are reconstructed as a sanity check (*cf.* Figs. 4.14(a) and 4.14(b)). The reconstructed signals are in excellent agreement with the original signals.

Figures 4.15(a) and 4.15(b) correspond to the maximum and minimum pressure fluctuations on the Ring C but these probes are not used for the IMD. The reconstructed signals are well reproduced, in particular for the maximum amplitude at C11 while at C12 some discrepancies are observed.

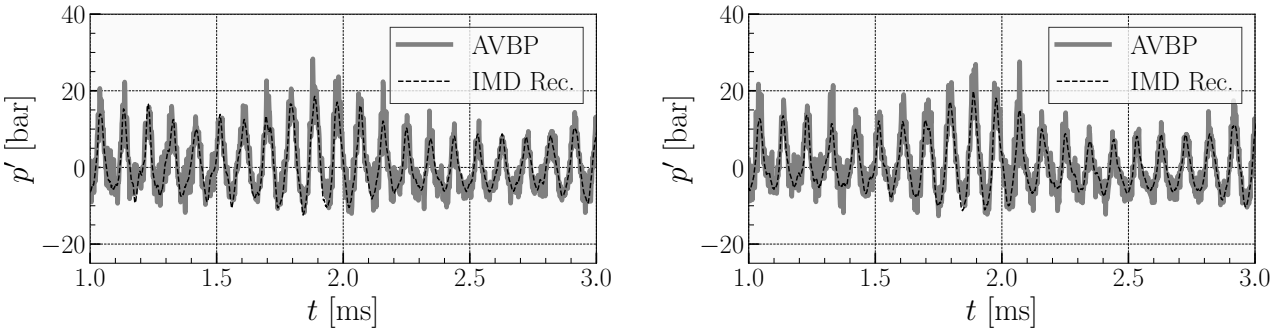
Figures 4.16(a) and 4.16(b) correspond to the pressure signals in the chamber, *i.e.* far from the measurement transducers. The overall agreement is good as the fluctuations are well reproduced but the peak amplitudes tend to be underpredicted.

Acoustic pressure signals are also reconstructed in the injectors. Injectors facing the antinode and node of pressure are referred to as "Injector A" and "Injector N", respectively.



(a) Probe C11 (RingC) (b) Probe C12 (RingC)

Figure 4.15: Acoustic pressure from LES ("AVBP") and signals reconstructed ("IMD Rec.") at Ring C (data not used for IMD).



(a) Probe Ch1 (chamber) (b) Probe Ch2 (chamber)

Figure 4.16: Acoustic pressure from LES ("AVBP") and signals reconstructed ("IMD Rec.") in the chamber.

Figure 4.17 shows the location 1 and 2 corresponding to InjA1 (Injector A, location 1) and InjN1 (Injector N, location 1) as well as InjA2 and InjN2.

Pressure signals for an injector A are presented in Figs. 4.18(a) and 4.18(b) for Probes InjA1 and InjA2, respectively. For Probe InjA2, the reconstructed signal is in excellent agreement with the LES.Even though the oscillations are globally in phase, the reconstructed signal is not predicting at the correct amplitudes.

Figures 4.19(a) and 4.19(b) illustrate the pressure signals of an injector N at locations $x = -1.7$ cm and $x = -0.2$ mm (*cf* Fig. 4.17) for Probe InjN1 and Probe InjN2, respectively. Similarly to the injector A, the reconstructed pressure signals for the injector N give an accurate prediction near the injection faceplate.

As for the validation test case in Sec. 3.3.5, the pressure field reconstructed by IMD predict accurately the high-pressure amplitudes but some discrepancies exist at low amplitudes.

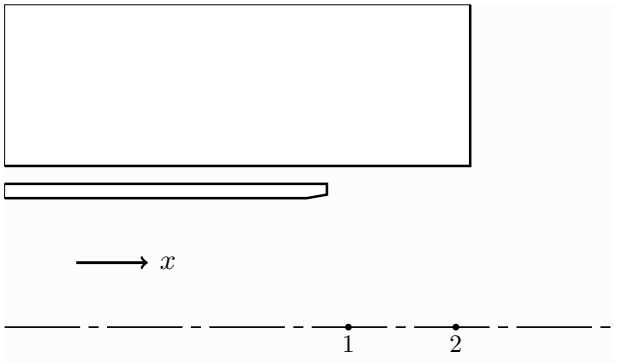
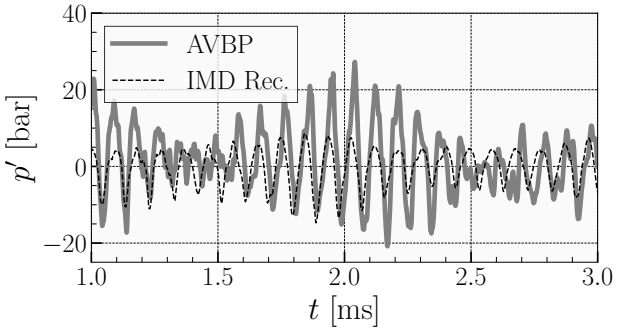
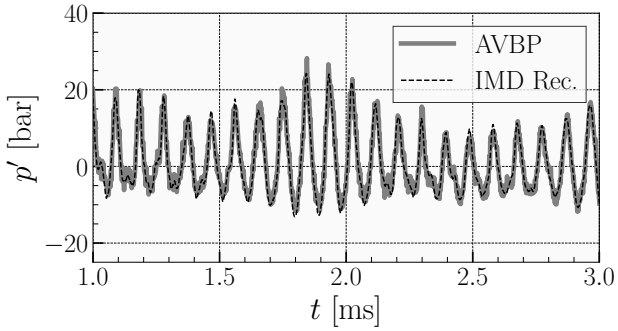


Figure 4.17: Drawing of the injector probes' location.

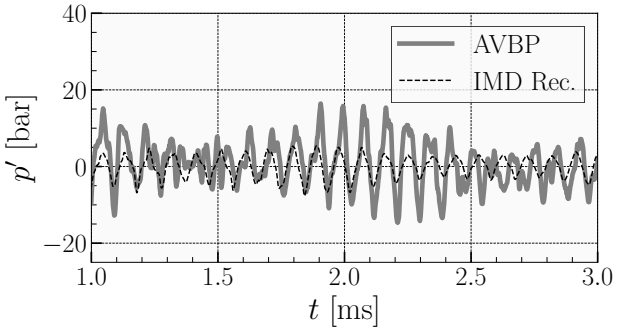


(a) Probe InjA1 (injector A)

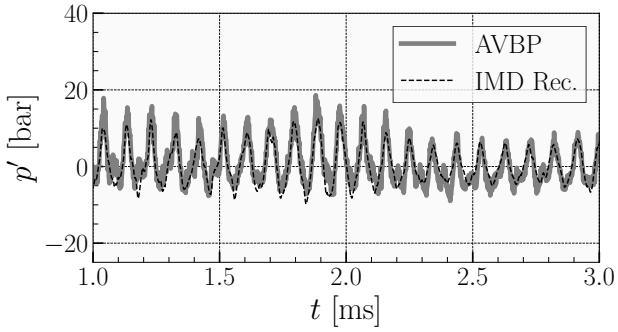


(b) Probe InjA2 (injector A)

Figure 4.18: Acoustic pressure from LES ("AVBP") and signals reconstructed ("IMD Rec.") in an injector A.



(a) Probe InjN1 (injector N)



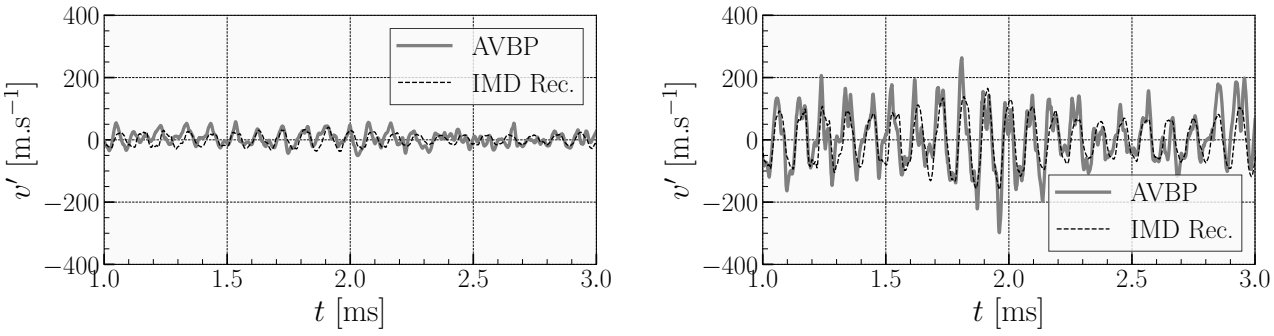
(b) Probe InjN2 (injector N)

Figure 4.19: Acoustic pressure from LES ("AVBP") and signals reconstructed ("IMD Rec.") in an injector N.

Acoustic velocity reconstruction

In this section, the reconstructed velocity signals are compared to signals measured in the LES90 case where the orientation of the first tangential induces v' velocity fluctuations in the chamber and in the injectors facing the nodal line ("injector N") and u' velocity fluctuations in the injectors facing the pressure antinode ("injector A"). Hence, these quantities will be shown here.

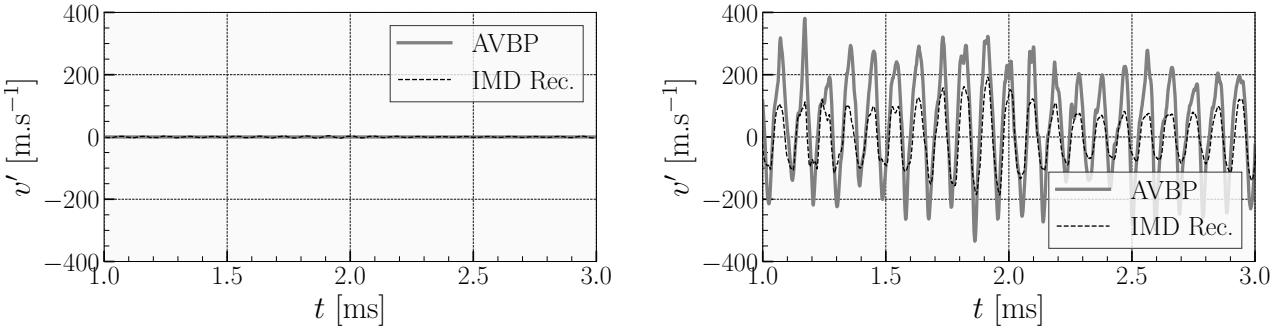
The results are presented in Figs. 4.20 to 4.24.



(a) Probe C1 (RingC) (b) Probe C2 (RingC)

Figure 4.20: Acoustic velocity v' from LES ("AVBP") and signals reconstructed ("IMD Rec.") at Ring C (data used for IMD).

First, the acoustic velocity is reconstructed at the probes C1 and C2 used for the determination of the complex amplitudes (*cf.* Figs. 4.20(a) and 4.20(b)). Small velocity fluctuations are present in probe C1 when compared to probe C2. The overall agreement between IMD reconstructed signals and AVBP signals is good although more complex flow features seem to be present in the LES.

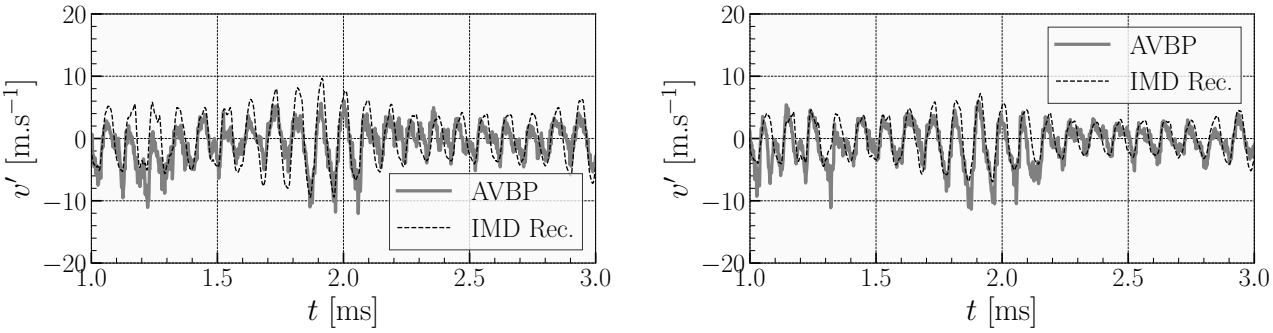


(a) Probe C11 (RingC) (b) Probe C12 (RingC)

Figure 4.21: Acoustic velocity v' from LES ("AVBP") and signals reconstructed ("IMD Rec.") at Ring C (data not used for IMD).

Probe C11 and C12 are shown in Figs. 4.21(a) and 4.21(b). They are located on the ring C but are not used for the IMD analysis. Extremely high levels of acoustic fluctuation

are observed for probe C12 with a maximum acoustic velocity of 400 m s^{-1} for $t \simeq 0.5$ ms (not shown here). The low velocity levels in probe C11 are reproduced by IMD. Even though the amplitudes are not well predicted, the reconstructed signals give a qualitatively good estimate of the acoustic velocity in these locations.

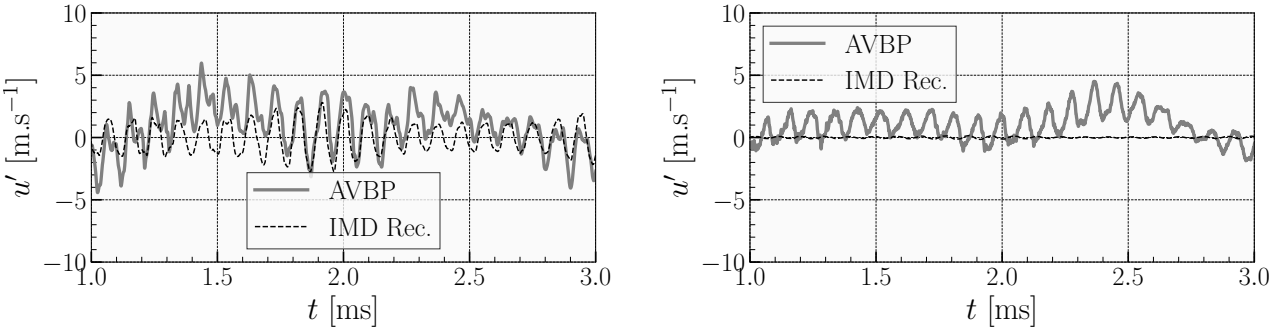


(a) Probe InjA1 (chamber)

(b) Probe InjA2 (chamber)

Figure 4.22: Acoustic velocity v' from LES ("AVBP") and signals reconstructed ("IMD Rec.") in the chamber.

In the chamber, in probes InjA1 and 255, the pressure signals are noisy due to the turbulent flow and combustion noise. Nonetheless, both probes are fairly well reconstructed.



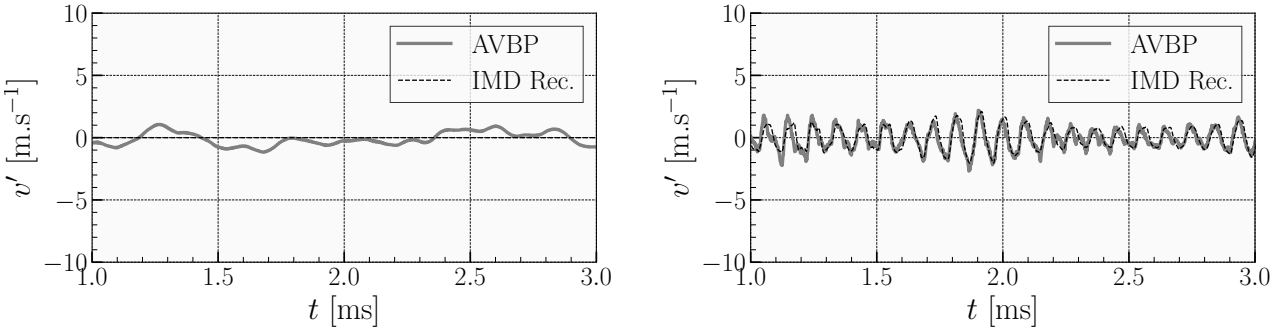
(a) Probe InjA1 (injector A)

(b) Probe InjA2 (injector A)

Figure 4.23: Acoustic velocity u' from LES ("AVBP") and signals reconstructed ("IMD Rec.") in an injector A.

The u' velocity signals for an injector A are presented in Figs. 4.23(a) and 4.23(b). For Probe InjA1, the acoustic velocity is qualitatively well reconstructed although more complex features, *e.g.* the low-frequency content of the signal, seem to be present. The signal reconstructed in Probe 105 is poorly reconstructed as the fluctuations are 2 orders of magnitudes lower that in the LES.

Finally, the maximum v' fluctuations due to the first tangential mode are located at the pressure nodes in the chamber. Hence, for an injector N, the quantity of interest is v'. Probes InjN1 and InjN2 ($x_{InjN1} = -1.7$ cm and $x_{InjN2} = -0.2$ mm, *cf* Fig. 4.17) corresponding to an injector N are shown in Figs. 4.24(a) and 4.24(b), respectively. Probe InjN1 has v'



(a) Probe InjN1 (injector N)

(b) Probe InjN2 (injector N)

Figure 4.24: Acoustic velocity v' from LES ("AVBP") and signals reconstructed ("IMD Rec.") in an injector N.

fluctuations of about 1 m s^{-1} but these fluctuations do not seem to be due to acoustics. The v' signal reconstructed by IMD has extremely low fluctuation level (about 10^{-4} m s^{-1}, not shown here). Conversely, the signal reconstructed in Probe InjN2 is in excellent agreement with the LES signal as both phase and peak amplitudes are accurately reproduced.

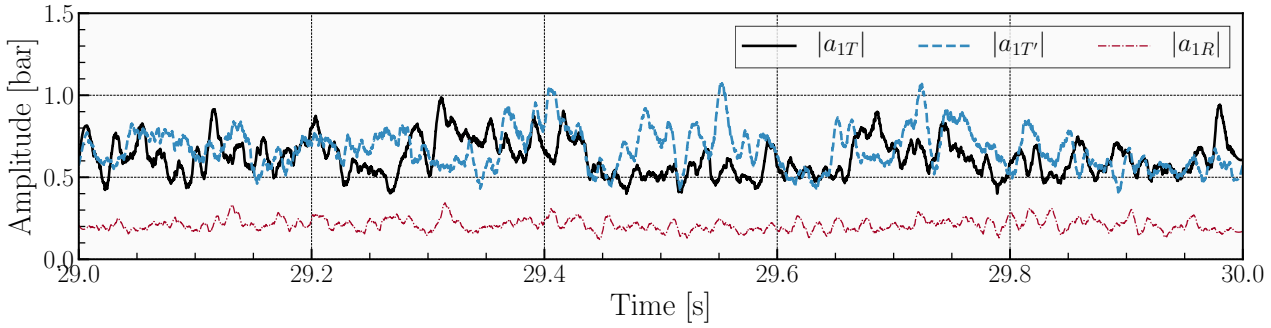
4.3 IMD of experimental signals

So far, the IMD methodology was used on signals obtained in numerical simulations. In this section, IMD is applied to the experimental pressure measurement of the LP1 and LP4 provided by the DLR (Lampoldshausen, Germany).

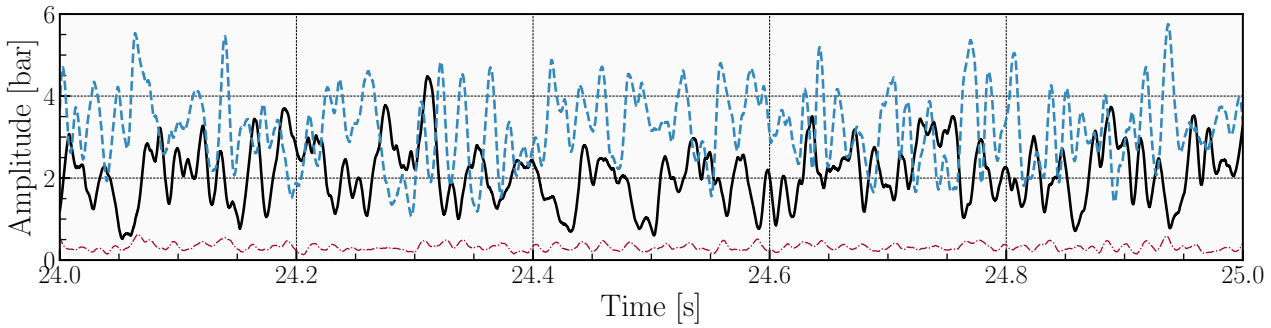
The IMD basis is identical to the one used in the previous section (*cf.* Sec. 4.2). The pressure measurements are located at the same locations (probes C1-C8).

Figure 4.25 shows the evolution of the modulus (*i.e.* the envelope) of the temporal amplitudes a_{1T}, $a_{1T'}$ and a_{1R} for the two operating points studied: LP1 (*cf.* Fig. 4.25(a)) and LP4 (*cf.* Fig. 4.25(b)).

For LP1 the levels of $|a_{1T}|$ and $|a_{1T'}|$ fluctuate around 0.6 bar and around 0.2 bar for $|a_{1R}|$. For LP4 the levels of $|a_{1T}|$ and $|a_{1T'}|$ fluctuate around 2 and 3 bar, respectively, and around 0.25 bar for $|a_{1R}|$. The cyclic-regime observed in the 4 LESs is not present in the experimental setup for these operating points.



(a) LP1



(b) LP4

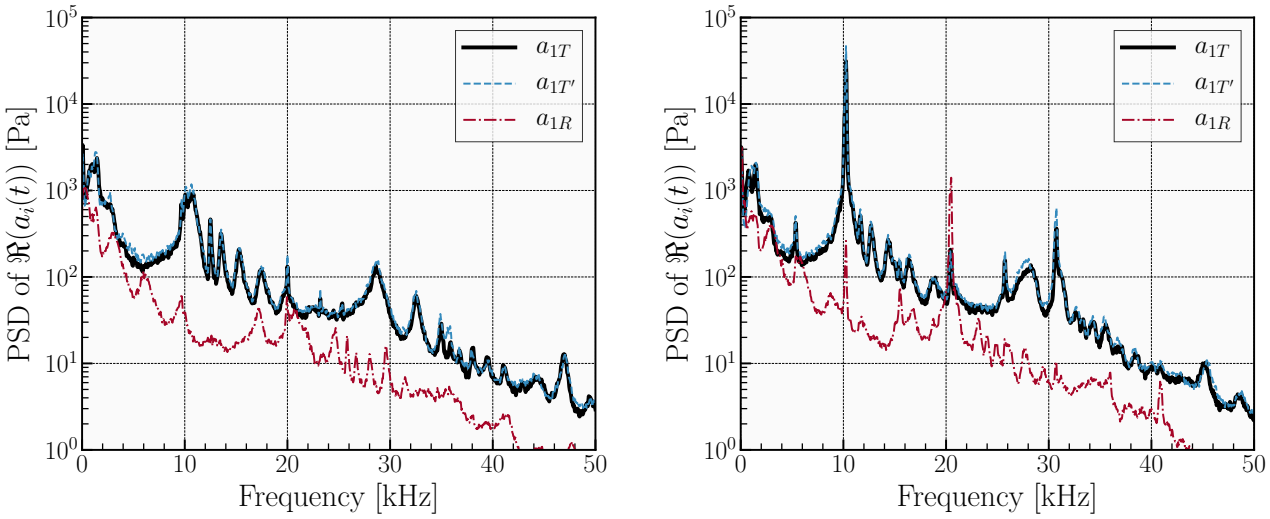
Figure 4.25: Modulus of complex amplitudes in time for (a) LP1 and (b) LP4.

The spectra shown in Fig. 4.26 correspond to the Power Spectral Density of the real part of the complex amplitudes a_i for the operating points LP1 (*cf.* Fig. 4.26(a)) and LP4 (*cf.* Fig. 4.26(b)).

For both operating points, the frequency contents of $\Re(a_{1T})$ and $\Re(a_{1T'})$ are similar: the main peak is located at 10.5 kHz and the secondary peaks are also captured. The PSD of $\Re(a_{1R})$ has a main peak at 20.5 kHz but it also has a strong low-frequency content. This effect

is caused by the choice of the probe locations making the IMD basis unable to discriminate between radial and longitudinal acoustic fluctuations.

The spectra shown here have the same frequency content as the ones in Fig. 4.4 (page 54) corresponding to the raw pressure measurements. The IMD spectra allow to identify the modes responsible for the peaks, *e.g.* the 20.5 kHz peak is mainly due to $\Re(a_{1R})$. It is an additional evidence that this peak is, in fact, due to the first radial mode as found in the numerical study of Urbano *et al.* [121].



(a) LP1 (b) LP4

Figure 4.26: Power Spectral Density for the complex amplitudes a_i for (a) LP1 and (b) LP4.

The orientation of the nodal line of the transverse mode is now analyzed in the experiment. The amplitudes and spectra shown here correspond to an IMD analysis of the raw experimental pressure measurements. As discussed in Sec. 4.2.3, DLR Lampoldshausen use a preprocessing stage in order to study the orientation of the nodal line of the first tangential mode.

This preprocessing comprises two steps: (1) an interpolation of the signal in order to provide shorter samples and (2) of a band-pass filtering stage with a bandwidth centered on the 1T's frequency. The objective of the filtering procedure is to remove from the analysis the perturbations that may have a transverse shape similar to the 1T but not the same longitudinal structure. It was used here in order to track the orientation θ of the nodal line of the 1T.

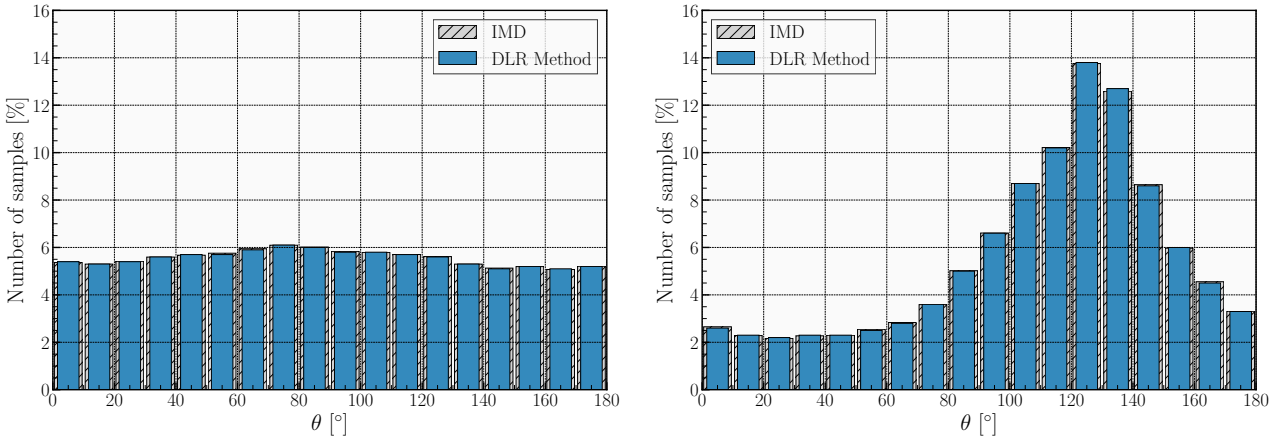
Equation 4.6 was used in order to study the angle θ. The obtained data is compared to the data of DLR Lampoldshausen in the histograms shown in Fig. 4.27. These histograms can be seen as Probability Density Functions (PDFs) as they indicate that probability for the angle θ to be in a 10° interval. Both method are used to analyze the experimental measurements of DLR Lampoldshausen over 1 s.

The agreement between IMD and the DLR method [127, 151, 164] is excellent for both operating points. The maximum error between the two methods is of 0.1%.

The results for LP1 show that the probability for θ to be in an interval is around 5 to 6%. The maximum probability is at $\theta = 90°$. No strong preferred orientation is observed in this operating condition.

Conversely, the PDF of θ for the operating point LP4 shows a strong preferred orientation around $\theta = 130°$. For instance, the probability of the angle θ to be in the interval $[120°, 130°]$ is 7 times higher than the probability of the angle θ to be in the interval $[20°, 30°]$.

It can be speculated that the preferred orientation in the experiment is caused by a breaking of the symmetry in the geometry and/or the flow distribution. Indeed, the pattern of the injectors may favor a given orientation through the dynamic response of the flames. Also, manufacturing tolerances may further break the geometric symmetry. Finally, asymmetric pressure distribution and turbulent flow phenomena in the injection manifolds may result in differential flow rates through the injection elements.



(a) LP1 (b) LP4

Figure 4.27: Histograms of the percentage of the presence of the angle θ on 10° intervals for the operating points (a) LP1 and (b) LP4.

4.4 Conclusion

The BKD experimental setup (DLR Lampoldshausen, Germany) was presented along with the operating points considered in this study (LP1 & LP4). After discussing some previous studies results, the Helmholtz eigenmodes corresponding to the resonant modes of the transverse combustion instability were presented. Then, the pressure signals from both numerical simulations and experimental measurements were analyzed using the IMD method presented and validated in Chapter 3.

The study is beyond some theoretical limitations of IMD:

1. a non-linear acoustic regime is reached, while IMD was derived in the linear acoustic framework.

2. the Helmholtz eigenmodes used to build the IMD basis are non-orthogonal due to the nozzle and H_2 injectors impedances considered in the Helmholtz simulation. However, the quasi-orthogonality condition is verified for the basis used here (Eq. 3.15, page 31).

3. consequently to the probe location choice, the discrimination between radial and longitudinal fluctuations is impossible. This issue could have been easily resolved as many probes are available in the LESs considered. However, the study was conducted under conditions similar to the diagnostics present in the experimental setup.

Although these limitations are present, IMD yields encouraging results. The contribution of each mode and the maximum associated acoustic fluctuations was satisfactorily found.

The frequency content of IMD's complex amplitudes yields insights on potential modes with first tangential and first radial structures. The orientation of the nodal line was studied for the four cases and the results were compared with the method of DLR [127, 151, 164] and a good agreement between the two methods was found.

The acoustic velocity field reconstructed from IMD's complex amplitude was found to be in overall good agreement with the LES signals, especially in the areas of interest: in the chamber (near the injection faceplate) and in the injectors (A & N).

Finally, experimental measurements provided by the P8 bench of DLR Lampoldshausen were studied with the proposed methodology. The spectral analysis of IMD's complex amplitudes is an additional information than, in agreement with Urbano *et al.* [121], the mode responsible for the 21 kHz combustion instability was found to be the first radial mode of the basis. The orientation of the nodal line found by IMD was compared to the results obtained by DLR with identically filtered signals and an excellent agreement was found between the two methods. It was found that, for the LP4 operating point, the nodal line has a preferred orientation around 130° while no clear preferred orientation was identified for the LP1 orientation point.

Chapter 5

Flame response to transverse acoustic modes in LRE

Although the IMD method, presented in Chapter 3 and used in Chapter 4, is a valuable source of information when investigating the evolution of the acoustic modes in the BKD, it does not bring a deeper understanding of the mechanisms leading to combustion instabilities.

One identified mechanism is that the unsteady heat release rate can add or remove acoustic energy from the acoustic field depending on its phasing with acoustic pressure fluctuations. Historically, this acoustic source/sink term is at the basis of the very first criterion used to predict the presence of thermoacoustic instabilities: *Rayleigh's criterion* [26, 27]. It states that if the time averaged product of these quantity is positive then energy is injected into the acoustic field, which might lead to thermoacoustic instabilities.

In this chapter, a LES database of transverse combustion instabilities in a 42-flame liquid rocket engine is used to identify, for each flame, the associated: (1) unsteady heat release, (2) Rayleigh source term. This is done for each of the two dominant transverse chamber modes. The goal of study is to identify which flames are to be held liable for the transverse combustion instabilities and to develop a deeper knowledge of the mechanisms responsible for such phenomena. These questions are timely to be addressed and their study give insights on which flow variables are the most relevant for an eventual flame-response model.

After recalling the context of the study in Sec 5.1, the used LES dataset is described in Sec. 5.2. The limit cycle predicted in the LES is analyzed in Sec. 5.3. Section 5.4 is devoted to the description of the global structure of the flame response and the relative contributions of the two dominant modes are discussed. Finally in Sec. 5.5 the physical mechanisms that drive the unsteady flame response are identified, with a focus on the specific injectors that play the most important role in the destabilization of the transverse mode.

This chapter is the product of a collective work which has been published in the Proceedings of the Combustion Institute *(2017) [136].*

5.1 Introduction

The occurrence of combustion instabilities has plagued many development programs for high-performance propulsion systems [6, 9, 10, 18]. In the aerospace industry, one of the most striking examples may be the development of the F1 engine for the Apollo mission, which required 1332 full-scale hot-fire tests and 108 injector design changes before meeting both stability and performance requirements [22]. The cost associated with such trial-and-error procedure can be prohibitive justifying the search for methods allowing the prediction of stability characteristics at the design stage.

With growing computational resources available to researchers and engineers, and the development of High Performance Computing, it is timely to address this problem with numerical tools that simultaneously solve for turbulence, acoustics and combustion. Indeed, high fidelity modeling strategies such as Large-Eddy Simulation (LES) have had considerable successes in predicting unstable operating points for gas turbine combustors [43, 44] or gaseous coaxial injectors [62, 168, 169]. With the recent development of LES for transcritical flows [100, 170–172], high-pressure liquid rocket engine stability can now be numerically studied [121]. Nevertheless, these methods are usually too cumbersome to allow explorations of the whole range of operating conditions. Moreover, it might even be a waste of resources to systematically use LES because it is likely that there are generic features pertaining to the injection units and system or to the combustion chamber, which do not require a high-fidelity simulation to be predicted.

One alternative to this "brute force" approach is the joint use of a flame-response model and an acoustic solver [130]. This has been demonstrated in a generic configuration [55] but also in more complex geometries including turbulent flames [57]. This strategy can help the analysis of unstable modes and deliver good predictions of stability maps [61]. This has also been tried for rocket engine configurations [62, 63] with some success. However, two key ingredients are required as inputs for this approach:

1. **A baseline flow field:**
   When solving the Helmholtz equation, the field of speed of sound is needed. If linearized Euler equations are chosen, the mean velocity field is also required.

2. **A model for the response of the flame to acoustic perturbations:**
   The driving mechanism for the amplification of acoustic perturbations involves the coupling with unsteady heat release rate fluctuations. This often arises through a complex mechanism combining nonlinear fluid mechanics and the flame response to incident acoustic perturbation. A global model for this complex interaction is then required to feed the acoustic solver.

The baseline flow can usually be obtained from lightweight computations or theory, but in some cases high-fidelity simulations are required because it directly influences the eigenfrequency values. However, the flame response is virtually impossible to derive from theoretical

considerations, except in some simple cases, and its accurate determination is central to the prediction of stability maps. Experimental determinations are easily obtained for atmospheric pressure systems but there are technical difficulties when operating at high-pressure. This is where the high-fidelity numerical simulations of the "brute force" approach can be of help.

In what follows, calculations will not be used to derive stability maps but for more modest goals:(1) Understanding physical mechanisms that drive the flame responses and (2) Obtain a quantitative evaluation of this flame response.

The objective of the present work is to use a time-resolved dataset of 3D solutions obtained by LES for the study of injector response during the limit cycle of a combustion instability. Also, with the intent to model the unsteady flame response to be fed into an acoustic solver, the question of which flow variables are most relevant is addressed. It is indicated by Yang and Anderson [22, chap. 1, p. 9] that the physical and chemical processes in the immediate vicinity of the chamber backplane are generally quite sensitive to the transverse velocity perturbations parallel to that plane and less susceptible to the unsteady motions acting in the main flow direction at right angles to that plane. On the other hand, much of the work in this domain (*e.g.* Crocco *et al.* [173]) emphasizes effects of unsteady pressure as the input for the flame response and this has led to some meaningful results. It is thus interesting to identify the processes that feed energy into the coupling modes and drive the unstable oscillations and more specifically compare effects of transverse velocities with those of pressure perturbations in the near vicinity of the injector backplane. This will be done here by making use of the high-fidelity simulation dataset.

5.2 LES dataset

The configuration studied is the BKD. It has been described in Chapter 4 (*cf.* Sec. 4.1.1) and more complete description can be found in Gröning *et al.* [124–126].

The LES has been carried out with the real-gas flow solver AVBP-RG [99] jointly developed by CERFACS, IFPEN and EM2C. A two-step Taylor-Galerkin scheme called TTG4A, is used, which is third order in space and fourth order in time [134, 135]. The solver accounts for multicomponent real-gas thermodynamics and transport [101, 102]. The Wall Adapting Linear Eddy (WALE) model is used to close the subgrid stress tensor [112] and an eddy-diffusivity approach is adopted for thermal and species subgrid contributions (constant turbulent Prandtl and Schmidt number: $\mathrm{Pr}_t = 0.6$, $\mathrm{Sc}_t = 0.6$). An infinitely-fast chemistry model [100], relying on the assumption of local chemical equilibrium and a β-pdf description of the filtered mixture fraction $\widetilde{Z}$, is adopted. Four species are considered (H_2, O_2, OH and H_2O) and source terms are computed following the method described in [100]. Specific mass flow rates and temperature of O_2 and H_2 ($\dot{m}_{O_2} = 5.75$ kg.s^{-1}, $\dot{m}_{H_2} = 0.96$ kg.s^{-1}, $T^{inj}_{O_2} = 111$ K and $T^{inj}_{H_2} = 96$ K) are imposed at the domes manifolds inlets using characteristic treatment of the boundary conditions [174], adapted to real-gas thermodynamics. The outlet nozzle is choked, requiring no boundary treatment. The walls are assumed to be adiabatic and are treated as no-slip boundaries in the injectors and as slip-boundaries in the chamber and in the domes.

The computational domain shown in Fig. 5.1 is discretized with a 70 M element mesh. The typical mesh resolution in the zone where the flames are established is $\Delta = 50$ μm. The

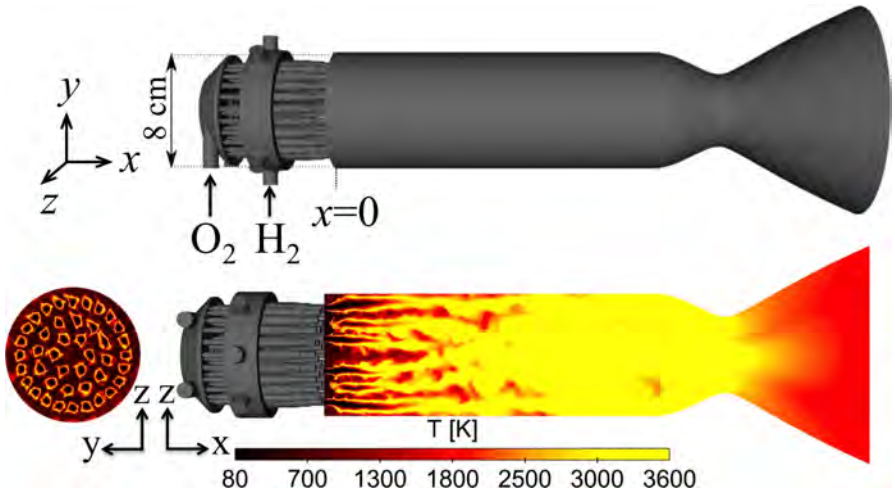


Figure 5.1: Overview of the computational domain for the BKD (top). Transverse (bottom left) and longitudinal (bottom right) cuts of instantaneous temperature field.

resulting CPU requirements are 100, 000 h on a BlueGene Q for the simulation of 1 ms (which corresponds to about ten times the period of the typical oscillation of the first azimuthal mode). A typical run is performed in parallel on 16, 384 cores so that the restitution time is reasonable despite the significant computational burden.[1]

A limit cycle is reached in the LES and the dynamics of the system is computed over a period of 7.5 ms. A detailed presentation of this simulation is given in [121] and the aim of the present work is to perform an in-depth analysis of the limit cycle and analyze the flame response. For this purpose, 200 snapshots of the full 3D solution were saved over 2 ms of the limit cycle (between 5 and 7 ms), which corresponds to 330 Gb of data. Acoustic and combustion fluctuations are analyzed, making use of Fourier transform of the 3D fields at the frequencies of interest.

5.3 Description of the limit cycle

During the limit-cycle predicted by the LES, pressure fluctuations of very large magnitude are recorded. The rms[2] value reaches $p'_{rms} = 0.15\, p_c$ which corresponds to 10.7 bar. Pressure spikes reaching +44 bar are sometimes observed.

The power spectral density (PSD) of pressure fluctuations at a sensor placed on the chamber wall 5.5 mm downstream the injector plate is displayed in Fig. 5.2. There are two dom-

[1] Because the AVBP solver can make use of hyperthreading on BlueGene Q architectures, there are 4 MPI processes per core resulting in a total of 65, 536 MPI processes for this computation.

[2] Root Mean Square

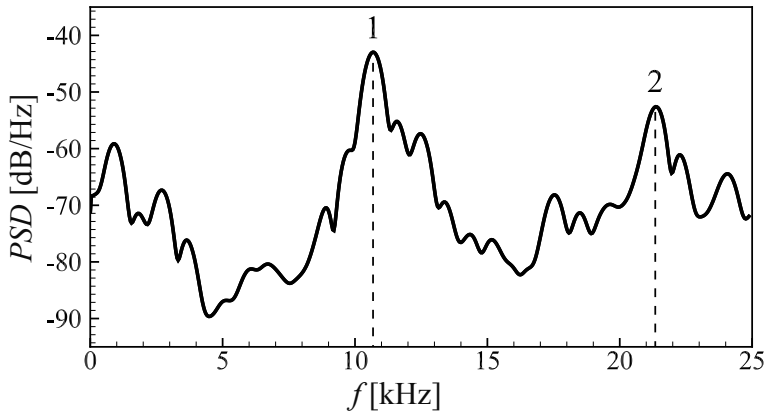


Figure 5.2: Power spectral density of pressure fluctuations at the chamber wall 5.5 mm downstream the injection plate.

inant frequencies at $f_1 = 10,700$ Hz and $f_2 = 21,400$ Hz, which are close and within 5 % of experimentally observed frequencies [124].

It is possible to extract the pressure distributions corresponding to these two frequencies by taking the Fourier transform of the 200 pressure fields accumulated in the dataset. While f_1 corresponds to the first transverse mode (labelled 1T) of the chamber (*cf.* Fig. 5.3), the mode shape at f_2 resembles the first radial mode (labelled 1R). In both cases these chamber

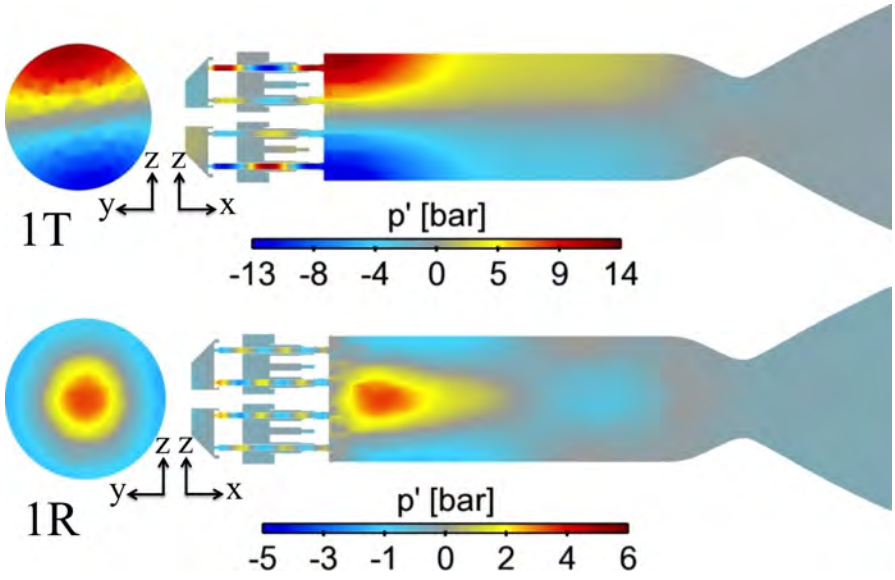


Figure 5.3: Spatial structure of the pressure fluctuations for the two dominant frequencies of Fig. 5.2 from the 3D-FT of 200 instantaneous LES fields.

modes are strongly coupled with the oxygen injectors where longitudinal fluctuations are observed. The hydrogen injectors do not seem to be affected by the pressure fluctuations in the chamber, which is consistent with their small radii (of the order of 0.25 mm). Nevertheless,

an examination of the velocity fields from the PSD (not shown) indicates that the hydrogen stream, at the injector exhaust and further downstream, experiences strong velocity fluctuations because of the eigenmodes in the chamber. This mechanism is discussed in Sec. 5.5.

Finally, the mode structures of Fig. 5.3 suggest that injectors located on the nodal line of the 1T mode will mostly experience transverse velocity fluctuations. Similarly, the 1R mode will produce a transverse acoustic velocity on the second injector ring.

5.4 Maps of flame response

The objective of this section is to quantify the unsteady response of the flames and deduce maps of the contribution of the two eigenmodes identified in Sec. 5.3. To this purpose, it is convenient to define boxes that isolate individual flames. First the three rings are separated by cylindrical boundaries, then neighboring flames by radial planes. All these boundaries are chosen to be at equal distances from neighboring injectors. Various quantities can then be integrated in these boxes over the whole length of the combustion chamber.

This processing method is applied to the unsteady heat release rate, q', extracted from the 3D-FT of both modes. The resulting maps of q' for each injector and both modes are displayed in Fig. 5.4. Regarding the 1T mode, the flames that exhibit the greatest response are those

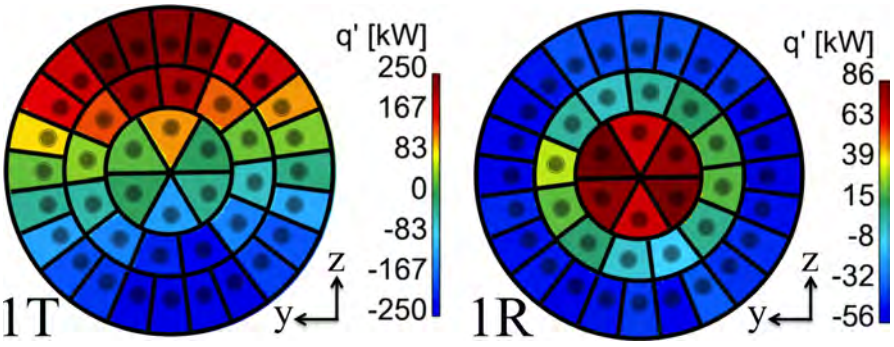


Figure 5.4: Maps of unsteady heat release rate integrated around each flame.

located in the region where the pressure fluctuations reaches its maximum (*cf.* Fig. 5.3). On the nodal line of the pressure field, the flame response is found to nearly vanish. This indicates that the flames respond weakly to the transverse velocity fluctuations of the 1T mode. Similar conclusions are drawn from the map of q' in the 1R mode: the inner and outer ring, corresponding to pressure antinodes, respond strongly and out of phase, while the middle injector ring is virtually inactive.

In order to quantify the impact of these fluctuations on the growth of the instability, it is useful to consider the Rayleigh index, defined as:[3]

[3]This definition would not be consistent with the acoustic energy conservation in a real gas because the

Here, we used $\gamma = 1.146$, which is the value in the burnt gases and $p_0 = 74.5$ bar, which is the mean static pressure in the chamber.

$$R = \frac{1}{T}\frac{\gamma - 1}{\gamma p_0}\int_T \int_V p'(t)\, q'(t) dV dt \tag{5.1}$$

where T is a time span that covers at least one period of the oscillations and V a volume that contains all the flames. This total Rayleigh index accounting for all pressure and heat release rate perturbation is $R = 125$ kW in the LES. This positive value is consistent with the fact that combustion is driving the instability and a limit cycle is reached in the LES. With the intent to separate the impact of the two dominant eigenmodes, the Rayleigh index, R_i, of each individual mode can be evaluated as:

$$R_i = \frac{\gamma - 1}{2\gamma p_0}\int_V |\tilde{q}_i|\,|\tilde{p}_i| cos(\phi_{\tilde{q}_i} - \phi_{\tilde{p}_i}) dV \tag{5.2}$$

where $\tilde{p}_i$ (respectively $\tilde{q}_i$) is the 3D-FT of pressure (respectively heat release rate) fluctuations. The phases ϕ correspond to the definition where $\tilde{p} = |\tilde{p}|e^{i\phi}$. Using Eq. (5.2), the respective contributions of the 1T and 1R modes are $R_1 = 42.2$ kW and $R_2 = 8.8$ kW. It follows that both modes are driving the instability and that the 1T mode accounts for 33.8% of the destabilization while the 1R mode contribution amounts to 7.0% of the total.

One may now focus on the contribution of individual injectors by examining maps of Rayleigh index integrated around each injector. Figure 5.5 presents the contributions of the 1T and 1R modes, normalized by the total Rayleigh index. First, regarding the 1T mode, the

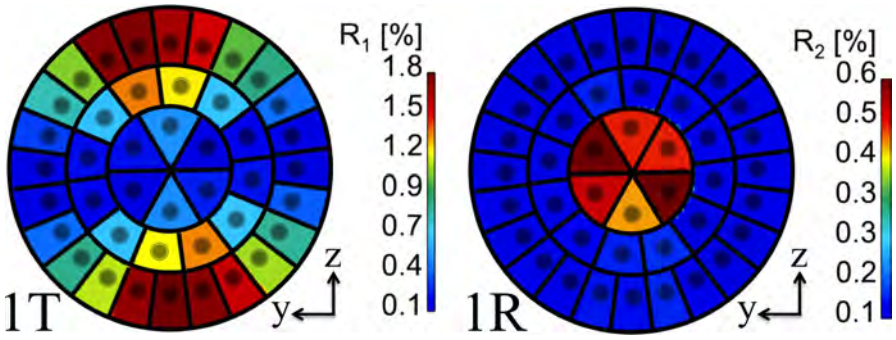


Figure 5.5: Maps of individual flames Rayleigh index for both 1T and 1R modes, normalized by the total Rayleigh index of the chamber.

shape of q' maps is recovered (*cf.* Fig. 5.4) with injectors at a pressure antinode contributing the most and those on the nodal line being virtually inactive. The maximum contribution of an individual injector is 1.8 %. For the 1R mode, only the six injectors of the inner ring have a significant contribution, with a maximum of 0.6%. It is interesting to note that despite the

normalization $(\gamma - 1)/(\gamma p_0)$ corresponds to a perfect gas. Here, we used constant values corresponding to the burnt gases in the chamber. The evaluation of the resulting discrepancies are left to further studies.

significant levels of q' on the outer ring (*cf.* Fig. 5.4), their phase does not seem to allow a positive contribution to the instability.

5.5 Individual injector dynamics

The question that one may now address is that of the physical mechanisms driving the unsteady response of these coaxial flames. The focus is set on the 1T mode, which contributes the most to the driving process, and two typical flames are singled out:

- An A-flame located at a pressure antinode. It was shown in Figs. 5.4 and 5.5 that these flames respond strongly to the bulk pressure fluctuation in the chamber.
- An N-flame located at a pressure node. These flames experience little pressure variations but a strong transverse velocity fluctuation. It was shown in Figs. 5.4 and 5.5 that they respond weakly in terms of heat release rate fluctuation.

The heat release rate fluctuations q', averaged over a volume comprising each flame are compared in Fig. 5.6, where q_0 is the time averaged heat release of the flame. As expected, the response of the A-flame is larger, consistent with Fig. 5.4. This confirms that these coaxial diffusion flames are more sensitive to pressure fluctuations than to the transverse velocity induced by the eigenmode.

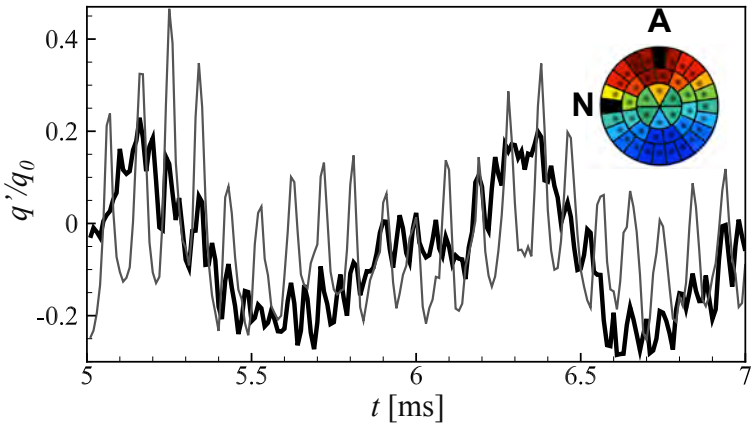


Figure 5.6: Comparison of heat release rate fluctuations for a: A-flame (thin gray line) and N-flame (bold black line).

One may now proceed with a detailed analysis of the A-flame. A schematic representation of the recessed coaxial injector of the BKD is shown in Fig. 5.7. When an acoustic mode is excited in the combustion chamber, the injector of an A-flame experiences a back-pressure fluctuation, p', at its exit plane, which in turn generates velocity fluctuations in both propellant streams. The velocity fluctuations, u'_{H_2} and u'_{O_2}, averaged over their respective cross section (an annulus for H_2 and a disk for O_2), at the location of the recess are compared in Fig. 5.8. They are normalized by the mean velocity $u_m = (u_{0,H_2} + u_{0,O_2})/2$ where subscript 0 indicates

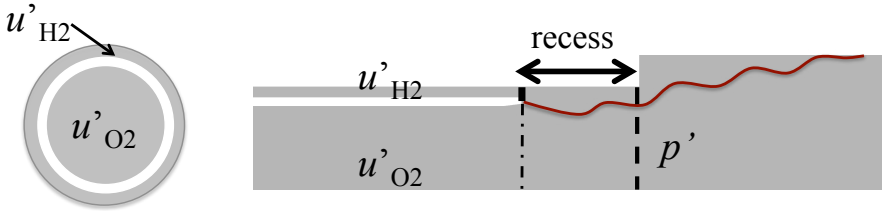


Figure 5.7: Schematic of the coaxial injector and reference surfaces for the extraction of velocities and pressure fluctuations used to evaluate the flame responses.

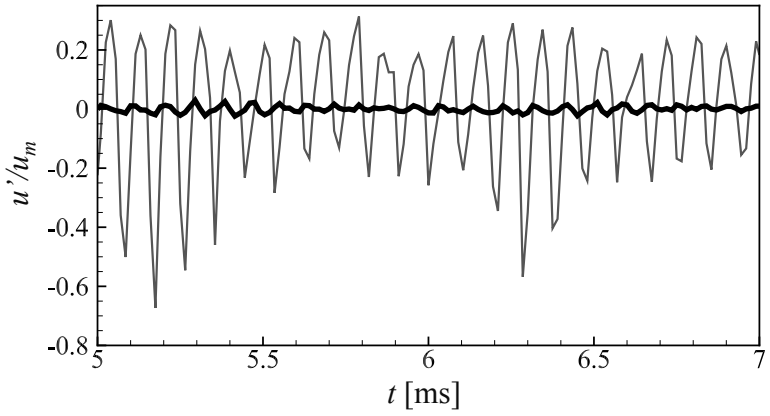


Figure 5.8: Velocity fluctuation at the location of the recess: u'_{H_2} (thin gray line) and u'_{O_2} (bold black line).

a time averaging. This choice for the normalization is supported by the fact that the flow downstream the coaxial injector resembles a pulsated mixing layer. It shows which stream oscillates the most with respect to the mean velocity. When each stream is normalized by its own mean velocity, which is much lower for the dense oxygen, the relative fluctuation levels are comparable and around 10%.

It appears that the O_2 velocity fluctuations are negligible compared to those of H_2. Both streams experience the same pressure perturbation but the corresponding u' depends on the impedance which is related both to geometric (area ratios) and thermodynamic (compressibility) effects. Specifically, the u' amplitude is inversely proportional to the characteristic impedance of the gas, which is the product of the density and speed of sound: ρc. The thermodynamic conditions at the location of the recess are: $(\rho c)_{O_2} = 7\,10^5$ kg.m^{-2}.s^{-1} and $(\rho c)_{H_2} = 1.8\ 10^4$ kg.m^{-2}.s^{-1}, which is 40 times higher for O_2 than for H_2. This possibly explains why the velocity fluctuations in the H_2 stream dominate in the present conditions.

To quantify the correlation between velocities or pressure and heat release perturbations

one may calculate the normalized cross correlation defined by:

$$r_{fg} = \frac{(f \star g)(\tau)}{\sigma_f \sigma_g} \tag{5.3}$$

where σ is the standard deviation. The maximum correlation between p' and q' is $r_{pq} = 80\%$ while it is 67% between $u'_{\mathrm{H_2}}$ and q' and falls down to 47% between $u'_{\mathrm{O_2}}$ and q'. These observations are confirmed by single injector simulations (not shown here), where the flame responses induced by H_2 or O_2 streams fluctuations are compared. Forcing the individual propellants velocities at the level measured in the full engine, *i.e.* around 10% of their mean, yields a much weaker flame response for O_2 than for H_2. Nevertheless bulk pressure fluctuations at the outlet of the injector also triggered significant levels of q'.

From these observations we can assume that $u'_{\mathrm{O_2}}$ is not the most relevant input variable for the flame response. One may then speculate that q' is driven by $u'_{\mathrm{H_2}}$ through the forcing of the shear layer, generating unsteady coherent structures affecting both wrinkling and local stretch of the flame eventually leading to heat release rate fluctuations. A mechanism for the

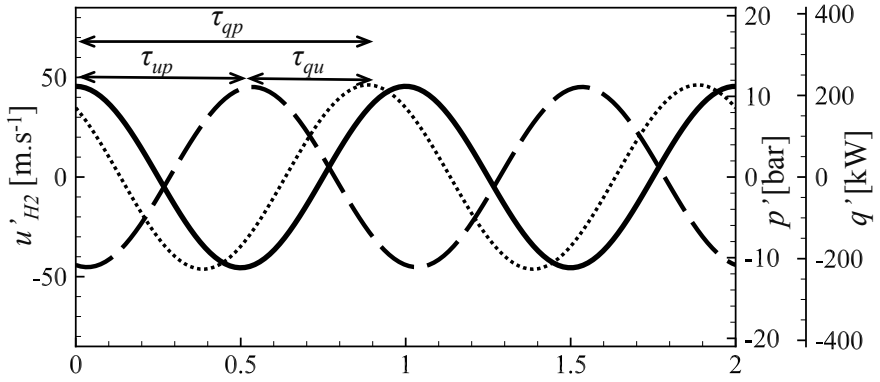


Figure 5.9: Fluctuations over two periods of the 1T mode ($T = 1/f_1$) for an A-flame: p' (solid line), $u'_{\mathrm{H_2}}$ (dashed line) and q' (dotted line). Reference surfaces are indicated in Fig.5.7

flame response is now proposed, based on the above rationale. Hydrogen velocity fluctuations are supposed to be central in this mechanism but the validation of this hypothesis requires additional tests. Mechanisms involving a direct response to pressure fluctuations, for example, should also be considered. The mechanism is summarized in Fig. 5.9, where the temporal evolution of p', $u'_{\mathrm{H_2}}$ and q', extracted from the FT at the 1T frequency, are shown over two cycles of the instability. Three time-delays are identified:

- The delay of $u'_{\mathrm{H_2}}$ with respect to p': τ_{up}.
- The delay of q' with respect to $u'_{\mathrm{H_2}}$: τ_{qu}.
- The delay of q' with respect to p': τ_{qp}.

Figure 5.9 suggests the present scenario for the A-flame response: the pressure fluctuation at the injector outlet generates a hydrogen velocity fluctuation after a time τ_{up}, which drives the shear layer and subsequently heat release rate fluctuations with a delay τ_{qu}. The overall delay $\tau_{qp} = \tau_{up} + \tau_{qu}$ is such that p' and q' are almost perfectly in phase, resulting in a positive Rayleigh index. While τ_{up} is mainly acoustic by nature, τ_{qu} represents the time for hydrodynamics and combustion to respond to the unsteady shear.

Finally, the overall response of an A-flame can be quantified by the gain, n and time-delay, τ of q' versus p':

$$n = \frac{|\tilde{q}|/q_0}{|\tilde{p}|/p_0} \qquad \tau = \frac{\phi_{\tilde{q}} - \phi_{\tilde{p}}}{2\pi f} \tag{5.4}$$

The present dataset is used to compute n and τ for the A-flames of the 1T mode. Here we give averaged values for the 8 outer A-flames that have the highest Rayleigh index (red regions in Fig. 5.5): $n = 1.1$ and $\tau = 0.9\ T$.

5.6 Conclusions

In this chapter, the Large-Eddy Simulation of a 42-injector reduced-scale rocket engine is used to analyze the limit cycle of a combustion instability. The post-processing of a time-resolved dataset of 3D solutions allows to isolate individual flame dynamics as well as the influence of different eigenmodes of the chamber. In this configuration two chamber modes dominate, one with a transverse shape and the other with a radial structure. For both modes, the magnitude of the flame response is maximum at pressure antinodes, while the flames located at a pressure node respond weakly, suggesting that the lateral motion caused by transverse velocity fluctuations does not effectively feed energy into acoustics for sustaining this instability. A mechanism is proposed in which the bulk pressure variation at the injector outlet generates unsteady shear through the variation of the hydrogen velocity, ultimately resulting in heat release rate fluctuations. For modeling purposes, it is suggested to consider the fluctuating pressure in the injection plane as the relevant input for the flame response. This option has been considered since the early studies on transverse combustion instabilities in rocket engines [173] and it receives here additional support from 3D unsteady numerical simulation.

Part II

Acoustic boundary conditions for time domain simulations

Context & Outline

Heat release rate oscillations and acoustic perturbations are linked through the thermoacoustic feedback loop. Combustion Instabilities (CIs) occur when these fluctuations become coherent, creating constructive interferences. In order to predict the occurrence of CIs in combustion devices, the flame response (*i.e.* the heat release oscillations caused by a given acoustic oscillation) and the acoustic oscillations in the entire combustion system must be accurately reproduced. The correct acoustic fluctuations can be obtained only if the acoustic properties of the boundaries are considered.

Acoustic properties, such as impedance or reflection coefficient, are defined in the spectral domain while the Navier-Stokes equations are in the time domain. Imposing acoustic properties at boundary conditions in DNS/LES thus requires attention and specific methods are needed to achieve this in a computationally efficient way, especially for high-fidelity Navier-Stokes simulations. These methods are referred to as "Time Domain Impedance Boundary Condition" (TDIBC) methods.

In this part of the manuscript, the focus is on such methods.

1. **Chapter 6: Derivation of a TDIBC method based on the reflection coefficient**
   The method is based on Fung and Ju's formalism [83, 84], referred to as "the Pole & Residue approach" here, which was further extended by Lin *et al.* [86]. The background and Fung and Ju's methodology are recalled before deriving and validating a TDIBC based on the reflection coefficient.

2. **Chapter 7: Use of TDIBC to impose time-delay**
   Although TDIBC methods should be able to impose any acoustic properties, one case remains difficult: the imposition of a time-delay. Such an acoustic property allows to truncate large portion of the domain to focus of areas of interest (*e.g.* the flame region). A modeling procedure is developed in order to use the TDIBC derived in Chapter 6 to impose time-delays. The method is validated for a one-dimensional wave simulation and is then used to truncate a portion of a combustion chamber where CIs occur: the INTRIG Burner operated at IMFT (Toulouse, France).

3. **Chapter 8: State-space approach for TDIBC and comparison with the Pole & Residue approach**
   The fundamentals of state-space modeling are recalled and the TDIBC method of Jaensch *et al.*, called Characteristic Based State-space Boundary Condition (CBSBC), is presented. The Pole & Residue and the state-space approaches are then compared and their mathematical equivalence is shown.

Chapter 6

Time domain impedance boundary condition

Boundary conditions are a critical issue in unsteady Navier-Stokes simulations of compressible flows, especially when acoustic plays a major role such as in Computational Aero-Acoustics (CAA) and thermoacoustic studies. In this context, unsteady boundary conditions allowing low levels of acoustic reflection called Navier-Stokes Characteristic Boundary Conditions (NSCBC) have been developed [114, 115, 175–179]. The acoustic reflection of NSCBC behave as a first order low pass filter: it reflects low frequency waves and absorbs high frequency waves [115, 116, 180–182]. In reality, acoustic elements can have much more diverse acoustic properties. As boundaries play a major role in acoustics, it is crucial to be able to accurately impose acoustic properties at the boundary conditions in Navier-Stokes simulations. As acoustic properties are complex-valued quantities defined in the frequency domain, a time domain translation of these quantities has to be found.

A possible approach is to evaluate numerically the time domain equivalent of those complex properties. This approach is to be avoided as it is conditionally unstable (causality constraint) and that both memory storage and CPU cost are high and, most of all, increasing in time. An alternative to this approach is to derive an equivalent mathematical expression that can be evaluated recursively. This leads to a constant memory storage and CPU cost in time. The Time Domain Impedance Boundary Condition (TDIBC) method used in this chapter is based on Fung and Ju's methodology [83, 84].

In this chapter the background on impedance boundary condition will be presented (Sec. 6.1). Section 6.2 will focus on the description of Fung and Ju's method [83, 84] and a new formulation using the reflection coefficient as a modeling quantity will be derived. Finally, the reflection coefficient based TDIBC will be validated in Sec. 6.3.

6.1 Introduction

Direct Numerical Simulation (DNS) or Large Eddy Simulation (LES) have become standard approaches for high-fidelity simulations of unsteady fully-compressible flows. In many configurations, accurate flow predictions can be reached only if the reflection of the acoustic waves at the boundaries is precisely defined and controlled [9, 114, 116, 183]. Impedance is a widely-used quantity to characterize the reflection of acoustic waves at boundaries. It is defined in the frequency domain whereas DNS/LES are performed in the time domain. There is a need for numerical methods permitting the imposition of impedance at the boundaries of a computational domain. This has been achieved by the derivation of Time Domain Impedance Boundary Conditions (TDIBC).

Both DNS and LES strive to lower numerical dissipation of acoustic waves so that they accurately propagate in the computational domain without energy loss. Additionally, the proper specification of impedances at boundary conditions can be critical for the flow stability. For example, using simplistic boundary conditions such as imposed velocity or pressure leads to fully-reflective acoustic conditions at the boundaries and to an artificial acoustic energy increase.

Acoustic waves are the manifestation of perturbations around a mean state: using the Reynolds decomposition, the pressure field can be expressed as $p(t) = p_0 + p'(t)$, where p_0 is the mean pressure and $p'(t)$ is the acoustic perturbation [9]. The characterization of an acoustic element is usually performed in the frequency domain by the use of a complex transform, such as the Fourier transform $\mathcal{F}$, *e.g.* the complex acoustic pressure is defined as $p(\omega) = \mathcal{F}(p'(t))$, where ω represents the angular frequency. The specific impedance $Z_*(\omega)$ is defined in the frequency domain as the non-dimensional ratio of complex pressure and velocity [96]:

$$Z_*(\omega) = \frac{1}{\rho_0 \, c_0} \frac{p(\omega)}{u_n(\omega)}, \tag{6.1}$$

where ρ_0 and c_0 are the mean density and speed of sound of the fluid, respectively. $Z_*(\omega)$ is a frequency-dependent complex-valued function. It is unbounded, and is thus not always convenient numerically so that TDIBC uses the reflection coefficient R and the wall softness S, which are acoustic quantities yielding the same information. They are defined using the impedance $Z_*(\omega)$:

$$R(\omega) = \frac{1 - Z_*(\omega)}{1 + Z_*(\omega)} \tag{6.2a}$$

$$S(\omega) = R(\omega) + 1 \tag{6.2b}$$

Unlike the specific impedance Z_*, both the reflection coefficient R and the wall softness S are bounded, which make them suitable quantities in a computational context. Figure 6.1 illustrates the definition of the outgoing and ingoing acoustic waves A_n^{out} and A_n^{in}, respectively.

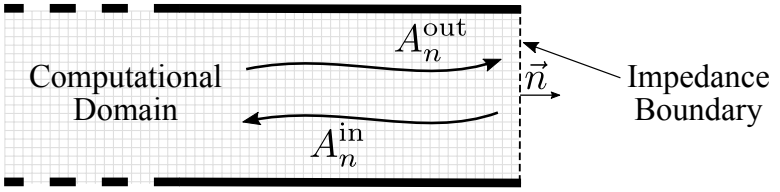


Figure 6.1: Orientation of ingoing and outgoing acoustic waves A_n^{in} and A_n^{out} on an Impedance Boundary Condition defined from the outward pointing normal $\vec{n}$.

A_n^{out} is oriented in the direction as the outward normal $\vec{n}$ and A_n^{in} is oriented in the opposite direction of $\vec{n}$. Following the definition of Fig. 6.1, outgoing and ingoing characteristic waves are:

$$A_n^{\text{out}}(\omega) = \vec{u}(\omega) \cdot \vec{n} + \frac{p(\omega)}{\rho_0\, c_0}, \quad A_n^{\text{in}}(\omega) = \vec{u}(\omega) \cdot \vec{n} - \frac{p(\omega)}{\rho_0\, c_0} \tag{6.3}$$

Substituting Eq. 6.1 in Eqs. 6.2a and 6.2b yields:

$$R(\omega) = \frac{A_n^{\text{in}}(\omega)}{A_n^{\text{out}}(\omega)} \tag{6.4a}$$

$$S(\omega) = \frac{A_n^{\text{in}}(\omega) + A_n^{\text{out}}(\omega)}{A_n^{\text{out}}(\omega)} \tag{6.4b}$$

Impedance, reflection coefficient and wall softness are defined in the frequency domain whereas DNS/LES are performed in the time domain. The time domain equivalent of $R(\omega)$ is obtained by using the inverse Fourier transform $R(t) = \mathcal{F}^{-1}(R(\omega))$ and $S(t) = \mathcal{F}^{-1}(S(\omega))$. However, the inverse Fourier transform of a product $\mathcal{F}^{-1}(R(\omega) \cdot A_n^{\text{out}}(\omega))$ yields a convolution integral. Equations 6.4a and 6.4b can be expressed in the time domain by using the inverse Fourier transform, leading to the following convolution integrals for Eq. 6.5a and 6.5b, respectively [184, 185]:

$$A_n^{\text{in}}(t) = \int_0^t R(\tau)\; A_n^{\text{out}}(t-\tau)\; d\tau \tag{6.5a}$$

$$= -A_n^{\text{out}}(t) + \int_0^t S(\tau)\; A_n^{\text{out}}(t-\tau)\; d\tau \tag{6.5b}$$

The bounds of the integrals in Eqs. 6.5a and 6.5b are reduced to $\tau \in [0, t]$ as:

- we assume that $S(t)$, $R(t)$, $A_n^{\text{in}}(t)$ and $A_n^{\text{out}}(t)$ are defined on the interval $t \in [0, +\infty]$,
- $A_n^{\text{in}}(t)$ must depend only on past and present values of $S(t)$, $R(t)$, $A_n^{\text{out}}(t)$ but cannot depend on *future* values for the causality constraint not to be violated.

These assumptions restrict the bounds of the convolution integrals as it is the case when using the causal inverse Laplace transform [186, 187]. Although mathematically equivalent to Eqs. 6.4a and 6.4b, Eqs. 6.5a and 6.5b are not directly applicable in high-fidelity compressible solvers because the direct evaluation of the convolution integral requires a large amount of memory. Indeed, $A_n^{\text{out}}(t)$ and $R(t)$ need to be stored at every iteration and at each of the

boundary faces.

For simple geometries, Nottin [188, 189] has solved Eq. 6.5a directly. In computationally intensive frameworks such as DNS/LES of turbulent flows, a more efficient compact-in-time method is required for the evaluation of $A_n^{\text{in}}(t)$, as shown in recent papers on this topic [83–86, 90, 91, 190, 191].

Advancements in the time domain impedance imposition in the electromagnetic community have driven novel acoustic boundary conditions for computational aeroacoustics [192–195]. For a time domain impedance imposition method to be robust and physically admissible, care must be taken not to violate the causality constraint [84, 196].

Özyoruk *et al.* [192, 193, 197] and Tam and Auriault [194] have developed a first formulation of TDIBC based on the z-transform and a Laurent series development of the impedance in the frequency domain resulting in a time domain Ordinary Differential Equation (ODE) problem. This formulation is conditionally unstable and may violate both physical admissibility and causality constraints, and thus is a threat to numerical stability [194].

Fung and Ju [83, 84] have proposed a causal formulation for TDIBC, based on the wall softness S. It relies on single partial fraction modeling in the frequency domain as discussed in Sec. 6.2.2. Fung and Ju's formulation has been validated for both Euler [83, 84] and, more recently, Navier-Stokes simulations [85, 86]. Originally based on a single partial fraction model, Fung and Ju's modeling technique has been extended to a sum of partial fractions by Lin *et al.* [86].

In the combustion community, a State-Space approach, called Characteristic Based State-space Boundary Condition (CBSBC), has been developed by Schuermans *et al.* [198], Kaess *et al.* [90] and Jaensch *et al.* [91], and used in Navier-Stokes simulations [90, 190, 191, 199–201]. CBSBC relies on control theory of linear time-invariant (LTI) systems to build a reflection coefficient model through first-order differential matrix equations [91]. Two formulations of CBSBC were proposed.

The first formulation of CBSBC is a state-space approach under the so called controllable form, *i.e.* based on the modeling of a transfer function as a rational polynomial. The transfer function represents the broadband reflection coefficient. It aims to impose a reflection coefficient with near-zero time-delay, similarly to Fung and Ju's method. For practical reasons, this formulation fails to handle pure time-delay. In pure time-delay imposition problems, the rational polynomial transfer function modeling requires a high number of Padé polynomial coefficients leading to ill-conditioned matrices, making this formulation difficult to use.

A second formulation of CBSBC was proposed by Jaensch *et al.* [190] specifically to impose pure time-delays. This approach consists in implementing a Linearized Euler Equations (LEE) solver for each of the impedance boundary conditions in the domain and perform the temporal integration using a first-order upwind scheme. The 1D spatial discretization needed

by the LEE solver is done by storing in memory a state matrix of dimension $2N \times 2N$, and three matrices of dimension $2 \times N$, where N is the number of nodes considered in the spatial discretization. In their work, Jaensch *et al.* [190] have shown that to impose a pure time-delay for a 1D wave propagation problem it was necessary to consider a number of nodes as high as $N = 1000$ in order to avoid acoustic energy dissipation. This formulation of CBSBC will be discussed in depth in Chapter 8 and the similarities with the formulation presented in Sec. 6.2.2 will be emphasized.

In this chapter, a reformulation of Fung and Ju's method based on the reflection coefficient R is proposed. This new formulation is mathematically equivalent to the extended formulation of TDIBC used by Lin *et al.* [86] but is more convenient when the acoustic boundary to be modeled is an inlet or an outlet. By contrast, the wall softness formulation is more suited for acoustic boundaries having near-wall acoustic properties, such as acoustic liners. Another benefit of the reflection coefficient formulation is that it can handle the imposition of pure time-delays. This specific topic will be discussed in Chapter 7.

In Sec. 6.2 the TDIBC method, based on the wall softness coefficient, developed by Fung and Ju and extended by Lin *et al.* [86], will be presented. It will then be extended to reflection coefficients. Section 6.3 will focus on the validation of TDIBC under the reflection coefficient formalism for both single-pole models (as Fung and Ju [83, 84]) and multi-pole models (as Lin *et al.* [86]).

6.2 Method

In this section, two formulations of TDIBC are presented. The first formulation, is the extended Fung and Ju method [83, 84, 86]. It is based on the wall softness coefficient (Eq. 6.2b) as an acoustic modeling quantity. The equations presented here are equivalent to the ones in Lin *et al.* [86] but they have been expressed so they are consistent with the current manuscript. The second formulation is based on the reflection coefficient (Eq. 6.2a) as an acoustic modeling quantity. The same mathematical procedure is followed as in Fung and Ju's method. It is especially suited for low-pass-filter-like acoustic boundaries such as open-end ducts (often used as inlet and outlets). It is also well suited for the imposition of pure time-delays as discussed in the next chapter.

6.2.1 Time domain imposition of complex wall softness coefficient

As discussed in Sec. 6.1, the resolution of Eq. 6.5b allows imposing a complex wall softness coefficient in the time domain but is memory and CPU consuming in DNS/LES simulations. The methodology developed by Fung and Ju [83, 84] and extended by Lin *et al.* [86], the wall softness $S(\omega)$ is approximated by the wall softness coefficient of the boundary condition S_{BC} expressed as a sum of rational function:

$$S(\omega) \simeq S_{\mathrm{BC}}(\omega, n_0) = \sum_{k=1}^{2n_0} \frac{\mu_k}{i\omega - p_k} \tag{6.6}$$

where $S_{\mathrm{BC}}(\omega, n_0)$ is the reflection coefficient model and the poles & residues (p_k, μ_k) must come as n_0 conjugate pairs:

$$p_{2k} = p_{2k-1}^* \quad ; \quad \mu_{2k} = \mu_{2k-1}^* \quad ; \quad k \in [1; n_0] \tag{6.7}$$

The poles and residues are complex-valued so that these conjugate pairs are needed to ensure that the wave imposed by TDIBC in the time domain is real-valued. The time domain equivalent of Eq. 6.6 is:

$$S_{\mathrm{BC}}(t, n_0) = \sum_{k=1}^{2n_0} \mu_k e^{p_k t} \tag{6.8}$$

The temporal wave $A_n^{\mathrm{in}}(t)$ corresponding to $S_{\mathrm{BC}}(\omega, n_0)$ is obtained by introducing $S_{\mathrm{BC}}(t, n_0)$ in Eq. 6.5b:

$$A_n^{\mathrm{in}}(t) = -A_n^{\mathrm{out}}(t) + \sum_{k=1}^{2n_0} \int_0^t \mu_k e^{p_k \tau} A_n^{\mathrm{out}}(t-\tau) d\tau \tag{6.9}$$

The convolution integral in Eq. 6.5b has been split into $2n_0$ convolution integrals, denoted I_k:

$$A_n^{\mathrm{in}}(t) = -A_n^{\mathrm{out}}(t) + \sum_{k=1}^{2n_0} I_k(t) \tag{6.10}$$

Using the properties of the exponential, I_k can be split into two contributions while integrating by part:

$$I_k(t) = I_k(t - \Delta t) e^{p_k \Delta t} + \mu_k \int_{t-\Delta t}^{t} e^{p_k \tau} A_n^{\mathrm{out}}(t-\tau) d\tau \tag{6.11}$$

Equation 6.11 shows that $I_k(t)$ can be evaluated recursively: the first term corresponds to the temporal integration over the interval $\tau \in [0,\ t - \Delta t]$ and the second term to the temporal integration over the interval $\tau \in [t - \Delta t,\ t]$. It provides a low memory storage method to compute the ingoing wave $A_n^{\mathrm{in}}(t)$. Indeed, the only stored quantities needed are $I_k(t - \Delta t)$ and $A_n^{\mathrm{out}}(t - \Delta t)$ as all the other quantities can be evaluated at time t. The associated CPU cost is also constant at every iteration. As the integral in Eq. 6.11 is over a time step Δt it is not computationally expensive. Using a trapezoidal quadrature rule, Eq. 6.11 can be numerically approximated at low computational cost [83, 84]:

$$I_k(t) = I_k(t - \Delta t) e^{p_k \Delta t} + \alpha_k A_n^{\mathrm{out}}(t) + \beta_k A_n^{\mathrm{out}}(t - \Delta t) \tag{6.12}$$

$$\alpha_k = \mu_k \left(\frac{e^{p_k \Delta t} - 1}{p_k^2 \Delta t} - \frac{1}{p_k} \right) \quad ; \quad \beta_k = \mu_k \left(\frac{e^{p_k \Delta t} - 1}{p_k^2 \Delta t} - \frac{e^{p_k \Delta t}}{p_k} \right) \tag{6.13}$$

The initial values of $I_k(t)$ and A_n^{out} are set to zero in the simulations [83–86]. However, one can make a checkpoint restart by initializing the $I_k(t)$ using stored values from previous a simulation. Using Eqs. 6.12 and 6.13, complex impedances can be imposed in DNS/LES solvers. A checkpoint restart is possible if the values of $I_k(t)$ are stored from the last iteration of the previous simulation.

6.2.2 Time domain imposition of complex reflection coefficient

In Sec. 6.2.1 the methodology to impose a complex wall softness coefficient in Fung and Ju's formalism was described. Here, the same mathematical properties will be used to resolve Eq. 6.5a, that is, using the reflection coefficient as an acoustic modeling quantity. Thus, this method provides a memory and CPU efficient way of imposing a complex reflection coefficient in DNS/LES. We approximate the reflection coefficient $R(\omega)$ with the reflection coefficient of the boundary condition R_{BC} expressed as a sum of rational function:

$$R(\omega) \simeq R_{\text{BC}}(\omega, n_0) = \sum_{k=1}^{2n_0} \frac{\mu_k}{i\omega - p_k} \tag{6.14}$$

where $R_{\text{BC}}(\omega, n_0)$ is the reflection coefficient model and the poles & residues (p_k,μ_k) must come as n_0 conjugate pairs (Eq. 6.7) to ensure that the imposed wave $A_n^{\text{in}}(t)$ is real valued. In the time domain, Eq. 6.14 becomes:

$$R_{\text{BC}}(t, n_0) = \sum_{k=1}^{2n_0} \mu_k e^{p_k t} \tag{6.15}$$

The temporal wave $A_n^{\text{in}}(t)$ corresponding to $R_{\text{BC}}(\omega, n_0)$ is obtained by introducing $R_{\text{BC}}(t, n_0)$ in Eq. 6.5a:

$$A_n^{\text{in}}(t) = \sum_{k=1}^{2n_0} \int_0^t \mu_k e^{p_k \tau} A_n^{\text{out}}(t-\tau) d\tau = \sum_{k=1}^{2n_0} I_k(t) \tag{6.16}$$

Equation 6.5a has been split into $2n_0$ convolution integrals I_k as in Eq. 6.10. Using Eqs. 6.12 and 6.13, we can impose a complex reflection coefficient in DNS/LES in cost-effective way. The convolution integrals can be evaluated using Eqs. 6.12 and 6.13.

6.2.3 Block diagram representation of multi-pole TDIBC

As discussed above, Fung and Ju's TDIBC [83, 84] was extended by Lin *et al.* [86]. In their work, Lin *et al.* extended the modeling procedure to a sum of $2n_0$ rational fractions while it was previously limited to 2 rational fractions ($n_0 = 1$ in Eq. 6.6). Figure 6.2 illustrates the resulting block diagram of the multi-pole formulation of TDIBC based on the reflection coefficient. The multi-pole TDIBC can be split into n_0 Linear Time Invariant (LTI) sub-systems. Each of these sub-systems is a single-pole single-residue LTI system (this will be the topic of Sec. 8.3.1). It takes the temporal outgoing wave $A_n^{\text{out}}(t)$ as an input and gives

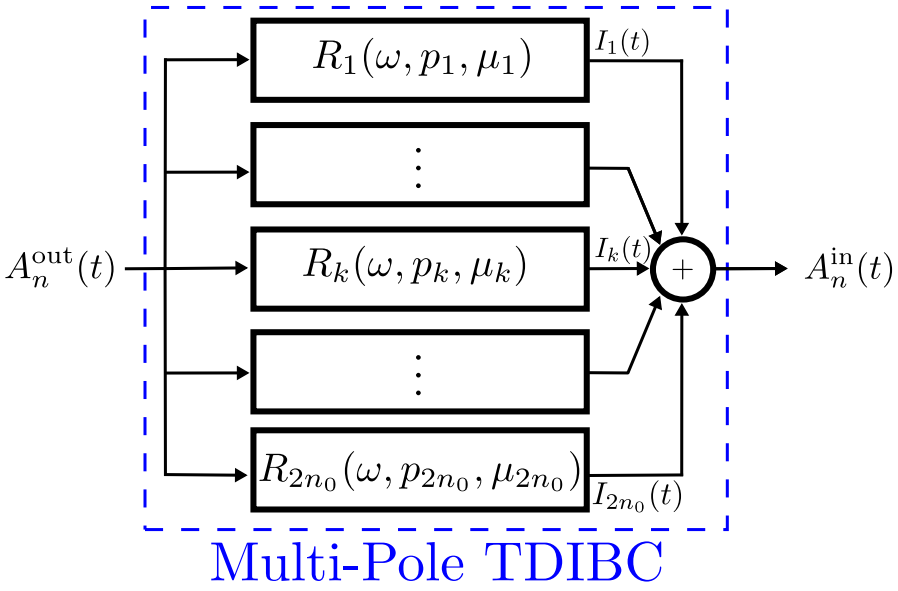


Figure 6.2: Block diagram of a multi-pole TDIBC under Fung and Ju's formalism.

an output $I_k(t)$. The sum of the contributions of each sub-system gives the ingoing wave (Eq. 6.16).

6.3 Validation of reflection-coefficient-based TDIBC

The validation of TDIBC will be conducted in this section. The test case consists in a one-dimensional wave propagation problem. The initial solution (*cf.* § Initial solution) is a right-traveling wave packet – the outgoing wave $A_n^{\text{out}}(t)$ – that will reflect on an impedance boundary condition on the right-hand side of the domain. The impedance boundary will have a given TDIBC model: a set of (p_k, μ_k) coefficients. The impedance boundary condition will impose an ingoing wave $A_n^{\text{in}}(t)$ that must fulfill the frequency-domain properties of the TDIBC model. This ingoing wave computed by TDIBC will then be compared to its analytical solution (*cf.* § Analytical solution), *i.e.* by computing the convolution integral (Eq. 6.5a).

Initial solution

The domain is one-dimensional and is defined by the coordinate $x \in [-1, 1]$ m. The initial solution is a wave packet centered in $x = 0$ m:

$$A_n^{\text{out}}(x, t = 0) = Ae^{-\alpha k^2 x^2} \cos(2\pi k x) \tag{6.17}$$

where $A = 1$, $\alpha = 0.8$ and $k = 7$. The exponential in Eq. 6.17 is a Gaussian wave of maximum amplitude A giving a compact support nature to the initial solution. Equation 6.17 is similar to the one used in Scalo *et al.* [85] to validate Fung and Ju's TDIBC (based on wall softness $S(\omega)$) in Navier-Stokes simulations. The cosine in Eq. 6.17 allows to give a strong frequency content at the wave of wavenumber $k = \omega/c_0$. The initial solution for the right traveling

wave is shown in Fig. 6.3 and the left traveling wave is set to zero. The acoustic pressure and velocity fields corresponding to $A_n^{\text{out}}(x, t = 0)$ are thus:

$$p^{'}(x, t = 0) = A_n^{\text{out}}(x, t = 0) \tag{6.18}$$

$$u^{'}(x, t = 0) = \frac{1}{\rho_0 c_0} A_n^{\text{out}}(x, t = 0) \tag{6.19}$$

The mean density is $\rho_0 = 1.14\ \text{kg}\,\text{m}^{-3}$ and the mean sound speed is $c_0 = 350\ \text{m}\,\text{s}^{-1}$.

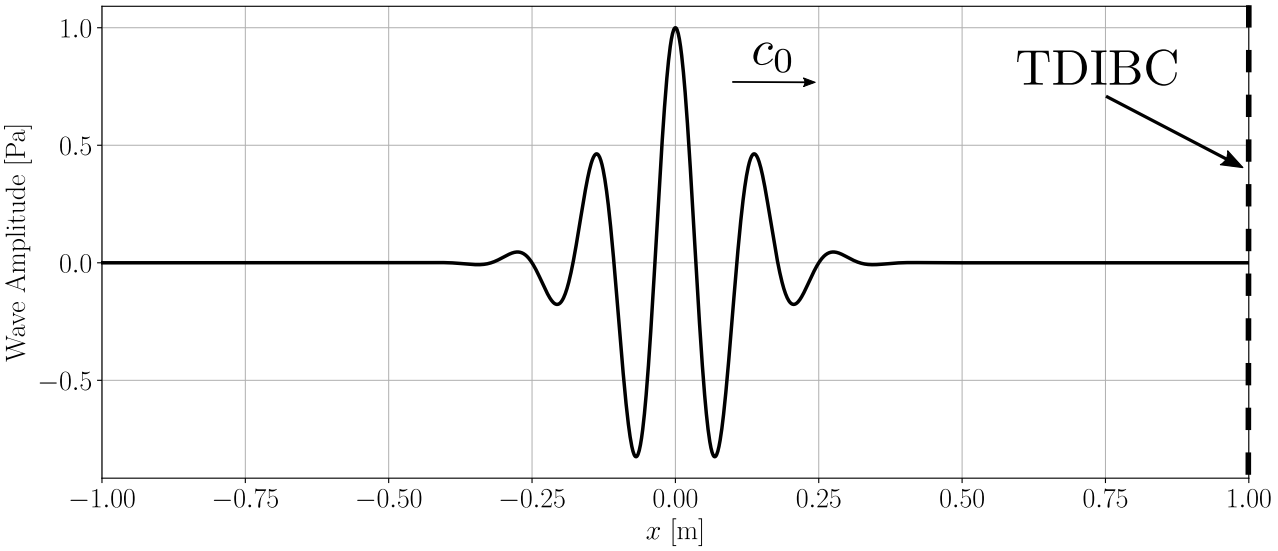


Figure 6.3: Initial solution for the outgoing wave $A_n^{\text{out}}(x, t = 0)$ for $A = 1$, $\alpha = 0.8$ and $k = 7$ in Eq. 6.17.

As the wave number chosen is $k = \omega/c_0 = 7$, the frequency content of the initial solution should be mostly around $f = kc_0 = 2450$ Hz. This is verified by taking the Fourier transform of the temporal outgoing wave $A_n^{\text{out}}(x = 1, t)$. The result is shown in Fig. 6.4. The Fourier transform of the wave packet is a Gaussian wave centered at the frequency $f_{\max} = kc_0 = 2450$ Hz where the maximum is $A_n^{\text{out}}(2\pi f_{\max}) = 1.35e^{-2}$ Pa. The frequency content of the initial solution will be used in the multi-pole model validation to analyze the results.

Analytical solution

The reflection coefficient modeled by TDIBC is known (Eq. 6.14) and its expression in the time domain is given by Eq. 6.15. The analytical solution of the ingoing wave $A_n^{\text{in}}(t)$ is then:

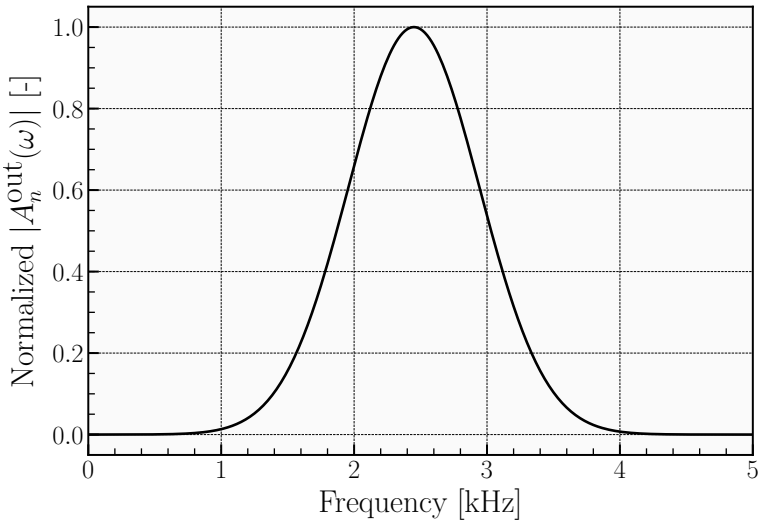


Figure 6.4: Modulus of the Fourier transform of the initial temporal Gaussian wave $\mathcal{F}(A_n^{\text{out}}(x = x_{\text{BC}}, t))$.

$$\begin{aligned} A_n^{\text{in}}(t) &= \int_0^t R_{\text{BC}}(\tau)\ A_n^{\text{out}}(t-\tau)\ d\tau \\ &= \sum_{k=1}^{n_0} \int_0^t R_k(\tau)\ A_n^{\text{out}}(t-\tau)\ d\tau \\ &= \sum_{k=1}^{n_0} \int_0^t \left[\mu_k e^{ip_k\tau} + \mu_k^* e^{ip_k^*\tau}\right] A_n^{\text{out}}(t-\tau)\ d\tau \end{aligned} \tag{6.20}$$

6.3.1 Validation of TDIBC based on reflection coefficient: single-pole

In this section, we validate TDIBC formulation based on the reflection coefficient for single pair of conjugate pole p_k and residue μ_k as a reflection coefficient model, that is $n_0 = 1$. The pole & residue used here are

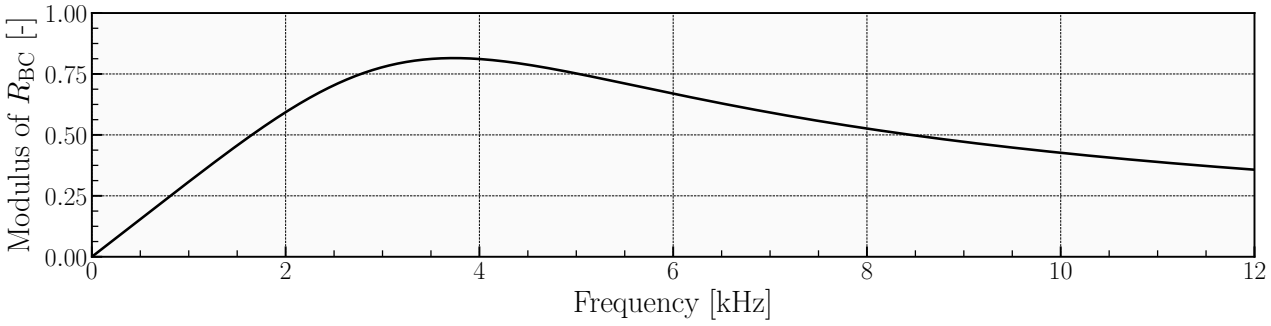
$$\begin{aligned} p_1 &= -16600 + i16600 \\ \mu_1 &= 13531 + i13531 \end{aligned} \tag{6.21}$$

The reflection coefficient modeled by p_1 and μ_1 is defined by Eq. 6.14 and is plotted in Fig. 6.5. The modulus of the reflection coefficient is shown in Fig. 6.5(a) and its phase is shown in Fig. 6.5(b). This model has a maximum modulus and a null phase at $f_1 = 3745$ Hz.

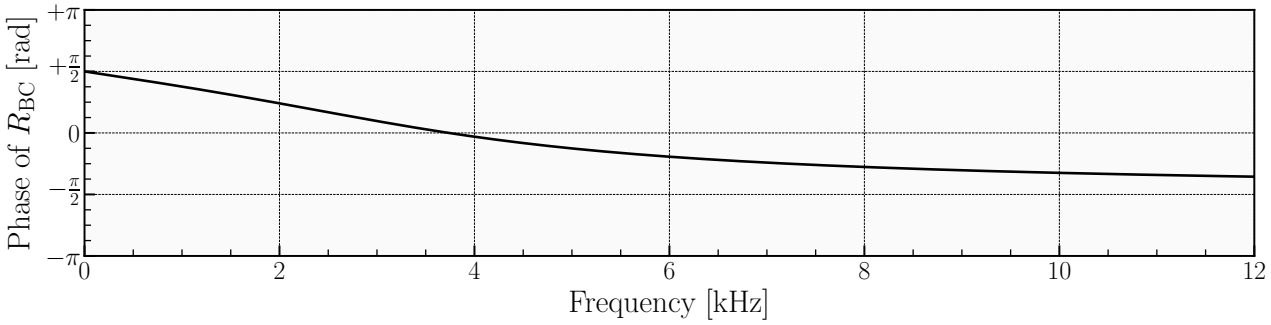
The simulation is conducted with the AVBP solver (*c.f.* Sec. 2.2.1) with TDIBC was implemented in this solver under the reflection coefficient formulation presented in Sec. 6.2.2. Here, the Euler equations are solved on a 500 cell mesh. The numerical scheme (TGCC) is third-order accurate in space and time [134, 135] and no artificial viscosity model is used.

The ingoing wave $A_n^{\text{in}}(t)$ prescribed by TDIBC is shown in Fig. 6.6. The TDIBC wave is compared with a numerical evaluation of Eq. 6.20. This numerical integration is performed using the integrate.quad function of the SciPy scientific library in Python [131].

As presented in the TDIBC methodology in Sec. 6.2.2, TDIBC is mathematically equivalent to the convolution integral in Eq. 6.20. Fig. 6.6 shows that the wave imposed by TDIBC is exactly equivalent to the analytical solution for a single pair of pole & residue. The ingoing wave has a lower maximum amplitude that the initial wave (*cf.* Fig. 6.6). This is consistent with the modeled reflection coefficient R_{BC} shown in Fig. 6.5 as its modulus is lower that unity at all frequencies. Additionally, we observe that the reflected wave is asymmetric while the initial wave is symmetric. This distortion of the wave was introduced by the phase of R_{BC}. If R_{BC} were purely real the reflected wave would be symmetric. This illustrates that TDIBC can, in fact, impose complex impedances (using the reflection coefficient) in time domain simulations.



(a) Modulus of $R_{\mathrm{BC}}(\omega)$



(b) Phase of $R_{\mathrm{BC}}(\omega)$

Figure 6.5: Modulus (a) and phase (b) of the reflection coefficient modeled by the boundary condition for p_1 and μ_1 in Eq. 6.21.

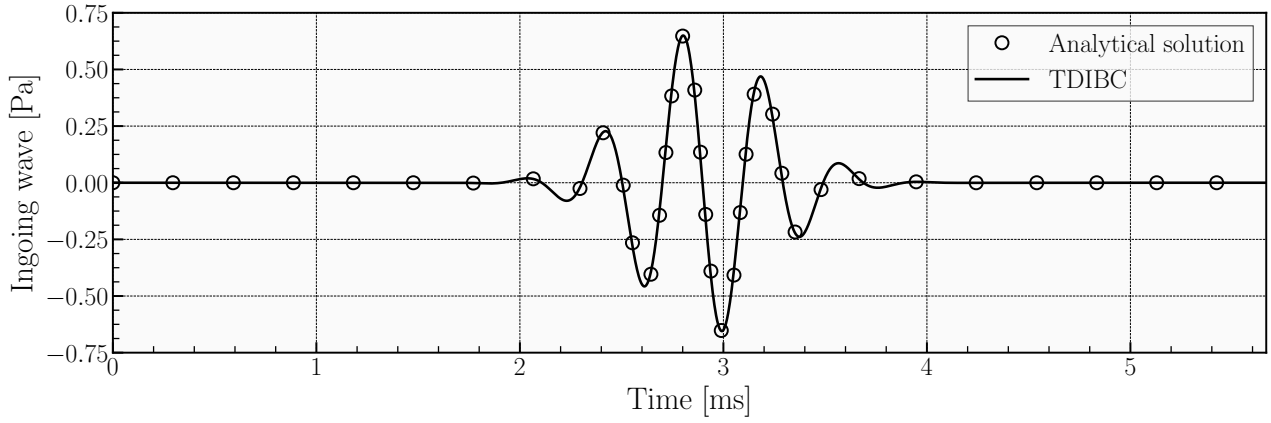


Figure 6.6: Validation of TDIBC based on the reflection coefficient for a single pair of conjugate pole p_1 and residue μ_1 ($n_0 = 1$ in Eq. 6.14). The ingoing wave imposed by TDIBC corresponds to model reflection coefficient R_{BC} (*cf.* Fig. 6.5) as it is exactly equal to the analytical solution. The analytical solution is computed by resolving the integral in Eq. 6.20.

6.3.2 Validation of TDIBC based on reflection coefficient: multi-pole

In this section, we validate the formulation of TDIBC based on the reflection coefficient for a multi-pole reflection coefficient model, as presented in Sec. 6.2.2. The test case used in Sec. 6.3.1 is used here to validate the multi-pole TDIBC.

Three poles reflection coefficient model

It is done using a three poles model: three pairs of conjugate poles p_k and residues μ_k for $k \in [1, n_0]$ and $n_0 = 3$. The poles & residues parameters are given in Table 6.1.

R_k	a_k	b_k	c_k	d_k	$\omega_{0,k}$ [rad s^{-1}]	f_0 [Hz]
$k=1$	5.00e+02	8.33e+00	-1.00e+03	6.00e+04	6.00e+04	9.55e+03
$k=2$	-1.00e+03	-1.00e+04	-1.00e+03	1.00e+02	1.00e+03	1.60e+02
$k=3$	5.00e+03	5.00e+03	-1.00e+04	1.00e+04	1.41e+04	2.25e+03

Table 6.1: Parameters of the poles & residues used for the validation of the multi-pole TDIBC.

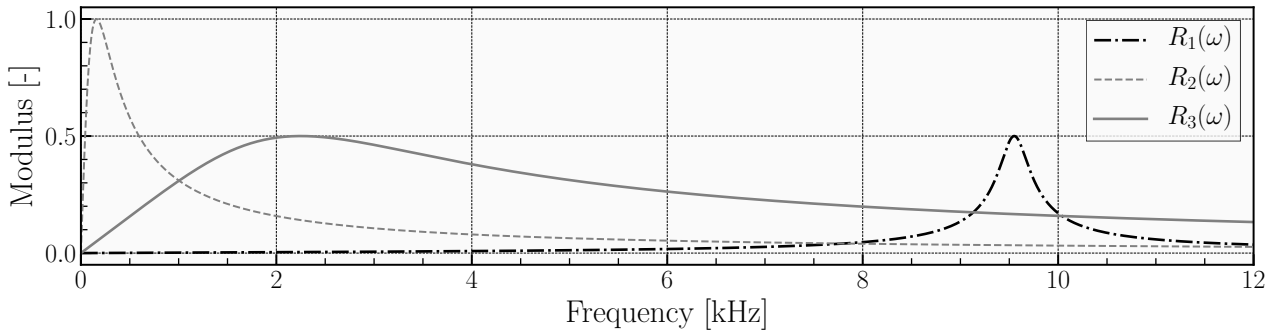
The details of the model are shown in Fig. 6.7 where each of the sub-systems's reflection coefficients is plotted. Figure 6.7(a) shows the modulus of R_1, R_2 and R_3 computed from Eq. 6.14 (page 103) using the parameters presented in Table 6.1. The properties of a single PBFs, presented in Sec. 6.2.2, can be observed on Fig. 6.7. For example, the resonant frequencies of each system (each PBF) can be seen at 160 Hz, 2.25 kHz and 9.55 kHz corresponding to $f_{0,2}$, $f_{0,3}$ and $f_{0,1}$, respectively. At these frequencies the phase is zero for each sub-system and the modulus (and the real part) is maximum.

The resulting broadband reflection coefficient $R_{\mathrm{BC}}(\omega)$ is given by the sum of the three PBFs and is shown in Fig. 6.8. Figure 6.8(a) shows the modulus of modeled reflection coefficient $R_{\mathrm{BC}}(\omega)$ and Fig. 6.8(b) its phase. The resulting broadband reflection coefficient could not be model by a single-pole single-residue model.

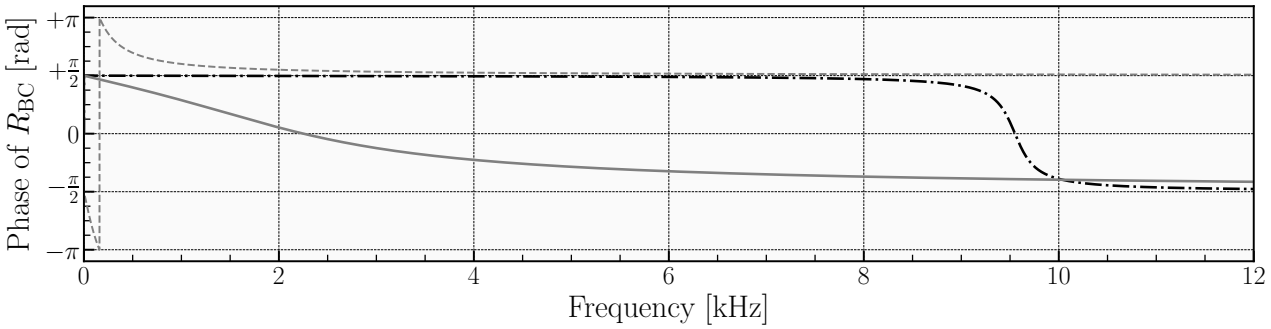
Results

The test case simulation used to validate the reflection coefficient based TDIBC for a single-pole model is used here. The reflection coefficient at the boundary condition located a $x = 1$ m is modeled by the three poles model (Table 6.1). The simulation is performed with AVBP using the same parameters than previously.

The results are shown in Fig. 6.9. The contributions I_1, I_2 and I_3 of each of the PBFs R_1, R_2 and R_3, respectively, to the ingoing wave A_n^{in} – the resulting ingoing wave imposed by the multi-pole TDIBC (black dashed line) – are shown.

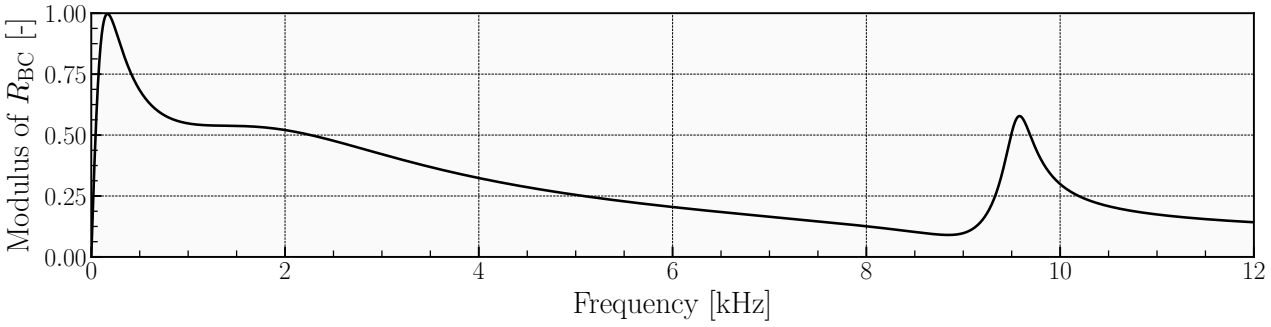


(a) Modulus of $R_{\mathrm{BC}}(\omega)$

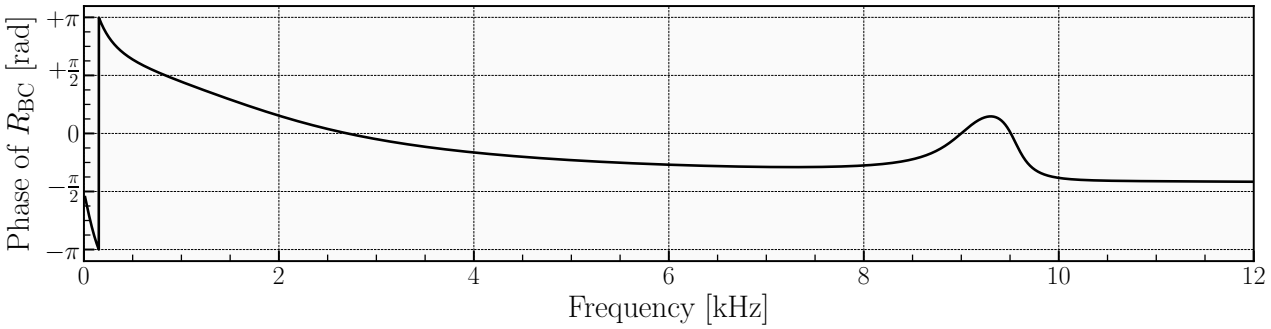


(b) Phase of $R_{\mathrm{BC}}(\omega)$

Figure 6.7: Modulus (a) and phase (b) of each sub-system $R_{\mathrm{k}}(\omega)$ in Table 6.1.



(a) Modulus of $R_{\mathrm{BC}}(\omega)$



(b) Phase of $R_{\mathrm{BC}}(\omega)$

Figure 6.8: Modulus (a) and phase (b) of the reflection coefficient $R_{\mathrm{BC}}(\omega)$ modeled by the boundary condition the three poles & residues presented in Table 6.1.

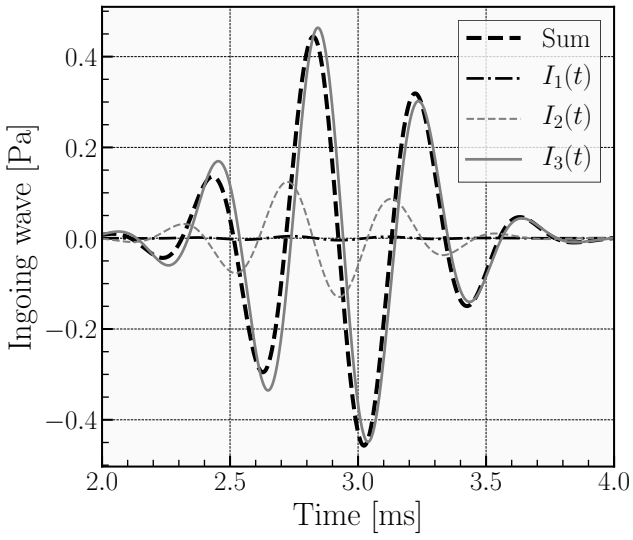


Figure 6.9: Output signal (I_k) from each sub-system R_k giving the global response, the ingoing wave A_n^{in}, of the multi-pole TDIBC (black dashed line).

I_1, I_2 and I_3 are not contributing to the ingoing wave at the same level and this behavior can be clarified by the frequency content of R_1, R_2 and R_3 (*c.f.* Fig. 6.7) on one hand and of the outgoing wave (*c.f.* Fig. 6.4) on the other hand:

1. The contribution I_1 to the ingoing wave is very small. This can be explained by the fact that the outgoing wave's frequency content is mainly contained in a frequency range between 1 kHz and 4 kHz (with a peak at 2.45 kHz, *c.f.* Fig. 6.4). On this frequency range, the modulus of R_1 is close to zero. As a consequence, the PBF R_1 only has a marginal impact on the imposed ingoing wave.

2. By performing the same analysis on R_2, the I_2 contribution can be explained. The modulus of R_2 is non-zero on the frequency range of interest and, hence, the contribution I_2 to the ingoing wave is significant.

3. Finally, contribution I_3 to the ingoing wave is predominant. This can be explained by the frequency content of R_3: the modulus is maximum on the frequency range of interest and the peak is located at the same frequency than the outgoing wave's peak (*c.f.* Fig. 6.4). On this frequency range the modulus of R_3 is higher than the modulus of R_2 and, thus, I_3 contributes more to the ingoing wave than I_2.

The ingoing wave $A_n^{\text{in}}(t)$ prescribed by the multi-pole TDIBC is compared to the analytical solution in Fig. 6.10. The procedure used to obtain the analytical solution in the single-pole model is used here: Eq. 6.20 is evaluated numerically. The multi-pole TDIBC is found to give exactly the same ingoing wave that the analytical solution and, similarly to the single-pole validation results:

1. The ingoing wave has a lower maximum amplitude than the initial wave (*cf.* Fig. 6.10) because the modulus of $R_{\text{BC}}(\omega)$ is strictly lower than unity for all frequencies.

2. The reflected wave (ingoing wave) is asymmetric even though the impinging wave (outgoing wave) is symmetric. This is due to the fact the $R_{\mathrm{BC}}(\omega)$ is complex and thus the phasing of the reflected wave is modified.

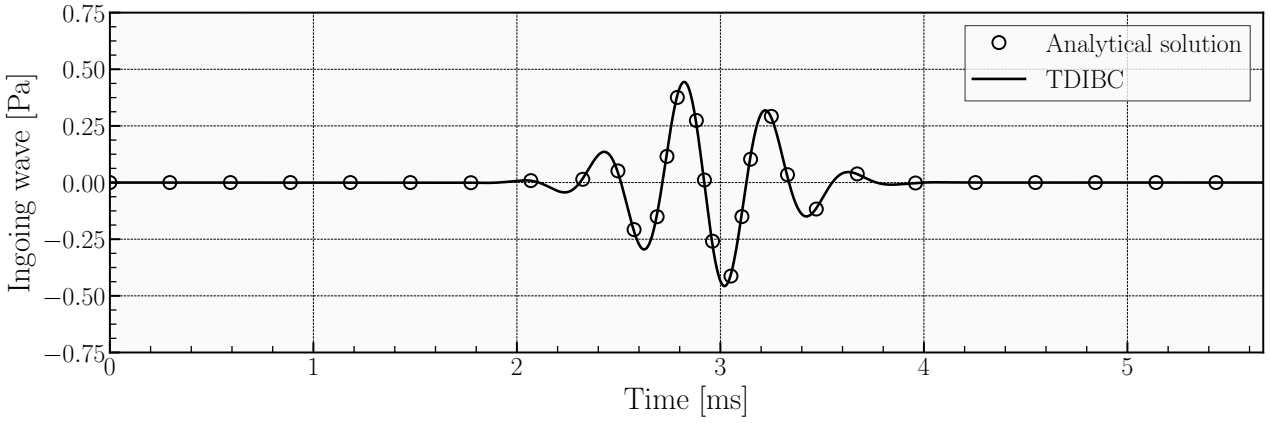


Figure 6.10: Ingoing wave prescribed by TDIBC compared to the analytical solution.

6.4 Conclusion

The need for Time Domain Impedance Boundary Conditions (TDIBC) was discussed and the concept necessary to understand Fung and Ju's methodology was presented. Lin *et al.* [86] extended the Fung and Ju's TDIBC [83, 84] framework and their method was derived.

Building upon these methods, a novel formulation of TDIBC, based on the reflection coefficient instead of the wall softness coefficient, was derived. In comparison to the wall softness TDIBC, the reflection coefficient based TDIBC is more suited for open-end-like acoustic boundaries as the high frequency behavior of the model is inherently correct. Another benefit of this formulation is that it is well suited for modeling a reflection coefficient corresponding to the imposition of a pure time-delay in the time domain: this will be the topic of the next chapter.

The reflection coefficient TDIBC was then validated for both single-pole model (as proposed by Fung and Ju [83, 84] and Scalo *et al.* [85]) and for a multi-pole model (as proposed by Lin *et al.* [86]).

Chapter 7

Delayed-time domain impedance boundary condition

A major benefit of impedance modeling is that it allows to truncate large portions of the computational domain. This is possible as inviscid planar acoustic wave propagation can be reproduced by imposing a so called *time-delayed reflection coefficient*. This property allows: (1) a gain of computational resources, (2) to study several geometries using the same computational domain along with D-TDIBC models. This chapter focusses on the imposition of time-delayed reflection using the formulation of TDIBC presented in Sec. 6.2.2.

Section 7.1 will present the definition of delayed reflection. Section 7.2 will introduce the fitting technique necessary to model a delayed reflection coefficient. In Sec. 7.3, D-TDIBC will be used to impose a time-delay in a 1D wave propagation test case. Finally, in Sec. 7.4 a thermoacoustically unstable combustion chamber is studied via a 2D DNS, while using a reduced domain along with D-TDIBC to model the truncated portion.

7.1 Time-delayed reflection coefficient

In many simulations of industrial systems, longitudinal acoustic waves propagate over large portions of the computational domain (*e.g.* in the exhaust pipe of a car engine, in the chimney on an industrial furnace or, in general, for ducts of both constant section and speed of sound). In such configurations the computational domain can be truncated of the portions corresponding to longitudinal acoustics and replaced by a model.

Figure 7.1 shows a system in which the portion from x_1 to x_2 is truncated (grey area). In this computational setup, the boundary condition located in $x = x_1$ must account for the acoustic properties of the truncated domain. This is possible if the boundary condition at $x = x_1$ imposes a *time-delay*, *i.e.* in the time domain, to the wave reflection [9**?**]: the resulting reflection coefficient is called *delayed reflection coefficient*, *i.e.* in the frequency domain. The delayed reflection coefficient R_τ is:

$$R_\tau = R(\omega)e^{-i\omega\tau} \qquad ; \qquad \tau = 2(x_2 - x_1)/c_0 \tag{7.1}$$

where τ is the time-delay (acoustic time for a wave to propagate back and forth over the distance $x_2 - x_1$ at a mean speed of sound c_0) and $i = \sqrt{-1}$ is the imaginary unit.

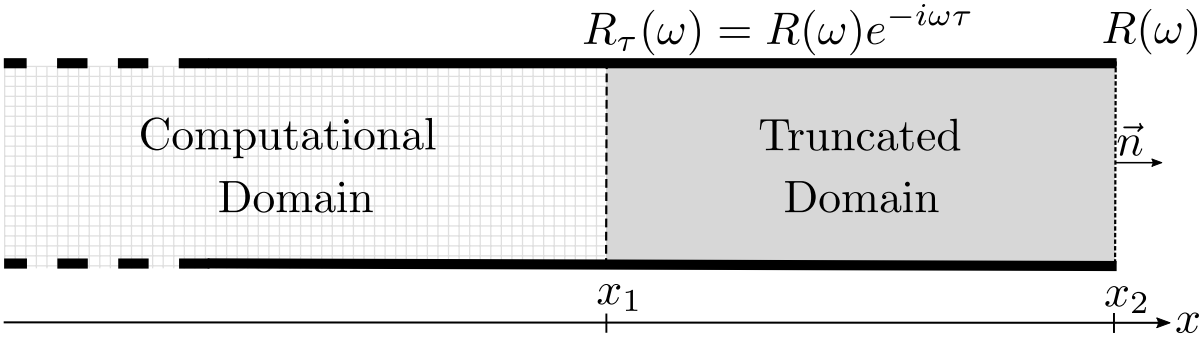


Figure 7.1: Typical case where the computational domain can be cut at $x = x_1$. The propagation of acoustic waves in the truncated portion (between x_1 and x_2) is accounted for by the reflection coefficient R_τ (Eq. 7.1).

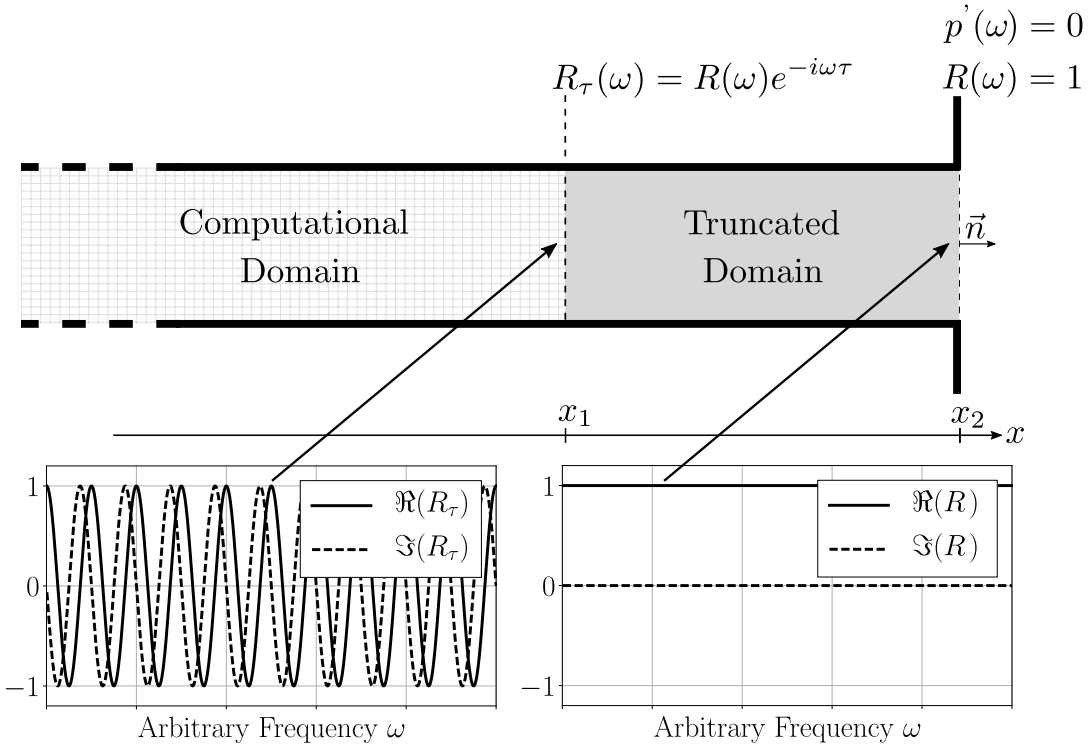
Figure 7.2 illustrates the impact of an arbitrary time-delay τ on two classical limit cases: the flanged open end, *i.e.* $p(\omega) = 0$, (*cf.* Fig. 7.2(a)) and the closed end, *i.e.* $u(\omega) = 0$, (*cf.* Fig. 7.2(b)). These cases have real reflection coefficients $R(\omega)$ at the acoustic boundary located in $x = x_2$. For all frequencies ω, the flanged open end corresponds to a reflection coefficient of $R(\omega) = 1$ and the closed end to $R(\omega) = -1$ (*c.f.* bottom right figures in Figs 7.2(a) and 7.2(b)). The delayed reflection coefficient $R_\tau(\omega)$ becomes complex-valued and frequency-dependent even though $R(\omega)$ is real and constant (*c.f.* bottom left figures in Figs 7.2(a) and 7.2(b)).

The methodology proposed by Fung and Ju [83, 84] is used to create a TDIBC formulation based on the reflection coefficient (*c.f.* Sec. 6.2.2). It relies on the determination of the poles and zeros of the reflection coefficient. The complex exponential $e^{-i\omega\tau}$ introduced by the time-delay (*c.f.* Eq. 7.1 and Fig. 7.2) has many poles and zeros and is, hence, challenging to model using Fung and Ju's methodology. The main objective of this paper is to propose and validate a methodology, called Delayed-Time Domain Impedance Boundary Condition (D-TDIBC), to model any delayed reflection coefficient under Fung and Ju's formalism.

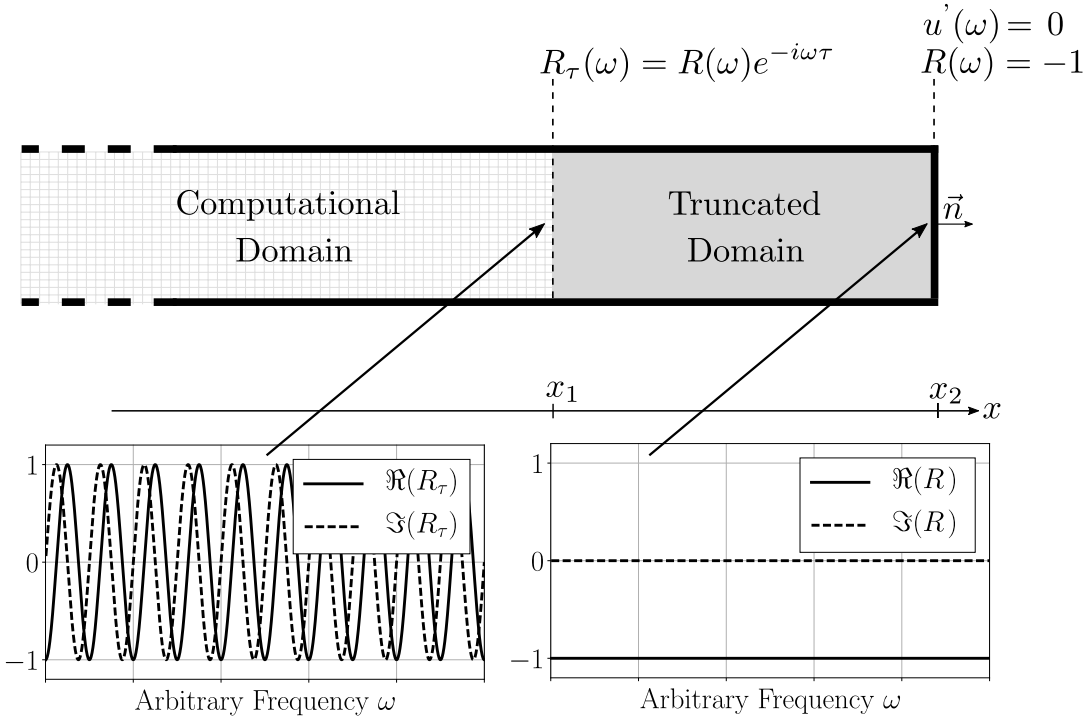
Here we focus on the reflection coefficient R as a modeling quantity even though the methodology proposed in Sec. 7.2 is generic and could apply for wall softness S.

7.2 Methodology

As discussed in Sec. 6.2.2, in order to impose the reflection coefficient $R(\omega)$ we need to determine the set of poles & residues $(p_k,\ \mu_k)$. There is no evidence of the uniqueness of the solution for a set of $(\mu_k,\ p_k)$. We propose here a method to determine the poles & residues



(a) Flanged open end: $p'(\omega) = 0$



(b) Closed end: $u'(\omega) = 0$

Figure 7.2: Acoustic variables for two theoretical limit cases: (a) the flanged open end, and (b) the closed end (hard wall) cases. Both configurations are fully reflective and have a purely real reflection coefficient R at all frequencies in $x = x_2$. The truncation of the grey areas can be modeled by the imposition of a time-delay τ. The delayed reflection coefficient R_τ, expressed in $x = x_1$, is complex. At the bottom of the figure both real (solid lines) and imaginary parts (dashed lines) of R_τ and R are shown on the left and right-hand sides, respectively.

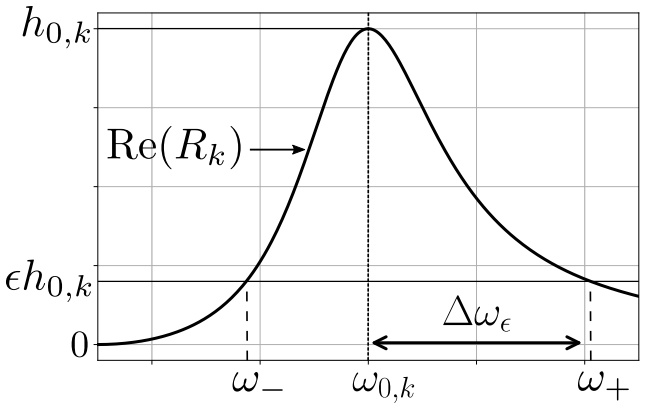


Figure 7.3: Real part of a typical PBF R_k (Eq. 7.3). Three properties are visualized: $\omega_{0,k}$, $h_{0,k}$ and $\Delta\omega_\epsilon$. At the resonant angular frequency $\omega_{0,k}$, the real part of R_k is maximum. The peak heigh $h_{0,k}$ is the value of $R_k(\omega)$ at $\omega = \omega_{0,k}$. For a given percentage ϵ ($\epsilon \in [0,\ 1]$), the half-width $\Delta\omega_\epsilon$ is defined on the right-hand side. ω_- and ω_+ are the solutions of the equation $\Re\left(R_k\right) = \epsilon$ and are used to define the width.

that is viable when modeling delayed reflection coefficients (Eq. 7.1). It is a tedious task as the delayed reflection coefficient $R_\tau(\omega)$ has many zeros introduced by the complex exponential $e^{-i\omega\tau}$. The method consists in an iterative least-square fit. At each iteration a rational fraction is added to the model until the model reflection coefficient $R_{\mathrm{BC}}(\omega)$ converges to the desired reflection coefficient $R(\omega)$.

In order to develop this fitting method, we will first describe the properties of the rational fractions in Eq. 6.14.

7.2.1 Pole Base Function properties

The reflection coefficient of the boundary condition $R_{\mathrm{BC}}(\omega, n_0)$ is a sum of n_0 rational fractions, called the Pole Base Functions (PBF), denoted R_k:

$$R_{\mathrm{BC}}(\omega, n_0) = \sum_{k=1}^{n_0} R_k(\omega) = \sum_{k=1}^{n_0} \underbrace{\left[\frac{\mu_k}{i\omega - p_k} + \frac{\mu_k^*}{i\omega - p_k^*}\right]}_{\text{Pole Base Function}} \tag{7.2}$$

Equation 7.2 can be recast by expressing the poles & residues in their algebraic forms, *i.e.* as $\mu_k = a_k + ib_k$ and $p_k = c_k + id_k$ with $a_k, b_k, c_k, d_k \in \mathbb{R}$. For each R_k, the causality constraint requires that $c_k < 0$. Lin *et al.* [86] demonstrated that a physical behavior of the boundary conditions in the low-frequency limit requires $b_k = -a_k c_k / d_k$, leading to:

$$R_k(\omega) = \frac{2a_k i\omega}{-\omega^2 - 2c_k i\omega + (c_k^2 + d_k^2)} \tag{7.3}$$

There are three degrees of freedom in Eq. 7.3, namely a_k, c_k and d_k. The objective of this section is to link these degrees of freedom to the properties of a PBF. A typical PBF is presented in Fig. 7.3 where three properties of the PBF can be identified: $\omega_{0,k}$, $h_{0,k}$ and $\Delta\omega_\epsilon$.

$\omega_{0,k}$ is the frequency where the real part of R_k is maximum: it is referred as the *resonant frequency*. $h_{0,k}$ is the peak height, that is, the value of $R_k(\omega)$ at $\omega = \omega_{0,k}$. The last property shown in Fig. 7.3 is the half-width $\Delta\omega_\epsilon$ defined for a given percentage ϵ of $h_{0,k}$ ($\epsilon \in [0,\ 1]$). Because the PBF is not symmetric, at a given percentage ϵ, two half-widths $\Delta\omega_\epsilon$ can be defined: one on the left hand side (using ω_-) and one on the right-hand side (using ω_+). A choice is made to consider only the right half-width shown in Fig. 7.3, hence overestimating the width.

One can show that [85, 86]:

$$\omega_{0,k}^2 = c_k^2 + d_k^2 \tag{7.4}$$

Equation 7.4 gives a first constraint, say on d_k. Substituting Eq. 7.4 into Eq. 7.3 and evaluating the resulting equation at $\omega = \omega_{0,k}$ yields:

$$R_k(\omega_{0,k}) = h_{0,k} = -\frac{a_k}{c_k} \tag{7.5}$$

Using the constraints in Eqs. 7.4 and 7.5, R_k becomes:

$$R_k(\omega) = \frac{2h_{0,k}c_k i\omega}{\omega^2 + 2c_k i\omega - \omega_{0,k}^2} \tag{7.6}$$

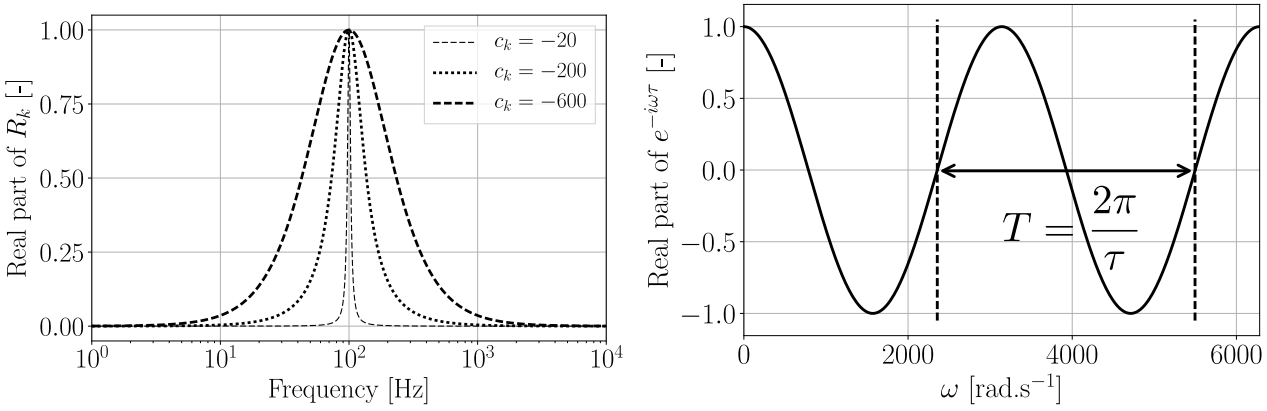
In Eq. 7.6, c_k is the only remaining degree of freedom. Figure 7.4(a) illustrates its effect on the width of a PBF R_k for a peak height $h_{0,k} = 1$ at the resonant frequency $f_{0,k} = \omega_{0,k}/2\pi = 100$ Hz. In the case of a pure delay the width is known: $R(\omega)$ is a periodic function of period $T = 2\pi/\tau$ (*cf.* Fig. 7.4(b)). As shown in Fig. 7.4(a), the real part of R_k goes to zeros for $\omega << \omega_{0,k}$ and $\omega >> \omega_{0,k}$. A consequence of this property is that a single PBF can fit a single peak between two consecutive zeros. For the pure delay the frequency range between two consecutive zeros is $T/2$. To adjust the width to the pure delay case, we need to find the value of c_k for a given ϵ such that:

$$\Re\left[R_k\left(\omega_{0,k} + \frac{T}{4}\right)\right] = \Re\left[R_k\left(\omega_{0,k} + \frac{\pi}{2\tau}\right)\right] = \epsilon \tag{7.7}$$

where $\Re(\cdot)$ and $\Im(\cdot)$ are the real and imaginary parts, respectively. Solving for c_k in Eq. 7.7, we obtain the criterion for a given time-delay τ:

$$c_k(\epsilon, \omega_{0,k}) = \frac{\tau\omega_{0,k} + \frac{\pi}{4}}{2\pi\omega_{0,k} + \tau}\sqrt{\frac{\epsilon}{1-\epsilon}} \tag{7.8}$$

Equations 7.4, 7.5 and 7.8 give constraints allowing to control the height and the width of a PBF for any resonant angular frequency $\omega_{0,k}$. These constraints are used in the algorithm allowing the determination of the set of poles & residues (p_k, μ_k) presented in the next section.



(a) (b)

Figure 7.4: (a) Influence of the c_k parameters for $f_{0,k} = \frac{1}{2\pi}\omega_{0,k} = 100$ Hz and $h_{0,k} = 1$. (b) Real part of a purely delayed reflection coefficient R_τ for a time-delay τ. The real part is a periodic function (cosine) of period $T = \frac{2\pi}{\tau}$.

7.2.2 Iterative multi-pole modeling technique

Now that the properties of a single PBF are known, it is possible to go back to Eq. 7.2 where a sum of n_0 PBFs are used to match a reflection coefficient $R(\omega)$. In the case of pure delay, it is a tedious task as the complex exponential function, introduced by the time-delay (*cf.* Eq. 7.1), has a large number of zeros. To tackle this issue an iterative fitting technique has been devised.

The least-square fit algorithm is used to minimize the distance of the target function $R(\omega)$ to the fit function $R_{\mathrm{BC}}(\omega)$ (Eq. 7.3) on both real and imaginary parts. The global least-square residual ξ is defined as the sum of the squared distance between $R(\omega)$ and $R_{\mathrm{BC}}(\omega)$:

$$\xi = \xi_R + \xi_I \tag{7.9}$$

where ξ_R and ξ_I are the least-square residuals on the real and imaginary parts, respectively. They are defined as the squared sum of the point-to-point oriented distance, E_R and E_I, between $R(\omega)$ and $R_{\mathrm{BC}}(\omega)$:

$$\xi_R = \sum_{i=1}^{m} E_R^2(\omega_i) = \sum_{i=1}^{m} \Re\left[R(\omega_i) - R_{\mathrm{BC}}(\omega_i)\right]^2 \tag{7.10}$$

$$\xi_I = \sum_{i=1}^{m} E_I^2(\omega_i) = \sum_{i=1}^{m} \Im\left[R(\omega_i) - R_{\mathrm{BC}}(\omega_i)\right]^2 \tag{7.11}$$

where m is the number of discrete values considered in the frequency array, i is the index of the points, $R(\omega_i)$ is the value of the target reflection coefficient at the ith point of the discrete angular frequency array ω_i and $R_{\mathrm{BC}}(\omega_i)$ is the value of the fit function at point i.

The fitting procedure is presented in the Algorithm 1. It starts with only one term: $n = 1$ in Eq. 7.2 (line 1 in the Algorithm 1). The conditional loop iterates until the number of PBF

n reaches the final value $n = n_0$. In line 3, we seek for the frequency where the error on the real part is maximum. The resonant frequency of R_n is then set to this frequency (line 4) and its peak height $h_{0,n}$ is chosen to cancel the error on the real part at that point (line 5). The c_n parameter is initialized using $\epsilon = 1\%$ in Eq. 7.8. Equations 7.4 and 7.5 are used to determine the values of d_n and a_n (line 7 and 8). Finally, the pole & residue (p_n, μ_n) of the nth PBF are initialized (lines 9 and 10). The optimization stage (line 11) minimizes the least-square residual ξ (*cf.* Eq. 7.9) and all of the values of the parameters p_k and μ_k are optimized for $k \in [1; n]$. Finally, the order of the model n is incremented so that an additional PBF can be added (line 12).

An example of iterative fit is presented in Sec. 7.3.2 where the model $R_{\mathrm{BC}}(\omega)$ is shown at several iterations of the Algorithm 1.

Algorithm 1: Preprocessing for D-TDIBC: find (p_k, μ_k) in Eq. 7.2 to model the target function $R(\omega)$

Input : n_0, ω_i, $R(\omega_i)$, τ
Output: (p_k, μ_k) for $k \in [1, n_0]$

1 $n \leftarrow 1$
2 **while** $n < n_0$ **do**
3 Find $\omega_{\max}$ such that the error on the real part is maximum $\equiv \{\omega_{\max} \mid \forall \omega_i : E_R(\omega_i) \leq E_R(\omega_{\max})\}$
4 Set $\omega_{0,n} = \omega_{\max}$ using Eq. 7.4
5 Set the resonant peak height to cancel the error on the real part $h_{0,n} = E_R(\omega_{\max})$ using Eq. 7.5
6 Set the parameter c_n using Eq. 7.8
7 Set the parameter d_n using Eq. 7.4
8 Set the parameter a_n using Eq. 7.5
9 $\mu_n \leftarrow a_n + i(-a_n c_n / d_n)$
10 $p_n \leftarrow c_n + i d_n$
11 Least-square fit: modify the values of p_k and μ_k for $k \in [1, n]$ to minimize ξ (*cf.* Eq. 7.9)
12 $n \leftarrow n + 1$
13 **end**

7.3 Validation for one-dimensional waves

Section 6.2.2 has provided the modeling methodology necessary to account for acoustic delays. In this section, the objective is twofold: (1) to demonstrate the applicability of the modeling procedure on a limit case: the delayed pure reflection, (2) to validate the ability of TDIBC to impose a time-delay to account for acoustic wave propagation in the truncated portion of the domain. In Sec. 7.3.1 we present the one-dimensional numerical setup used for validation. The methodology proposed in Sec. 7.2 will be used to model a reflection coefficient corresponding to a pure delay. In Sec. 7.3.3 a time domain simulation is used to demonstrate that D-TDIBC imposes the correct time-delay τ, wave amplitude and phase.

7.3.1 Test case presentation

The aim of the simulation is to study the propagation of a Gaussian acoustic wave in the domain Ω defined on $x \in [-1, 1.75]$ m (*cf.* Fig. 7.5(a)). The mean speed of sound is $c_0 = 350\ \mathrm{m\,s^{-1}}$. This perturbation will propagate on the positive x direction. The physical domain is split into two sub-domains: $\Omega = \Omega_c + \Omega_m$. The computational domain Ω_c is $x \in [-1, 1]$ m and the modeled domain Ω_m is $x \in [1, 1.75]$ m (gray area in Fig. 7.5(a)). The D-TDIBC is used to model the wave propagation in Ω_m. At the left boundary condition ($x = x_l = -1$ m) the reflection coefficient is $R_l = 1$ and at the right boundary condition ($x = x_r = 1.75$ m) the reflection coefficient is $R_r = -1$. In the computational domain, the reflection coefficient at $x = 1$ m accounting for R_r has to be modeled by a time-delay (*cf.* Sec. 7.1) leading to $R_r|_{x=1\ \mathrm{m}} = -e^{-i\omega\tau}$. The time-delay corresponding to this modeled domain is $\tau = 2(x_r - x_{\mathrm{BC}})/c_0 = 4.28$ ms. The acoustic time for the initial wave located in x_0 to travel back at its initial position is $T = 2(x_r - x_0)/c_0 = 10.0$ ms.

7.3.2 Delayed reflection coefficient modeling

To impose a pure time-delay, the D-TDIBC method first requires to build a model for the delayed reflection coefficient using the Algorithm 1 (*cf.* Sec. 7.2). In theory, the delayed reflection coefficient $R_r|_{x=1\ \mathrm{m}} = -e^{-i\omega\tau}$ must be modeled up to infinite frequencies. In practice it is not feasible as it would require an infinite number of PBFs. In numerous applications the frequencies of interest are limited to a given range (*cf.* Fig. 7.5(b)) and it is sufficient to model $R(\omega)$ below a cutoff frequency f_{c}. For $f > f_{\mathrm{c}}$, a non-reflecting boundary condition is used. For example, for the setup presented in Fig. 7.5(a), the frequency content of the initial Gaussian wave is below 1 kHz so that the chosen cutoff frequency is $f_{\mathrm{c}} = 1$ kHz. A low-pass filter is applied to the theoretical delayed reflection by multiplying the delayed reflection coefficient by an envelope function ψ allowing a smooth transition from 1 to 0 over a frequency range:

$$\psi(f) = \frac{1}{2}\left[1 - \tanh\left(\frac{f - f_{\mathrm{c}}}{\delta}\right)\right] \tag{7.12}$$

where f is the frequency and δ is a constant that specifies the frequency range of the transition from 1 to 0 (*cf.* Fig. 7.5(b)). The envelop function ψ keeps the phase of the delayed reflection coefficient unchanged. The target function to be modeled is then:

$$R(\omega) = \psi(f) \times R_r|_{x=1 \text{ m}} \tag{7.13}$$

Figure 7.6 shows the model at iterations 1, 2, 5 and 20 of the Iterative Multi-Pole Modeling Technique (Algorithm 1). $R(\omega)$ is the filtered delayed reflection coefficient shown in Fig. 7.5(b) and $R_{\text{BC}}\omega)$ is the reflection coefficient model at a given iteration defined in Eq. 6.14. Their real and imaginary parts are shown in the top and bottom plots, respectively. At each iteration the method finds the biggest point-to-point oriented distance between the real parts (Eq. 7.10) of $R(\omega)$ and $R_{\text{BC}}\omega)$. Figure 7.6(a) shows the model at the end of the first iteration. The initial solution of $R_{\text{BC}}(\omega)$ targets the first peak in the real part where $\Re(R(\omega)) = 1$. In Fig. 7.6(b), the targeted peak is where $\Re(R(\omega)) = -1$. At an iteration i, initial guesses for p_i and μ_i are found to target a single peak at the time. Figure 7.6 illustrates how the fit propagates from low to high frequencies. The algorithm is considered converged after 20 iterations as the maximum point-to-point error on the modulus is below 1%, where we define the error as $E = \max\left(|R(\omega) - R_{\text{BC}}(\omega,\ n_0 = 20)| \right)$. The D-TDIBC model used here is, thus, made of 20 poles & residues (p_k, μ_k), *i.e.* only 40 complex constants.

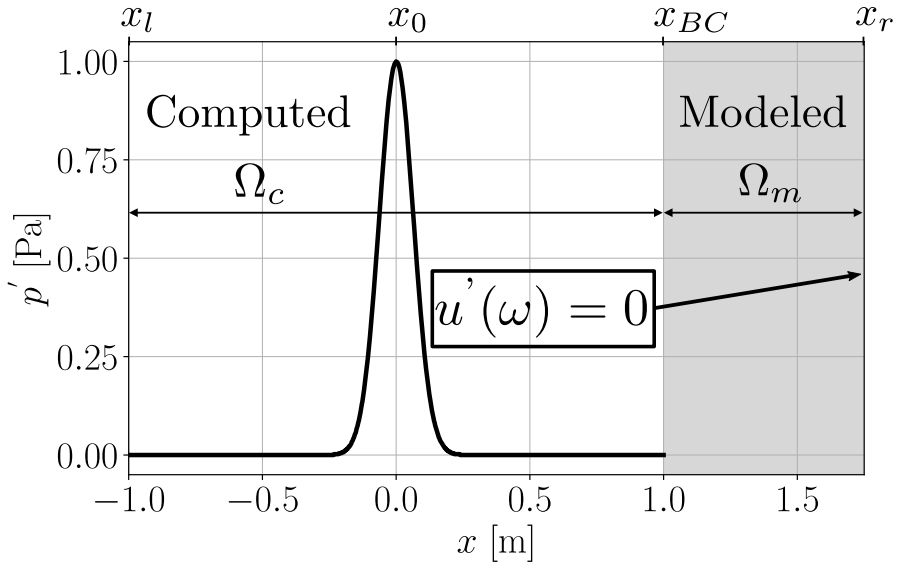
7.3.3 One-dimensional wave propagation

In this section, the behavior of the D-TDIBC is investigated first on a basic one-dimensional wave propagation problem. Then the time domain response of each PBF is inspected to highlight the mechanism of D-TDIBC.

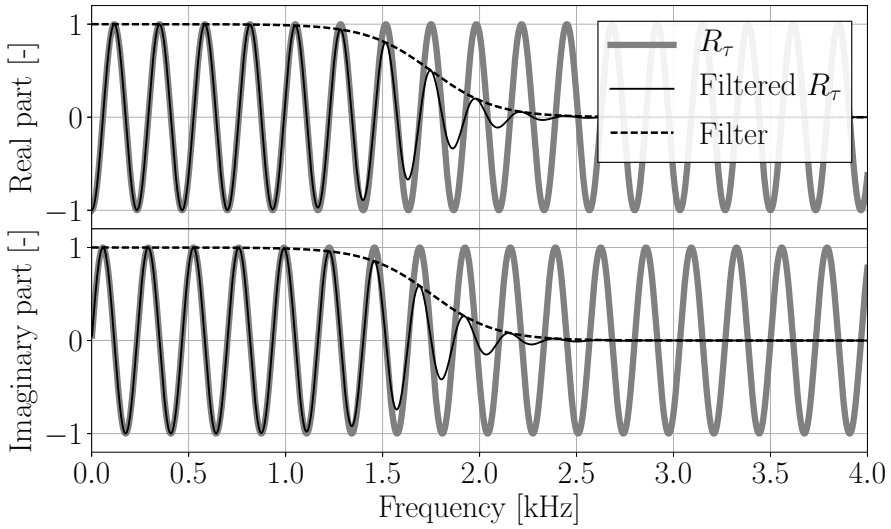
The one-dimensional wave propagation is computed using the AVBP solver. AVBP is a three-dimensional fully compressible Navier-Stokes equation solver. A two-step Taylor-Galerkin scheme, called TTGC is used. TTGC is third-order accurate in space and time [134, 135]. Characteristics boundary conditions (NSCBC) are used [114, 115, 176, 183]. In the NSCBC framework, the characteristic waves are evaluated at the boundaries. TDIBC prescribes the ingoing characteristic wave from the outgoing characteristic wave and is, thus, consistent with the NSCBC formalism.

As the reflection coefficient modeled in x_r is $R_r = -1$, the wave is *a priori* expected to be fully reflected: the amplitude of the reflected wave must be equal to the one of the incident wave. As R_r is real-valued, the reflected wave is expected to be centered in $x = 0$ m after a time $t = T$ (*cf.* Sec. 7.3.1).

Figure 7.7 illustrates the propagation of the pressure wave from time $t = 0$ up to $t = T$. At $t = 0$ the pressure field corresponds to the initial solution shown in Fig. 7.5(a). At $t = 0.25T$ the wave has propagated in the positive x direction and is crossing the boundary condition

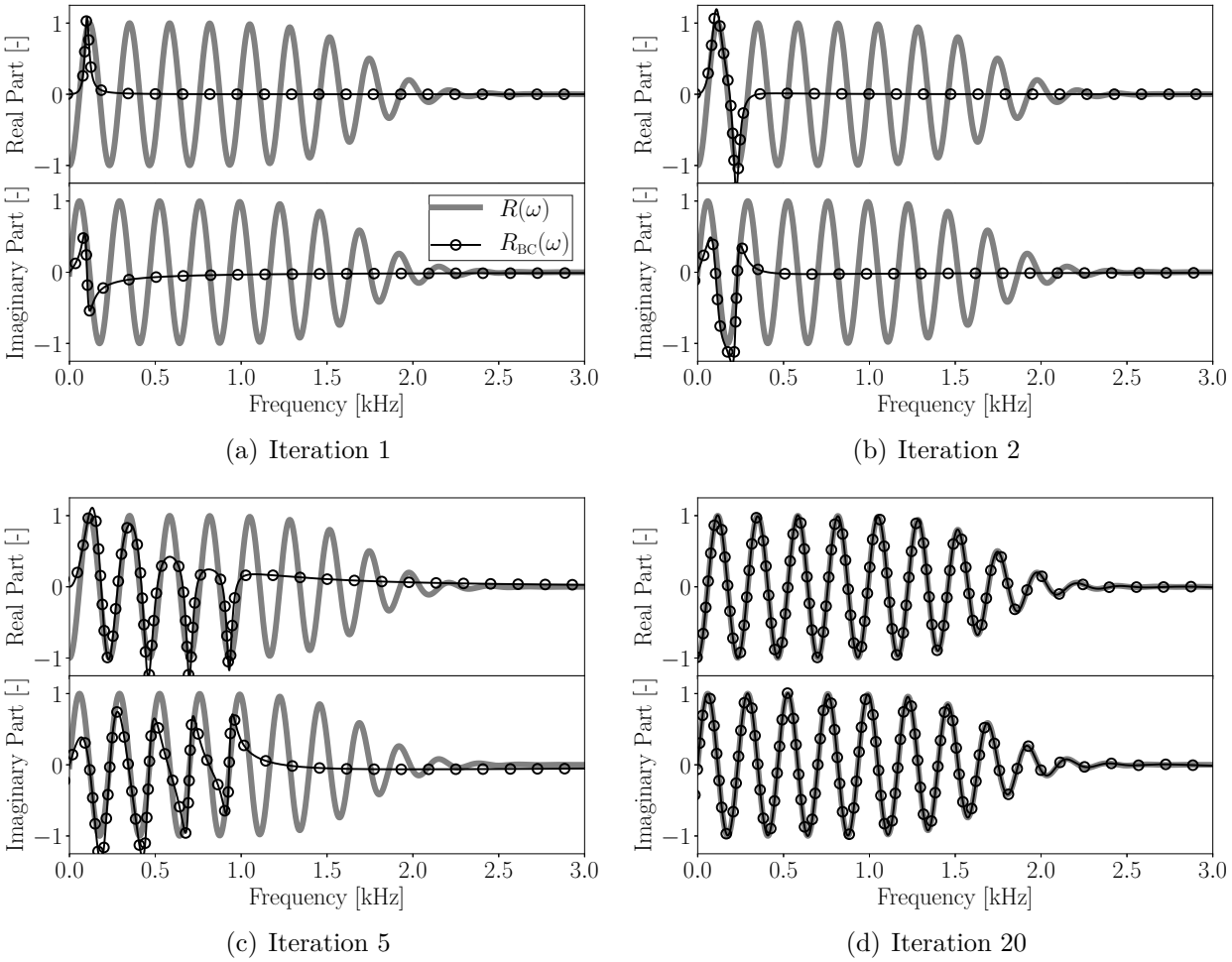


(a)



(b)

Figure 7.5: (a) Initial solution and visualization of the computational (Ω_c) and modeled (Ω_m) domains. (b) Theoretical (gray solid line) and filtered (black solid line) delayed reflection coefficients. The filter shape (Eq. 7.12) is shown (black dashed line).



(a) Iteration 1

(b) Iteration 2

(c) Iteration 5

(d) Iteration 20

Figure 7.6: Reflection coefficient $R_{\mathrm{BC}}(\omega)$ modeled by the Iterative Multi-Pole Modeling Technique algorithm (Algorithm 1 in Sec. 7.2.2) a several iterations. An accurate model is obtained for $n_0 = 20$, where n_0 is the number of PBF R_k as in Eq. 7.2.

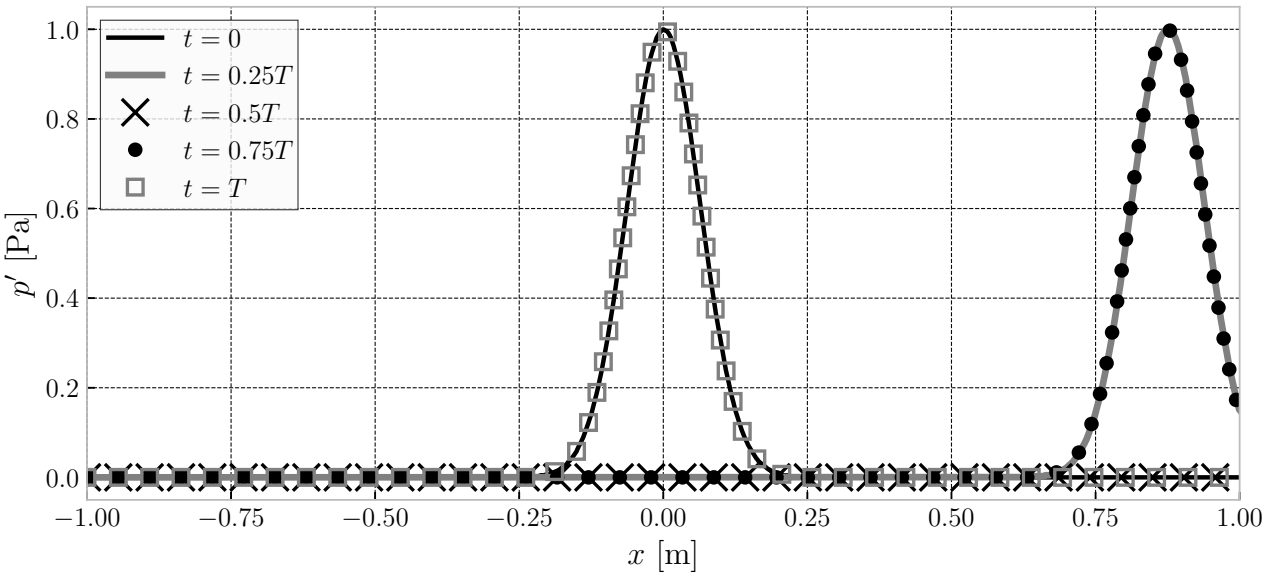


Figure 7.7: Propagation and reflection of a Gaussian pressure wave in the domain $\Omega_c + \Omega_m$ by simulating only Ω_c. The acoustic properties of Ω_m are imposed using D-TDIBC.

at $x = x_{\text{BC}} = 1$ m. At $t = 0.5T$ the pressure wave has completely left the computational domain. This result is expected: at time $t = 0.5T$ the wave is propagating inside the modeled domain Ω_m, *i.e.* the truncated portion (gray area in Fig. 7.5(a)). If one were to compute the complete domain, at $t = 0.5T$ the acoustic pressure $p'(x)$ would be zero for $x \in [-1, 1]$ m. At $t = 0.75T$ the pressure wave is re-injected in the computational domain by the boundary condition. The reflected pressure wave has the same amplitude than the incident wave (1 Pa) as expected. At $t = T$ the reflected Gaussian wave is centered at $x = 0$ m which means that the time-delay is precisely prescribed by D-TDIBC.

The acoustic pressure and velocity at the boundary are recorded at the boundary condition at $x_{\text{BC}} = 1$ m during the simulation. The results are shown in Fig. 7.8(a). Additionally, the acoustic energy E_a contained in the domain is shown. For the sake of clarity, each variable is normalized by its maximum. At first no acoustic activity is seen as the wave propagates inside the domain, the acoustic energy is maximum.

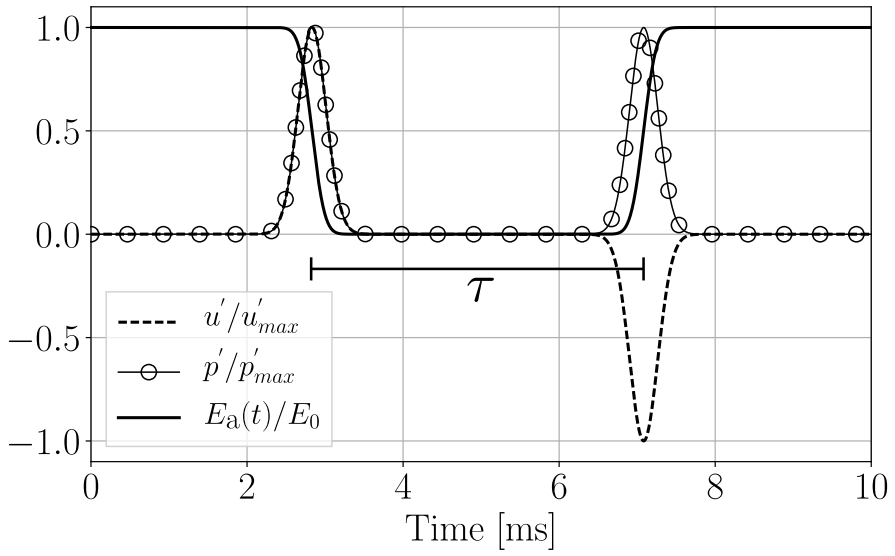
The acoustic pressure p' at the boundary in Fig. 7.8(a) is consistent with the results in Fig. 7.7. At first no acoustic pressure is seen by the boundary until the Gaussian wave crosses the boundary at $t \simeq 0.25T \simeq 2.5$ ms. After the wave has crossed the boundary, the acoustic pressure returns to zero. After the time-delay τ (*cf.* Fig. 7.8(a)) at $t \simeq 0.75T \simeq 7.5$ ms the reflected wave is re-entering the computational domain with the same amplitude as the incident wave. Finally the acoustic pressure p' returns to zero. The amplitude of the reflected acoustic velocity u' ($t \simeq 0.75T \simeq 7.5$ ms) is also the same as the incident wave ($t \simeq 0.25T \simeq 2.5$ ms) although the sign is changed: u' is negative. This indicates that the wave is traveling in the negative x direction after the reflection at $x_r = 1.75$ m. This result is consistent with the imposition of a reflection coefficient $R_r = -1$ in x_r. When the wave crosses the boundary

the acoustic energy initially contained in the domain is lost due to the acoustic flux at the boundary condition in x_{BC}. The acoustic energy contained in the domain retrieves its initial value when the reflected wave re-enters the domain. This stresses the fact that D-TDIBC conserves the acoustic energy while imposing a time-delay.

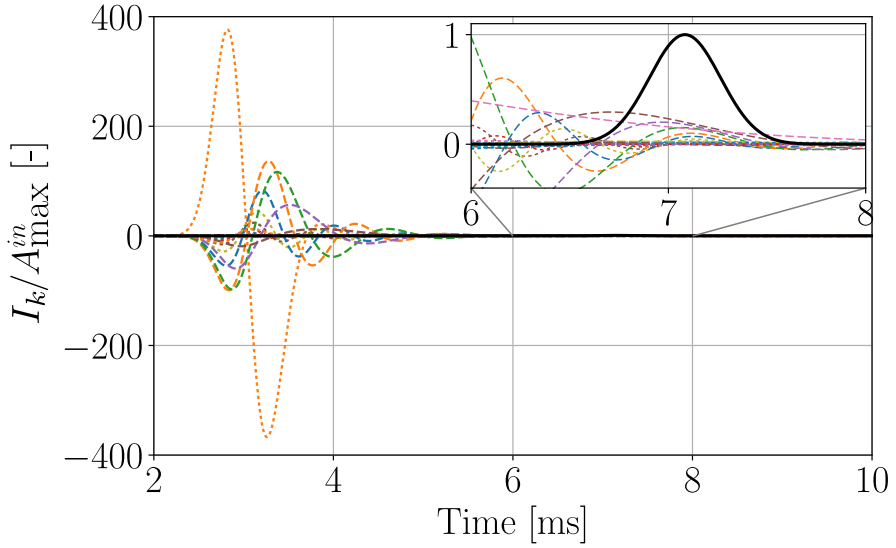
In their work, Jaensch *et al.* [190] solve a similar problem: they impose a pure time-delay at a boundary condition with a one-dimensional incident Gaussian wave. As discussed in Sec. 6.1, their method uses a first order upwind numerical scheme to discretize the one-dimensional LEE over the truncated domain. Their method is, thus, inherently dissipative and the dissipation decreases linearly with the cell size of the spatial discretization[1]. In order to achieve a dissipation level comparable to the one obtained here, it was necessary to use 1000 points. As a consequence, in the state-space model used, the state matrix is of dimension 2000×2000, *i.e.* 4 million scalar values. D-TDIBC seems to yield comparable results for a lower memory storage requirement as only 40 complex constants were used to model the delayed reflection coefficient.

Figure 7.8(b) illustrates the contribution I_k of each PBF R_k (scaled by the maximum amplitude of the resulting ingoing wave $A^{\mathrm{in}}_{\mathrm{max}} = \max(A^{\mathrm{in}}_n(t)) = 1$ Pa). The ingoing wave $A^{\mathrm{in}}_n(t)$ imposed by D-TDIBC is the sum of all the I_k. Before $t \simeq 7$ ms the ingoing wave is null: the PBFs are canceling each other out. At $t \simeq 7$ ms this canceling effect stops and the individual contributions of the PBFs add up to create the re-entering characteristic wave. This stresses how the modeling procedure of $R(\omega)$ is critical for an accurate prediction of acoustic delays as the canceling effect is due to a complex interaction with each of the PBFs R_k of the model.

[1]The numerical scheme used in their study is first order accurate in space and time. Other formulations with higher spatial and temporal order schemes are possible.



(a)



(b)

Figure 7.8: (a) Acoustic velocity (dashed line) and pressure (solid line with circles) at the boundary condition. (b) Temporal response of 20 PBF (dashed and dotted lines) and of the ingoing wave imposed by the D-TDIBC (black solid line)

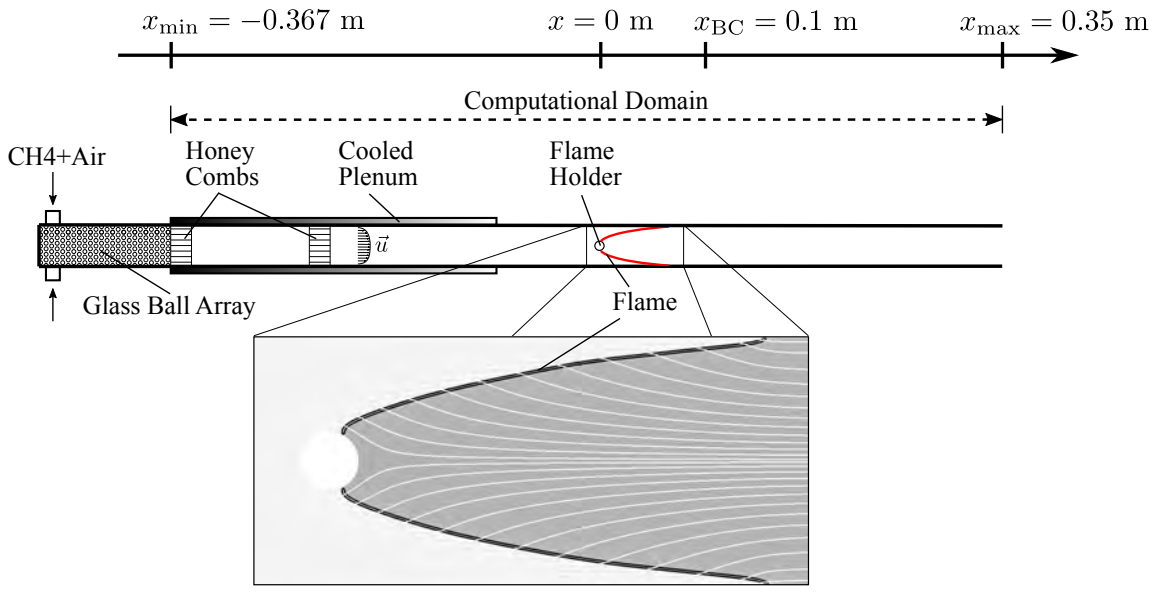


Figure 7.9: Sketch of a transverse cut of the INTRIG Burner (top). The computational domain of the FULL configuration goes from the glass balls array ($x = -0.367$ m) to the exhaust ($x = 0.35$ m) while it is cut (at $x = x_{\mathrm{BC}} = 0.1$ m) in the TRUNCATED configuration. A zoom (bottom) of the flame region of the initial solution used in DNS is shown. The light grey and dark grey regions represent the zero and high CO_2 mass fraction levels. The streamlines are plotted in white.

7.4 Validation for a combustion chamber

In this section, we investigate the thermoacoustic instability [202] in a laminar experimental setup called INTRIG Burner (IMFT, Toulouse). First, a DNS of the full setup (called "FULL") is conducted. A second DNS (called "TRUNCATED") in which the computational domain is truncated after the flame is conducted. In the TRUNCATED case, D-TDIBC is used to model the acoustic properties of the truncated domain as in Sec. 7.3.3. The results obtained using D-TDIBC will be compared with those of the FULL configuration. Several recent studies have used TDIBCs methods in combustion setups [190, 199–201].

7.4.1 Experimental setup

The INTRIG Burner is used to study a lean premixed laminar methane-air flame attached on a cylinder. The operating point corresponds to an equivalence ratio $\phi = 0.75$ and a bulk velocity of the fresh gases of $u_b = 0.8\ \mathrm{m\,s^{-1}}$. The associated laminar flame speed and adiabatic temperature are $s_l = 0.23\ \mathrm{m\,s^{-1}}$ and $T_{ad} = 1920$ K.

The experimental rig is shown in Fig. 7.9. The gaseous methane-air premixture is injected upstream of the glass ball array located at $x = -0.367$ m. The flow is then laminarized by the glass balls and the honey comb panels. A lean premixed methane-air laminar flame attaches to a cylindrical stainless steel flame holder of with a diameter $d = 8$ mm. The combustion chamber has a constant cross section of h = 34 mm by l = 94 mm.

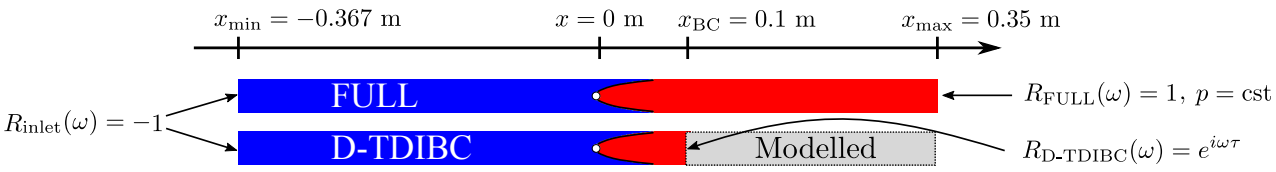


Figure 7.10: Schematic of the computational domains and BC used for the two simulations: FULL and TRUNCATED cases.

Case	Length	N_{cell}	$\Delta x_{\min}$	Inlet BC	Outlet BC	BC type
FULL	0.717 m	625000	60 µm	$R(\omega) = -1$	$R_{\mathrm{FULL}}(\omega) = 1$	NSCBC
TRUNCATED	0.467 m	545000	60 µm	$R(\omega) = -1$	$R_{\text{D-TDIBC}}(\omega) = e^{-i\omega\tau}$	D-TDIBC

Table 7.1: Parameters used in the two simulations.

7.4.2 Numerical setup

As the flow is two-dimensional, 2D Direct Numerical Simulation (DNS) approach can be used [79, 159, 203]. A 19-species mechanism (called LU19) is used [113] for the modeling of chemical kinetics. Schmidt and Prandtl numbers are assumed constant: Pr = 0.6 and Sc = 0.6. The FULL mesh is composed of 625 000 cells. The reduced mesh is composed of 545 000 cells, *i.e.* a reduction of 13 %. The flame thickness is $\delta_L^0 = 680$ µm and at least 11 points are used to resolve the flame front with a mesh resolution at the flame of $\Delta x = 60$ µm [79, 159, 203]. A typical flame, here at a stable operating point, is shown in Fig. 7.9 (bottom).

The inlet acoustic boundary (glass balls at $x = -0.367$ m) is a hard wall (*i.e.* $u(\omega) = 0$ m s^{-1} at all frequencies). It was checked in the experiment that this is a good approximation [79]. This assumption is close to realistic conditions as the inlet BC corresponds to the glass balls array. The outlet acoustic boundary (at $x = 0.35$ m) is an open end (*i.e.* $p(\omega) = 0$ Pa at all frequencies). A more accurate model of the outlet's reflection coefficient should be considered if one were willing to compute precisely the thermoacoustic stability of the configuration. However, the goal of this section is more modest: it aims to validate D-TDIBC. The simple acoustic conditions used here are, hence, acceptable as the reference case is a numerical simulation.

Two simulations are carried out and investigated in this section (*cf.* Fig. 7.10): the "FULL" and the "TRUNCATED" cases. The outlet boundary condition of the FULL domain is located as $x = 0.35$ m and the outlet D-TDIBC boundary condition of the TRUNCATED domain is located at $x = 0.1$ m. Figure 7.10 shows the computational domain and the boundary conditions used in the three simulations. The grey area in the TRUNCATED case corresponds to the domain where the acoustic wave propagation is modeled by a time-delay imposed by D-TDIBC. Table 7.4.2 summarizes the parameters used in the simulation.

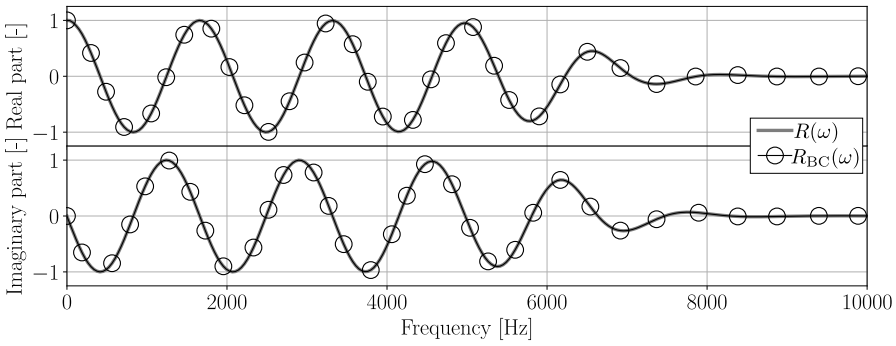


Figure 7.11: Model of the delayed reflection coefficient $R_{\mathrm{BC}}(\omega)$ with $n_0 = 18$ (*cf.* Eq. 6.14) for a time-delay of $\tau = 0.30$ ms in the laminar combustor of Fig. 7.9.

7.4.3 D-TDIBC: reflection coefficient model

The Iterative Multi-Pole Modeling Technique presented in Sec. 7.2 is used to model the acoustic wave propagation in the truncated part of the INTRIG Burner. The outlet boundary condition of the FULL and TRUNCATED domains are located at $x_{\max} = 0.35$ m and $x_{\mathrm{BC}} = 0.10$ m, respectively. Consequently the length of the domain to be modeled by D-TDIBC is $L = 0.25$ m. The value of x_{BC} must be large enough to ensure that combustion is complete and only acoustics take place between x_{BC} and $x_{\max}$. Moreover the sound speed must be homogeneous in this zone. This condition has been verified *a posteriori* by analyzing the results of the FULL configuration simulation: the sound speed fluctuations are less than 0.5% of the mean value $c_0 = 830\ \mathrm{m\,s^{-1}}$. The time-delay to impose is thus $\tau = 2L/c_0 = 0.3$ ms.

According to duct acoustics theory, plane waves propagates in ducts at frequencies lower that a cutoff frequency f_c [**?**]. This frequency is given by the speed of sound c_0 and the lowest height in the cross section. In the INTRIG setup, the plane waves propagate at frequencies lower that $f_{\mathrm{c}} = 3.5$ kHz. The filtering procedure used in (Sec. 7.3.2) is applied here so that the frequencies lower than $f_{\mathrm{c}} = 3.5$ kHz are accurately modeled. The results are shown in Fig. 7.11. The reflection coefficient model used here consists in a set of 18 (p_k, μ_k).

7.4.4 Results and discussion

When carrying out DNS, thermoacoustic instabilities are found in the two cases of Fig. 7.10: the flame oscillates and couples to the acoustic modes of the setup [202]. Figure 7.12(a) illustrates the Sound Pressure Level (SPL) spectra expressed in dB and defined as $\mathrm{SPL} = 20\log(p/p_{\mathrm{ref}})$ based on a reference pressure level of $p_{\mathrm{ref}} = 2 \cdot 10^{-5}$ Pa.

The FULL simulation, *i.e.* computing the full domain, shows a strong acoustic activity with many amplified acoustic modes. The four first modes have frequencies of 203 Hz, 534 Hz, 782 Hz and 1150 Hz, respectively. The mode shapes can be obtained by (1) performing a spectral analysis at several axial locations of the burner, (2) extracting the amplitude of the Fourier transform at the peak frequency in Fig. 7.12(a) and (3) normalizing by the

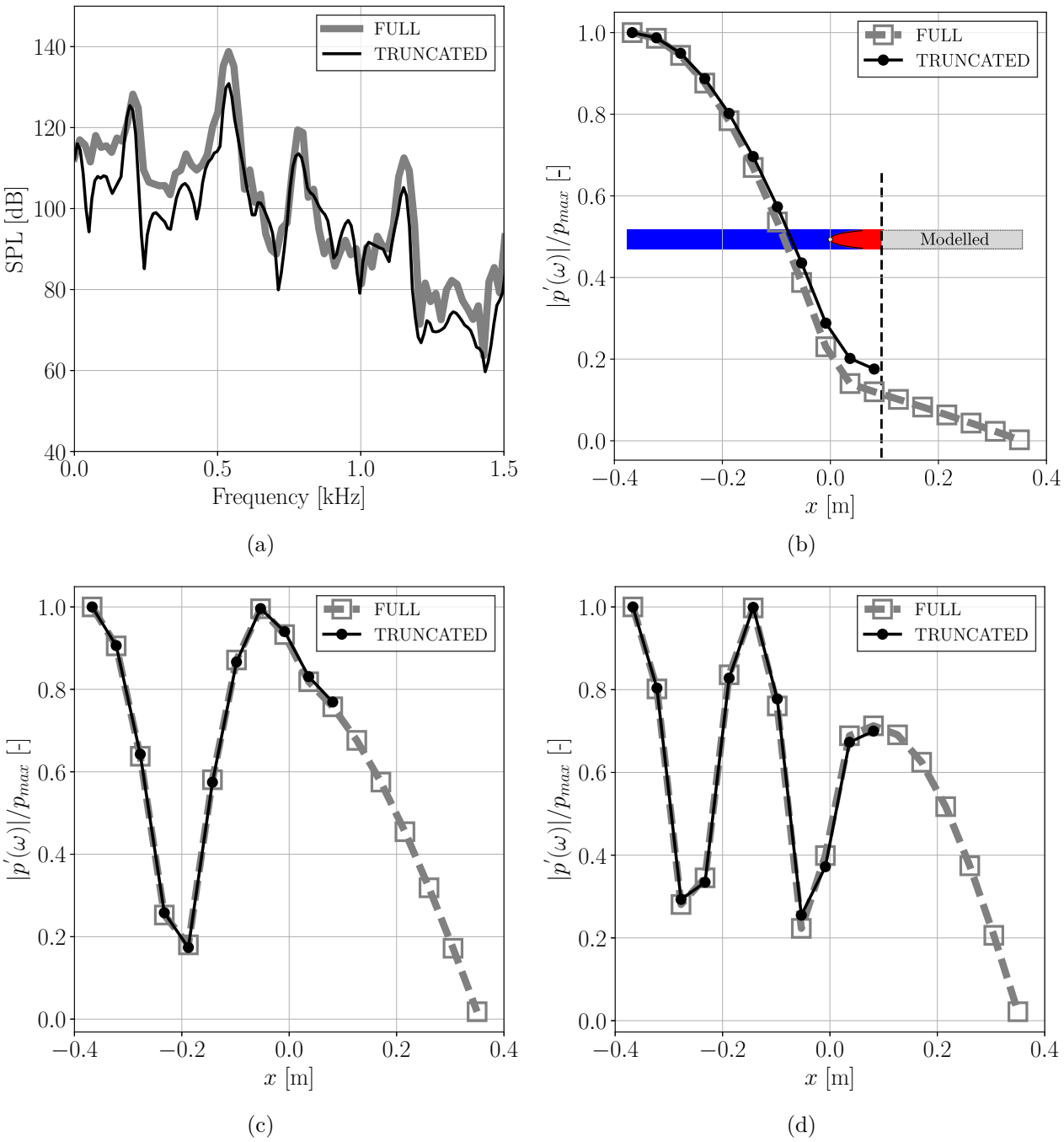


Figure 7.12: (a) spectra obtained for the FULL and the TRUNCATED simulations. D-TDIBC allows an accurate prediction of the thermoacoustic stability observed in the FULL configuration. The spectra are based on a probe located at $x = -8.5$ mm. The shapes of the first (b), second (c) and third (d) modes are shown. The markers correspond to the probes in the simulation (lines are added for the sake of clarity).

maximum pressure amplitude. The three first modes observed in the FULL simulation are a quarter wave mode (*cf.* Fig. 7.12(b)), a three-quarter wave mode (*cf.* Fig. 7.12(c)) and a five-quarter wave mode (*cf.* Fig. 7.12(d)).

The TRUNCATED simulation also exhibits thermoacoustic instabilities and is in good agreement with the FULL simulation. Figure 7.12(a) illustrates the ability of D-TDIBC to accurately predict: the frequencies, the amplitudes and the broadband acoustic activity levels. Figures 7.12(b), (c) and (d) illustrate the mode shapes of the unstable modes obtained with D-TDIBC. The agreement on the modes shapes is excellent.

Figure 7.12 demonstrates that D-TDIBC can recover the acoustic eigenmodes of a domain while simulating only a part of it. It also gives the opportunity to investigate the thermoacoustic stability of different setups while simulating the same computational domain: the length of the truncated domain can be adjusted in the same DNS simply by introducing a different time-delay at the boundary $x = x_{\mathrm{BC}}$ (*cf.* Fig. 7.9).

7.5 Conclusion

Truncating large portions of a computational domain where only inviscid plane waves propagate is possible using a TDIBC. In the time domain, modeling the truncated part is equivalent to adding a "time-delay" to the reflection of the waves. In the frequency domain, it is equivalent to imposing a "delayed reflection coefficient". The reflection coefficient based TDIBC derived in Chapter 6 requires a model, *i.e.* a set of complex poles p_k and residues μ_k, in the frequency domain. For delayed reflection coefficient, this modeling is a tedious task due to the complex exponential introduces by the delay.

In this chapter, a novel modeling strategy allowing to model delayed reflection coefficients has been derived from the properties of a Pole Base Function (*i.e.* the "template" function of the Pole & Residue modeling). The modeling methodology relies on an iterative least-square fitting procedure where the number of degrees of freedom increases at each iteration. Once the model of the delayed reflection coefficient is obtained, one can use the Pole & Residue TDIBC based on the reflection coefficient proposed in Chapter 6 to impose a time-delay in temporal simulations such as in LES/DNS. The joint use of the modeling method for delayed reflection coefficients and the reflection coefficient based TDIBC is referred here as "Delayed-Time Domain Impedance Boundary Condition" (D-TDIBC).

The methodology is validated on a one-dimensional Gaussian wave propagation case simulated with AVBP. The results show that the delayed reflection coefficient is accurately modeled using the iterative least-square fitting procedure. The time-delay is correctly imposed in the temporal simulation without any loss of acoustic energy.

A thermoacoustically unstable combustion setup – the INTRIG burner operated at IMFT (Toulouse, FRANCE) – is used as a final test case: 2D DNS of an unstable laminar methane-air flame is performed using a reduced domain along with D-TDIBC to model the truncated portion. Results are in excellent agreement with the DNS over the complete domain. The unstable modes frequencies, amplitudes and shapes are accurately predicted.

The results demonstrate that D-TDIBC offers a flexible and cost-effective approach for numerical investigations of aeroacoustics and thermoacoustics.

Chapter 8

TDIBC: the state-space approach

State space modeling is a common practice in control theory of linear time-invariant (LTI) systems, *i.e.* systems with fully linear response and constant properties. As pointed by several authors [90, 190, 198, 204], an acoustic boundary in the linear regime can be considered as a LTI system as its properties do not evolve in time and, consequently, a state-space model can be used to implement impedance boundary conditions in Navier-Stokes simulations.

The goal of this chapter is to highlight the links between two TDIBC methods: (1) the pole & residue approach (Fung and Ju [83, 84], Scalo *et al.* [85], Lin *et al.* [86]) and (2) the state-space approach (Jaensch *et al.* [190]).

Section 8.1 will recall the background of state-space modeling before discussing its application to time domain impedance boundary conditions in Sec. 8.2: the CBSBC method of Jaensch *et al.* [190] is presented. In Sec. 8.3, the pole & residue approach will be recast under the CBSBC formalism. First, a single-pole model will be considered and an elementary state-space corresponding to any single-pole model will be presented. Finally, a generic state-space model under the CBSBC formalism will be derived from a multi-pole TDIBC model of order n_0. Numerical simulations will be conducted and the two aforementioned state-space models will be compared to the pole & residue TDIBC and to analytical solutions.

8.1 Introduction to the state-space representation

Many dynamical systems can be modeled by a finite order differential equation in the time domain, which can be recast as a set of first order ordinary differential equations (ODEs). From this set of ODEs a matrix-based representation, called a *state-space models*, can be derived.

Many state-space models (also known as "the Markovian representation") can be constructed from a set of ODEs. State-space models rely on the fact that any finite order linear differential equation can be expressed as a vector of first-order differential equation [187]. In particular, LTI systems can be easily modeled using the state-space representation. In fact, the state-space modeling is a mathematical tool that is convenient to model and study many complex dynamical systems in a simple and generic representation.

A state-space model relies on the so called *state variables*. They are the variables fully describing the evolution of a system in absence of external forcing. For example, to describe a free-falling object (that is neglecting the drag force) the system can be fully described using two *state variables*: the position and velocity of the object. Although many state-space models can be derived from a single set of first order ODEs, the minimum number of *state variables* needed to model a system is unique. The number of *state variables* is referred to as the "order of the state-space".

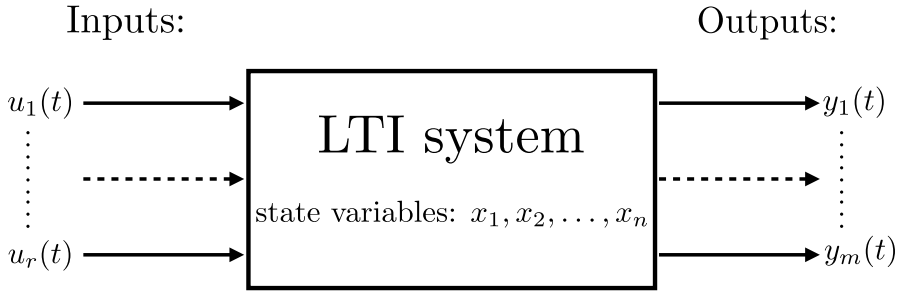


Figure 8.1: Linear time-invariant system with n state variables, r inputs and m outputs.

Figure 8.1 shows a schematic of a generic LTI system with r inputs, m outputs and n *state variables*. The state variables form the *state vector* $\mathbf{x}$, the inputs form the *input vector* $\mathbf{u}$, and the outputs form the *output vector* $\mathbf{y}$ as in Eq. 8.1. The *order* n of the state-space model is given by the size of the *state vector* $\boldsymbol{x}$. If $r = 1$ and $m = 1$ the system is a single-input single-output (SISO) system and if $r > 1$ and $m > 1$ the system is a multiple-input multiple-output (MIMO) system.

$$\boldsymbol{x} = \begin{bmatrix} x_1 \\ x_2 \\ \vdots \\ x_n \end{bmatrix} \quad ; \quad \boldsymbol{u} = \begin{bmatrix} u_1 \\ u_2 \\ \vdots \\ u_r \end{bmatrix} \quad ; \quad \boldsymbol{y} = \begin{bmatrix} y_1 \\ y_2 \\ \vdots \\ y_m \end{bmatrix} \tag{8.1}$$

The choice of the state variables x_i is not unique but the minimum order n of a system is. It corresponds to the number of Degrees Of Freedom (DOF) of the system. The state-space model is built using two matrix equations: the *state equation* and the *output equation*.

8.1.1 The state equation

A mathematical description of dynamical systems can be made using n-th order differential equations. These equations can be recast as a set of coupled first-order ordinary differential equations. In the general case, each state variable's time derivative can be expressed as a

function of all the state variables, inputs and time. The general state equation is:

$$\begin{aligned} \dot{x}_1 &= f_1(\mathbf{x}, \mathbf{u}, t) \\ \dot{x}_2 &= f_2(\mathbf{x}, \mathbf{u}, t) \\ \vdots &= \vdots \\ \dot{x}_n &= f_n(\mathbf{x}, \mathbf{u}, t) \end{aligned} \tag{8.2}$$

where the Newton notation is used to expressed the time derivative $\dot{x}_i \equiv dx_i/dt$. In the general case, the functions f_i can be dependent in time and non-linear. However, when studying LTI systems many simplifications can be done. First, the linearity of the system implies that the superposition principle is respected. Hence, the functions f_i are linear operators: the time derivative of the state variables x_i can be expressed as a linear combination of $\boldsymbol{x}$ and $\boldsymbol{u}$. The second useful property of an LTI system is that its characteristics do not evolve in time (time-invariant). Consequently, the coefficients used in the linear combination are constant in time. Equation. 8.2 can thus be simplified for LTI systems leading to a set of coupled first-order linear differential equations with constant coefficients:

$$\begin{aligned} \dot{x}_1 &= a_{11}x_1 + a_{12}x_2 + \cdots + a_{1n}x_n \quad + \quad b_{11}u_1 + b_{12}u_2 + \cdots + b_{1r}u_r \\ \dot{x}_2 &= a_{21}x_1 + a_{22}x_2 + \cdots + a_{2n}x_n \quad + \quad b_{21}u_1 + b_{22}u_2 + \cdots + b_{2r}u_r \\ \vdots &= \vdots \\ \dot{x}_n &= a_{n1}x_1 + a_{n2}x_2 + \cdots + a_{nn}x_n \quad + \quad b_{n1}u_1 + b_{n2}u_2 + \cdots + b_{nr}u_r \end{aligned} \tag{8.3}$$

This set of equations can be recast in the matrix form as:

$$\begin{bmatrix} \dot{x}_0 \\ \dot{x}_1 \\ \vdots \\ \dot{x}_n \end{bmatrix} = \begin{bmatrix} a_{11} & a_{12} & \dots & a_{1n} \\ a_{21} & a_{22} & \dots & a_{2n} \\ \vdots & & & \vdots \\ a_{n1} & a_{n2} & \dots & a_{nn} \end{bmatrix} \begin{bmatrix} x_0 \\ x_1 \\ \vdots \\ x_n \end{bmatrix} + \begin{bmatrix} b_{11} & b_{12} & \dots & b_{1r} \\ b_{21} & b_{22} & \dots & b_{2r} \\ \vdots & & & \vdots \\ b_{n1} & b_{n2} & \dots & b_{nr} \end{bmatrix} \begin{bmatrix} u_1 \\ u_2 \\ \vdots \\ u_r \end{bmatrix} \tag{8.4}$$

The state equation is usually expressed in the matrix form. Making abstraction of the size of the input, output and state vectors, Eq. 8.4 can be written in the compact form:

$$\dot{\boldsymbol{x}} = \boldsymbol{A}\boldsymbol{x} + \boldsymbol{B}\boldsymbol{u} \tag{8.5}$$

In Eq. 8.5, the bold upper case refers to the matrices in Eq. 8.4 and the bold lower case to the vectors in Eq. 8.1. The matrix $\boldsymbol{A}$ is referred to in the literature as "the state matrix" or "the system matrix" and is of dimension: $\dim[\boldsymbol{A}(\cdot)] = n \times n$ where n is the order of the state-space model (*i.e.* the number of state variables). It corresponds to the a_{ij} coefficients in Eq. 8.4. The state matrix predicts the future values of the state variables $x_i(t)$ at time t knowing the values of the state variables $x_i(t_0)$ at the initial time t_0 if no input is given to the system.

The matrix $\boldsymbol{B}$ is referred to in the literature as "the input matrix" and is of dimension: $\dim[\boldsymbol{B}(\cdot)] = n \times r$ where r is the number of inputs of the system (*cf.* Fig. 8.1). It corresponds

to the b_{ij} coefficients in Eq. 8.4. The $\boldsymbol{B}$ matrix accounts for the change of the state variables values due to the input vector $\boldsymbol{u}$.

The state equation, thus, describes the evolution of the system through the change of the state variables values. However, in many cases the variables of interest for engineering purposes are not the state variables. In order to provide meaningful engineering quantities, a second step is necessary: the so-called *output equation*.

8.1.2 The output equation

As for the state variables, the choice of the output of a system is not unique. The output variables y_i are the system variable of interest. As seen in Sec. 8.1.1, LTI systems allow simplifications. In this context, the output variables can directly be written as a linear combination of the state variables x_i and the input variables u_i. For m output variables, the output equation can then be written:

$$\begin{aligned} y_1 = &\ c_{11}x_1 + c_{12}x_2 + \ldots + c_{1n}x_n &+ &\ d_{11}u_1 + d_{12}u_2 + \cdots + d_{1r}u_r \\ y_2 = &\ c_{21}x_1 + c_{22}x_2 + \ldots + c_{2n}x_n &+ &\ d_{21}u_1 + d_{22}u_2 + \cdots + d_{2r}u_r \\ \vdots = &\ \vdots \\ y_m = &\ c_{m1}x_1 + c_{m2}x_2 + \ldots + c_{mn}x_n &+ &\ d_{m1}u_1 + d_{m2}u_2 + \cdots + d_{mr}u_r \end{aligned} \tag{8.6}$$

Similarly to the state equation, the output equation (Eq. 8.6) is usually expressed in the matrix form:

$$\begin{bmatrix} y_0 \\ y_1 \\ \vdots \\ y_n \end{bmatrix} = \begin{bmatrix} c_{11} & c_{12} & \ldots & c_{1n} \\ c_{21} & c_{22} & \ldots & c_{2n} \\ \vdots & & & \vdots \\ c_{m1} & c_{m2} & \ldots & c_{mn} \end{bmatrix} \begin{bmatrix} x_0 \\ x_1 \\ \vdots \\ x_n \end{bmatrix} + \begin{bmatrix} d_{11} & d_{12} & \ldots & d_{1r} \\ d_{21} & d_{22} & \ldots & d_{2r} \\ \vdots & & & \vdots \\ d_{m1} & d_{m2} & \ldots & d_{mr} \end{bmatrix} \begin{bmatrix} u_1 \\ u_2 \\ \vdots \\ u_r \end{bmatrix} \tag{8.7}$$

Equation 8.7 can be synthesized in the compact form as:

$$\boldsymbol{y} = \boldsymbol{C}\boldsymbol{x} + \boldsymbol{D}\boldsymbol{u} \tag{8.8}$$

In Eq. 8.8, the bold upper case refers to the matrices in Eq. 8.7 and the bold lower case to the vectors in Eq. 8.1.

The matrix $\boldsymbol{C}$ is referred to in the literature as "the output matrix" and is of dimension: $\dim[\boldsymbol{C}(\cdot)] = m \times n$. It corresponds to the c_{ij} coefficients in Eq. 8.7. The $\boldsymbol{C}$ matrix account for the change in the output variables due to the state variables.

The matrix $\boldsymbol{D}$ is referred to in the literature as "the feedthrough matrix" or "the feedforward matrix". The feedthrough matrix accounts for the direct impact of the system inputs to the system outputs without any change of state variables. For many systems, the $\boldsymbol{D}$ matrix

is the zero matrix. In the general case, the $\boldsymbol{D}$ matrix is of dimension: $\dim[\boldsymbol{D}(\cdot)] = m \times r$. It corresponds to the d_{ij} coefficients in Eq. 8.7.

8.1.3 Block diagram of a state-space

Any state-space model can be represented as a block diagram. This representation gives insight on the role played by the matrices in both the state equation and the output equation. In Fig. 8.2 the LTI system shown in Fig. 8.1 is expanded: it shows a block diagram of the LTI system modeled using a state-space model. The SSM is represented using the compact form of Eqs. 8.5 and 8.8.

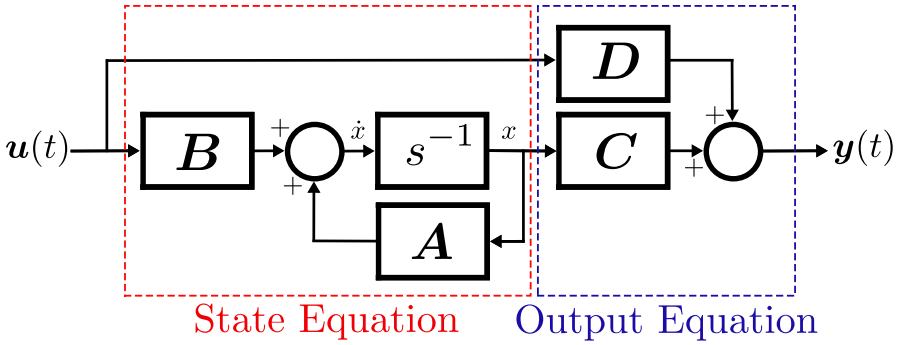


Figure 8.2: Block diagram of a linear time-invariant system modeled using a state-space representation.

The s^{-1} block is an integration block ($x = s^{-1}\dot{x}$) as $s = i\omega = i2\pi f$ is the Laplace variable, i is the imaginary unit ($i = \sqrt{-1}$), f is the frequency and ω is the angular frequency.

On the left hand side of Fig. 8.2 we can see the input vector $\boldsymbol{u}(t)$ (*cf.* Eq. 8.1) and on the right-hand side the output vector $\boldsymbol{y}(t)$. The red box corresponds to the state equation (Eq. 8.5) and the blue box corresponds to the output equation (Eq. 8.8). The block diagram allows to visualize several features of the state-space model:

- the state equation:
  - The state matrix $\boldsymbol{A}$ corresponds to the change of state vector $\boldsymbol{x}$ due to itself. This change is made through the modification of the time derivative of the state vector $\dot{\boldsymbol{x}}$.
  - The input matrix $\boldsymbol{B}$ corresponds to the change of state vector $\boldsymbol{x}$ due to the input vector $\boldsymbol{u}$. This change is made through the modification of the time derivative of the state vector $\dot{\boldsymbol{x}}$.
- the output equation:
  - The output matrix $\boldsymbol{C}$ gives the contribution of the state vector $\boldsymbol{x}$ to the output vector $\boldsymbol{y}$.
  - The feedthrough matrix $\boldsymbol{D}$ gives the contribution of the input vector $\boldsymbol{u}$ to the output vector $\boldsymbol{y}$.

8.2 CBSBC: the state-space model approach for TDIBC

Acoustic boundary conditions are dynamical systems and, in the linear regime, can be considered as LTI systems. their properties are defined in the frequency domain and the time domain response fulfilling these properties can be prescribed by the use of a state-space model. This approach was used by several authors.

Zhong *et al.* [204] used the state-space approach to model the acoustic admittance (inverse of impedance). The state-space model utilized by Zhong *et al.* is in the Controllable Canonical Form.

Similarly, the Characteristic Based State-space Boundary Condition (CBSBC) has been developed by Schuermans *et al.* [198], Kaess *et al.* [90] and Jaensch *et al.* [91] and used in Navier-Stokes simulations [90, 91, 190, 191]. This method relies on state-space modeling of the reflection coefficient.

Two formulations of CBSBC were proposed by Jaensch *et al.* [91]:

1. **CBSBC-LEE: Linearized Euler Equations in a 1D cavity**
   A first formulation of CBSBC, referred to in this manuscript as "**CBSBC-LEE**", is proposed by Jaensch *et al.* specifically to impose pure time-delays. This approach consists in implementing a Linearized Euler Equation (LEE) solver for each of the impedance boundary conditions in the domain and in performing the temporal integration using a first-order upwind scheme. It will not be further discussed in this manuscript.

2. **CBSBC-TF: Transfer Function**
   The second formulation of CBSBC, referred to in this manuscript as "**CBSBC-TF**", is a state-space approach under the so-called Controllable Canonical Form. This form of state-space model can be built by:

   (a) Identifying the transfer function between the inputs and outputs of the system in the frequency domain. In the CBSBC-TF formalism the only input is the outgoing wave $A^{\text{out}}(t)$ and the only output is the ingoing wave $A^{\text{in}}(t)$. In this case, the transfer function is the reflection coefficient.

   (b) Fitting the broadband reflection coefficient as a rational polynomial fraction. The order of the state-space is given by the order of the denominator's polynomial and the numerator's polynomial order should be lower or equal to the order of the denominator.

   (c) Using the inverse Laplace transform in order to obtain an ODE (*cf.* Appendix C).

   (d) Recasting the ODE as a set of first order ODE.

   (e) Deriving a state-space model from the set of first order ODEs.

This formulation of CBSBC aims to imposing broadband reflection coefficients in the time domain. In theory, this formulation should be capable of imposing pure time-delays such as in Chapter 7.

However, in practice, modeling a delayed reflection coefficient as a rational polynomial is exceedingly difficult as the reflection coefficient is a complex exponential in the frequency domain. It is due to the high number of zeros introduced by the complex exponential as discussed in Chapter 7 (Sec. 7.1 on page 115). In this case, the CBSBC model requires a very high number of Padé polynomial coefficients leading to very large matrices and numerical issues (such as inverting ill-conditioned matrices).

The CBSBC-TF method will be detailed in Sec. 8.2.1. For the sake of readability, the CBSBC method will be formulated here under the notations used in Chapters 6 and 7.

8.2.1 Characteristic Based State-space Boundary Condition: transfer function modeling

As discussed above, a popular way of building a state-space model is by modeling the transfer function as a rational polynomial. This choice was made by Jaensch *et al.* [91]. In their work, the authors propose to model the complex reflection coefficient in the Laplace space (*cf.* Appendix C) as a rational polynomial function:

$$R(s) = \frac{A^{\text{in}}(s)}{A^{\text{out}}(s)} = \frac{\beta_n s^n + \beta_{n-1} s^{n-1} + \cdots + \beta_1 s + \beta_0}{\alpha_m s^m + \alpha_{m-1} s^{m-1} + \cdots + \alpha_1 s + \alpha_0} \tag{8.9}$$

where the coefficients β_i with $i \in [0, n]$ and α_i with $i \in [0, m]$ are real-valued constants and $m \geq n$. Equation 8.9 can be written:

$$R(s) = \frac{N(s)}{D(s)} = \frac{\sum_{k=0}^{n} \beta_k s^k}{\sum_{k=0}^{m} \alpha_k s^k} \tag{8.10}$$

where $N(s)$ and $D(s)$ are the polynomials in the numerator and denominator, respectively. As $N(s)$ and $D(s)$ are polynomials in the frequency domain, Eqs. 8.9 and 8.10 correspond to an ODE of order m in the time domain:

$$\frac{d^m A^{in}}{dt^m} + \alpha_{m-1} \frac{d^{m-1} A^{in}}{dt^{m-1}} + \cdots + \alpha_1 \frac{dA^{in}}{dt} + \alpha_0 A^{in} = \beta_n \frac{d^n A^{out}}{dt^n} + \beta_{n-1} \frac{d^{n-1} A^{out}}{dt^{n-1}} + \cdots + \beta_1 \frac{dA^{out}}{dt} + \beta_0 \tag{8.11}$$

where $\frac{d^i f}{dt^i}$ is the ith time derivative of a function f.
A single-input single-output (SISO) state-space model can be built from Eq. 8.11 [190]

$$\dot{\boldsymbol{x}} = \boldsymbol{A}\boldsymbol{x} + \boldsymbol{B}u \tag{8.12}$$

$$y = \boldsymbol{C}\boldsymbol{x} + \boldsymbol{D}u \tag{8.13}$$

The state vector $\boldsymbol{x}$ is defined as the time derivative of the temporal outgoing wave $A^{\text{out}}(t)$:

$$\boldsymbol{x} = \begin{bmatrix} 1 \\ \frac{d}{dt} \\ \vdots \\ \frac{d^{m-1}}{dt^{m-1}} \end{bmatrix} \cdot A^{\text{out}}(t) \tag{8.14}$$

Following the definition of the waves $A^{\text{in}}(t)$ and $A^{\text{out}}(t)$ shown in Fig. 6.1 (page 99), the state-space model has only a single input, *i.e.* the input vector $\boldsymbol{u}$ in Eq. 8.5 reduces to a scalar input u,

$$u(t) = A^{\text{out}}(t) \tag{8.15}$$

and a single output, *i.e.* the output vector $\boldsymbol{y}$ in Eq. 8.8 reduces to a scalar output y.

$$y(t) = A^{\text{in}}(t) \tag{8.16}$$

The state matrix $\boldsymbol{A}$ is built using the polynomial coefficient of the denominator $D(s)$ in Eq. 8.10 [190]:

$$\boldsymbol{A} = \begin{bmatrix} 0 & 1 & 0 & \dots & 0 \\ \vdots & 0 & 1 & \ddots & \vdots \\ \vdots & & \ddots & \ddots & 0 \\ 0 & \dots & \dots & 0 & 1 \\ -\alpha_0 & -\alpha_1 & \dots & -\alpha_{m-2} & -\alpha_{m-1} \end{bmatrix} \tag{8.17}$$

The input matrix $\boldsymbol{B}$ (*cf.* Eq. 8.12) is [190] :

$$\boldsymbol{B} = \begin{bmatrix} 0 \\ \vdots \\ 0 \\ 1 \end{bmatrix} \tag{8.18}$$

The output matrix $\boldsymbol{C}$ in Eq. 8.13 is [190] :

$$\boldsymbol{C} = [\beta_0 - \beta_m\alpha_0, \quad \beta_1 - \beta_m\alpha_1, \quad \dots, \quad \beta_{m-2} - \beta_m\alpha_{m-2}, \quad \beta_{m-1} - \beta_m\alpha_{m-1}] \tag{8.19}$$

and the $\boldsymbol{D}$ matrix in Eq. 8.8 reduces to a scalar [190] :

$$D = \beta_m \tag{8.20}$$

This method has been successfully applied to Navier-Stokes simulations by several authors [90, 91, 190, 191]. The objective of the next section is to investigate the links between the CBSBC method and the pole & residue TDIBC method of Fung and Ju.

8.3 Link between state-space and pole & residue method

In Chapter 6 the theory of TDIBC as proposed originally by Fung and Ju has been presented. This method uses the wall softness $S(\omega)$ as the impedance modeling quantity. A similar method has been derived in Sec. 6.2.2 based on the reflection coefficient $R(\omega)$. The objective of this section is to highlight the links between the reflection-coefficient-based pole & residue TDIBC and CBSBC-TF.

In Sec. 8.3.1 a state-space model will be derived from a single-pole model (*i.e.* a single pair of residues and poles) which is compared to the CBSBC-TF formalism. Section 8.3.2 will focus on the generalization of the TDIBC multi-pole model under the CBSBC-TF formalism.

8.3.1 Single pole base function as a controllable form state space

The objective of this section is to build a CBSBC-TF model corresponding to a generic single-pole TDIBC ($n_0 = 1$ in Eq. 6.14, *cf* page 103).

Derivation

As presented in Chapter 6 (Sec. 6.2.2), the use of the pole-based TDIBC requires the modeling of the reflection coefficient as a sum of partial fraction as in Eq. 6.14. Since the pole-based TDIBC consists of a linear superimposition of partial fraction we focus, first, on a single conjugate pair of pole & residue p_k and μ_k. For a single Pole Base Function (*cf.* Sec. 6.2.2), that is $n_0 = 1$ in Eq. 6.14, the reflection coefficient modeled by TDIBC is:

$$R(s) = \frac{A^{\text{in}}(s)}{A^{\text{out}}(s)} = \frac{\mu_1}{s - p_1} + \frac{\mu_1^*}{s - p_1^*} \tag{8.21}$$

The reflection coefficient in Eq. 8.21 can be expressed as a rational polynomial:

$$R(s) = \frac{\beta_1 s + \beta_0}{s^2 + \alpha_1 s + \alpha_0} \tag{8.22}$$

where:

$$\begin{cases} \alpha_0 &= c^2 + d^2 \\ \alpha_1 &= -2c \\ \beta_0 &= -2(ac + bd) = 0 \\ \beta_1 &= 2a \end{cases} \tag{8.23}$$

for:

$$\mu_1 = a + ib \quad ; \quad p_1 = c + id \tag{8.24}$$

The coefficient β_0 (the phase parameter at the low frequency limit) is set to zero [86]. The rational polynomial function of Eq. 8.22 can be expressed as in Eq. 8.10 where:

- the numerator $N_1(s)$ is a polynomial of order $n = 1$,
- the denominator $D_1(s)$ is a polynomial of order $m = 2$.

The reflection coefficient of a single Pole Base Function model can, hence, be expressed as follows:

$$R(s) = \frac{A^{\text{in}}(s)}{A^{\text{out}}(s)} = \frac{\beta_1 s}{s^2 + \alpha_1 s + \alpha_0} \tag{8.25}$$

Applying the inverse Laplace transform (*cf.* Appendix C) to Eq. 8.25 we can recover a temporal ODE (*cf.* Eq. 8.11):

$$\frac{d^2 A^{in}}{dt^2} + \alpha_1 \frac{dA^{in}}{dt} + \alpha_0 A^{in} = \beta_1 \frac{dA^{out}}{dt} \tag{8.26}$$

Or, in the state-space form:

$$\underbrace{\frac{d}{dt}\begin{bmatrix} A^{\text{out}} \\ \frac{dA^{\text{out}}}{dt} \end{bmatrix}}_{\dot{\boldsymbol{x}}} = \underbrace{\begin{bmatrix} 0 & 1 \\ -\alpha_0 & -\alpha_1 \end{bmatrix}}_{\boldsymbol{A}} \underbrace{\begin{bmatrix} A^{\text{out}} \\ \frac{dA^{\text{out}}}{dt} \end{bmatrix}}_{\boldsymbol{x}} + \underbrace{\begin{bmatrix} 0 \\ 1 \end{bmatrix}}_{\boldsymbol{B}} \cdot \underbrace{A^{\text{out}}(t)}_{u} \tag{8.27}$$

$$\underbrace{A^{\text{in}}(t)}_{y} = \underbrace{\begin{bmatrix} 0 & \beta_1 \end{bmatrix}}_{\boldsymbol{C}} \underbrace{\begin{bmatrix} A^{\text{out}} \\ \frac{dA^{\text{out}}}{dt} \end{bmatrix}}_{\boldsymbol{x}} + \underbrace{0}_{D} \cdot \underbrace{A^{\text{out}}(t)}_{u} \tag{8.28}$$

Using Eq. 8.23 the state-space model that uses the Pole Base Function parameters (Eq. 7.3) is:

$$\frac{d}{dt}\begin{bmatrix} A^{\text{out}} \\ \frac{dA^{\text{out}}}{dt} \end{bmatrix} = \begin{bmatrix} 0 & 1 \\ -c^2 - d^2 & 2c \end{bmatrix} \begin{bmatrix} A^{\text{out}} \\ \frac{dA^{\text{out}}}{dt} \end{bmatrix} + \begin{bmatrix} 0 \\ 1 \end{bmatrix} \cdot A^{\text{out}}(t) \tag{8.29}$$

$$A^{\text{in}}(t) = \begin{bmatrix} 0 & 2a \end{bmatrix} \begin{bmatrix} A^{\text{out}} \\ \frac{dA^{\text{out}}}{dt} \end{bmatrix} \tag{8.30}$$

A mathematical proof that any single-pole model can be expressed as a CBSBC model has been derived. Equations. 8.29 and 8.30 are mathematically equivalent to the single-pole model presented in Eq. 8.21.

The next section focuses on generalizing this result as it presents the derivation of a CBSBC model from multi-pole models.

8.3.2 Multiple Pole Base Functions as a controllable form state space

The objective of this section is to build a CBSBC-TF model corresponding to a multi-pole TDIBC model of order n_0 (*cf.* Sec. 6.2.2).

Derivation

The sum in Eq. 6.14 can be truncated to an arbitrary order n_0. The truncated sum to the order n_0 is referred to as S_{n_0} and can be expressed as a sum of n_0 rational polynomial functions:

$$S_{n_0}(s) = \sum_{k=1}^{n_0} \frac{\beta_{1,k} s}{s^2 + \alpha_{1,k} s + \alpha_{0,k}} = \sum_{k=1}^{n_0} \frac{A_k}{B_k} \tag{8.31}$$

where A_k and B_k are the numerator and denominator of the kth rational polynomial function, respectively. The sum S_{n_0} itself can be expressed as a rational polynomial function with a numerator N_{n_0} and a denominator D_{n_0}.

$$S_{n_0} = \sum_{k=1}^{n_0} \frac{2a_k s}{(s - p_k)(s - p_k^*)} = \sum_{k=1}^{n_0} \frac{A_k}{B_k} = \frac{N_{n_0}}{D_{n_0}} \tag{8.32}$$

For a single Pole Base Function ($n_0 = 1$ in Eq. 6.14), we have:

$$S_1 = \frac{N_1}{D_1} = \frac{A_1}{B_1} \tag{8.33}$$

Equation 8.33 was used directly to determine N_1 and D_1 in Sec. 8.3.1. which is equivalent to Eq. 8.25. For a higher order n_0, we can evaluate N_{n_0} and D_{n_0}. Recursively for $n_0 = 2$, $n_0 = 3$ and $n_0 = 4$, we have:

$$S_2 = \frac{N_2}{D_2} = \frac{A_1}{B_1} + \frac{A_2}{B_2} = \frac{A_1 B_2 + A_2 B_1}{B_1 B_2} \tag{8.34}$$

$$S_3 = \frac{N_3}{D_3} = \frac{A_1}{B_1} + \frac{A_2}{B_2} + \frac{A_3}{B_3} = \frac{A_1 B_2 B_3 + B_1 A_2 B_3 + B_1 B_2 A_3}{B_1 B_2 B_3} \tag{8.35}$$

$$S_4 = \frac{N_4}{D_4} = \frac{A_1}{B_1} + \frac{A_2}{B_2} + \frac{A_3}{B_3} + \frac{A_4}{B_4} = \frac{A_1 B_2 B_3 B_4 + B_1 A_2 B_3 B_4 + B_1 B_2 A_3 B_4 + B_1 B_2 B_3 A_4}{B_1 B_2 B_3 B_4} \tag{8.36}$$

Equations 8.34, 8.35 and 8.36 show by recurrence that the generic expression for the numerator N_{n_0} and the denominator D_{n_0} of the sum S_{n_0} are:

$$N_{n_0} = \sum_{k=1}^{n_0} A_k \prod_{\substack{i=1 \\ i \neq k}}^{n_0} B_i \tag{8.37}$$

$$D_{n_0} = \prod_{i=1}^{n_0} B_i \tag{8.38}$$

In order to build a state-space model as in CBSBC, we need to express S_n under the form:

$$S_{n_0} = \frac{N_{n_0}}{D_{n_0}} = \frac{\sum_{l=0}^{n} \beta_l s^l}{\sum_{k=0}^{m} \alpha_k s^k} \tag{8.39}$$

where we have to find the α_k and β_l coefficients corresponding to the Pole Base Functions parameters and $\alpha_m = 1$ by definition. As seen in Eq. 8.31, A_k and B_k are polynomials of order 1 and 2, respectively. From Eqs. 8.37 and 8.38 it follows that the polynomials N_{n_0} and D_{n_0} are of order $n = 2n_0 - 1$ and $m = 2n_0$, respectively.

Denominator

The denominator D_{n_0} in Eq. 8.38 can be expressed as:

$$D_{n_0}(s) = \prod_{i=1}^{n_0} B_k(s) = \prod_{i=1}^{n_0} (s - p_k)(s - p_k^*) \tag{8.40}$$

We can define a vector $\boldsymbol{s}$ containing all of the roots s_i of the polynomials $D_{n_0}(s)$:

$$\boldsymbol{s} \;=\; \left[p_1,\ p_1^*,\ p_2,\ p_2^*,\ \ldots,\ p_{n_0},\ p_{n_0}^*\right] = [s_1,\ s_2,\ \ldots,\ s_{2n_0}] \tag{8.41}$$

$$\begin{cases} s_i & = 0 \quad ; \quad i = 0 \\ s_{2i} & = p_i \quad ; \quad i \in [1; n_0] \\ s_{2i-1} & = p_i^* \quad ; \quad i \in [1; n_0] \end{cases} \tag{8.42}$$

The first root $s_0 = 0$ is not useful for the determination of the coefficients α_k in Eq. 8.39. However, it is used in the next section to determine the coefficients β_l. Using the roots s_i, Eq. 8.40 can be recast:

$$D_{n_0} = \prod_{i=1}^{2n_0} s - s_i \tag{8.43}$$

In Eq. 8.43, the polynomial D_{n_0} is factorized. In the TDIBC formalism proposed by Douasbin *et al.* [87–89] the s_i are found while fitting the reflection coefficient. To build a state-space model as in CBSBC we need to identify the coefficients of the polynomial as in Eq. 8.10. To do so, one can use Viète's formula [205–207] which allows to determine the polynomials coefficients if its roots are known. As the pole-based TDIBC modeling is based on the determination of the roots s_i, the α_k in Eq. 8.10 can be found. The coefficients α_k of the polynomial D_{n_0} of order $m = 2n_0$ are:

$$\alpha_k \;=\; (-1)^{2n_0-k} \cdot \sigma(2n_0 - k, \boldsymbol{s}) \tag{8.44}$$

which further simplifies into[1]:

$$\boxed{\alpha_k = (-1)^k \cdot \sigma(2n_0 - k, \boldsymbol{s})} \tag{8.45}$$

where $\sigma_j(\boldsymbol{s}) = \sigma(j, \boldsymbol{s})$ denotes the elementary symmetric polynomial of order j of the vector $\boldsymbol{s}$ [207, 208]:

$$\sigma(j, \boldsymbol{s}) = \sigma_j(s_1, s_2, \cdots, s_{2n_0-1}, s_{2n_0}) = \sum_{1 \le i_1 < i_2 \cdots < i_j \le 2n_0} s_{i_1} s_{i_2} \cdots s_{i_j} \tag{8.46}$$

[1]The expression $(-1)^{2n_0}$ is always equal to unity for all $n_0 \in \mathbb{N}$. The function $f(x) = (-1)^x$ is an even function, hence: $(-1)^{-k} = (-1)^k \ ; \ \forall k \in \mathbb{N}$.

For example, for $n_0 = 2$ the elementary symmetric polynomials from the order $j = 0$ to $j = 2n_0 = 4$ are:

$$\sigma(0, \boldsymbol{s}) = \sigma_0(s_1, s_2, s_3, s_4) = 0 \tag{8.47}$$
$$\sigma(1, \boldsymbol{s}) = \sigma_1(s_1, s_2, s_3, s_4) = s_1 + s_2 + s_3 + s_4 \tag{8.48}$$
$$\sigma(2, \boldsymbol{s}) = \sigma_2(s_1, s_2, s_3, s_4) = s_1s_2 + s_1s_3 + s_1s_4 + s_2s_3 + s_2s_4 + s_3s_4 \tag{8.49}$$
$$\sigma(3, \boldsymbol{s}) = \sigma_3(s_1, s_2, s_3, s_4) = s_1s_2s_3 + s_1s_2s_4 + s_1s_3s_4 + s_2s_3s_4 \tag{8.50}$$
$$\sigma(4, \boldsymbol{s}) = \sigma_4(s_1, s_2, s_3, s_4) = s_1s_2s_3s_4 \tag{8.51}$$

Computationally, the elementary symmetric polynomial $\sigma(j, \boldsymbol{s})$ can be computed using the Newton-Girard formula by taking the determinant of a matrix $\boldsymbol{N_g}$ [209–211]:

$$\sigma(j, \boldsymbol{s}) = (-1)^{j-1} \det \boldsymbol{N_g} \tag{8.52}$$

where $\boldsymbol{N_g}$ is the $j \times j$ matrix:

$$\det \boldsymbol{N_g} = \begin{vmatrix} 1s_1 & 1 & 0 & 0 & \cdots & 0 \\ 2s_3 & s_1 & 1 & 0 & \ddots & 0 \\ 3s_3 & s_2 & s_1 & 1 & \ddots & 0 \\ 4s_4 & s_3 & s_2 & s_1 & \ddots & 0 \\ \vdots & \vdots & \vdots & \vdots & \ddots & 1 \\ js_j & s_{j-1} & s_{j-2} & \cdots & \cdots & s_1 \end{vmatrix} \tag{8.53}$$

Numerator

In order to find the β_k coefficients we have to recast Eq. 8.37. First, the A_k in Eq. 8.32 can be factorized:

$$A_k = 2a_k s = 2a_k(s - s_0) \tag{8.54}$$

where a_k is the real part of the residue μ_k as defined in Sec. 6.2.2 and $s_0 = 0$ as defined by Eq. 8.42. Using Eq. 8.54, Eq. 8.37 can be recast as:

$$N_{n_0} = \sum_{k=1}^{n_0} 2a_k(s - s_0) \prod_{\substack{i=1 \\ i \neq k}}^{n_0} (s - p_i)(s - p_i^*) \tag{8.55}$$

As in Eq. 8.43 the product in Eq. 8.55 can be recast using the $\boldsymbol{s}$ vector defined in Eq. 8.41.

$$N_{n_0} = \sum_{k=1}^{n_0} 2a_k(s - s_0) \prod_{\substack{i=1 \\ i \neq [k,k+1]}}^{2n_0} s - s_i \tag{8.56}$$

The $s - s_0$ term can be introduced in the product as well by changing the starting index to $i = 0$:

$$N_{n_0} = \sum_{k=1}^{n_0} 2a_k \prod_{\substack{i=0 \\ i \neq [k,k+1]}}^{2n_0} s - s_i \tag{8.57}$$

Equation 8.57 is not convenient as the index i in each of the term of the sum k can take all the values form $i = 0$ to $i = 2n_0$ except $i = k$ and $i = k + 1$. For clarity's sake, we can define a new vector $\boldsymbol{r}$:

$$\boldsymbol{r}(k) = [r_1(k),\ r_2(k),\ \ldots,\ r_{2n_0-2}(k)] \tag{8.58}$$

where $r_i(k)$ is:

$$\begin{cases} r_i(k) &= s_i \quad \text{if} \quad i < k \\ r_i(k) &= s_{i+2} \quad \text{if} \quad i \geq k \end{cases} \tag{8.59}$$

The numerator N_{n_0} in Eq. 8.57 can then be recast as:

$$N_{n_0} = 2 \sum_{k=1}^{n_0} \left[a_k \prod_{i=0}^{2n_0-2} s - r_i(k) \right] \tag{8.60}$$

The factorized form of the numerator polynomial N_{n_0} in Eq. 8.60 allows to apply Viète's formula as in Eq. 8.44, leading to [205–207]:

$$\boxed{\beta_l = (-1)^l \ \cdot \ 2 \sum_{k=1}^{n_0} \left[a_k \cdot \sigma\Big(2n_0 - 1 - l,\ \boldsymbol{r}(k) \Big) \right]} \tag{8.61}$$

State-space model of pole-based TDIBC model of order n_0

Once the α_k and β_l polynomial coefficients have been determined using Eq. 8.45 and Eq. 8.61, a state-space model in the CBSBC formalism can be built using Eqs. 8.12 to 8.20. In Sec. 8.3.2 it was shown that the polynomials N_{n_0} and D_{n_0} are of order $n = 2n_0 - 1$ and $m = 2n_0$, respectively. As $n = m - 1$, the coefficients $\beta_m = 0$ in Eqs. 8.12 to 8.20, leading to the simplified SISO CBSBC model:

$$\dot{\boldsymbol{x}} = \underbrace{\begin{bmatrix} 0 & 1 & 0 & \dots & 0 \\ \vdots & 0 & 1 & \ddots & \vdots \\ \vdots & & \ddots & \ddots & 0 \\ 0 & \dots & \dots & 0 & 1 \\ -\alpha_0 & -\alpha_1 & \dots & -\alpha_{m-2} & -\alpha_{m-1} \end{bmatrix}}_{\boldsymbol{A}} \boldsymbol{x} + \underbrace{\begin{bmatrix} 0 \\ \vdots \\ 0 \\ 1 \end{bmatrix}}_{\boldsymbol{B}} A^{\text{out}}(t) \tag{8.62}$$

$$A^{\text{in}}(t) = \underbrace{[0, \quad \beta_1, \quad \dots, \quad \beta_{m-2}, \quad \beta_{m-1}]}_{\boldsymbol{C}} \boldsymbol{x} \tag{8.63}$$

The output matrix $\boldsymbol{C}$ (Eq. 8.19) is modified and the feedthrough matrix $\boldsymbol{D}$ (Eq. 8.20) is the zero matrix as $\beta_m = 0$. The coefficients α and β are found using Eqs. 8.45 and 8.61, respectively. It should be noted that for $n_0 = 1$, the state-space model in Eqs. 8.62 and 8.63 reduces to the one presented for a single-pole model (Eqs. 8.29 and 8.30).

The derivation above is a mathematical proof that any multi-pole TDIBC model of order n_0 (*cf.* Eq. 8.31) can be recast as a state-space model in the CBSBC formalism (*cf.* Eqs. 8.62 and 8.63).

8.3.3 Numerical simulations: CBSBC & pole & residue

In Sec. 8.3, a state-space model in the CBSBC-TF formalism has been derived from a single-pole TDIBC models. It was generalized to a sum of n_0 single-pole models in Sec. 8.3.2.

The objective of this section is to run numerical simulations with the state-space models for both single-pole and multi-pole models and to draw a comparison with the validation results obtained in Chapter 6 (Sec. 6.3.1 and 6.3.2).

CBSBC-TF model from single-pole model TDIBC

The test case used in Sec. 6.3.1 to validate TDIBC based on the reflection coefficient is used in this section. A state-space model corresponding to a single pair of conjugate pole p_1 and residue μ_1 is built here using the relations presented in Sec. 8.3.1. The pole p_1 and residue μ_1 are the ones used the in Sec. 6.3.1 (Eq. 6.21, *cf* page 106).

The simulation is conducted using the temporal signals recorded from the AVBP simulation[2] in Sec. 6.3.1 at the TDIBC. This state-space model corresponds to the pole-based TDIBC in the formalism of CBSBC-TF for a single conjugate pair of poles. The state-space model is built using the scipy.signal.StateSpace function of the SciPy library (Scientific Python library). The function scipy.signal.lsim is used to simulate the output of the system, that is,

[2]From the pressure, the velocity, the density and the speed of sound, the temporal amplitude of the outgoing characteristic wave can be reconstructed and used as the input signal in a state-space model for a TDIBC in the CBSBC-TF formalism.

the temporal amplitude of the ingoing wave $A_n^{\text{in}}(t)$.

The results of the simulation are shown in Fig. 8.3. The ingoing wave $A_n^{\text{in}}(t)$ prescribed by CBSBC-TF is in excellent agreement with the one prescribed by the pole & reside TDIBC formalism. As both methods are mathematically equivalent under the formalism proposed in Sec. 8.3.1 this result is expected. Obviously, CBSBC-TF is in excellent agreement with the analytical solution (convolution integral in Eq. 6.20) as it prescribes the same ingoing wave as TDIBC, which was found to give an exact solution in Sec. 6.3.1.

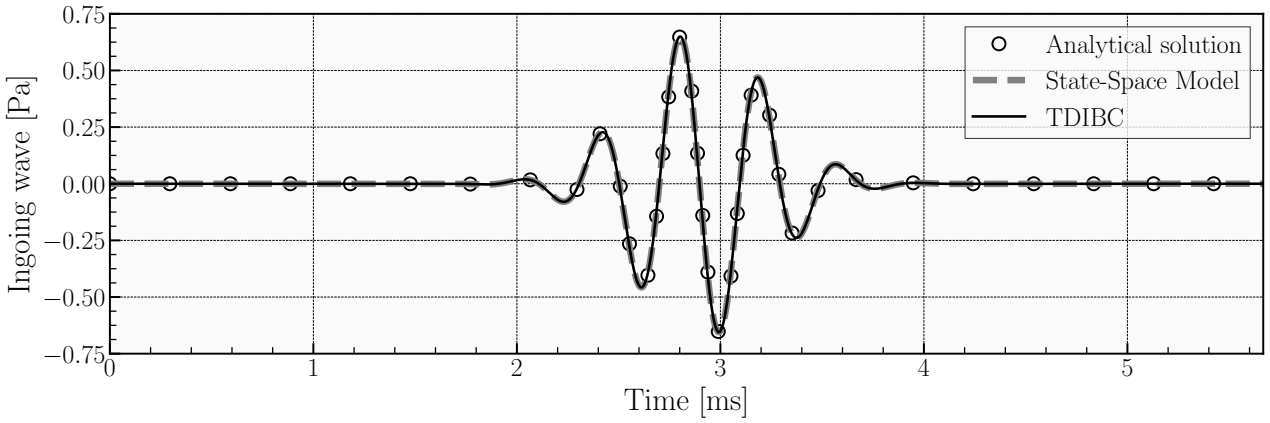


Figure 8.3: Comparison of the ingoing wave corresponding to the analytical solution, the state-space model built from the multi-pole TDIBC model and the multi-pole TDIBC model.

CBSBC-TF model from multi-pole model TDIBC

This section aims to running a numerical simulation with the CBSBC-TF model derived from a multi-pole TDIBC model as presented in Sec. 8.3.2. The formulation of CBSBC-TF proposed in Sec. 8.3.2 is generic and should be mathematically equivalent to a multi-pole model for any order n_0 in Eq. 6.14 (*cf* page 103) .

A CBSBC-TF model is constructed from the reflection coefficient model used in Sec. 6.3.2 to validate the multi-pole TDIBC based on reflection coefficient. This model is composed of three pairs of conjugate poles & residues and its parameters are compiled in Table 6.1 on page 109.

The test case used here is identical to the one used for the validation of the multi-pole TDIBC based on the reflection coefficient (Sec. 6.3.2). Here, the reflection coefficient at $x = 1$ m is imposed using CBSBC-TF [90, 91, 190] rather than using Fung and Ju's formulation.

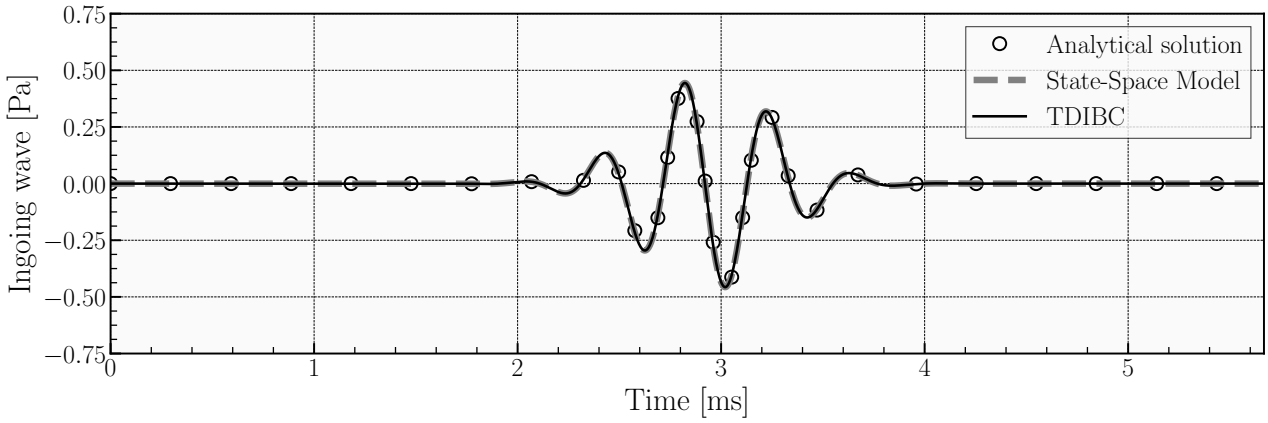


Figure 8.4: Comparison the ingoing wave for the analytical solution, the CBSBC-TF model built from the multi-pole model and the multi-pole model.

The simulation is conducted and the temporal ingoing wave prescribed by CBSBC-TF is compared to:

- TDIBC based on the reflection coefficient as presented in Sec. 6.2.2 and validated in Sec. 6.3.2,
- the analytical solution computed from Eq. 6.20.

Figure 8.4 shows the results. The CBSBC-TF based on the multi-pole model gives the same temporal ingoing wave that the multi-pole TDIBC. As the multi-pole TDIBC was validated in Sec. 6.3.2, CBSBC-TF obviously retrieves the wave corresponding to the analytical solution.

8.4 Discussion

8.4.1 Limitations

The simulations conducted with the state-space models derived from pole & residue models were found to give identical results with both original models and analytical solutions. Due to the mathematical equivalence between the two models, this result was expected.

However, an attempt to construct a high order state-space in the CBSBC-TF formalism lead to numerical issues. D-TDIBC models, *e.g.* the one used in Sec. 7.3 (Chapter 7, page 122), consists in a high number n_0 of conjugate pairs of poles and residues. It was used here in an attempt to derive a CBSBC-TF model suited for time-delays. In the D-TDIBC framework, a high order n_0 does not lead to numerical issues as the outgoing is simply the sum of each single-pole model contribution.

Conversely, numerical issues are encountered when determining the polynomial coefficients α and β in the equivalent state-space (such as in Eqs. 8.62 and 8.63). These numerical issues

are due to the computation of the determinant (in Eq. 8.53) when evaluating the elementary symmetric polynomials using the Newton-Girard formula. In other words, the determination of the polynomial coefficients α and β requires $2n_0$ multiplications of complex variables (the poles p_k) which may lead to very high numbers, returning "Not-a-Number" values.

There is a need for further studies on the possible use of matrices preconditioner to compute this determinant.

8.4.2 Perspectives

Both the pole & residue and CBSBC-TF approaches are robust and flexible methods allowing the imposition of the acoustic properties at a boundary conditions in LES and DNS. Also, both of them have advantages and drawbacks:

1. **CBSBC-TF**

   + This approach allows a great flexibility in the modeling of a broadband reflection coefficient due to the rational polynomial fit technique.
   + It allows to use network models easily.
   + It allows to introduce external acoustic forcing.
   − Pure time-delays cannot be modeled as the rational polynomial fitting fails to model the complex exponential function.
   − It requires an integration of ODEs in the matrix form in the DNS/LES solver.
   − Large matrices may need to be stored.

2. **Pole & Residue**

   + This approach does not require matrix manipulations.
   + Only a few constants need to be stored.
   + Easy to implement.
   + Stable and causal by construction of the model.
   + Can impose pure time-delays in a CPU & memory efficient way.
   − Modeling procedure is more tedious than the rational polynomial fit.

Moreover, Jaensch *et al.* [91] have proposed another formulation to impose time-delays (referred to as CBSBC-LEE in this manuscript). This formulation has not been deeply discussed in this manuscript. CBSBC-LEE should be considered as one-dimensional linearized Euler equations solver. The boundary condition is to be considered as a one-dimensional cavity where: (1) the beginning of the cavity is the boundary condition in the simulation and (2) the end of the cavity is a boundary with a real reflection coefficient (no phase-shift is introduced). The time-delay is reproduced as the LEE solves for the wave propagation in

the cavity: the time-delay is the time taken by the wave to travel back and forth in the truncated domain (*cf.* Sec.7.1, page 115). It was found by Jaensch *et al.* [91] that this approach was both dispersive and dissipative (due to the first-order upwind scheme used) and that the resulting state-space needs to be of high order (around 2000 state variables). Consequently, large matrices need to be stored to achieve results comparable to the pole & residue approach.

An interesting perspective is to conjugate the various formulations of TDIBC in order to take advantage of the benefits of each of the methods used. Figure 8.5 shows an example of block diagram were TDIBCs are used in cascade.

As D-TDIBC was found to impose pure time-delays accurately [87], it is used here to tackle this specific task. The input signal of D-TDIBC is the outgoing wave $A^{\text{out}}(t)$ evaluated by the LES/DNS solver at the impedance boundary condition.

The output signal of D-TDIBC (the delayed outgoing wave) is given to a near-zero delay TDIBC (*e.g.* CBSBC-TF) as an input signal. Contrary to CBSBC-LEE, the reflection coefficient of this TDIBC is *complex* and the reflection coefficient has been modeled using a robust method suited for this purpose.

The output of the system is the ingoing wave $A^{\text{in}}(t)$ that is imposed by a Dirichlet boundary condition in the LES/DNS solver.

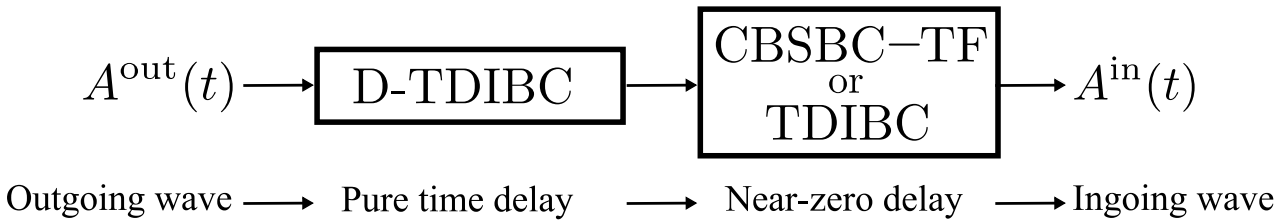


Figure 8.5: Block diagram of a example of Time Domain Impedance Boundary Conditions used in cascade.

8.5 Conclusion

The treatment of acoustic waves at the boundary conditions is a critical issue in LES and DNS, especially when studying combustion instabilities. Indeed, the thermoacoustic stability of a system can be assessed by the acoustic energy balance equation which is highly dependent on two factors: (1) the source/sink term (the Rayleigh criterion) and (2) the acoustic fluxes at the boundaries. Acoustic boundaries influence both of the aforementioned factors as: (1) the Rayleigh term may stabilize or destabilize the system depending on the phasing of the acoustic waves and (2) the acoustic fluxes depend on the modulus of reflection coefficients.

In this chapter, the fundamentals of Linear Time Invariant state-space modeling were recalled and the state-space representation of an acoustic boundary used by Jaensch *et al.* [91] in the Characteristic Based State-space Boundary Condition (CBSBC) was presented.

The focus was on the controllable canonical form formulation of CBSBC (referred to in this manuscript as CBSBC-TF). The link between the pole & residue TDIBC formulation (presented in Chapter 6 used in Chapter 7) and CBSBC-TF was discussed. It was shown that any pole & residue model can be recast as a state-space model in the CBSBC-TF formalism.

Numerical simulations were conducted to verify that no numerical issues were induced by the CBSBC-TF model create from a set of poles & residues. A perfect agreement was found between the two TDIBC formulations. However, when taking into account a large number of poles & residues (such as needed when imposing a pure time-delay), numerical issues were encountered when constructing the equivalent CBSBC-TF model. These numerical issues are due to ill-condition matrices when determining the coefficients of the state-space.

From this analysis, it follows that both approaches (pole & residue and CBSBC-TF) are flexible and reliable methods to impose an impedance (using the reflection coefficient) at a boundary condition. On one hand, the pole & residue is causal and stable by construction (the real part of the poles is negative which ensure the stability) and it was found to be robust and efficient to model both broadband reflection coefficients and pure time-delays. On the other hand, CBSBC-TF offers a great flexibility when modeling a broadband reflection coefficient due to the rational polynomial fit but this formulation was found to be inadequate to model time-delays.

CBSBC-LEE is an alternative characteristic-based state-space formulation which was developed specifically to handle time-delays. However, the reflection coefficient imposed by this method is a *real* delayed reflection coefficient (real reflection coefficient imposed after a time-delay τ) when, in fact, the physical reflection coefficient could be complex (complex reflection coefficient imposed after a time-delay τ).

An interesting perspective would be to keep the best of the two methods by combining them. This is possible, in theory, in the LTI framework where both TDIBC can be used in cascade. The advantage of such a system is that time-delay imposition and the complex physical reflection coefficient are dealt with separately making the modeling stage easier.

Time delays were found to be imposed in a cheap, memory efficient way by D-TDIBC (*cf.* Chapter 7) while undelayed reflection coefficient modeling is, in principle, effortless using CBSBC-TF. This broadband reflection coefficient can also be imposed by TDIBC such as in Chapter 6.

Conclusion and perspectives

In this manuscript, the study of several aspect allowing the investigation of combustion instabilities have been discussed. After recalling the governing equations and the numerical tools used here, the focus was on (1) the behavior of the dynamics of the acoustic modes during limit cycle, (2) the study of the flame response in a liquid rocket engine and (3) their possible driving mechanisms and the development and use of boundary conditions allowing to impose complex acoustic impedance in Euler and Navier-Stokes simulations.

Part I was dedicated on the study of a 42 H_2/O_2 injectors reduced-scale liquid rocket engine. First, a method called Instantaneous Modal decomposition (IMD) has been derived. It relies on the decomposition of a small number of pressure probes' signals as a weighted sum of Helmholtz eigenmodes. The weights are called "complex amplitudes" as they correspond to the temporal evolution of each of the eigenmodes. They are identified by projection of the pressure signals onto an orthogonal basis where the eigenmodes are the unit vectors. Although only a few pressure probes are needed for the analysis, the eigenmodes are three dimensional so that, the entire 3D acoustic field can be approximated using IMD's complex amplitudes. This can be useful in the combustion instability community as the acoustic velocity fluctuations are known to be a driving mechanism of flame/acoustic coupling.

IMD was validated on a cavity where five small cylinders are plugged to a larger cylinder as a simplified liquid rocket engine system. IMD gives a good estimate of the temporal evolution of the acoustic modes in the setup and the frequency of oscillation is recovered. The entire acoustic field is reconstructed with good agreement.

Second, IMD is applied to the BKD setup under one stable and one unstable conditions. Both LES and experimental pressure signals are studied using the eigenmodes identified in previous studies as the dominant modes in the setup.

The temporal amplitudes identified from the LES' pressure signals allow to study the dynamics of each acoustic mode considered and the initial orientation of the first tangential nodal line is found to affect the level of acoustic oscillation. The evolution of the nodal line orientation is further investigated using IMD's amplitudes which yields results in agreement with a method developed by DLR to this purpose. Although the first tangential mode is not identified as a rotating mode, the orientation varies by about 20° to 30° during the simulation.

The acoustic velocity and pressure fields are well approximated, especially in areas of interest for such applications, *i.e.* in the chamber near the injection faceplate and in the injector posts.

The temporal amplitudes corresponding to the experimental measurements have a much richer dynamics than in the LES and the spectra of IMD's amplitudes support the fact that the CIs in the operating point LP4 are due to the first tangential and the first radial modes. The orientation of the nodal line is reconstructed using IMD and the result are in excellent agreement with the DLR method. It is found that the nodal line has a preferred orientation around 130° while no clear preferred orientation was identified for the LP1 orientation point.

Next, a study a 3D time-resolved LES database of the BKD is done by a post-processing that allows to isolate the individual flame dynamics. The flame response to the two dominant acoustic modes – the first tangential and first radial modes – is studied. For both of these modes, the magnitude of the flame response is maximum for the flames facing the pressure anti-nodes of the combustion chamber. Conversely, the flames located at a pressure node respond weakly, suggesting that the lateral motion caused by transverse velocity fluctuations does not effectively feed energy into acoustics for sustaining this instability.

Focusing on the flame feeding most of the energy to the acoustic field, a mechanism is proposed in which the bulk pressure variation at the injector outlet generates unsteady shear through the variation of the hydrogen velocity, ultimately resulting in heat release rate fluctuations. The results indicate that the fluctuating pressure in the injection plane may be the relevant input for the flame response model. In fact, this input variable has been considered in the pioneer work of L. Crocco [173] in 1962 on transverse combustion instabilities in rocket engines. It receives here additional support from 3D unsteady numerical simulation.

Part II was focusing on Time Domain Impedance Boundary Conditions. The methodology of Fung and Ju [83, 84] and it was extended to model any reflection coefficient. The results show that the reflection coefficient is accurately imposed for both single-pole and multi-pole models.

A feature of impedance (or reflection coefficient) modeling is that it can account for one-dimensional acoustic wave propagation in the domain so that it can be used to truncate portion of the computational mesh. To achieve such a result, the TDIBC should model a complex exponential in the frequency domain which is equivalent to imposing a delay, called "time-delay", to the waves' reflection in the time domain. A modeling algorithm able to build TDIBC models accounting for such reflection coefficient was proposed and validated. The results show that the time-delay is accurately reproduced for one-dimensional wave propagation. Then, a thermoacoustically unstable methane-air laminar combustion setup was used as a final test case. A reference simulation comprising the entire domain was performed and the Delayed-TDIBC (D-TDIBC) was used to simulate the same setup on a shorter domain. The results show that both simulations are in excellent agreement as the power spectral density spectra are very close and that the mode shapes of the three first unstable modes are found

to be identical. The results demonstrate that D-TDIBC offers a flexible and cost-effective approach for numerical investigations of aeroacoustics and thermoacoustics.

Finally, another strategy for TDIBC, called Characteristic Based State-space Boundary Condition (CBSBC) [91], is presented. The controllable canonical form formulation of CBSBC was studied and it was shown that any Pole & Residue TDIBC model can be recast as a CBSBC model. Numerical simulations were performed with the two TDIBC strategies using (1) Pole & Residue models and (2) Pole & Residue models recast as CBSBC models. The agreement between both TDIBCs is excellent. However, high-order Pole & Residue models, such as the ones necessary for time-delay imposition, may result in ill-conditioned matrices when being recast as CBSBC models. From this study, it becomes clear that each of the approaches offers a reliable and flexible method to impose complex reflection coefficients in Euler and Navier-Stokes simulations.

The results presented in this manuscript offer new perspectives for future work.

First, as IMD's main interest relies on the acoustic velocity reconstruction, it should be used on experimental setup where hot wire measurements can be easily performed. Such a study will be useful to validate the added value of IMD in experimental studies were the velocity measurement are not possible.

The study of the individual response of each of the 42 flames has allowed to gain insights on the possible driving mechanisms for such flames. This topic should be further studied to determine the influence of bulk pressure fluctuations in the injection plane and bulk velocity fluctuations in the hydrogen and oxygen posts. Preliminary LESs of a single BKD flame have shown that the BKD flames are influenced differently by two kinds of velocity fluctuations. This study is in progress and has not been discussed in the manuscript. Preliminary results are shown in discussed in the Appendix D.

The Pole & Residue TDIBC based on the reflection coefficient is promising and should be applied on other configurations to test the robustness of such methods. Recent studies [212] have stressed the fact that most of the acoustic dissipation taking place in aero-engines are due to perforated plates and dilution holes. Although acoustic dissipation due to these features have been studied [213–217] and that dissipation models exists [218–221], it is still an active field of research and the systematic use of TDIBC could lead to significant improvements in the assessment of thermoacoustic instability.

Imposing a time-delay is now possible and this feature should be used on more complex geometries. Although it has been mentioned in this thesis, the capacity to investigate several geometries with a single domain has not been demonstrated. In future work, D-TDIBC should be used to study the effect of the length of a part of the domain, *e.g.* the length of a plenum, on the stability of the system.

Finally, the state-space (CBSBC) and the Pole & Residue approaches could be used in cascade in order to take advantage of the benefits of both methods.

Appendix A

D-TDIBC Model: 1D wave propagation problem

R_k	a_k	b_k	c_k	d_k	$\omega_{0,k}$ [rad s^{-1}]	f_0 [Hz]
$k = 1$	4.91e+05	4.56e+05	-3.23e+03	3.48e+03	4.75e+03	7.56e+02
$k = 2$	-1.10e+04	-7.38e+03	-9.52e+02	1.42e+03	1.71e+03	2.72e+02
$k = 3$	-8.21e+04	-3.92e+04	-1.38e+03	2.89e+03	3.20e+03	5.09e+02
$k = 4$	-1.33e+05	-4.66e+04	-1.50e+03	4.29e+03	4.54e+03	7.23e+02
$k = 5$	-6.17e+04	-1.39e+04	-1.30e+03	5.79e+03	5.93e+03	9.44e+02
$k = 6$	-3.22e+04	-5.12e+03	-1.15e+03	7.26e+03	7.35e+03	1.17e+03
$k = 7$	-1.73e+04	-2.04e+03	-1.03e+03	8.73e+03	8.79e+03	1.40e+03
$k = 8$	-1.19e+02	2.65e+07	-2.17e+02	-9.77e-04	2.17e+02	3.46e+01
$k = 9$	-2.11e+00	6.77e+04	-1.89e+00	-5.88e-05	1.89e+00	3.01e-01
$k = 10$	-9.15e+03	-8.40e+02	-9.34e+02	1.02e+04	1.02e+04	1.63e+03
$k = 11$	-1.32e+05	-1.15e+05	-7.95e+03	9.11e+03	1.21e+04	1.92e+03
$k = 12$	6.55e+02	5.49e+02	-5.20e+02	6.20e+02	8.09e+02	1.29e+02
$k = 13$	-5.04e+03	-4.09e+02	-9.40e+02	1.16e+04	1.16e+04	1.85e+03
$k = 14$	-2.25e+03	-1.70e+02	-9.78e+02	1.30e+04	1.30e+04	2.07e+03
$k = 15$	-3.80e+01	-8.77e+07	-7.84e+01	3.40e-05	7.84e+01	1.25e+01
$k = 16$	-7.67e+03	-9.34e+02	-1.80e+03	1.48e+04	1.49e+04	2.37e+03
$k = 17$	6.89e+00	1.17e-01	-1.61e+02	9.46e+03	9.46e+03	1.51e+03
$k = 18$	-1.50e+01	1.75e+06	-2.93e+01	-2.51e-04	2.93e+01	4.67e+00
$k = 19$	3.82e+03	3.80e+02	-1.50e+03	1.50e+04	1.51e+04	2.40e+03
$k = 20$	-6.06e+00	-7.54e+05	-9.40e+00	7.56e-05	9.40e+00	1.50e+00

Table A.1: poles & residues used in the one-dimensional pure delayed Gaussian wave propagation problem.

Appendix B

D-TDIBC Model: 2D reactive DNS of the INTRIG Burner

R_k	a_k	b_k	c_k	d_k	$\omega_{0,k}$ [rad s^{-1}]	f_0 [Hz]
$k=1$	1.91e+05	-5.06e+04	-8.06e+03	-3.04e+04	3.14e+04	5.00e+03
$k=2$	-3.24e+06	-1.10e+07	-1.83e+04	5.39e+03	1.91e+04	3.04e+03
$k=3$	1.47e+06	1.97e+06	-1.17e+04	8.74e+03	1.46e+04	2.32e+03
$k=4$	5.20e+05	2.55e+05	-9.61e+03	1.96e+04	2.18e+04	3.47e+03
$k=5$	1.33e+03	-3.60e+09	-2.74e+03	-1.01e-03	2.74e+03	4.37e+02
$k=6$	5.06e+02	-1.41e+09	-1.06e+03	-3.81e-04	1.06e+03	1.69e+02
$k=7$	7.45e+05	1.08e+06	-3.97e+04	2.75e+04	4.83e+04	7.69e+03
$k=8$	-2.45e+03	-2.62e+02	-3.78e+03	3.54e+04	3.56e+04	5.66e+03
$k=9$	3.15e+04	4.45e+03	-5.68e+03	4.02e+04	4.06e+04	6.46e+03
$k=10$	6.28e-03	-1.01e+05	-6.28e-03	-3.93e-10	6.28e-03	1.00e-03
$k=11$	2.16e+02	-3.31e+07	-3.85e+02	-2.51e-03	3.85e+02	6.13e+01
$k=12$	1.86e+01	2.39e-03	-1.08e-02	8.46e+01	8.46e+01	1.35e+01
$k=13$	7.04e-01	3.79e-14	-4.51e-12	8.38e+01	8.38e+01	1.33e+01
$k=14$	5.11e+03	6.29e+02	-6.01e+03	4.88e+04	4.92e+04	7.83e+03
$k=15$	2.66e+05	1.33e+05	-2.10e+04	4.20e+04	4.70e+04	7.47e+03
$k=16$	1.89e+01	2.85e+05	-6.39e+01	4.24e-03	6.39e+01	1.02e+01
$k=17$	6.76e+03	1.68e+03	-5.56e+03	2.23e+04	2.30e+04	3.66e+03
$k=18$	5.92e+01	-6.50e+01	-1.14e+02	-1.04e+02	1.54e+02	2.45e+01

Table B.1: poles & residues used in the two-dimensional reactive DNS of the INTRIG Burner.

Appendix C

Laplace transform

The study of a time varying function $f(t)$ is often done using spectral analysis, that is the study of the function f in the frequency domain. In the frequency domain, one can either use the Fourier or the Laplace space. The Fourier space uses the frequency f of the angular frequency $\omega = 2\pi f$, which are real-valued. The study in Fourier space is performed using the bi-lateral Fourier Transform $\mathcal{F}$, that is for negative and positive times: $t \in [-\infty, \infty]$. In the Laplace space, the Laplace variable $s = \sigma + i\omega$ is the complex frequency where i it the imaginary unit $i = \sqrt{-1}$. Studies in the Laplace space are often limited to positive times, that is $t > 0$ as the one-sided causal Laplace transform $\mathcal{L}$ is used.

$$F(s) = \mathcal{L}\left[f(t)\right] = \int_0^\infty f(t)e^{-st}dt \tag{C.1}$$

A following property of the one-sided Laplace transform in Eq. C.1 is that the Laplace transform of a function is a holomorphic function of the variable s, that is infinitely complex differentiable at the neighborhood of all points in the domain [186, 187]. This property allows for the time derivative of a function to map to the Laplace transform $F(s)$:

$$\mathcal{L}\left[\frac{df(t)}{dt}\right] = sF(s) \tag{C.2}$$

This property makes it very-well suited to the linear differential equations problems found in many engineering applications. Using Eq. C.2, time domain linear differential equations can be transformed into a polynomial in the frequency domain and *vice versa*.

The inverse Laplace transform of the one-sided Laplace transform is:

$$f(t) = \mathcal{L}^{-1}\left[F(s)\right] = \frac{1}{2\pi i}\lim_{R\to\infty}\int_{\sigma 1-iR}^{\sigma_1+iR} F(s)e^{st}ds \tag{C.3}$$

These relations are extremely useful in control theory and are fundamental for the state-space modeling approach.

Appendix D

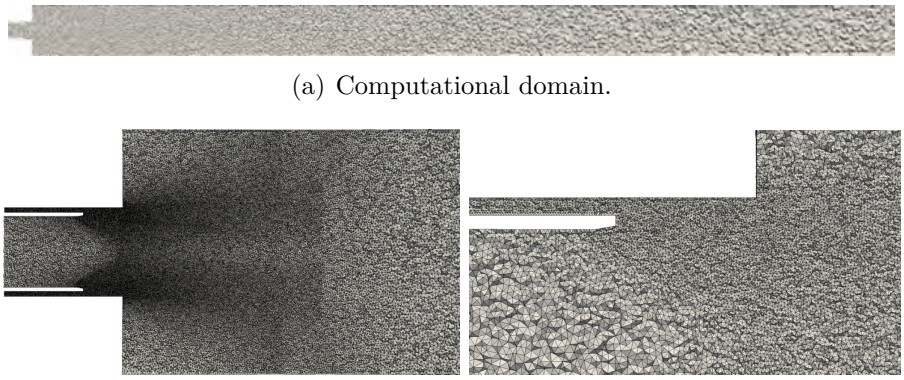
Single BKD flame simulation

A preliminary study of a single-injector configuration illustrated how the flame responds to a pulsation in the hydrogen stream with the formation of large coherent structures at the edges of the dense oxygen core. Further studies will be dedicated to the quantification of the flame response, through Flame Transfer Functions, as well as the comparison of the response to hydrogen and oxygen stream pulsation. This appendix is from Urbano et al. *[222] (EUCASS conference paper).*

The analysis conducted in Chapter. 5 indicates that the coaxial diffusion flames typically used in liquid rocket engines respond in a fairly complex way to transverse acoustic modes. The overall picture is that the flames driving the instability are those near the pressure antinode, which in fact only experience a bulk pressure fluctuation at the injector outlet and negligible transverse velocity fluctuations. It was speculated by Urbano et al. [121] that these flames do not directly respond to the pressure fluctuation but rather to the subsequent fluctuations of reactants' mass flow rates. As a consequence, it is assumed that the study of a single flame submitted to fluctuating flow rate could be relevant for the understanding of the physical mechanisms driving the response of flames located at a pressure antinode in a transverse mode. In this Section, we present preliminary results in this line of thought.

The computational domain and mesh are presented in Fig. D.1. The fuel and oxidizer manifolds have been cut out and only a short length of the injector was kept. The length of the combustion chamber is equal to that of the full engine (cf. Fig. D.1(a)) and in order to maintain the confinement of the flame, the cross-section corresponds to 1/42 of the real chamber. A zoom on the mesh in the near-injector region is shown in Figs. D.1(b) and D.1(c). The resolution in the wake of the lip separating the two streams is $\Delta = 35$ μm and it is kept over one injector diameter. The mesh is then slowly coarsened. Finally, this computation is performed with the exact same numerical parameters and models as that of the full engine and only the operating conditions of LP4 are considered.

The dynamics of this type of flame is very strong, even under steady-state conditions. Indeed, the large velocity difference between the hydrogen ($u_{H_2} = 318$ ms^{-1}) and oxygen ($u_{O_2} = 12.9$ ms^{-1}) streams generates a strong shear enhancing the heat release rate and favoring the development of vortices. An instantaneous iso-surface of the temperature field



(a) Computational domain.

(b) Injector. (c) Recess.

Figure D.1: Longitudinal cuts through the mesh for the LES of the single injector.

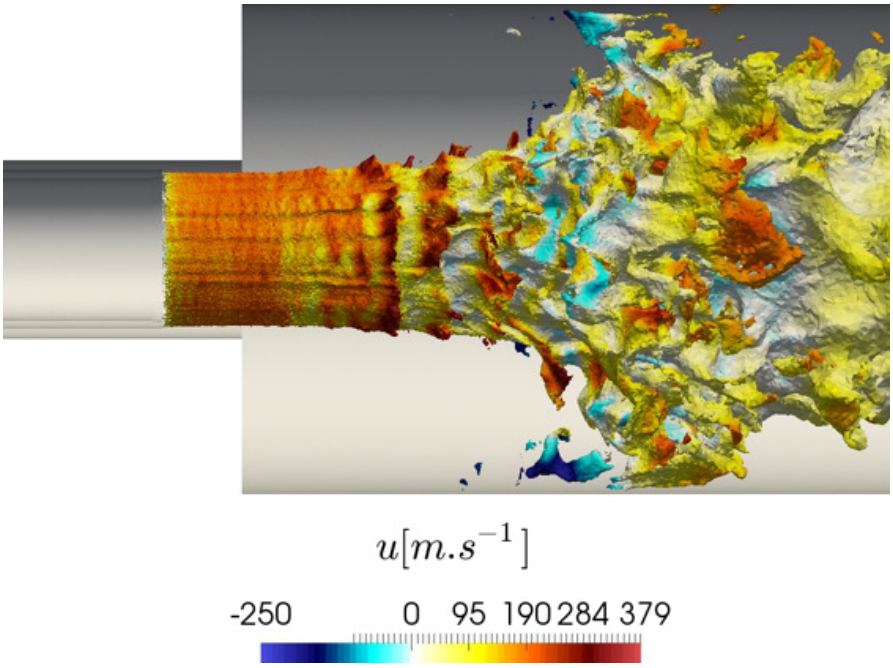


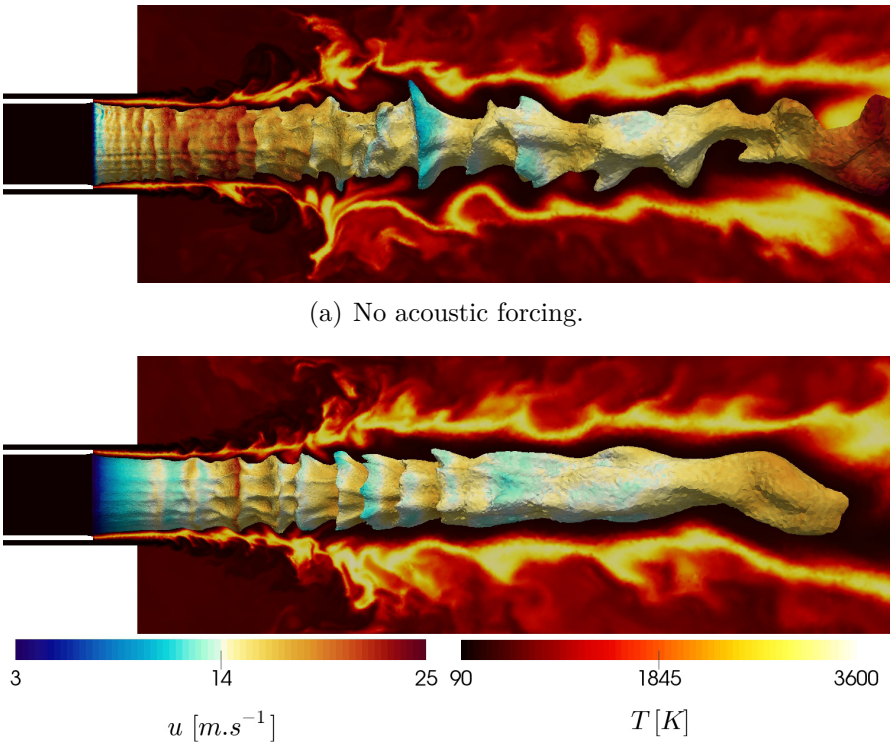
Figure D.2: Instantaneous temperature iso-surface colored by axial velocity, without acoustic forcing.

is shown in Fig. D.2. In the recessed region, the flame remains almost cylindrical but at the entrance of the combustion chamber, vortical structures quickly develop. After two injector diameters, the flame expands abruptly, a behavior typically observed in experiments under these conditions. Downstream of this sudden expansion, the flame is much less convoluted as seen at the far right of Fig. D.2.

Once the flame length is statistically converged (in this case after 25 ms, which corresponds to 1.5 flow-through time of the oxygen stream), the configuration is submitted to acoustic fluctuations. As shown in Chapter 5, the flames responding the most to the transverse mode are those located at a pressure anti-node. Consequently, forcing a single flame with a bulk

pressure fluctuation may be a valid procedure. However, it is suspected that the actual mechanism through which the flame responds involves velocity fluctuations in the oxygen and/or hydrogen streams. In this preliminary study, we focus on the influence of hydrogen velocity fluctuations. Indeed, because the hydrogen stream is much faster, at similar levels of relative fluctuations, the variations of shear stress and strain on the flame can be expected to be larger. These parameters are known to favor the formation of vortical structures and increase the reaction rates, two mechanisms usually involved in the unsteady flame response.

We choose here to force the hydrogen stream at 15 % of its bulk velocity, which is in the range observed in the LES of the full engine [136]. The frequency is that of the first transverse mode, which is unstable for LP4. Figure D.3 compares instantaneous fields of the forced and unforced cases. An iso-surface of density ($\rho = 500$ kg.m^{-3}) illustrates the dynamics of the dense oxygen jet and a longitudinal cut of instantaneous temperature shows the shape of the flame. The differences in the temperature fields are not obvious on these snapshots: both



(a) No acoustic forcing.

(b) Acoustic forcing of hydrogen stream.

Figure D.3: LES of the single injector: longitudinal cut of temperature and iso-surface of density ($\rho = 500$ kg.m^{-3}) colored by axial velocity.

show a fairly flat flame in the recessed region, followed by an intense wrinkling at the region of sudden expansion. the flame then becomes smoother. However, the dense oxygen cores appear qualitatively different. For the case without acoustic forcing (Fig. D.3(a)), small-scale wrinkles are formed from the beginning of the mixing layer. These structures grow and merge to form structures of the same size as the jet diameter around the location of the flame radial expansion. For the forced case (Fig. D.3(b)), the small-scale structures are not apparent in

the early stages. Instead, structures of roughly constant wavelength grow after the recessed region, which are dictated by the frequency of the acoustic forcing. The dense core length appears to be shortened which must be confirmed on averaged fields. At this point is the study, only a qualitative analysis has been performed. In the next steps, time series of heat release rate will be used to measure the gain and phase of the flame response.

Bibliography

[1] R. F. Sawyer. Science based policy for adressing energy and environmental problems. *Proc. Combust. Inst.* , 32:45–56, 2009.

[2] Michael Jefferson. A global energy assessment. *Wiley Interdisciplinary Reviews: Energy and Environment*, 5(1):7–15, 2016.

[3] Aylin Çiğdem Köne and Tayfun Büke. Forecasting of co 2 emissions from fuel combustion using trend analysis. *Renewable and Sustainable Energy Reviews*, 14(9):2906–2915, 2010.

[4] Dale M Brown and Bernard Gorowitz. Combustion control apparatus and method. European Patent Application No 0 677 706 A1, 95/42, General Electric Company, 1993.

[5] Nicolas Docquier and Sébastien Candel. Combustion control and sensors: a review. *Progress in energy and combustion science*, 28(2):107–150, 2002.

[6] S. Candel, D. Durox, T. Schuller, N. Darabiha, L. Hakim, and T. Schmitt. Advances in combustion and propulsion applications. *European Journal of Mechanics - B/Fluids*, 40(0):87 – 106, 2013.

[7] S. Candel, D. Durox, and T. Schuller. Flame interactions as a source of noise and combustion instabilities. In *10th AIAA/CEAS Aeroacoustics Conference - AIAA 2004-2928*, 2004.

[8] S. Candel, D. Durox, S. Ducruix, A.L. Birbaud, N. Noiray, and T. Schuller. Flame dynamics and combustion noise : progress and challenges. *International Journal of Aeroacoustics*, 8:1–56, 2009.

[9] T. Poinsot and D. Veynante. *Theoretical and Numerical Combustion*. Third Edition, 2011.

[10] T. Lieuwen. *Unsteady Combustor Physics*. Cambridge Univ Press, 2012.

[11] D. G. Crighton, A. P. Dowling, J. E. Ffowcs Williams, M. Heckl, and F. Leppington. *Modern methods in analytical acoustics*. Lecture Notes. Springer Verlag, New-York, 1992.

[12] T. P. Bui, W. Schröder, and M. Meinke. Acoustic perturbation equations for reacting flows to compute combustion noise. *International Journal of Aeroacoustics*, 6:335–355, 2007.

[13] A. H. Lefebvre. *Gas Turbines Combustion*. Taylor & Francis, 1999.

[14] FEC Culick, V Burnley, and G Swenson. Pulsed instabilities in solid-propellant rockets. *Journal of Propulsion and Power*, 11(4):657–665, New York, NY, American Institute of Aeronautics and Astronautics, 1995.

[15] S. Candel. Combustion dynamics and control: progress and challenges. *Proc. Combust. Inst.* , 29(1):1–28, 2002.

[16] Catherine J Goy, Stuart R James, and Suzanne Rea. Monitoring combustion instabilities: E. on uk's experience. *Progress in Astronautics and Aeronautics*, 210:163, 2005.

[17] Ying Huang and Vigor Yang. Dynamics and stability of lean-premixed swirl-stabilized combustion. *Prog. Energy Combust. Sci.* , 35(4):293–364, 2009.

[18] F. E. C. Culick and P. Kuentzmann. *Unsteady Motions in Combustion Chambers for Propulsion Systems*. NATO Research and Technology Organization, 2006.

[19] F. E. C. Culick. Combustion instabilities in liquid-fueled propulsion systems- an overview. In *AGARD 72B PEP meeting*, 1988.

[20] Joseph C Oefelein and Vigor Yang. Comprehensive review of liquid-propellant combustion instabilities in f-1 engines. *J. Prop. Power* , 9(5):657–677, 1993.

[21] T. Poinsot. Prediction and control of combustion instabilities in real engines. *Proc. Combust. Inst.* , pages 1–28, 2017.

[22] Yang and Anderson. Liquid rocket engine combustion instability, progress in astronautics and aeronautics. *AIAA*, 169, 1995.

[23] M. Ihme, H. Pitsch, and H. Bodony. Radiation of noise in turbulent flames. *Proc. Combust. Inst.* , 32:1545–1554, 2009.

[24] M. J. Brear, F. Nicoud, M. Talei, A. Giauque, and E. R. Hawkes. Disturbance energy transport and sound production in gaseous combustion. *Journal of Fluid Mechanics*, 707:53–73, 8 2012.

[25] MK Myers. Transport of energy by disturbances in arbitrary steady flows. *J. Fluid Mech.* , 226:383–400, 1991.

[26] L. Rayleigh. The explanation of certain acoustic phenomena. *Nature*, July 18:319–321, 1878.

[27] L. Rayleigh. *The Theory of Sound*. Mac Millan (reprinted by Dover, New York, 1945), 1894.

[28] F. Nicoud and T. Poinsot. Thermoacoustic instabilities: should the rayleigh criterion be extended to include entropy changes ? *Combust. Flame*, 142:153–159, 2005.

[29] A. Trouvé, D. Veynante, K. N. C. Bray, and T. Mantel. The coupling between flame surface dynamics and species mass conservation in premixed turbulent combustion. In *Proc. of the Summer Program* , pages 95–124. Center for Turbulence Research, NASA Ames/Stanford Univ., 1994.

[30] T. Poinsot, S. Candel, and A. Trouvé. Application of direct numerical simulation to premixed turbulent combustion. *Prog. Energy Combust. Sci.* , 21:531–576, 1996.

[31] T. Poinsot. Using direct numerical simulation to understand turbulent premixed combustion (plenary lecture). *Proc. Combust. Inst.* , 26:219–232, 1996.

[32] T. Poinsot, M. Baum, A. Trouvé, and S. Candel. Simulation directe de la combustion turbulente. *Images des mathématiques - CNRS*, pages 89–99, 1996.

[33] L. Vervisch and T. Poinsot. Direct numerical simulation of non premixed turbulent flames. *Ann. Rev. Fluid Mech.* , 30:655–692, 1998.

[34] D. Thevenin. Three-dimensional direct simulations and structure of expanding turbulent methane flames. *Proc. Combust. Inst.* , 30:in press, 2004.

[35] Alexei Y Poludnenko and Elaine S Oran. The interaction of high-speed turbulence with flames: Global properties and internal flame structure. *Combustion and Flame*, 157(5):995–1011, 2010.

[36] A. N. Kolmogorov. The local structure of turbulence in incompressible viscous fluid for very large reynolds numbers. *C. R. Acad. Sci. , USSR*, 30:301, 1941.

[37] A. N. Kolmogorov. A refinement of hypothesis concerning the local structure of turbulence in a viscous incompressible fluid at high reynolds number. *J. Fluid Mech.* , 62:82, 1962.

[38] S. B. Pope. *Turbulent flows*. Cambridge University Press, 2000.

[39] Suresh Menon and Wen-Huei Jou. Large-eddy simulations of combustion instability in an axisymmetric ramjet combustor. *Combustion Science and Technology*, 75(1-3):53–72, 1991.

[40] H. Pitsch. Large eddy simulation of turbulent combustion. *Ann. Rev. Fluid Mech.* , 38:453–482, 2006.

[41] P. Schmitt, T. Poinsot, B. Schuermans, and K. P. Geigle. Large-eddy simulation and experimental study of heat transfer, nitric oxide emissions and combustion instability in a swirled turbulent high-pressure burner. *J. Fluid Mech.* , 570:17–46, 2007.

[42] G. Staffelbach, L.Y.M. Gicquel, G. Boudier, and T. Poinsot. Large eddy simulation of self-excited azimuthal modes in annular combustors. *Proc. Combust. Inst.* , 32:2909–2916, 2009.

[43] Benedetta Franzelli, Eleonore Riber, Laurent Y.M. Gicquel, and Thierry Poinsot. Large eddy simulation of combustion instabilities in a lean partially premixed swirled flame. *Combust. Flame*, 159(2):621 – 637, 2012.

[44] P. Wolf, G. Staffelbach, L. Gicquel, J-D Muller, and T. Poinsot. Acoustic and large eddy simulation studies of azimuthal modes in annular combustion chambers. *Combust. Flame*, 159(11):3398–3413, November 2012.

[45] Romain Garby, Laurent Selle, and Thierry Poinsot. Large-eddy simulation of combustion instabilities in a variable-length combustor. *C. R. Acad. Sci. Mecanique*, 341(1 - 2):220 – 229, 2013.

[46] Christian Kraus, Laurent Selle, Thierry Poinsot, Christoph M Arndt, and Henning Bockhorn. Influence of heat transfer and material temperature on combustion instabilities in a swirl burner. *J. Eng. Gas Turb. and Power* , 139(5):051503, 2017.

[47] F. Nicoud, L. Benoit, C. Sensiau, and T. Poinsot. Acoustic modes in combustors with complex impedances and multidimensional active flames. *AIAA J.* , 45:426–441, 2007.

[48] F. Nicoud and K. Wieczorek. About the zero mach number assumption in the calculation of thermoacoustic instabilities. *Int. J. Spray and Combustion Dynamic*, 1:67–112, 2009.

[49] Moritz Schulze, Annafederica Urbano, Max Zahn, Martin Schmid, Thomas Sattelmayer, and Michael Oschwald. Thermoacoustic feedback analysis of a cylindrical combustion chamber under supercritical conditions. In *50th AIAA/ASME/SAE/ASEE Joint Propulsion Conference*, page 3776, 2014.

[50] Moritz Schulze and Thomas Sattelmayer. Linear stability assessment of a cryogenic rocket engine. *International Journal of Spray and Combustion Dynamics*, 2016.

[51] L. Crocco. Aspects of combustion instability in liquid propellant rocket motors. Part I. *J. American Rocket Society* , 21:163–178, 1951.

[52] L. Crocco. Aspects of combustion instability in liquid propellant rocket motors. part II. *J. American Rocket Society* , 22:7–16, 1952.

[53] Sébastien Ducruix, Daniel Durox, and Sébastien Candel. Theoretical and experimental determinations of the transfer function of a laminar premixed flame. *Proc. Combust. Inst.* , 28(1):765–773, 2000.

[54] T. Schuller, D. Durox, and S. Candel. A unified model for the prediction of laminar flame transfer functions: comparisons between conical and v-flames dynamics. *Combust. Flame*, 134:21–34, 2003.

[55] N. Noiray, D. Durox, T. Schuller, and S. Candel. A unified framework for nonlinear combustion instability analysis based on the flame describing function. *J. Fluid Mech.* , 615:139–167, 2008.

[56] A.L. Birbaud, D. Durox, and S. Candel. Upstream flow dynamics of a laminar premixed conical flame submitted to acoustic modulations. *Combust. Flame*, 146(3):541–552, 2006.

[57] L. Selle, L. Benoit, T. Poinsot, F. Nicoud, and W. Krebs. Joint use of compressible large-eddy simulation and Helmholtz solvers for the analysis of rotating modes in an industrial swirled burner. *Combust. Flame*, 145(1-2):194–205, 2006.

[58] A. Giauque, T. Poinsot, and F. Nicoud. Validation of a flame transfer function reconstruction method for complex turbulent configurations. *14th AIAA/CEAS Aeroacoustics Conference (29th AIAA Aeroacoustics Conference)*, May 2008.

[59] Emilien Courtine, Laurent Selle, and Thierry Poinsot. DNS of intrinsic thermoacoustic modes in laminar premixed flames. *Combust. Flame*, in press:–, 2015.

[60] A. Ghani, T. Poinsot, L. Gicquel, and G. Staffelbach. LES of longitudinal and transverse self-excited combustion instabilities in a bluff-body stabilized turbulent premixed flame. *Combust. Flame*, 162 (11):4075–4083, 2015.

[61] C. F. Silva, F. Nicoud, T. Schuller, D. Durox, and S. Candel. Combining a Helmholtz solver with the flame describing function to assess combustion instability in a premixed swirled combustor. *Combust. Flame*, 160(9):1743 – 1754, 2013.

[62] Laurent Selle, Rodolphe Blouquin, Marie Théron, Luc-Henry Dorey, Martin Schmid, and William Anderson. Prediction and analysis of combustion instabilities in a model rocket engine. *J. Prop. Power* , 30(4):078–990, jun 2014.

[63] Jutta Pieringer, Thomas Sattelmayer, and Felix Fassl. Simulation of combustion instabilities in liquid rocket engines with acoustic perturbation equations. *J. Prop. Power* , 25(5):1020–1031, sep 2009.

[64] R Glav and M Åbom. A general formalism for analyzing acoustic 2-port networks. *Journal of Sound and Vibration*, 202(5):739–747, 1997.

[65] C. O. Paschereit and W. Polifke. Characterization of lean premixed gas-turbine burners as acoustic multi-ports. In *Bulletin of the American Physical Society / Division of Fluid Dynamics*, San Francisco, California, USA, 1997.

[66] BBH Schuermans, W Polifke, and CO Paschereit. Modeling transfer matrices of premixed flames and comparison with experimental results. *ASME, International Gas Turbine and Aeroengine Congress and Exhibition, Indianapolis, IN*, 1999.

[67] W. Polifke, C. Paschereit, and K. Doebbeling. Constructive and destructive interference of acoustic and entropy waves in a premixed combustor with a choked exit. *Int. J. Acoust. Vib.* , 6:135–146, 2001.

[68] T Sattelmayer and W Polifke. Assessment of methods for the computation of the linear stability of combustors. *Combustion Science and Technology*, 175(3):453–476, 2003.

[69] T. Schuller, D. Durox, and S. Candel. Self-induced combustion oscillations of laminar premixed flames stabilized on annular burners. *Combust. Flame*, 135:525–537, 2003.

[70] J. Kopitz, A. Huber, T. Sattelmayer, and W. Polifke. Thermoacoustic stability analysis of an annular combustion chamber with acoustic low order modeling and validation against experiment. In *Int'l Gas Turbine and Aeroengine Congress & Exposition*, ASME GT2005-68797 , Reno, NV, U.S.A., 2005.

[71] Jan Kopitz and Wolfgang Polifke. Cfd-based application of the nyquist criterion to thermo-acoustic instabilities. *Journal of Computational Physics*, 227(14):6754–6778, 2008.

[72] R. Kaess, W. Polifke, T. Poinsot, N. Noiray, D. Durox, T. Schuller, and S. Candel. Cfd-based mapping of the thermo-acoustic stability of a laminar premix burner. In *Proc. of the Summer Program* , pages 289–302, Center for Turbulence Research, NASA AMES, Stanford University, USA, 2008.

[73] N. Noiray, M. Bothien, and B. Schuermans. Investigation of azimuthal staging concepts in annular gas turbines. *Combust. Theor. Model.* , pages 585–606, 2011.

[74] N Noiray and B Schuermans. On the dynamic nature of azimuthal thermoacoustic modes in annular gas turbine combustion chambers. *Proceedings of the Royal Society A: Mathematical, Physical and Engineering Sciences*, 469(2151):20120535, December 2012.

[75] Nicolas Noiray and Bruno Schuermans. Theoretical and experimental investigations on damper performance for suppression of thermoacoustic oscillations. *Journal of sound and vibration*, 331(12):2753–2763, 2012.

[76] J.-F. Parmentier, P. Salas, P. Wolf, G. Staffelbach, F. Nicoud, and T. Poinsot. A simple analytical model to study and control azimuthal instabilities in annular combustion chambers. *Combust. Flame*, 159(7):2374–2387, 2012.

[77] Michael Bauerheim, Jean-Francois Parmentier, Pablo Salas, Franck Nicoud, and Thierry Poinsot. An analytical model for azimuthal thermoacoustic modes in an annular chamber fed by an annular plenum. *Combust. Flame*, 161(5):1374 – 1389, 2014.

[78] Tobias Hummel, Constanze Temmler, Bruno Schuermans, and Thomas Sattelmayer. Reduced-order modeling of aeroacoustic systems for stability analyses of thermoacoustically noncompact gas turbine combustors. *Journal of Engineering for Gas Turbines and Power*, 138(5), 2016.

[79] Maxence Brebion. *Joint numerical and experimental study of thermoacoustic instabilities*. PhD thesis, Institut de Mécanique des Fluides de Toulouse, 2017.

[80] W. Polifke and C. O. Paschereit. Determination of thermo-acoustic transfer matrices by experiment and computational fluid dynamics. In *ERCOFTAC bulletin*, page 38, 1998.

[81] C. O. Paschereit and E. Gutmark. Control of thermoacoustic instabilities in a premixed combustor by fuel modulation. In AIAA Paper 99-0711, editor, *37th AIAA Aerospace Sciences Meeting and Exhibit*, Reno, NV, 1999.

[82] W. Polifke, A. Poncet, C. O. Paschereit, and K. Doebbeling. Reconstruction of acoustic transfer matrices by instationnary computational fluid dynamics. *J. Sound Vib.* , 245(3):483–510, 2001.

[83] K. Y. Fung and H. B. Ju. Broadband time-domain impedance models. *AIAA J.* , 39(8):1449–1454, 2001.

[84] K-Y Fung and Hongbin Ju. Time-domain impedance boundary conditions for computational acoustics and aeroacoustics. *Int. J. Comput. Fluid Dynamics* , 18(6):503–511, 2004.

[85] Carlo Scalo, Julien Bodart, and Sanjiva K. Lele. Compressible turbulent channel flow with impedance boundary conditions. *Phys. Fluids* , 27(3), 2015.

[86] Jeffrey Lin, Carlo Scalo, and Lambertus Hesselink. High-fidelity simulation of a standing-wave thermoacoustic–piezoelectric engine. *J. Fluid Mech.* , 808:19–60, 2016.

[87] Quentin Douasbin, Carlo Scalo, Laurent Selle, and Thierry Poinsot. Delayed-time domain impedance boundary condition *[in review]*. *J. Comput. Phys.* , 2017.

[88] Quentin Douasbin, Carlo Scalo, Laurent Selle, and Thierry Poinsot. Modeling approach for delayed time domain impedance boundary condition. *23rd AIAA/CEAS Aeroacoustics Conference*, page 3506, 2017.

[89] Q Douasbin, L Selle, T Poinsot, and C Scalo. Causal multi-pole approximation of delayed time domain impedance boundary conditions (d-tdibc). *23rd AIAA/CEAS Aeroacoustics Conference*, 2017.

[90] Roland Kaess, Andreas Huber, and Wolfgang Polifke. Time-domain impedance boundary condition for compressible turbulent flows. In *14th AIAA/CEAS Aeroacoustics Conference, Vancouver, May*, pages 5–9, 2008.

[91] Stefan Jaensch, Carlo Sovardi, and Wolfgang Polifke. On the robust, flexible and consistent implementation of time domain impedance boundary conditions for compressible flow simulations. *J. Comput. Phys.* , 314:145–159, 2016.

[92] Albert Einstein. Die grundlage der allgemeinen relativitätstheorie. *Annalen der Physik und Chemie*, 1916.

[93] K. K. Kuo. *Principles of combustion.* John Wiley & Sons, Inc., Hoboken, New Jersey, 2005 Second Edition.

[94] Stéphane Sanquer, Pascal Bruel, and Bruno Deshaies. Some specific characteristics of turbulence in the reactive wakes of bluff bodies. *AIAA J.* , 36(6):994–1001, 1998.

[95] S. Kotake. On combustion noise related to chemical reactions. *J. Sound Vib.* , 42:399–410, 1975.

[96] M. L. Munjal. *Acoustics of Ducts and Mufflers*. John Wiley & Sons, 1986.

[97] Center for Turbulence Research, editor. *Analysis of a transverse combustion instability in a full rocket engine under supercritical conditions*, Stanford, CA, USA, L. Selle, A. Urbano, Q. Douasbin, T. Schmitt and S. Ducruix. Proceedings of the Summer Program 2016.

[98] T. Schmitt. *Simulation des grandes échelles de la combustion turbulente en régime supercritique*. PhD thesis, Université de Toulouse - Ecole doctorale MEGeP, CERFACS - CFD Team, Toulouse, June 2009.

[99] T. Schmitt, L. Selle, A. Ruiz, and B. Cuenot. Large-eddy simulation of supercritical-pressure round jets. *AIAA J.* , 48(9):2133–2144, September 2010.

[100] T. Schmitt, Y. Méry, M. Boileau, and S. Candel. Large-eddy simulation of methane/oxygen flame under transcritical conditions. *Proc. Combust. Inst.*, 33, 2011.

[101] Giorgio Soave. Equilibrium constants from a modified redlich-kwong equation of state. *Chem. Eng. Sci.* , 27(6):1197–1203, 1972.

[102] S. H. Chung and C. K. Law. An integral analysis of the structure and propagation of premixed flames. *Combust. Flame*, 72:325–336, 1988.

[103] T. Schönfeld and M. Rudgyard. Steady and unsteady flows simulations using the hybrid flow solver avbp. *AIAA J.* , 37(11):1378–1385, 1999.

[104] V. Moureau, G. Lartigue, Y. Sommerer, C. Angelberger, O. Colin, and T. Poinsot. Numerical methods for unsteady compressible multi-component reacting flows on fixed and moving grids. *J. Comput. Phys.* , 202(2):710–736, 2005.

[105] N Gourdain, L Gicquel, M Montagnac, O Vermorel, M Gazaix, G Staffelbach, M Garcia, JF Boussuge, and T Poinsot. High performance parallel computing of flows in complex geometries: I. methods. *Comput. Sci. Disc.*, 2:015003, 2009.

[106] P. D. Lax and B. Wendroff. Systems of conservation laws. *Commun. Pure Appl. Math.* , 13:217–237, 1960.

[107] J. Donea. Taylor-galerkin method for convective transport problems. *Int. J. Numer. Meth. Fluids* , 20(1):101–119, 1984.

[108] J. Donéa, S. Giuliani, H. Laval, and L. Quartapelle. Time-accurate solution of advection-diffusion problems by finite elements. *Comput. Methods Appl. Mech. Eng.* , 45:123–145, 1984.

[109] J. Donea, L. Quartapelle, and V. Selmin. An analysis of time discretization in the finite element solution of hyperbolic problems. *J. Comput. Phys.* , 70:463–499, 1987.

[110] J. Donea and A. Huerta. *Finite Element Methods for Flow Problems*. John Wiley & Sons Inc, New York, 2003.

[111] CERFACS. *AVBP Handbook - http://cerfacs.fr/∼ avbp/AVBP_V5.X/HANDBOOK*. CERFACS, 2009.

[112] F. Nicoud, J. Baggett, P. Moin, and W. Cabot. New approximate boundary conditions for les. part 1: Finding the answer via an optimal control strategy. In *APS/DFD meeting*, volume 44 of *Bull. Amer. Phys. Soc.*, New York, 1999.

[113] Tianfeng Lu and Chung K Law. A criterion based on computational singular perturbation for the identification of quasi steady state species: A reduced mechanism for methane oxidation with no chemistry. *Combust. Flame*, 154(4):761–774, 2008.

[114] T. Poinsot and S. Lele. Boundary conditions for direct simulations of compressible viscous flows. *J. Comput. Phys.* , 101(1):104–129, 1992.

[115] L. Selle, F. Nicoud, and T. Poinsot. The actual impedance of non-reflecting boundary conditions: implications for the computation of resonators. *AIAA J.* , 42(5):958–964, 2004.

[116] Wolfgang Polifke, Clifton Wall, and Parviz Moin. Partially reflecting and non-reflecting boundary conditions for simulation of compressible viscous flow. *J. Comput. Phys.* , 213(1):437 – 449, 2006.

[117] W.E. Arnoldi. The principle of minimized iterations in the solution of the matrix eigenvalue problem. *Quart. Appl. Math*, 9(1):17–29, 1951.

[118] M. Sadkane. A block Arnoldi-Chebyshev method for computing the leading eigenpairs of large sparse unsymmetric matrices. *Numerische mathematik*, 64(1):181–193, 1993.

[119] R. Lehoucq and D. Sorensen. Arpack: Solution of large scale eigenvalue problems with implicitly restarted arnoldi methods. www.caam.rice.edu/software/arpack. Technical report, User's guide, 1997.

[120] G. W. Stewart. A Krylov–Schur Algorithm for Large Eigenproblems. *SIAM J. Matrix Anal. Appl.*, 23(3):601–614, March 2001.

[121] A Urbano, L Selle, G Staffelbach, B Cuenot, T Schmitt, S Ducruix, and S Candel. Exploration of combustion instability triggering using Large Eddy Simulation of a multiple injector liquid rocket engine. *Combust. Flame*, 169:1–12, May 2016.

[122] S Ducruix, T Schuller, D Durox, and S Candel. Combustion dynamics and instabilities: elementary coupling and driving mechanisms. *J. Prop. Power* , 19(5):722–734, 2003.

[123] D. Durox, T. Schuller, N. Noiray, and S. Candel. Experimental analysis of nonlinear flame transfer functions for different flame geometries. *Proc. Combust. Inst.* , 32(1):1391–1398, 2009.

[124] Stefan Gröning, Dmitry Suslov, Michael Oschwald, and Thomas Sattelmayer. Stability behaviour of a cylindrical rocket engine combustion chamber operated with liquid hydrogen and liquid oxygen. In *5*$^{\text{th}}$ *European Conference for Aeronautics and Space Sciences (EUCASS)*, Munich, July 2013.

[125] Stefan Gröning, Dmitry Suslov, Justin Hardi, and Michael Oschwald. Influence of hydrogen temperature on the acoustics of a rocket engine combustion chamber operated with LOX/H_2 at representative conditions. In *Space Propulsion 2014*, Cologne, May 2014. Association aéronautique et astronautique de France (3AF).

[126] Stefan Gröning, Justin S Hardi, Dmitry Suslov, and Michael Oschwald. Injector-Driven Combustion Instabilities in a Hydrogen/Oxygen Rocket Combustor. *J. Prop. Power* , 32(3):560–573, May 2016.

[127] Justin Hardi, Michael Oschwald, Samuel Webster, Stefan Gröning, Scott Beinke, Wolfgang Armbruster, Nicolas Blanco, Dmitry Suslov, and Bernhard Knapp. High frequency combustion instabilities in liquid propellant rocket engines: research programme at dlr lampoldshausen. In *Proceedings*, Munich, Germany, 2016. Thermoacoustic Instabilities in Gas Turbines and Rocket Engines: Industry meets Academia.

[128] Geoffrey Searby, Mohammed Habiballah, Aurélie Nicole, and Emmanuel Laroche. Prediction of the efficiency of acoustic damping cavities. *Journal of Propulsion and Power*, 24(3):516–523, 2008.

[129] Danning You, David D Ku, and Vigor Yang. Acoustic waves in baffled combustion chamber with radial and circumferential blades. *Journal of Propulsion and Power*, 2013.

[130] Jacqueline O'Connor, Vishal Acharya, and Timothy Lieuwen. Transverse combustion instabilities: Acoustic, fluid mechanic, and flame processes. *Prog. Energy Combust. Sci.* , 49:1–39, 2015.

[131] Eric Jones, Travis Oliphant, Pearu Peterson, et al. Scipy: Open source scientific tools for python. "http://www.scipy.org/", 2001–now.

[132] C. Sensiau, F. Nicoud, and T. Poinsot. A tool to study azimuthal and spinning modes in annular combustors. *Int. Journal Aeroacoustics*, 8(1):57–68, 2009.

[133] Quentin Douasbin, Stefan Groöning, Annafederica Urbano, Laurent Selle, Justin S. Hardi, Wolfgang Armbruster, and Michael Oschwald. Joint experimental, les and helmholtz analysis of self-excited combustion instabilities in a hydrogen-oxygen rocket combustor. June 2015.

[134] L. Quartapelle and V. Selmin. High-order Taylor-Galerkin methods for non-linear multidimensional problems., 1993.

[135] Olivier Colin and Michael Rudgyard. Development of high-order taylor–galerkin schemes for les. *J. Comput. Phys.* , 162(2):338 – 371, 2000.

[136] A. Urbano, Q. Douasbin, L. Selle, G. Staffelbach, B. Cuenot, T. Schmitt, S. Ducruix, and S. Candel. Study of flame response to transverse acoustic modes from the {LES} of a 42-injector rocket engine. *Proc. Combust. Inst.* , 36(2):2633 – 2639, 2017.

[137] Justin Hardi, Stefan Gröning, Samuel Webster, Scott Beinke, Dmitry Suslov, and Michael Oschwald. Review of experimental test cases for modeling high frequency combustion instability. In *52nd AIAA/SAE/ASEE Joint Propulsion Conference*, page 4893, 2016.

[138] Thomas Fiala, Thomas Sattelmayer, Stefan Gröning, Justin Hardi, Robert Stützer, Samuel Webster, and Michael Oschwald. Comparison between excited hydroxyl radical and blue radiation from hydrogen rocket combustion. *Journal of Propulsion and Power*, 2016.

[139] Sanford Gordon and Bonnie J McBride. *Computer program for calculation of complex chemical equilibrium compositions and applications*, volume 1. National Aeronautics and Space Administration, Office of Management, Scientific and Technical Information Program, 1994.

[140] W Mayer, J Telaar, R Branam, G Schneider, and J Hussong. Raman measurements of cryogenic injection at supercritical pressure. *Heat and Mass Transfer*, 39(8-9):709–719, 2003.

[141] W.O.H. Mayer and R. Branan. Atomization characteristics on the surface of a round liquid jet. *Exp. Fluids* , 36:528–539, 2004.

[142] Daniel T. Banuti and Klaus Hannemann. Supercritical pseudo-boiling and its relevance for transcritical injection. In *50th AIAA/ASME/SAE/ASEE Joint Propulsion Conference*. American Institute of Aeronautics and Astronautics, 2014.

[143] DT Banuti. Crossing the widom-line–supercritical pseudo-boiling. *The Journal of Supercritical Fluids*, 98:12–16, 2015.

[144] D. Y. Peng and D. B. Robinson. A new two-constant equation of state. *Ind. Eng. Chem., Fundam.*, 15(1):59–64, 1976.

[145] Kenneth G Harstad, Richard S Miller, and Josette Bellan. Efficient high-pressure state equations. *AIChE journal*, 43(6):1605–1610, 1997.

[146] B. E. Poling, J. M. Prausnitz, and J. P. O'Connell. *The properties of gases and liquids*. McGraw-Hill, 5th edition, 2001.

[147] J. Bellan. Supercritical (and subcritical) fluid behavior and modeling: drops, streams, shear and mixing layers, jets and sprays. *Prog. Energy Combust. Sci.* , 26:329–366, 2000.

[148] P. Schmitt. *Simulation aux grandes échelles de la combustion étagée dans les turbines à gaz et son interaction stabilité-polluants-thermique*. Phd thesis, INP Toulouse, 2005.

[149] A Urbano and L Selle. Driving and damping mechanisms for transverse combustion instabilities in liquid rocket engines. *J. Fluid Mech.* , 820:R2–12, May 2017.

[150] Peter Welch. The use of fast fourier transform for the estimation of power spectra: a method based on time averaging over short, modified periodograms. *IEEE Transactions on audio and electroacoustics*, 15(2):70–73, 1967.

[151] Mark Sliphorst, Stefan Gröning, and Michael Oschwald. Theoretical and Experimental Identification of Acoustic Spinning Mode in a Cylindrical Combustor. *J. Prop. Power* , 27(1):182–189, January–February 2011.

[152] P Palies, D Durox, T Schuller, and S Candel. Experimental study on the effect of swirler geometry and swirl number on flame describing functions. *Combust. Sci. Technol.* , 183(7):704–717, 2011.

[153] P Palies, T Schuller, D Durox, L Y M Gicquel, and S Candel. Acoustically perturbed turbulent premixed swirling flames. *Phys. Fluids* , 23(3):037101–15, 2011.

[154] P. Palies, D. Durox, T. Schuller, and S. Candel. Nonlinear combustion instability analysis based on the flame describing function applied to turbulent premixed swirling flames. *Combust. Flame*, 158(10):1980 – 1991, 2011.

[155] F. E. Marble and S. Candel. Acoustic disturbances from gas nonuniformities convected through a nozzle. *J. Sound Vib.* , 55:225–243, 1977.

[156] Ignacio Duran and Stephane Moreau. Solution of the quasi-one-dimensional linearized euler equations using flow invariants and the magnus expansion. *J. Fluid Mech.* , 723:190–231, 005 2013.

[157] F. Duchaine, S. Mendez, F. Nicoud, A. Corpron, V. Moureau, and T. Poinsot. Conjugate heat transfer with large eddy simulation application to gas turbine components. *C. R. Acad. Sci. Mécanique*, 337(6-7):550–561, 2009.

[158] Daniel Mejia, Laurent Selle, Rudy Bazile, and Thierry Poinsot. Wall-temperature effects on flame response to acoustic oscillations. *Proc. Combust. Inst.* , 35(3201-3208):3, August 2014.

[159] M Miguel-Brebion, D Mejia, P Xavier, F Duchaine, B Bedat, L Selle, and T Poinsot. Joint experimental and numerical study of the influence of flame holder temperature on the stabilization of a laminar methane flame on a cylinder. *Combust. Flame*, 172:153–161, 2016.

[160] D. J. Harrje and F. H. Reardon. Liquid propellant rocket instability. Technical Report Report SP-194, NASA, 1972.

[161] Ben T Zinn and Manual E Lores. Application of the galerkin method in the solution of non-linear axial combustion instability problems in liquid rockets. *Combustion Science and Technology*, 4(1):269–278, 1971.

[162] Matthew P Juniper. Triggering in thermoacoustics. *International Journal of Spray and Combustion Dynamic* , 4(3):217–237, 2012.

[163] Simon J Illingworth, Iain C Waugh, and Matthew P Juniper. Finding thermoacoustic limit cycles for a ducted burke-schumann flame. *Proc. Combust. Inst.* , 34(1):911–920, 2013.

[164] Mark Sliphorst. *High frequency combustion instabilities of LOx/CH4 spray flames in rocket engine combustion chambers*. PhD thesis, Technische Universiteit Delft, 2011.

[165] Abraham Savitzky and Marcel JE Golay. Smoothing and differentiation of data by simplified least squares procedures. *Analytical chemistry*, 36(8):1627–1639, 1964.

[166] Abraham Savitzky. A historic collaboration. *Analytical chemistry*, 61(15):921A–923A, 1989.

[167] Sophocles J Orfanidis. *Introduction to signal processing*. Prentice-Hall, Inc., 1995.

[168] Matthew E. Harvazinski, William E. Anderson, and Charles L. Merkle. Analysis of self-excited combustion instabilities using two- and three-dimensional simulations. *J. Prop. Power* , 29(2):396–409, mar 2013.

[169] S. Srinivasan, R. Ranjan, and S. Menon. Flame dynamics during combustion instability in a high-pressure, shear-coaxial injector combustor. *Flow, Turb. and Combustion* , 94(1):237–262, 2015.

[170] J.C. Oefelein. Mixing and combustion of cryogenic oxygen-hydrogen shear-coaxial jet flames at supercritical pressure. *Combust. Sci. Technol.* , 178(1):229–252, 2006.

[171] M. Masquelet, S. Menon, Y. Jin, and R. Friedrich. Simulation of unsteady combustion in a lox-gh2 fueled rocket engine. *Aerosp. Sci. Technol.* , 13(8):466–474, 2009.

[172] L Hakim, A Ruiz, T Schmitt, M Boileau, G Staffelbach, S Ducruix, B Cuenot, and S Candel. Large eddy simulations of multiple transcritical coaxial flames submitted to a high-frequency transverse acoustic modulation. *Proc. Combust. Inst.* , 35(2):1461–1468, 2015.

[173] Luigi Crocco, David T. Harrje, and Frederick H. Reardon. Transverse combustion instability in liquid propellant rocket motors. *ARS J.*, 32(3):366–373, jan 1962.

[174] T. Poinsot, T. Echekki, and M. G. Mungal. A study of the laminar flame tip and implications for premixed turbulent combustion. *Combust. Sci. Technol.* , 81(1-3):45–73, 1992.

[175] M. Baum, T. J. Poinsot, and D. Thévenin. Accurate boundary conditions for multicomponent reactive flows. *J. Comput. Phys.* , 116:247–261, 1994.

[176] F. Nicoud. Defining wave amplitude in characteristic boundary conditions. *J. Comput. Phys.* , 149(2):418–422, 1998.

[177] F. Nicoud. On the amplitude of waves in characteristic boundary conditions for euler equations. Technical Report TR/CFD/98/21, CERFACS, 1998.

[178] J. W. Kim and D. J. Lee. Generalized characteristic boundary conditions for computational aeroacoustics. *AIAA J.* , 38:2040–2049, 2000.

[179] Guido Lodato, Pascale Domingo, and Luc Vervisch. Three-dimensional boundary conditions for direct and large-eddy simulation of compressible viscous flows. *J J. Comput. Phys.* , 227(10):5105–5143, 2008.

[180] Yann Moguen, Pascal Bruel, and Erik Dick. Boundary conditions for semi-implicit low mach number flow calculation. In *6th European Congress on Computational Methods in Applied Sciences and Engineering (ECCOMAS-2012)*. Vienna University of Technology, 2012.

[181] Yann Moguen, Pascal Bruel, and Erik Dick. Semi-implicit characteristic-based boundary treatment for acoustics in low mach number flows. *J. Comput. Phys.* , 255:339–361, 2013.

[182] Yann Moguen, Pascal Bruel, Vincent Perrier, and Erik Dick. Non-reflective inlet conditions for the calculation of unsteady turbulent compressible flows at low mach number. *Mechanics & Industry*, 15(3):179–189, 2014.

[183] G. Lodato, P. Domingo, and Vervisch L. Three-dimensional boundary condtions for direct and large-eddy simulation of compressible viscous flow. *J. Comput. Phys.* , 227(10):5105–5143, 2008.

[184] Nelson Dunford, Jacob T Schwartz, William G Bade, and Robert G Bartle. *Linear operators*. Interscience publishers, 1971.

[185] W. Rudin. *Functional Analysis*. International series in pure and applied mathematics. McGraw-Hill, 1991.

[186] G. A. Korn and T. M. Korn. *Mathematical handbook for scientists and engineers. Definitions, Theorems, and Formulas for Reference and Review*. McGraw-Hill Book Company, 1968.

[187] M.B. Priestley. *Spectral analysis and time series*. Probability and mathematical statistics. Academic Press, 1982.

[188] Christophe Nottin. Overview on research activities for numerical prediction and control of combustion instabilities in ramjet powered missiles. *NATO Unclassified Report*, 2012.

[189] Christophe Nottin. *Développement de méthodes de prévision des instabilités de combustion dans les foyers prémélangés*. PhD thesis, Ecole Centrale Paris, 2002.

[190] S Jaensch, M Merk, EA Gopalakrishnan, S Bomberg, T Emmert, RI Sujith, and W Polifke. Hybrid cfd/low-order modeling of nonlinear thermoacoustic oscillations. *Proc. Combust. Inst.* , 36(3):3827–3834, 2017.

[191] J-M Lourier, Michael Stöhr, Berthold Noll, Stefanie Werner, and Andreas Fiolitakis. Scale adaptive simulation of a thermoacoustic instability in a partially premixed lean swirl combustor. *Combust. Flame*, 2017.

[192] Yusuf Özyörük and Lyle N Long. A time-domain implementation of surface acoustic impedance condition with and without flow. *J. Comput. Acoust.* , 5(03):277–296, 1997.

[193] Yusuf Özyörük, Lyle N Long, and Michael G Jones. Time-domain numerical simulation of a flow-impedance tube. *J. Comput. Phys.* , 146(1):29–57, 1998.

[194] Christopher KW Tam and Laurent Auriault. Time-domain impedance boundary conditions for computational aeroacoustics. *AIAA J.* , 34(5):917–923, 1996.

[195] KY Fung, Hongbin Ju, and BhanuPrakash Tallapragada. Impedance and its time-domain extensions. *AIAA J.* , 38(1):30–38, 2000.

[196] Sjoerd W Rienstra. Impedance models in time domain, including the extended helmholtz resonator model. *AIAA J.* , 2686, 2006.

[197] Y Ozyoruk and Lyle N Long. Time-domain calculation of sound propagation in lined ducts with sheared flows. *AIAA J.* , 38(5):768–773, 2000.

[198] Bruno Schuermans, Holger Luebcke, Denis Bajusz, and Peter Flohr. Thermoacoustic analysis of gas turbine combustion systems using unsteady cfd. *ASME Turbo Expo 2005: Power for Land, Sea, and Air*, pages 287–297, 2005.

[199] P Tudisco, R Ranjan, S Menon, S Jaensch, and W Polifke. Application of the time-domain impedance boundary condition to large-eddy simulation of combustion instability in a shear-coaxial high pressure combustor. *Flow, Turb. and Combustion* , 99(1):185–207, 2017.

[200] P Tudisco, R Ranjan, and S Menon. Simulation of transverse combustion instability in a multi-injector combustor using the time-domain impedance boundary conditions. *Flow, Turbulence and Combustion*, pages 1–22, 2017.

[201] Malte Merk, Wolfgang Polifke, Renaud Gaudron, Marco Gatti, Clément Mirat, and Thierry Schuller. Measurement and simulation of combustion noise and dynamics of a confined swirl flame. *AIAA J.* , pages 1–13, 2018.

[202] L. Rayleigh. On the theory of resonance. *Phil. Trans. R. Soc. Lond.*, 161:77–118, 1870.

[203] Pradip Xavier, Abdulla Ghani, Daniel Mejia, Maxence Miguel-Brebion, Michaël Bauerheim, Laurent Selle, and Thierry Poinsot. Experimental and numerical investigation of flames stabilised behind rotating cylinders: interaction of flames with a moving wall. *J. Fluid Mech.* , 813:127–151, 2017.

[204] Siyang Zhong, Xin Zhang, and Xun Huang. A controllable canonical form implementation of time domain impedance boundary conditions for broadband aeroacoustic computation. *J. Comput. Phys.* , 313, 2016.

[205] François Viète. *Opera Mathematica*. Bonaventure et Abraham Elzevier, 1646.

[206] Albert Girard. *Invention Nouvelle En L'Algebre*. Hachette Livre - Bnf, 2013 edition, 1629.

[207] Benjamin Bold. *Famous Problems of Geometry and how to Solve Them*. Dover Books on Mathematics. Dover Publications, 1969.

[208] Peter Borwein and Tamás Erdélyi. *Polynomials and Polynomial Inequalities*, volume 161. Springer Science & Business Media, 2012.

[209] Raymond Seroul. *Programming for Mathematicians*. Universitext - Springer-Verlag. Springer Berlin Heidelberg, 2000.

[210] CC Cardogan. The möbius function and connected graphs. *Journal of Combinatorial Theory, Series B*, 11(3):193–200, 1971.

[211] G.H. Hardy, J.E. Littlewood, and G. Pólya. *Inequalities*. Cambridge University Press, 1952.

[212] Franchine Ni. *Accounting for complex flow-acoustic interactions in a 3D thermo-acoustic Helmholtz solver*. PhD thesis, Université de Toulouse, April 2017.

[213] N. Noiray, D. Durox, T. Schuller, and S. Candel. Passive control of combustion instabilities involving premixed flames anchored on perforated plates. *Proc. Combust. Inst.* , 31:1283–1290, 2007.

[214] A. Most, N. Savary, and C. Bérat. Reactive flow modelling of a combustion chamber with a multiperforated liner. In *43rd AIAA/ASME/SAE/ASEE Joint Propulsion Conference & Exhibit*, 2007.

[215] E. Gullaud, S. Mendez, C. Sensiau, F. Nicoud, and T. Poinsot. Effect of multiperforated plates on the acoustic modes in combustors. *C. R. Acad. Sci. Mécanique*, 337(6-7):406–414, 2009.

[216] S. Mendez and F. Nicoud. Adiabatic homogeneous model for flow around a multiperforated plate. *AIAA J.* , 46(10):2623–2633, 2008.

[217] Emmanuel Motheau and T Lederlin. Les investigation of the flow through an effusion-cooled aeronautical combustor model. *Flow, turbulence and combustion*, 88(1-2):169–189, 2012.

[218] M. S. Howe. On the theory of unsteady high reynolds number flow through a circular aperture. *Proc. R. Soc. Lond. A , Mathematical and Physical Sciences*, 366(1725):205–223, 1979.

[219] J.-L. Champion, P. Di Martino, and X. Coron. Influence of flow characteristics on the discharge coefficient of a multiperforated wall. In *Turbo Expo 2005, Reno Hilton, Reno Tahoe, Nevada USA, June 6-9 2005*, volume GT2005-68904, 2005.

[220] S. H. Lee, J. G. Ih, and K. S. Peat. A model of acoustic impedance of perforated plates with bias flow considering the interaction effect. *J. Sound Vib.* , 303(3-5):741–752, 2007.

[221] S. Mendez and J. Eldredge. Acoustic modeling of perforated plates with bias flow for large-eddy simulations. *J. Comput. Phys.* , 228(13):4757–4772, 2009.

[222] Annafederica Urbano, Quentin Douasbin, and Laurent Selle. Analysis of coaxial-flame response during transverse combustion instability. In *Proceedings of the 7th European Conference for Aeronautics and Space Sciences*, Milano, Italy, 3-6 july 2017, 2017. EUCASS.